

THERMODYNAMIC CHARACTERISATION OF  
SEMI-SOLID PROCESSABILITY IN ALLOYS BASED  
ON AL-SI, AL-CU AND AL-MG BINARY SYSTEMS

Thesis submitted for the degree of

Doctor of Philosophy

at the University of Leicester

by

**Duyao Zhang**, BEng

Department of Engineering

University of Leicester

March 2015

## Summary

The processing window is important for the semisolid processability of alloys. Applications of semi-solid metal (SSM) processing, especially aluminium alloys have been expanding for their excellent mechanical properties. However, the alloys well suited and commercially used for SSM processing today are limited in types. The main purpose of this Ph.D. project is to understand what makes an alloy suitable for SSM processing on both aspects of thermodynamics and kinetics.

This research started with a fundamental study of binary alloys based on Al-Si, Al-Cu and Al-Mg systems (wt%): Al-1Si, Al-5Si, Al-12Si and Al-17Si; Al-1Cu, Al-2Cu and Al-5Cu; Al-0.5Mg, Al-3Mg and Al-5.5Mg. These are representative of Si, Cu and Mg contents in commercial alloys used for SSM processing. The Single-Pan Scanning Calorimeter (SPSC) and Differential Scanning Calorimeter (DSC) were used to investigate the liquid fraction changes during heating and cooling of these binary alloys. Thermo-Calc and DICTRA (Diffusion-Controlled TRAnsformations) software have been used to predict the fraction liquid versus temperature taking into account both thermodynamics and kinetics. Comparison of the predictions with experimental data revealed that the simulation results show the same pattern with experimental results in the fraction liquid-temperature relationship. However, the SPSC results are closer to the prediction than DSC curves are, even with the relatively large sample size associated with SPSC. This is potentially a significant result as predicting the liquid fraction versus temperature for the heating of a billet for semi-solid processing remains one of the challenges. The results also suggest that the fraction liquid sensitivity to time should be identified as a critical parameter of the process window for semi-solid processing in addition to the fraction liquid sensitivity to temperature. For microstructure investigation, microanalysis techniques, including Scanning Electron Microscopy (SEM) and micro-indentation testing, have been used on polished sections, and compared to theoretical predictions.

In addition, some parts of this project are in cooperation with General Research Institute for Nonferrous Metals (GRINM), which aims to design and develop high performance semi-solid alloys. Thermodynamic analysis (both predictions and experiments) were carried out on thixoformed 319s (2.95Cu, 6.10Si, 0.37Mg, wt%) and 201 (4.80Cu,

0.7Ag, wt%) aluminium alloys. SEM techniques and Transmission Electron Microscopy (TEM) were used for the microstructural characterisation. The results showed that the DSC curves were sensitive to microsegregation in SSM alloys and resulted in a lower liquid fraction than the cast alloys calculated through the integration method from the DSC results.  $\text{Al}_2\text{Cu}$  phase in SSM alloys 319s and 201 can be dissolved into matrix up to 0.4 % before melting temperature under 3K/min heating rate when compared with 10K/min heating rate. The DSC scan rate should be carefully selected as higher heating rate can inhibit dissolution of the intermetallic phases during heating leading to less accurate liquid fractions predictions.

**This thesis is dedicated to my parents**

**Bao Zhen Zhang and Yue Ju Wang**

## Acknowledgments

I would like to express my sincere gratitude to my academic supervisors, Prof Helen Atkinson and Prof Hongbiao Dong for their supervision, encouragement and enthusiastic support throughout my Ph.D. Your advice on both research as well as on my career have been priceless. Without your efforts and guidance, I would not have accomplished my study. The studentship support provided by Department of Engineering, University of Leicester is gratefully acknowledged.

My sincere thanks also goes to my undergraduate tutor, Professor Bingshe Xu, for pushing me to succeed since my first day of University and engendering my desire to further my interest in materials science.

I also want to thank GRINM for the supply of materials and Prof Qiang Zhu for the helpful discussion and valuable comments.

I would like to thank all the staff in the Mechanics of Materials group at The University of Leicester who have given me support during project, especially Mr Graham Clarke for his time and patience in training me in the skills necessary to undertake my studies. Dr David Weston, Dr Simon Gill and Dr Simon Lawes are also thanked for their valuable discussions and notable contributions to the current work.

A special thanks to my friends and research students in the department: Mike Dodge, Richard Earp, Yu Xie, Scott Simmonds, Adam Brown, Sinan Kandemir, Sinan Savas, Huijuan Dai, Cheng Feng, Zhaonan Dong, Hualong Zheng, Kang Du, Lei Fu, Chen Li and Dr Jie Shen for the help and friendship. Thank you for providing me a very warm and comfortable study environment that I have been here.

All the technicians involving in this project are appreciated for their continued assistance.

Finally, I would particularly like to express my deepest thank to my beloved wife Rui Li, for her love and continuous support. I also would like to thank my aunt Xiaoling for her moral and financial support.

# Table of Contents

<b>Summary.....</b>	<b>I</b>
<b>Acknowledgments .....</b>	<b>IV</b>
<b>List of Symbols .....</b>	<b>IX</b>
<b>Chapter 1 Introduction .....</b>	<b>1</b>
<b>Chapter 2 Literature Review .....</b>	<b>3</b>
2.1 <i>Aluminium Alloy Development.....</i>	3
2.1.1 Al-Si Binary Alloy .....	4
2.1.1.1 Commercial Al-Si Alloys .....	7
2.1.2 Al-Cu Binary Alloys.....	8
2.1.2.1 Commercial Al-Cu Alloys .....	9
2.1.3 Al-Mg Binary Alloys.....	9
2.1.3.1 Commercial Al-Mg Alloys .....	10
2.1.4 High Strength Casting Aluminium Alloy 201 .....	10
2.1.5 Al-Si-Cu 319 Type Alloy .....	12
2.2 <i>Semi-Solid Metal (SSM) Processing .....</i>	14
2.2.1 Background.....	14
2.2.2 Types of SSM Processing.....	14
2.2.2.1 Rheocasting.....	15
2.2.2.2 Thixoforming .....	16
2.2.3 Advantages of SSM Processing.....	18
2.2.4 Criteria of SSM Processability .....	19
2.3 <i>Thermodynamics .....</i>	22
2.3.1 The Three Laws of Thermodynamics.....	22
2.3.2 Constant-Pressure Processes .....	23
2.3.3 The Enthalpy Change .....	24
2.3.4 Latent Heat .....	24
2.3.5 Heat Capacity .....	25
2.3.6 Phase Diagram and Lever Rule .....	25
2.3.7 The Heat Capacity $C_P$ and Heat Content of an Alloy.....	27
2.4 <i>Theory of Solidification.....</i>	29
2.4.1 Nucleation.....	29
2.4.1.1 Homogeneous Nucleation.....	30
2.4.1.2 Heterogeneous Nucleation.....	31
2.4.2 Nucleation Rate .....	32

2.4.3 Dendrite Growth .....	32
2.4.4 Homogenization and Solutionising .....	33
2.5 <i>Thermodynamic Prediction</i> .....	34
2.5.1 Equilibrium Model .....	34
2.5.2 Scheil Model.....	35
2.5.3 Thermodynamic Prediction of SSM Processability .....	37
2.5.3.1 Predictions by Kazakov .....	37
2.5.3.2 Predictions by Fan and Co-workers.....	38
2.5.3.3 Predictions by Camacho .....	39
2.5.3.4 Predictions by Liu .....	40
2.5.3.5 Predictions by Other Authors .....	41
2.6 <i>Theory of Melting</i> .....	42
2.6.1 Lindemann Criterion .....	43
2.6.2 Born Criterion.....	44
2.6.3 Defect Induced Melting.....	44
2.6.4 Surface Melting .....	47
2.6.5 Melting of Low Melting Phase or Impurities .....	50
2.7 <i>Objectives of the Work</i> .....	50
<b>Chapter 3 Background of Prediction and Experiment .....</b>	<b>52</b>
3.1 <i>Thermodynamic Prediction</i> .....	52
3.1.1 CALPHAD Modelling of Thermodynamics .....	53
3.1.2 Thermo-Calc Software .....	54
3.1.3 Diffusion-Controlled Transformations (DICTRA) Software.....	54
3.1.3.1 Mobilities.....	56
3.1.3.2 Boundary Conditions .....	57
3.2 <i>Calorimetry</i> .....	57
3.2.1 Differential Scanning Calorimetry (DSC).....	58
3.2.1.1 Heat Flux DSC.....	59
3.2.1.2 Liquid Fraction Measurement.....	62
3.2.1.3 Problems with DSC .....	64
3.2.2 Single-Pan Scanning Calorimeter (SPSC).....	65
3.2.2.1 Introduction.....	65
3.2.2.2 Enthalpy Calculations .....	66
3.2.2.3 Liquid Fraction Measurement.....	68
3.3 <i>X-Ray Diffraction</i> .....	68
3.4 <i>Vickers Hardness</i> .....	70
<b>Chapter 4 Experimental Procedure .....</b>	<b>72</b>
4.1 <i>Introduction</i> .....	72
4.2 <i>As-received Materials</i> .....	72

4.2.1 Pure Aluminium .....	72
4.2.2 Binary Alloys.....	72
4.2.3 319s Alloy and 201 Alloy.....	74
4.3 <i>Thermodynamic Prediction by Thermo-Calc and DICTRA</i> .....	75
4.3.1 Equilibrium and Scheil Predictions by Thermo-Calc.....	75
4.3.2 DICTRA Simulation.....	76
4.3.2.1 Solidification Path Model .....	76
4.3.2.2 Cell Size Impact.....	77
4.3.2.3 Heating and Re-heating .....	77
4.3.2.4 Element Composition Profiles at one Specific Temperature .....	78
4.3.3 Diffusion Coefficients of Si, Cu and Mg in FCC(Al) and Liquid(Al) Phases	78
4.4 <i>Heat Treatment for Alloy 319s and Alloy 201</i> .....	79
4.5 <i>Experimental Investigation by SEM</i> .....	79
4.6 <i>Experimental Investigation by TEM</i> .....	80
4.7 <i>Experimental Investigation by XRD</i> .....	82
4.8 <i>Thermal Analysis by DSC</i> .....	83
4.9 <i>Thermal Analysis by SPSC</i> .....	83
4.10 <i>Hardness Testing</i> .....	84
<b>Chapter 5 Results.....</b>	<b>85</b>
5.1 <i>Introduction</i> .....	85
5.2 <i>Starting Materials for Thermal Analysis</i> .....	85
5.2.1. Microstructures .....	85
5.2.1.1 Al-Si Binary Alloys. ....	85
5.2.1.2 Al-Cu Binary Alloys .....	88
5.2.1.3 Al-Mg Binary Alloys .....	89
5.2.2 Hardness Properties .....	90
5.3 <i>Prediction Results</i> .....	92
5.3.1 Equilibrium and Scheil Calculations by Thermo-Calc.....	92
5.3.2 DICTRA Simulation Results .....	95
5.3.2.1 Diffusion Coefficients of Si, Cu and Mg in FCC(Al) and Liquid(Al) Phases.....	95
5.3.2.2 Cell Size Impact.....	96
5.3.2.3 Element Composition Profiles at one Specific Temperature .....	99
5.3.2.4 Liquid Fraction Calculated by DICTRA .....	100
5.3.2.5 Heating and Re-heating .....	107
5.4 <i>Thermal Analysis by DSC</i> .....	109
5.4.1 DSC Traces Results .....	109
5.4.2 Calculated Liquid Fraction by DSC .....	116



5.5 Thermal Analysis by SPSC.....	126
5.5.1 SPSC Study with Pure Aluminium.....	126
5.5.2 Calculated Liquid Fraction by SPSC.....	128
5.6 Comparison between Predictions and Experiments .....	135
5.7 Study of 319s Alloy.....	141
5.7.1 Determination of the Dissolution from DSC Traces .....	141
5.7.2 SPSC Analysis.....	146
5.7.3 XRD Analysis.....	148
5.7.4 Microstructures.....	150
5.8 Study of 201 Alloy .....	156
5.8.1 Determination of the Dissolution from DSC Traces .....	156
5.8.2 SPSC Analysis.....	158
5.8.3 Microstructures.....	160
5.8.4 Predictions by Thermo-Calc.....	165
<b>Chapter 6 Discussion .....</b>	<b>167</b>
6.1 Effects of Alloy Elements on Microstructures.....	167
6.2 Effects of Alloy Elements on Hardness .....	167
6.3 Simulations of Aluminium Binary alloys.....	168
6.3.1 Equilibrium and Scheil by Thermo-Calc.....	168
6.3.2 DICTRA Simulation vs. Scheil and Equilibrium Mode.....	169
6.3.2.1 Differences between DICTRA and Thermo-prediction.....	169
6.3.2.2 Cell Size Impact on DICTRA Simulation .....	170
6.3.2.3 Heating Behaviour Simulations by DICTRA .....	170
6.4 The Experimental Results vs. Prediction Results.....	171
6.5 Process Window.....	174
6.6 Dissolution of Al <sub>2</sub> Cu Phase in 319s and 201 Alloys .....	179
<b>Chapter 7 Conclusions.....</b>	<b>181</b>
<b>Chapter 8 Further Work.....</b>	<b>183</b>
<b>References.....</b>	<b>185</b>
<b>Appendices.....</b>	<b>196</b>
Appendix A: Code for DICTRA Solidification Simulation (Al-Si Alloy).....	196
Appendix B Code for DICTRA Solidification Simulation (Al-Cu Alloy).....	198
Appendix C Code for DICTRA Solidification Simulation (Al-Mg Alloy).....	200
Appendix D Code for DICTRA Heating Simulation (Al-5.08wt%Si Alloy) .....	202
Appendix E Code for DICTRA Re-heating Simulation (Al-5.08wt%Si Alloy).....	204

## List of Symbols

$C$	Heat capacity	$\Delta S_{f,\alpha}$	Entropy of fusion of phase $\alpha$
$U$	Internal energy	$\Delta U$	Total internal energy in change of the system
$q$	Heat	$w$	Work done
$\Delta S$	Change in entropy	$H$	Enthalpy
$\Delta H$	Enthalpy change	$T_m$	Melting temperature
$P$	Pressure	$V$	Volume
$q_P$	System heat under constant pressure	$L$	Latent heat
$C_P$	Heat capacity in constant pressure	$k$	Distribution coefficient
$C_{P,S}$	Heat capacity of solid	$C_{P,L}$	Heat capacity of liquid
$c_S$	Solid composition	$c_L$	Liquid composition
$c_0$	Initial composition	$D_S$	Diffusion in the solid
$m_S$	Slope of solidus	$m_L$	Slope of liquidus
$D_L$	Diffusion in the liquid	$f_S$	Fraction of solid
$f_L$	Fraction of liquid	$T_L$	Temperature at liquidus
$\Delta s_f$	Difference in the slope of the Gibbs free energy-temperature plot of two phases	$\Delta g$	Gibbs free energy difference between solid and liquid per unit volume
$r$	Radius	$\sigma$	Interface energy
$G$	Gibbs free energy	$S$	Entropy
$\Delta G$	Change in Gibbs free energy	$r^*$	Critical radius
$\sigma_{LC}$	Surface energy of liquid-nucleus interface	$\sigma_{CS}$	Surface energy of nucleus-solid interface
$\sigma_{LS}$	Surface energy of liquid-solid, interface	$\theta$	Angle
$I_{heter}$	Exponential kinetic coefficient	$k_B$	Boltzmann's constant
$I_{heter}^0$	Pre-exponential coefficient	$n_j$	Amount in moles of species j present in the system
$\mu_j$	Chemical potential of species j	$N$	Number of species in the system
$a_{ij}$	Number of units of component i per species j	$M$	Number of components in the system
$r_i$	Number of moles of component	$T$	Temperature
$T_{RP}$	Temperature of the reference pan thermocouple	$T_S$	Temperature of the sample
$T_R$	Temperature of the reference	$T_F$	Temperature of the furnace

$T_{SP}$	Temperature of the sample pan thermocouple	$T_f$	End of melting temperature
$\Delta T_{FS}$	$T_F - T_S$	$\Delta T_{FR}$	$T_F - T_R$
$\Delta T_{RS}$	$T_R - T_S$	$\Delta T_{RSP}$	$T_R - T_{SP}$
$\Delta T_{DS}$	Temperature differences between inner and outer crucible for sample	$\Delta T_{DE}$	Temperature differences between inner and outer crucible for empty
$\Delta T_{DC}$	Temperature differences between inner and outer crucible for calibrant	$m$	Mass
$a$	Heat transfer coefficient	$t$	Time
$C_C$	Change in heat substance per degree of the calibrant	$C_S$	Change in heat substance per degree of the sample
$C_E$	Change in heat substance per degree of the empty pan	$\Delta T$	Change in temperature
$\Delta S_m$	Entropy change	$R$	Gas constant
$W_l$	Number of independent ways of realizing the molten state	$W_S$	Number of independent ways of realizing the solid state
$\nu$	Frequency	$c$	Lindemann constant
$E_m$	Energy barrier	$T^*$	Temperature at which the vacancy decomposition happens
$C_m$	The concentration of migrating atoms	$\Delta G_k^*$	Gibbs energy barrier
$M_k$	Atomic mobility	$M_k^0$	Frequency factor
$z$	Heating rate	$F$	Load
$d^*$	Diameter of the impression	$a^*$	Atomic spacing
$d$	Spacing	$Q$	Activation energy
$D_0$	Diffusion coefficient	$\lambda$	Wavelength

# Chapter 1 Introduction

This work is motivated by our interest in developing a prediction model for simulating the liquid fraction as a function of temperature for aluminium series alloys. Aluminium alloys with a wide range of unique properties are used in engineering structures. The development of light parts using aluminium materials has been studied with die-casting and squeeze casting, which can directly fabricate the object shape in the liquid state. However, porosity occurs in die-castings from the turbulent flow of the molten metal into the die cavity. In the squeeze-casting process, the initial superheated molten metal shortens the die life. To overcome these problems, semi-solid metal (SSM) processing has been widely studied. SSM processing is an advanced method for material forming using the thixotropic behaviour of materials with non-dendritic microstructure in the semisolid state to form near net shaped products [1].

The typical alloying elements of aluminium alloys are copper (Cu), magnesium (Mg), silicon (Si) and zinc (Zn). As the major alloying elements, they offer a possibility of modifying mechanical or physical properties while keeping the good castability. However, the processability of an alloy for SSM processing is limited by several factors (as discussed in Section 2.2). Assessing the processability of alloys is therefore significant for semisolid processing. Liu *et al.* [2] argued that the existence of a ‘knee’ in the fraction liquid versus temperature for hypoeutectic alloys at around 50% liquid allows control of the process of thixoforming. More recently, Curle *et al.* [3, 4] demonstrated, both pure Al and binary Al-Si eutectic alloy can be rheo- or semi-solid processed because of the solidification kinetics during the thermo-arrest despite the fact that there is no freezing range. In order to gain a deeper understanding of the above, the first part of this work focuses on the kinetic behaviour during melting and solidification to understand the SSM processability of alloys. The research is carried out with a multifaceted approach including characterisation, thermodynamic modelling, and analysis. Study is carried out on a range of selected aluminium binary alloys, which represent the Si, Cu and Mg contents in commercial alloys used for semi-solid processing. To determine the liquid fraction as a function of the temperature of the alloys, thermodynamic predictions were evaluated by Thermo-Calc and DICTRA software. Thermo-Calc (Version: TCW5) software was used to predict the phases in both equilibrium and non-equilibrium (Scheil) solidification. DICTRA, which allows

diffusion (i.e. kinetics) to be taken into account alongside thermodynamic prediction, was used to simulate the liquid fraction during solidification. The predictions were compared with experimental results from Differential Scanning Calorimeter (DSC) and also from Single-Pan Scanning Calorimeter (SPSC).

The SPSC is a novel calorimetry technique developed by Dong and Hunt [5] to solve the smearing effect in a conventional DSC. The advantages of the new calorimeter include enclosing the sample in a uniform temperature and providing a large thermal resistance between the sample and its surroundings. It overcomes the problems of DSC (i.e. the measured temperature difference is not proportional to the difference in heat capacity between the sample and reference; the sample thermocouple doesn't measure the temperature of the sample since a large temperature difference arises between the sample and the sample thermocouple) by simple engineering solutions. The differences between predictions and experiments were investigated. The effects of the level of added alloy content on the microstructures and the SSM processability of binary alloys were evaluated.

Currently, the excellent mechanical properties and castability of Al-Si-Cu-Mg (319) alloy make it popular for automotive and aerospace applications. Moreover, further demand for higher strength casting commercial aluminium alloys (i.e. 201 alloy) is also foreseeable. Copper, as an important alloying element in aluminium alloys, may contribute to the strength age hardening response but increases hot tearing. During the processing, these alloying elements may form different intermetallic compounds, so in the second part of this work, how the intermetallic compounds affect the calculations of liquid fraction under calorimetrical analysis was evaluated. Both thixoformed 319s (2.95Cu, 6.10Si, 0.37Mg, wt%) and 201 (4.80Cu, 0.7Ag, wt%) aluminium alloys were chosen for this work. The dissolution of copper intermetallics, especially the  $\text{Al}_2\text{Cu}$  phase, was investigated using DSC. The differences of melting of the copper intermetallic phases between SSM processing state and re-solidification state, relating the dissolution of the  $\text{Al}_2\text{Cu}$  phase with endothermic peaks during DSC runs were evaluated. SEM and TEM techniques were used for the microstructural characterisation. Post-forming heat treatment was carried out for the optimisation of homogenisation kinetics of thixoformed structures containing spheroidal primary crystals.

## **Chapter 2 Literature Review**

The following chapter contains six main sections:

The first section gives a brief overview of aluminium-silicon, aluminium-copper and aluminium-magnesium binary alloys, this is then followed by information on high strength casting aluminium alloy 201 and Al-Si-Cu-Mg base alloy (319) in terms of the role of alloying elements, phases present, solidification characteristics, heat treatment and homogenization.

The second section features SSM processing including the background, determination of liquid fraction, processability and types of forming process. The focus is on the critical parameters of SSM processability, which is the main interest of this thesis.

An objective of this project is to use a novel scanning calorimeter to measure the enthalpy change and heat capacity of the sample as a function of temperature, and then calculate the liquid fraction function. In the third section, the background theory of materials thermodynamics will be discussed briefly, including enthalpy change, latent heat and phase diagram to assist understanding the thermal analysis during heating and cooling in calorimetry.

In the fourth and fifth sections, solidification theory and information on thermodynamic simulation models, both equilibrium and non-equilibrium ones are described. In addition, the thermodynamic predictions of SSM processability are discussed.

The sixth section includes a brief description of melting theory. Then, a summary of the objectives of this project is given.

### ***2.1 Aluminium Alloy Development***

Aluminium alloys are widely used in applications ranging from food packaging to the aerospace industry. They are attractive because of a number of desirable physical properties, including advantageous strength to weight ratio, fracture toughness and corrosion resistance.

### **2.1.1 Al-Si Binary Alloy**

Alloys with silicon as the major alloying addition are of the most importance among the aluminium casting alloys. The Al-Si system has high fluidity imparted by the relatively large volumes of eutectic. The advantages of Al-Si casting alloys include high resistance to corrosion and good weldability in addition to the fact that the silicon phase reduces both shrinkage during solidification and the coefficient of thermal expansion of the cast product [6].

The Al-Si system is a simple binary eutectic with limited solubility of aluminium in silicon and limited solubility of silicon in aluminium [7]. Two solid solution phases are known in the Al-Si system according to the equilibrium phase diagrams (Fig. 2.1): FCC (Al) and diamond cubic Si [8]. The solubility of silicon in aluminium reaches a maximum 1.65wt% at the eutectic temperature, and the maximum solubility of Al in Si is 0.016% at% at 1190 °C [9]. The only invariant reaction in the system, other than the melting of pure Al and pure Si, is the eutectic transformation of liquid solution to solid solution of Al and nearly pure Si, which occurs at 577.6 °C,  $L \rightarrow Al_{eut} + Si_{eut}$ . (L is the liquid phase) [9]. Fig. 2.1 shows that the Al-Si eutectic can form as follows:

1. Directly from the liquid in the case of a silicon concentration of 12.6% (i.e., for eutectic Al-Si alloy),
2. In the presence of primary aluminium in the case of silicon contents <12.6% (i.e., for hypoeutectic Al-Si alloys), and
3. In the presence of primary silicon crystals in the case of silicon contents >12.6% (for hypereutectic Al-Si alloys).

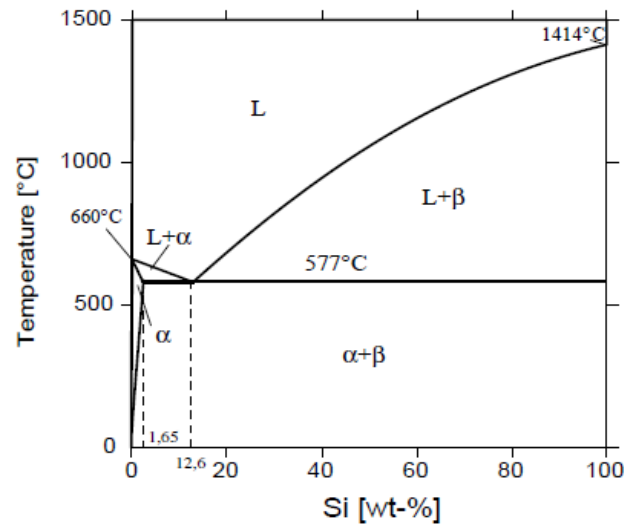


*Fig. 2.1 The Al-Si binary phase diagram*

Silicon can reduce the alloy thermal expansion coefficient, increase corrosion and wear resistance, and improve alloy machining characteristics [10]. When the Al-Si alloy solidifies, the primary aluminium forms and grows in dendrites or the silicon phase forms and grows in angular primary particles. When the eutectic point is reached, the eutectic Al-Si phases nucleate and grow until the end of solidification. At room temperature, hypoeutectic alloys consist of a soft and ductile primary aluminium phase and a hard and brittle eutectic silicon phase. Hypereutectic alloys usually contain coarse, angular primary silicon particles as well as a eutectic silicon phase (see Fig. 2.2).

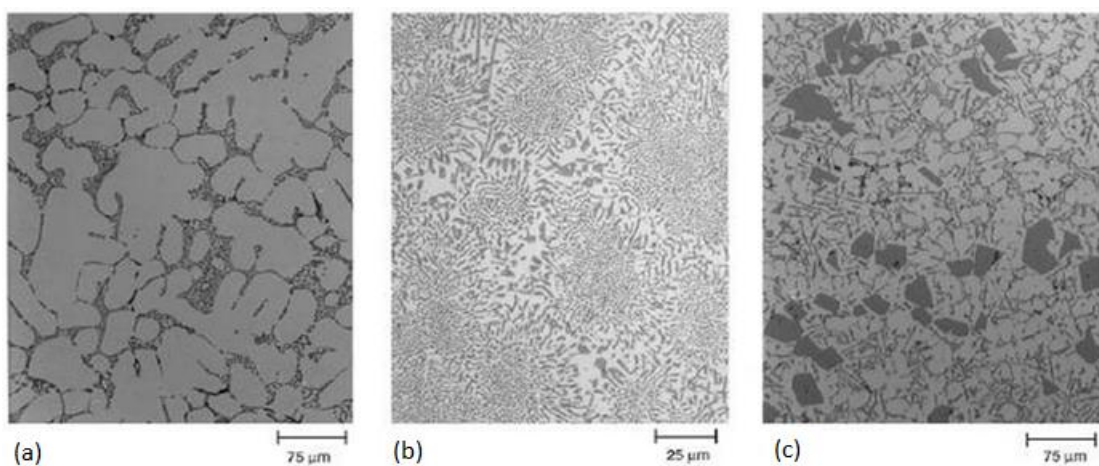


*Fig. 2.2 SEM image of commercial cast Al-Si alloys. (a) Microstructure of hypoeutectic alloy (1.65-12.6 wt% Si). (b) Microstructure of eutectic alloy (12.6 wt% Si). (c) Microstructure of hypereutectic alloy (>12.6 wt% Si) [11]*



The effect of composition on mechanical properties of Al-Si alloys was studied by Torabian *et al.* [12] as shown in Table 2.1. All the alloys were cast in the same condition. It can be observed that as the silicon percentage in the alloy increases, the strength properties reach a peak at the eutectic compositions. However, the hardness increases and the elongation decrease continuously with increasing silicon content. This is mainly due to the size, shape and distribution of silicon particles in the structures. Silicon is present as fine particles and is uniformly distributed in the structure, and hence the strength properties increase. But when the primary silicon appears as coarse polyhedral particles, the strength properties decrease with increasing silicon content, but the hardness continues increasing because of the increase in the silicon content [13].

Composition (wt%)	Ultimate tensile strength (MN m <sup>-2</sup> )	0.2% tensile proof stress (MN m <sup>-2</sup> )	Elongation (%)	Hardness (VHN)	Density (kg m <sup>-3</sup> ×10 <sup>3</sup> )
Al-2%Si	127.3	52.6	12.4	39.5	2.68
Al-4%Si	142.2	58.3	10.2	47.3	2.67
Al-6%Si	155.7	64.8	9.6	55.6	2.65
Al-8%Si	169.6	71.5	7.2	61.6	2.62
Al-11.6%Si	185.4	80.0	5.8	67.0	2.59
Al-12.5%Si	189.0	82.5	5.4	70.0	2.57
Al-15%Si	183.25	77.7	4.7	72.5	2.55
Al-17%Si	175.8	73.7	3.0	76.6	2.53
Al-20%Si	172.4	72.0	2.5	81.0	2.50

*Table 2.1 Mechanical properties of cast Al-Si alloys [12]*

Al-Si binary alloys usually contain other elements such as copper, magnesium, manganese, zinc, and iron in composition. The solubility of these elements in aluminium usually increases with increasing temperature. Si, Mn, and Fe usually tend to form an Al<sub>12</sub>(Fe, Mn)<sub>3</sub>Si phase. The wide variety of intermetallic phases in aluminium alloys occur because aluminium is highly electronegative and trivalent [13, 14].

### ***2.1.1.1 Commercial Al-Si Alloys***

Due to economic and environmental demands, it is becoming increasingly important to reduce vehicle weight. For such an objective, Al-Si alloys such as Al 356.0 (Al-7Si-0.3Mg, wt%) and Al 390.0 (Al-17.0Si-4.5Cu-0.6Mg, wt%) [15] have been commercially used to produce an engine block due to their high strength over weight ratio. However, commercial uses for hypereutectic alloys are comparatively limited. This is because high Si content makes them difficult to cast and machine. It adds a large amount of heat capacity when high Si content is alloyed into Al, which must be removed from the alloy to solidify during the casting operation. Major variation in the sizes of the primary Si particles can be found in different areas of the cast structure, causing significant heterogeneity in the mechanical properties. The primary crystals of Si must be refined so that higher hardness and wear resistance can be acquired. Due to these reasons, hypereutectic alloys are not very cost-effective to fabricate because they have a broad solidification range that results in poor castability and requires extra foundry processes to control the microstructure and the high heat of fusion. On the other hand, the usage of hypoeutectic and eutectic alloys is very widespread in industries for low temperature applications. However, there is less use for high temperature applications in the range 25°C to 400°C because the mechanical properties such as tensile strength tends to degrade [16].

The mechanical properties of Al-Si base alloys have been reviewed in [10, 17, 18]. It is pointed out that the silicon phase, intermetallic precipitates and casting defects are all responsible for the alloys' fatigue and wear properties. Coarse silicon usually reduces fatigue life due to microcrack initiation. Higher silicon content can increase alloy wear resistance as it increases the hardness of alloys. Fine precipitates can usually strengthen the alloy while sharp and coarse precipitates degrade these two properties. Casting defects such as porosity and inclusions usually reduce the alloy's fatigue and wear resistance due to microcrack initiation. Alloying elements can form fine precipitates, refine grain size, modify the silicon phase morphology, and reduce the effects of defects and thus can usually increase both fatigue and wear resistance.

### 2.1.2 Al-Cu Binary Alloys

Copper is one of the most important alloying elements for aluminium, because of its appreciable solubility and strengthening effect. Many commercial alloys contain copper, either as the major addition or among the principal alloying elements, in the concentrations of 1 to 10%. It is used frequently in combination with magnesium.

The aluminium-rich end of the phase diagram is eutectic Al-Al<sub>2</sub>Cu. The eutectic temperature is 548.2 °C, and the composition of the eutectic liquid is Al-33.2wt%Cu in equilibrium with an aluminium-rich solid solution containing 5.7 wt% copper [14]. The Al<sub>2</sub>Cu intermetallic phase has a range of compositions from 53.3 to 53.9 wt% at 400 °C, compositions slightly deficient in copper for the quoted stoichiometry. The binary phase diagram is shown in Fig. 2.3 as below.

The precipitation reactions are as follows [19]: supersaturated solid solution → coherent platelike GP (Guinier- Preston) zones//{001}<sub>Al</sub> → coherent plate like  $\theta''$ //{001}<sub>Al</sub> → semicoherent platelike  $\theta'$ //{001}<sub>Al</sub> → noncoherent  $\theta$ .  $\theta$  is Al<sub>2</sub>Cu. Those precipitations are not showing in Fig. 2.3 because the phase diagram is under equilibrium condition.

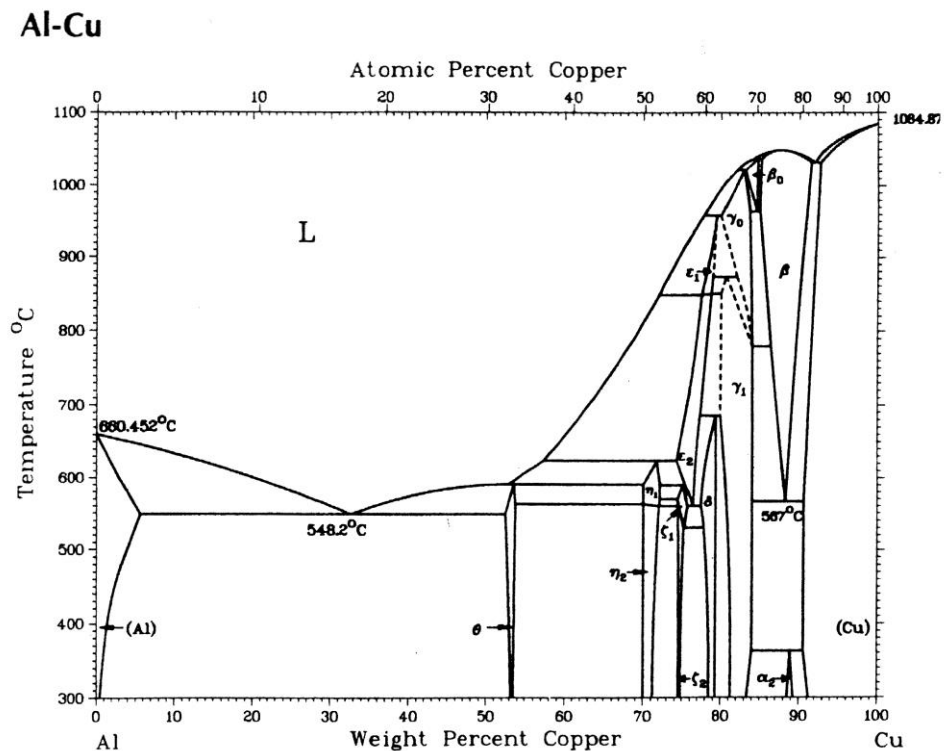


Fig. 2.3 The Al-Cu binary phase diagram [20]

### ***2.1.2.1 Commercial Al-Cu Alloys***

Alloys with Cu as the major alloying addition were the first to be widely used for aluminium alloy castings. The alloys have good properties with age-hardening heat treatment. There are only a few commercial alloys based on the binary system. For example, alloy 2011 (Al-5.5wt%Cu) is used where good machining characteristics are required [21]. Another binary alloy is alloy 2219 (Al-6.3wt%Cu), which is used for forging sheets and plates.

Alloys based on the Al-Cu system but with controlled additions of other elements are widely used. Several compositions are available which have elevated the temperature properties. Examples are alloy 242 which is Al-4Cu-2Ni-1.5Mg and alloy 238 (Al-10Cu-3Si-0.3Mg, wt%). Alloy 238 is mainly used for permanent mould casting soleplates while alloy 242 has been used for the air-cooled cylinder heads for aircraft engines [21].

### ***2.1.3 Al-Mg Binary Alloys***

Aluminium and magnesium alloys would achieve weight reduction and high efficiency of production. Under equilibrium conditions, the concentration of magnesium in the aluminium structure is 0.21 at.% at room temperature; maximum solubility at 450 °C has been reported as 16.23 at.% [22], or 18.6 at.% [23]. The Al-Mg binary phase diagram is presented in Fig. 2.4. The main alloying element, Mg, is added for strength. Mg has a high solubility in solid solution and a similar size with aluminium in atomic radius and therefore it provides the most effective enhancement of strength among all alloying additions in the aluminium solid solution.

At 38 at% Mg, the phase diagram predicts the formation of thermodynamically stable  $\text{Al}_3\text{Mg}_2$  precipitates accompanied by a reduction of the Mg left in solid solution. The precipitation should begin at about 450 °C. Mg forms small  $\beta$  coherent clusters. The precipitation of the  $\text{Al}_3\text{Mg}_2$  phase occurs only upon the dissolution of these clusters. The mechanical properties of the material are primarily controlled by the Mg atoms in solid solution [24].

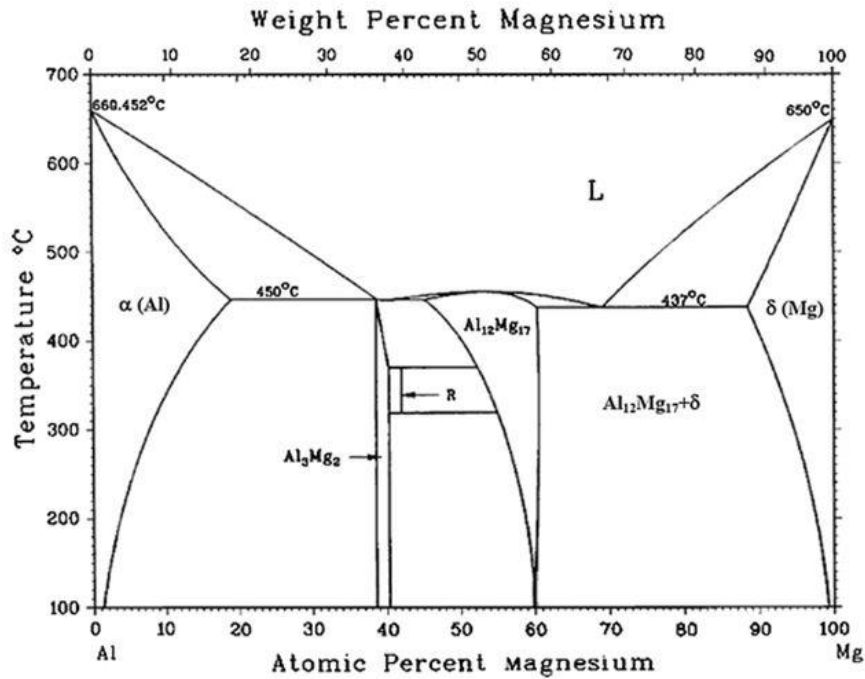


Fig. 2.4 The Al-Mg binary phase diagram [25]

#### 2.1.3.1 Commercial Al-Mg Alloys

Commercial Al-Mg alloys also contain elements such as Mn, Fe, Si or Cr and Ti. These elements form the second phase particles due to limited solubility in solid solution. Although these elements have a minor influence on the strength of Al alloys, they have a significant influence in annealing behaviour, i.e. they are an important factor in the grain size control [26].

The Mg content of the commercial alloys A356 and A357 ranges from 0.3 to 0.4 wt% and from 0.45 to 0.7 wt%, respectively. In general, it has been reported that higher Mg content increases the yield stress while decreasing the ductility and the fracture toughness [27-29]. Besides its major effect on the age-hardening potential, Mg depresses the eutectic temperature and makes the eutectic Si structure more heterogeneous [30].

#### 2.1.4 High Strength Casting Aluminium Alloy 201

The high strength casting alloy 201 has the nominal composition Al-4.7Cu-0.7Ag-0.3Mg-0.3Mn-0.2Ti, wt%. This alloy is an important commercial alloy, because it has excellent mechanical properties and good formability. The added silver completely

changes the precipitation process, causing the orthorhombic  $\Omega$  main hardening precipitation form of the tetragonal  $\theta$  phase [21]. 480 MPa yield strength and 550 MPa tensile strength with 10% elongation to fracture have been reported. The solidification process between formation of the dendrites and the main eutectic reaction of forming  $\text{Al}_2\text{Cu}$  were reported by Bäckerd *et al.*[31] as shown in Table 2.2. The first intermetallic phase to form from liquid is of the  $\text{Al}_6(\text{MnFeCu})$  type, followed by a peritectic reaction, where the phase will transform into the  $\text{Al}_{20}\text{Mn}_3\text{Cu}_2$  phase. Then the main eutectic reaction 3 occurs, where also the copper-containing phase  $\text{Al}_7\text{FeCu}_2$  may precipitate. Finally, less than 1% of the total volume of the remaining melt may form the  $\text{Al}_2\text{MgCu}$  and  $\text{Mg}_2\text{Si}$  phase in reaction 4.

Reactions	Suggested Temperature ( °C)
1. $\text{Liq.} \rightarrow \alpha\text{-Al}$	651-649
$\text{Liq.} \rightarrow \text{Al} + \text{Al}_6(\text{MnFeCu})$	649
2. $\text{Liq.} + \text{Al}_6(\text{MnFeCu}) \rightarrow \text{Al} + \text{Al}_{20}\text{Mn}_3\text{Cu}_2$	616
3. $\text{Liq.} \rightarrow \text{Al} + \text{Al}_2\text{Cu} + \text{Al}_{20}\text{Mn}_3\text{Cu}_2 + \text{Al}_7\text{FeCu}_2$	537
4* $\text{Liq.} \rightarrow \text{Al} + \text{Al}_2\text{Cu} + \text{Al}_2\text{MgCu} + \text{Mg}_2\text{Si}$	500

*Table 2.2 Reactions during solidification of alloy 201 (Al-4.10Cu-0.51Ag-0.31Mn-0.28Mg-0.19Ti-0.02Si-0.01Fe, wt%) \* Reaction 4 does not appear on the curves but the phases are found by metallography and SEM/EDX [31]*

The 201 alloy is commonly used in aerospace parts and it is also suitable for semi-solid applications due to its wide solidification range [32]. Fig. 2.5 shows a typical thixoformable microstructure of alloy 201 [33]. The tensile strength showed an obvious increasing to 490 MPa after thixoforming when comparing with as-cast alloy.

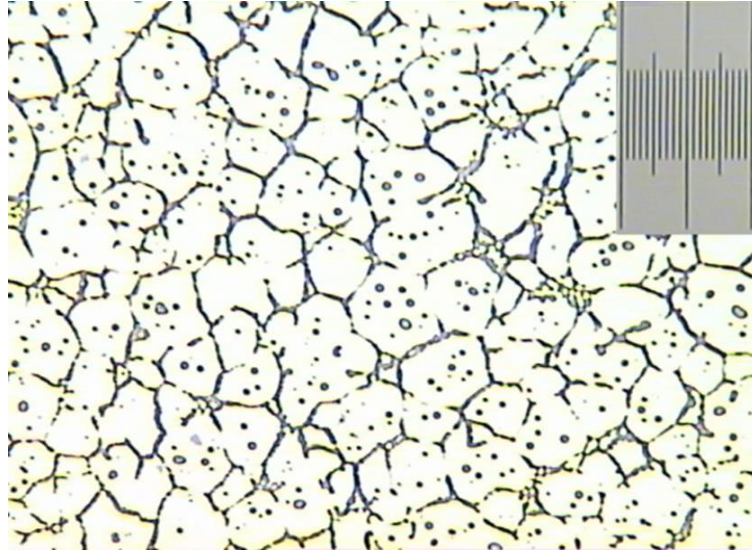


*Fig. 2.5 Thixoformed microstructure of A201, scale bar: 100 $\mu$ m [33]*

### **2.1.5 Al-Si-Cu 319 Type Alloy**

The excellent castability and good mechanical properties of hypoeutectic 319 aluminium alloy (Al-6Si-3.5Cu-0.1Mg, wt%) makes it popular in automotive industry. It also has excellent corrosion resistance and low costs of recycling. The structural features and mechanical properties of 319 alloy has been investigated by many authors [31, 34-38]. It is well known that added copper increases the strength of Al-Si-Cu alloys, which is due to the influence of copper in the precipitation behaviour of the alloys during the age-hardening treatment. The investigated 319 alloys have two main solidification stages, formation of aluminium dendrites followed by development of two phase eutectic (Al-Si). However, the added alloying elements Cu and Mg, as well as impurities such as Fe and Mn lead to more complex solidification reactions. Therefore, the microstructure presents many intermetallic phases. The solidification reactions are reported by Bäckerud *et al.*[31] and Samuel *et al.*[34] in Table 2.3 and Table 2.4 respectively.

Reactions	Suggested Temperature ( °C)
1. Liq. $\rightarrow$ $\alpha$ -Al	609
2a. Liq. $\rightarrow$ Al + Al <sub>15</sub> (FeMn) <sub>3</sub> Si <sub>2</sub>	590
2b. Liq. $\rightarrow$ Al + Si + Al <sub>5</sub> FeSi	590
3. Liq. $\rightarrow$ Al + Si + Al <sub>5</sub> FeSi	575
4. Liq. $\rightarrow$ Al + Al <sub>2</sub> Cu + Si + Al <sub>5</sub> FeSi	525
5. Liq. $\rightarrow$ Al + Al <sub>2</sub> Cu + Si + Al <sub>5</sub> Mg <sub>8</sub> Cu <sub>2</sub> Si <sub>6</sub>	507

*Table 2.3 Reactions during solidification of alloy 319 (Al-5.7Si-3.4Cu-0.62Fe-0.1Mg-0.92Zn-0.14Ti-0.36Mn, wt%) by B äckerud et al. [31]*

Reactions	Suggested Temperature ( °C)
1. (Al) Dendrite network	610
2. Precipitation of eutectic Si	562
3. Precipitation of Al <sub>6</sub> Mg <sub>3</sub> FeSi <sub>6</sub> + Mg <sub>2</sub> Si	554
4. Precipitation of Al <sub>2</sub> Cu	510
5. Precipitation of Al <sub>5</sub> Mg <sub>8</sub> Cu <sub>2</sub> Si <sub>6</sub>	490

*Table 2.4 Reactions during solidification of alloy 319 (Al-5.95Si-3.56Cu-0.04Mg-0.145Ti-0.01Ni-0.02Mn-0.11Fe, wt%) by Samuel et al. [34]*

The two solidification sequences differ slightly in Table 2.3 and 2.4. After crystallization of Al dendrites, the phase Al<sub>15</sub>Mn<sub>3</sub>Si<sub>2</sub> together with Al<sub>5</sub>FeSi identified by B äckerud was not reported by Samuel probably because of the difference of Mn content used in alloys. The Al-Si eutectic reaction temperature 562 °C for Samuel is much lower than 575 °C for B äckerud. Samuel suggested that this temperature was depressed by increasing the Si content of the alloy. The precipitation of Al<sub>6</sub>Mg<sub>3</sub>FeSi<sub>6</sub> and Mg<sub>2</sub>Si at 554 °C could be detected by Samuel due to a high Mg concentration according to [39], where these precipitations could be easily observed. The four-phase Al+Al<sub>2</sub>Cu+Si+Al<sub>5</sub>FeSi reaction at 525 °C recorded by B äckerud relates to the start of Al<sub>2</sub>Cu precipitation. According to Li *et al.* [40], this reaction point should involve Al<sub>5</sub>Mg<sub>8</sub>Cu<sub>2</sub>Si<sub>6</sub> together in Al<sub>2</sub>Cu.



## 2.2 Semi-Solid Metal (SSM) Processing

### 2.2.1 Background

SSM processing is an advanced technology for forming material with non-dendritic microstructure in the semi-solid state to near net shaped products [1]. SSM technology also leads to the alloys with excellent properties. This method is different from conventional metal forming techniques such as forging and casting, which utilise either solid or liquid state routes.

SSM processing originates from a development at MIT in the early 1970s by Spencer *et al.* [41] during a study of hot tear formation of solidifying metal. The process involved stirring the Sn-15Pb alloy during solidification, and then injecting it directly into a die to produce a solid component. They discovered that the microstructure of the solid was changing from the dendritic morphology to a more spherical form during stirring (as shown in Fig. 2.6). Meanwhile, stirring brought a dramatic decrease in shear stress and viscosity. The spheroids of solid in the liquid could easily flow over each other providing a non-restricting microstructural network and a fluid semi-solid metal. This partially solidified metal or alloy exhibits fluidity similar to that of heavy machine oil and the thixotropic behaviour which is necessary for semi-solid processing [42].

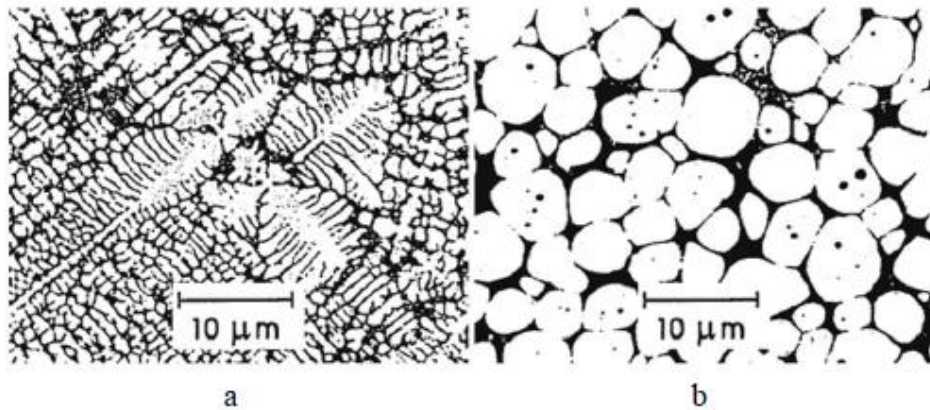


Fig. 2.6 (a) dendritic microstructure in an as-cast sample, (b) a typical globular microstructure in a semisolid alloy [43]

### 2.2.2 Types of SSM Processing

Subsequently, Flemings and his team developed the process in two ways: “rheocasting” and “thixoforming” (Fig. 2.7). Briefly, rheocasting is without intermediate solidification

when cooling alloys into a non-dendritic slurry semisolid state before injection into a die. Thixoforming is used to describe the near net shaping of a partially melting non-dendritic alloy slug within a metal die (called thixocasting if in a closed die, or thixoforging if in an open die) and involves re-heating up from the solid state [44].

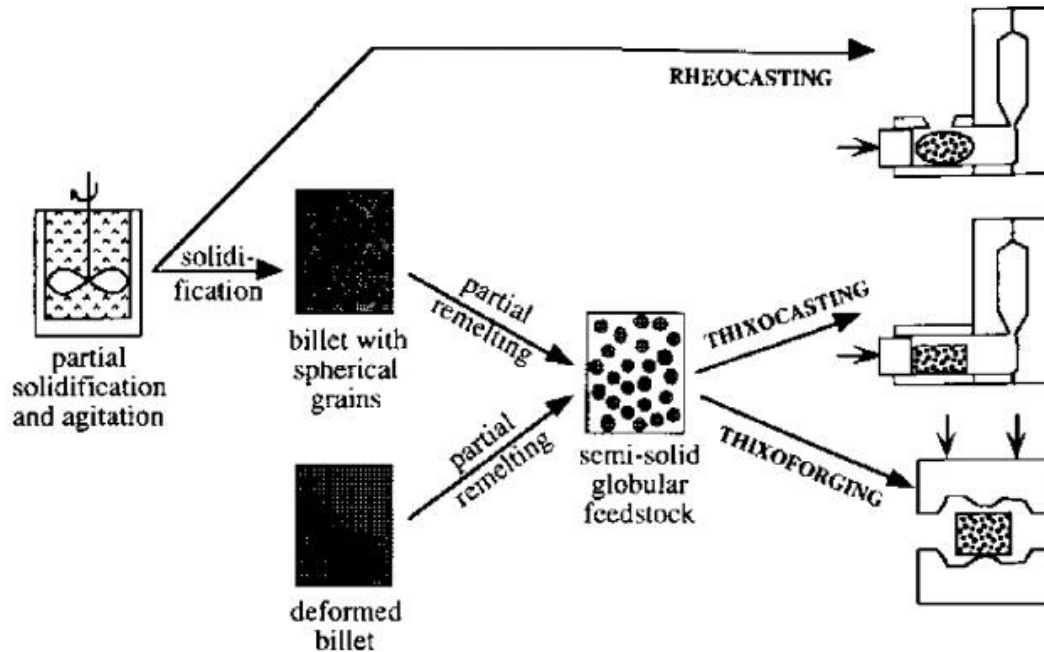
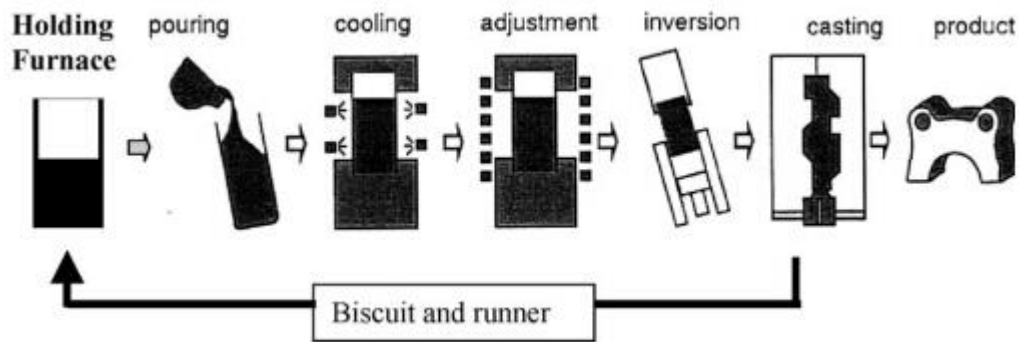


Fig. 2.7 Schematic illustration of different routes for semisolid metal processing [44]

### 2.2.2.1 Rheocasting

Rheocasting refers to the process of direct injection of the semi-solid slurry into a die without an intermediate solidification step to produce finished product. A non-dendritic microstructure can be obtained by shearing the alloy during cooling into the semi-solid state. This technology offers efficiency in production and energy management as it shapes component directly from semi-solid slurries [42].

The new rheocasting (NRC) process has been developed by UBE Industries Ltd [45, 46]. This process involves pouring molten materials that were heated to a temperature slightly above the liquidus state into a designed steel crucible and then the semisolid slurry is formed by controlled cooling for a globular microstructure before the material is transferred to a forming machine as shown in Fig. 2.8.



*Fig. 2.8 Schematic diagram of the new rheocasting (NRC) process. The inversion procedure causes the oxide skin on the exposed surface to run into the runner and biscuit [45-47]*

The NRC process has lower unit costs over thixoforming, due to the lower starting material cost. In addition, the NRC process does not require specially treated thixotropic feedstock materials [46]. However, rheocasting and NRC processes have some disadvantages of re-introduction of liquid metal processing issues, which are also encountered in direct slurry methods [48, 49].

#### **2.2.2.2 Thixoforming**

Thixoforming is an intermediate process where a thixoformable alloy is heated to a temperature between the solidus and liquidus temperature and pressed into a die. The semi-solid condition generally contains 30-50% liquid fraction [47, 50].

In Fig. 2.7, thixoforming can have two types: thixocasting and thixoforging. In terms of the volume fraction of solid, thixoforging refers to those routes resulting in relatively high solid fraction, i.e. above about 50 vol.% is higher than thixocasting [51]. Fig. 2.9 illustrates the distinctions between thixocasting and thixoforging. Thixocasting refers to the process where the alloy is completely solid at the beginning and is heated into the semisolid state where it will have a non-dendritic microstructure. It is reheated into the semisolid state with relatively high liquid fraction and then cast.

In thixoforging, the shaping is achieved in an open die (e.g. die halves [52]) instead of a closed die after heating a suitable material into the semi-solid state. A ram is employed to bring the parts of the die together. The direct insertion of the slurry into the die reduces material use because of the lack of runners, gate and press discard.

In thixoforging, an appropriate size of cylindrical slug is usually heated into the semi-solid state by induction heating which provides accurate and short time. This first stage of the thixoforging process (uniform heating and partial remelting) is complicated but very significant in terms of obtaining an accurately controlled solid fraction of spherical particles uniformly dispersed in a liquid matrix. During re-heating of slugs, the parameters of the process such as uniformity and precision of heating time and heating temperature have huge impact on the quality of components to be produced [42].

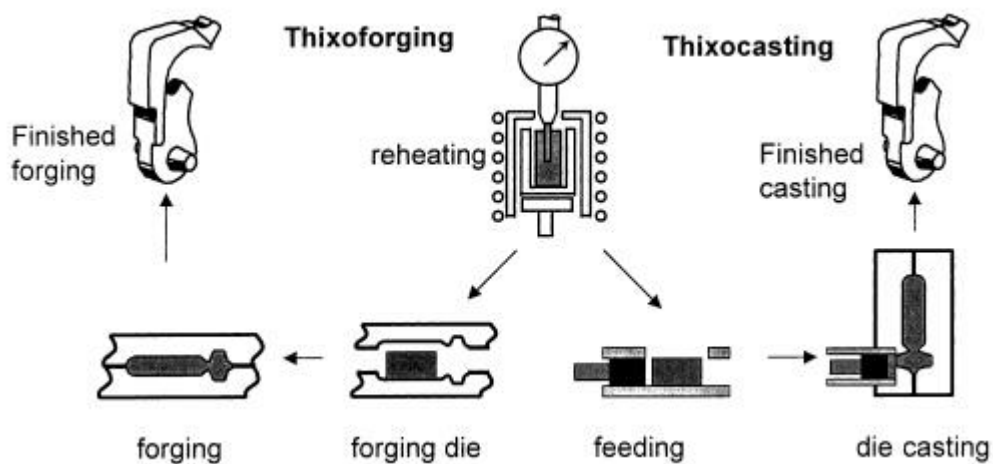


*Fig. 2.9 Schematic illustration of thixoforging processes [42]*

The liquid fraction of slugs can be very sensitive to temperature; a small change in temperature can result in a large difference in liquid fraction [42]. Too high a temperature will lead to difficulties for slug handling, while too low will lead to coalesced phases existing in the microstructure, which complicates die filling affecting the rheological properties. Therefore, the temperature should be accurately controlled and measured during the process for repeatability. The induction coil should be specifically designed to obtain a consistent temperature range through the slug because a non-uniform temperature distribution may bring segregation of liquid/solid phases during die filling. As a result, the solid/liquid fraction will be changed. Time is also a critical parameter for the processing; too long a heating time can cause structural coarsening and too short may generate incomplete die filling due to poor spheroidisation of solid particles.

Overall, it should be pointed out that the thixoforming parameters have to be considered carefully for successful SSM processing. At the forming stage, the shape of the die, correct die temperature and the ram velocity should to be optimised for complete die filling [53].

### ***2.2.3 Advantages of SSM Processing***

SSM processing combines the advantages of conventional forging and traditional casting and has already become the standard manufacturing route for a number of automotive parts [42]. In conventional casting, the primary dendrites normally grow and interact with each other. As a result, when only a small amount of the melt freezes, the viscosity of the melt increases rapidly and fluidity drops drastically. However, in SSM processing, the dendrites are broken (e.g. by vigorous agitation during the solidification), and reasonable fluidity of the melt can be maintained until the solid content reaches as much as 60%. In addition, each broken dendrite becomes a separate crystal and this refines the grains without the addition of grain refiner. In this process, shrinkage and cracking from casting are reduced because the alloy is already partly solidified in advance. Another advantage of this process is that the composite castings can be easily produced by adding fibres or particles. Benefits of SSM processing against the conventional casting and forging were summarised by Kirkwood [54]:

- 1) An energy efficient process which is easily automated and controlled (resulting in consistency), with production rates similar to pressure die casting or better.
- 2) Smooth filling of the die, with no air entrapment and low shrinkage porosity, giving parts of high integrity and allowing the employment of heat treatable alloys possessing superior mechanical properties.
- 3) Less thermal shock to the die, resulting in longer die life and the possibility of semisolid forming of high melting point alloys such as steels and super alloys.
- 4) Finer and more uniform microstructures, again leading to enhanced properties
- 5) Better yield from the raw slug and weight savings in the components because of improved design. These weight savings can be the decisive factor in making the process cost effective.

The first commercial attempt at alloy development especially suited for thixoforming was carried out by Pechiney [55]. Al-6Si-1Cu-Mg alloy was designed based on A357 alloy compositions for thixoforming in the T5\* condition. The properties of this alloy after thixoforming match or exceed those of permanent mould cast A356 alloy in the T6\* conditions. There have also been researches on modified hypereutectic alloys based on A390 alloy [56, 57].

*T: Heat treated to a stable condition, excluding annealing; T5\*: Rapidly cooled from elevated forming temperature and then artificially aged; T6\*: Solution heat treated, quenched and then artificially aged*

#### **2.2.4 Criteria of SSM Processability**

However, SSM processing is not suitable for every material. There are several critical parameters for alloys. Many researchers have proposed the requirements for SSM processing [58-60]. More recently, as suggested by Liu *et al.* [2] for semisolid processing, the critical parameters must be as follows:

1. The highest ‘knee’ on the fraction liquid versus temperature curve should occur between 30 and 50% liquid (see Fig. 2.10). It is because liquid formation tends to be controllable in this stage. Kinetically, the rate of liquid formation with time (i.e. the rate of melting of  $\alpha$  solid solution spheroids) above the knee tends to be slower than that below.
2. Fraction liquid sensitivity at 0.4 fraction liquid (mid-way through the working range of 30-50% liquid),  $(df_L/dT)_{f_L=0.4}$ , should be as small as possible (i.e. less than  $0.03 \text{ K}^{-1}$ ). This is because in induction heating, time is required for conduction of heat inwards through the billet and if the liquid fraction in the outer skin exceeds 0.5 then it is likely that liquid will start to drip off the outside.
3. The solidification interval, the temperature interval between the liquidus and solidus, should not be too wide (i.e. 130 K) because of susceptibility to hot tearing.

According to Liu *et al.* [2], alloy 2014 has a wide solidification interval (131K by DSC) and little if any eutectic liquid making it prone to the formation of porosity and not suitable for thixoforming. In Fig. 2.10, the casting alloy A365 and the forging alloy 2014 are compared in terms of DSC measurements and thermodynamic prediction

(assuming both equilibrium and Scheil conditions). For alloy A356, the slope between 30% liquid and 50% liquid is very steep, but Liu *et al.* argue that the existence of a ‘knee’ at around 50% liquid allows control of the process, which is the reason why alloy A356 is so suitable for thixoforming. The highest ‘knee’ is the reaction temperature for the binary eutectic. The amount of liquid at the ‘knee’ is the amount of eutectic in the structure. In Fig. 2.10, the highest knee in the DSC curve is above the knee of predictions. This may be due to kinetic factors. Above the knee, it is the  $\alpha$ -solid solution spheroids which are melting and the rate is slower than when the eutectic is melting. The knee is smooth because this process is occurring at different stages at various places in the material. It would normally be expected that the fraction liquid should not change too rapidly with the temperature in the working window, but it does for A356, where 0.3-0.5 fraction liquid is thought to be desirable for thixoformability.

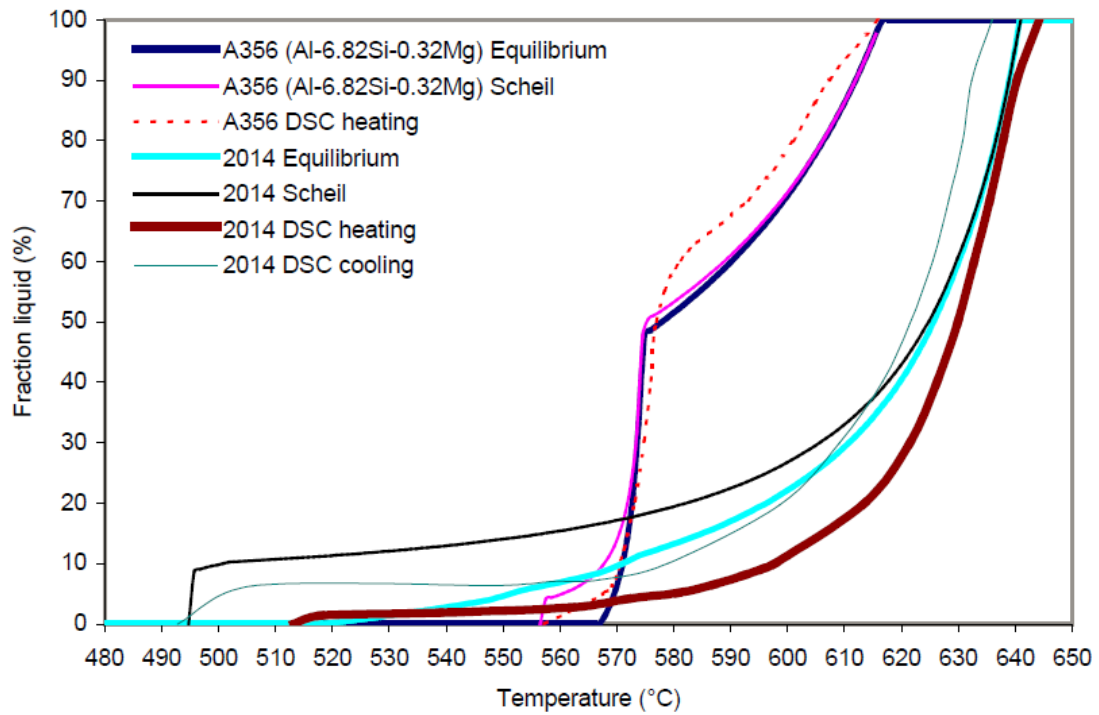


Fig. 2.10 Fraction liquid vs. temperature from MTDATA and DSC (rate 10K/min) for as-cast alloy A356 (Al-6.82Si-0.32Mg-0.022Cu-0.005Zn-0.112Fe-0.1Ti-0.013Pb-0.042Sn-0.006Ni-0.005Cr, wt%), and as-extruded alloy 2014 (Al-3.91Cu-0.47Mg-0.83Si-0.29Fe-0.55Mn, wt%) [2]

More recently, Nafisi *et al.* [59] evaluated the fraction solid dilemma using three methods: quantitative metallography, thermodynamic calculation and thermal analysis (computer aided cooling curve analysis (CA-CCA)) for Al-7wt%Si alloy and 319 alloy.

The results indicated that the increased cooling rate leads to a shorter solidification time and as a consequence the critical points are shifted. The solid fraction over-estimation measured by the quantitative metallography is due to inefficient quenching methods, which lead to more primary  $\alpha$ -Al formation.

It should be noted that recently, Curle *et al.* [3, 4] have demonstrated that both pure Al and binary Al-Si eutectic composition alloy can be rheo- or semi-solid processed using the CSIR-RCS (rheo casting system) combined with HPDC (high pressure die casting), despite the fact that both materials would be conventionally regarded as not suitable (with no solidus-liquidus interval) for semi-solid processing. Curle *et al.* stated that thermal arrest occurs because the latent heat of fusion is released during the solidification process, with the time necessary for fusion being determined by the heat extraction rate. Solidification or phase transformation does not happen instantaneously and hence the liquid and solid phases can coexist despite the fact that thermodynamically the transition from liquid to solid both for pure Al and for eutectic should occur at the single melting temperature. The high heat extraction rate during HPDC and the kinetics of solidification during thermal arrest make the possible capture of the semi-solid structure in time.

Figs. 2.11 and 2.12 give the microstructure of pure Al and Al-Si eutectic alloy respectively from Curle *et al.* [3, 4]. They show the characteristic globular or spherical semisolid state microstructure.

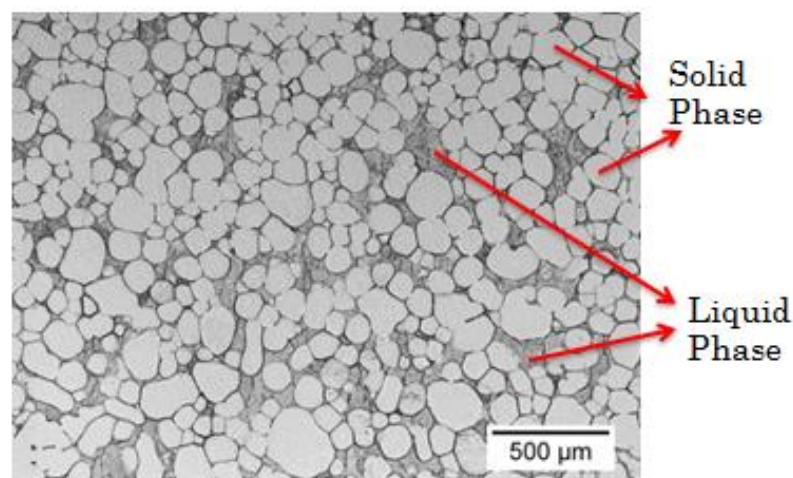


*Fig. 2.11 Internal microstructure of the pure aluminium metal after rheocasting [3]*



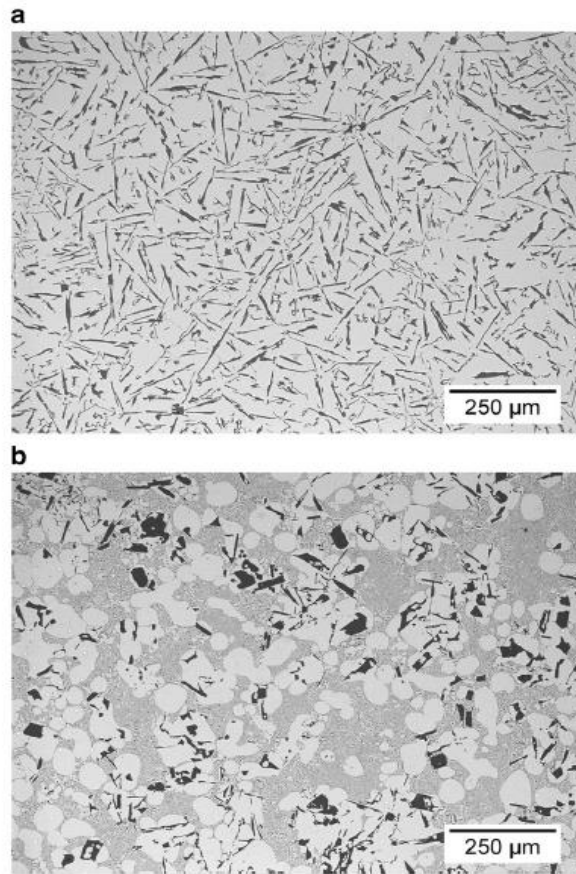


*Fig. 2.12 Microstructures of unmodified Al–Si binary eutectic processed (a) by solidifying with air cooling after normal casting (b) by rheo-processing and HPDC (Unetched) [4]*

The possibility of semisolid processing an alloy that thermodynamically has no solidification interval makes a big challenge to the traditional theory of suitability of semisolid processing. Therefore, it is significant to develop the criteria of thixoformability, which is the objective of this research.

## **2.3 Thermodynamics**

### **2.3.1 The Three Laws of Thermodynamics**

In thermodynamic theory, three laws define the fundamental physical quantities (such as energy, entropy) that characterize thermodynamic systems [61-65].

The first law of thermodynamics is defined [61] as “The increase in internal energy of a system is equal to the difference between the heat put into the system from the

surroundings and the work done by the system on the surroundings.” Mathematically this can be expressed by:

$$\Delta U = U_2 - U_1 = q - w \quad 2.1$$

where  $\Delta U$  is the total internal energy change of the system from state 1 to state 2,  $q$  is the heat added to the system and  $w$  is the work done by the system.

The second law of thermodynamics states [62] that any isolated system evolves until it reaches an equilibrium state. An isolated system is said to be in equilibrium when for all practical purposes its thermodynamic properties do not change with time. The mathematical expression of the second law, for an isolated system, is simply [63];

$$\Delta S_{total} \geq 0 \quad 2.2$$

where “total” means that both the system and its surroundings are included.  $S$  is entropy of the isolated system and is a measure of the amount of energy which is unavailable to do work. For a solid to liquid change,

$$\Delta S = \frac{\Delta H}{T_m} \quad 2.3$$

$\Delta S$  is the change in entropy of the system,  $T_m$  is the melting temperature,  $\Delta H$  is the enthalpy change of melting which will be described in Section 2.3.3.

The third law of thermodynamics indicates that the entropy of a system approaches a constant value as the temperature approaches zero [64].

Based on the above laws of thermodynamics, physical quantities are calculated in different systems. In this project, samples in calorimeters are all under constant pressure. In the following sections, the constant-pressure processes and the important physical quantities of this system will be discussed.

### **2.3.2 Constant-Pressure Processes**

In a thermodynamic system, if the volume changes at constant pressure from state  $a$  to  $b$ , the work done by the system is:

$$w = \int_a^b P dV = P \int_a^b dV = P(V_b - V_a) \quad 2.4$$

Combining Equations 2.1 and 2.4 gives:

$$(U_2 + PV_2) - (U_1 + PV_1) = q_p \quad 2.5$$

where  $q_p$  is the heat of a system under constant pressure  $P$ ,  $V$  is the system volume.

### 2.3.3 The Enthalpy Change

The expression  $U + PV$  in Equation 2.5 is called the enthalpy and is given by the symbol  $H$ , so we can express the enthalpy as:

$$H = U + PV \quad 2.6$$

where  $U$  is the internal energy,  $PV$  is the external energy. The enthalpy [66] is a thermodynamic function of a system which is equivalent to the sum of the internal energy and external energies of the system.

In metallurgical processes, volume change is negligible. Therefore given the assumption that  $P$  is constant  $P\Delta V \rightarrow 0$  in Equation 2.6 and hence:

$$\Delta H = \Delta U \quad 2.7$$

The enthalpy change under a constant-pressure process simply equals the heat change in the system.

### 2.3.4 Latent Heat

Latent heat can be defined as the heat absorbed or released by a substance during a phase change [67].

Therefore, latent heat  $L$  at constant pressure is:

$$L = (U_2 - U_1) + P(V_2 - V_1) = H_2 - H_1 = \Delta H = q_p \quad 2.8$$

Thus the enthalpy change during a constant pressure process simply equals the amount of heat admitted to or withdrawn from the system during the process.

### 2.3.5 Heat Capacity

The heat capacity  $C$ , is defined [68] as the ratio of the heat absorbed  $dq$  to the resulting increase in temperature  $dT$  :

$$C = \frac{dq}{dT} \quad 2.9$$

where  $dq$  is the heat supplied to a substance and  $dT$  is the change in temperature. When the change is at constant pressure, the heat capacity  $C_p$  at constant pressure is defined as:

$$C_p = \left( \frac{dq}{dT} \right)_p \quad 2.10$$

In a reversible constant pressure process,  $dq = dH$ , so,

$$C_p = \left( \frac{\partial H}{\partial T} \right)_p \quad 2.11$$

When a phase change is involved, the effective heat capacity  $C_p$  of pure matter becomes infinite at its melting point (as Fig. 2.13 shows).

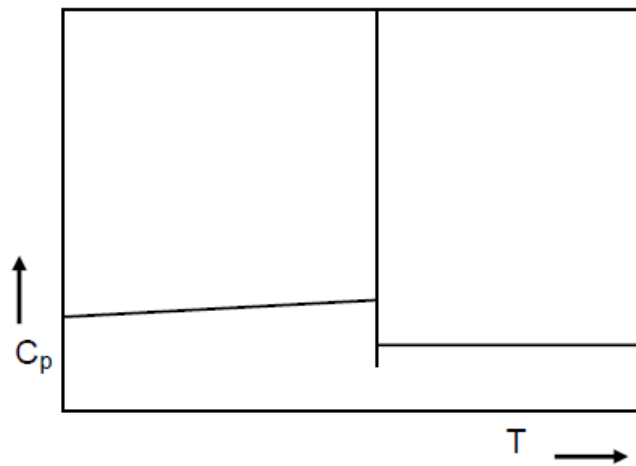


*Fig. 2.13 Schematic image of the heat capacity of a pure metal as a function of temperature*

### 2.3.6 Phase Diagram and Lever Rule

A phase diagram is a diagram that shows the phases and the phase compositions at each combination of the temperature and overall composition. The phase diagram is a crucial

part of metallurgy and material science. It shows the equilibrium states of a mixture. A schematic representation of a phase diagram is given below in Fig. 2.14.

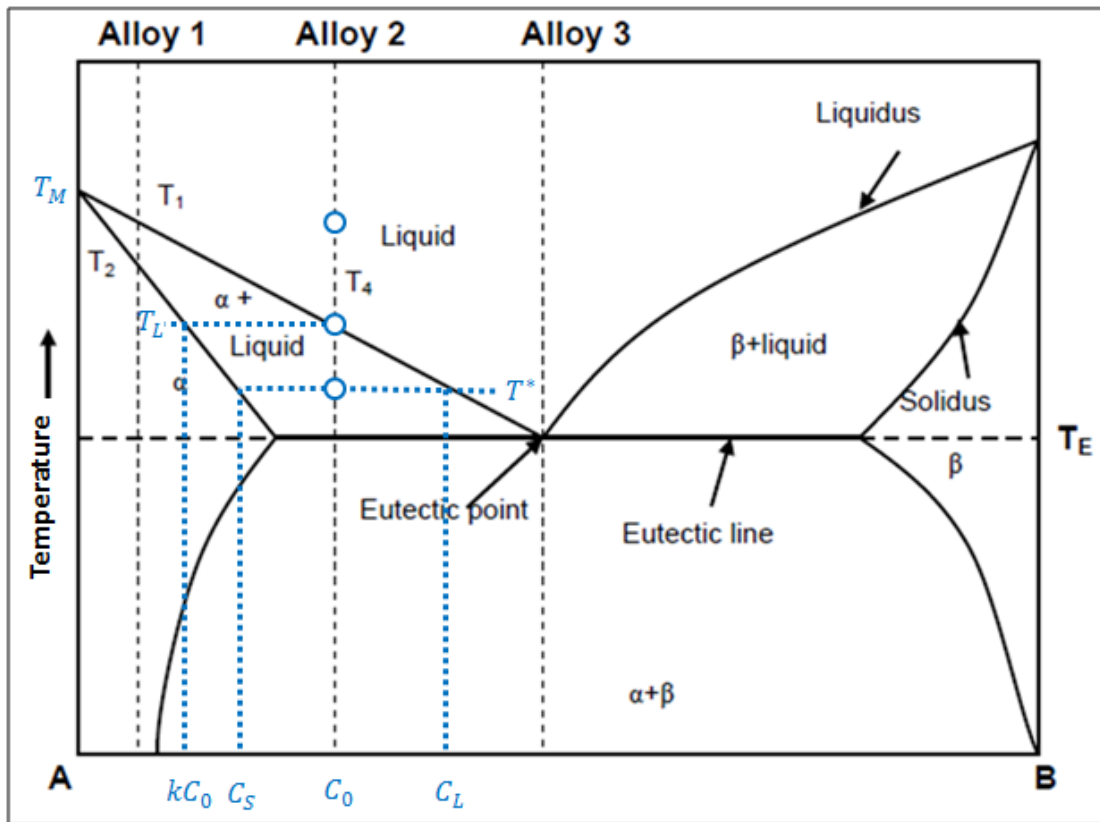


Fig. 2.14 Schematic representation of a phase diagram,  $k = c_S / c_L$  [69]

If an alloy consists of more than one phase, the fraction of each phase present can be found by applying the lever rule to the phase diagram. It can be explained by considering a simple balance in Fig. 2.14. The solute compositions (blue in Fig. 2.14) in the solid,  $c_S$ , and the liquid,  $c_L$ , vary along the solidus and liquidus lines, respectively. The ratio  $c_S / c_L$  is referred to as the equilibrium partition or distribution coefficient,  $k$ .

In the equilibrium condition, there is ideal diffusion in the solid and complete mixing in the liquid ( $D_S = \infty, D_L = \infty$ ). A liquid with an initial concentration  $c_0$ , solidifies at  $T = T_L$  with the first solid to form having a composition  $k \cdot c_0$ . The mass balance that remains effective during the whole solidification process can be written as:

$$c_S \cdot f_S + c_L \cdot f_L = c_0 \quad 2.12$$

where  $f_S$  and  $f_L$  are the fraction of solid and liquid phase respectively. With  $f_S = 1 - f_L$  and  $k = c_S/c_L$ , a relationship between the liquid fraction  $f_L$ , and the temperature  $T$ , can be written as:

$$f_L = \frac{C_0 - C_S}{C_L - C_S} = \frac{\frac{T_L}{m_L} - \frac{T}{m_S}}{\frac{T_L}{m_L} - \frac{T}{m_S}} = \frac{T_L - T \cdot k}{T(1 - k)} \quad 2.13$$

where  $m_S$  is the slope of solidus and  $m_L$  is the slope of liquidus.

### 2.3.7 The Heat Capacity $C_P$ and Heat Content of an Alloy

Fig. 2.15 is a schematic description of the heat content (enthalpy) and effective heat capacity of a binary system (corresponding to Fig. 2.14).

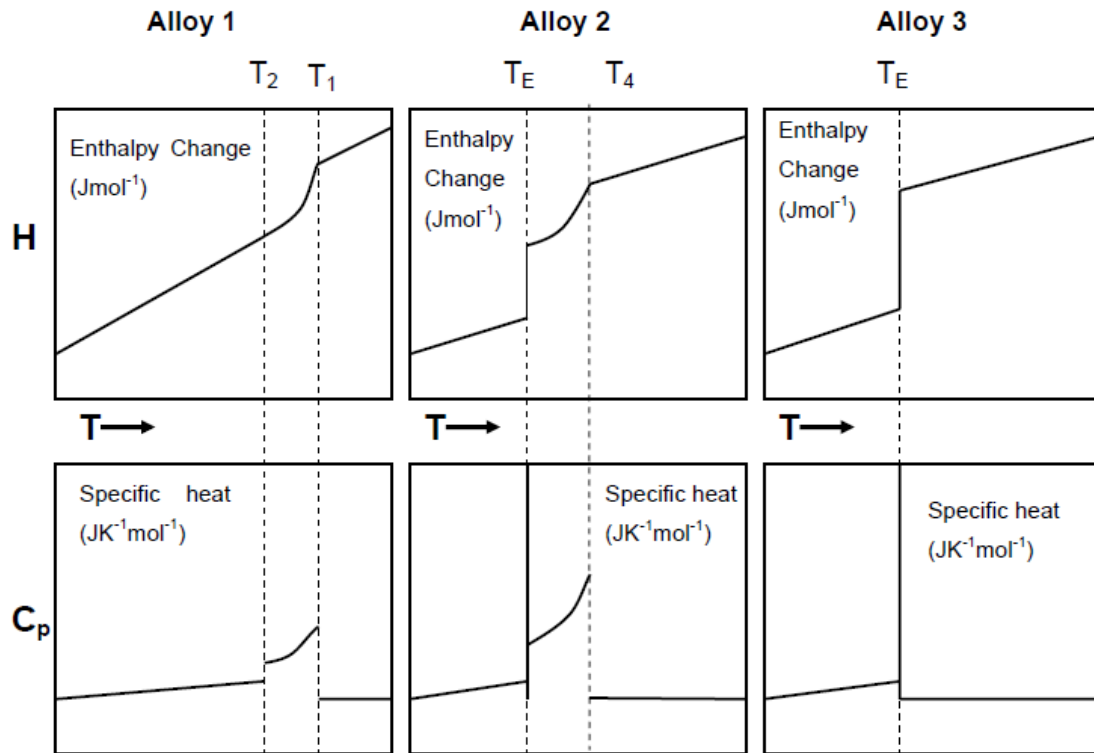


Fig. 2.15 Schematic representation of heat capacity and heat content of binary system [69]

For alloy 1, a solid solution  $\alpha_L$  exists in the system from room temperature to  $T_2$ . After adding heat to the system, the temperature increases as the heat is absorbed as true specific heat. Once the temperature increases above  $T_2$ , liquid starts to form slowly and all solid melts at equilibrium temperature  $T_1$ . More heat is required to produce a given

temperature change due to the latent heat during melting. The heat capacity depends on true heat capacity of  $\alpha$ , liquid properties and also on the latent heat of the reaction. If the temperature is higher than  $T_1$ , only liquid is present and heat capacity remains constant.

Alloy 2 starts to melt at the eutectic temperature so  $\alpha + \beta$  react to provide liquid. In a two-component system, this is an invariant reaction so that the heat capacity goes to infinity and the enthalpy has a sudden change. After the eutectic melts, the system contains *liquid* +  $\alpha$ . By adding extra heat, the  $\alpha$  melts slowly as temperature increases. The effective heat capacity depends on the actual heat capacity as well as on the latent heat of melting.

Alloy 3 is at the eutectic composition. The eutectic melts at the eutectic temperature as heat is added to the system. As for alloy 3 there is sudden change in enthalpy and heat capacity goes to infinity as shown in Fig. 2.15. At the eutectic temperature, solid melts entirely.

The exact shape of the enthalpy graph against temperature depends on the shape of the phase diagram and also depends on how close the system is to equilibrium. Assuming that the true heat capacity  $C_p$  is equal in both phases, at a given temperature  $T$  the enthalpy of a mixture of solid and liquid is given by [69];

$$H = C_p T + f_L L \quad 2.14$$

where  $L$  is the latent heat and is not a function of  $f_L$  and  $T$ , and  $f_L$  is the liquid fraction. By differentiating the above equation with respect to  $T$ , the effective heat capacity is:

$$\frac{dH}{dT} = C_p + L \frac{df_L}{dT} \quad 2.15$$

The expression  $f_L$  and  $\frac{df_L}{dT}$  can be estimated assuming equilibrium between the two phases. By using the lever rule (Eq. 2.13) and differentiating to obtain  $\frac{df_L}{dT}$ , we can get:

$$\frac{dH}{dT} = C_p + \frac{-k^2}{T_L(1-k)} L \quad 2.16$$

## **2.4 Theory of Solidification**

Solidification is a common material transformation. It plays an important role in many of the processes used in many industries for production of metal and alloy components, especially in calorimetric processes. All alloys, when solidified from a molten state under certain conditions, form dendrites. Alloys are then composed of thousands to millions of tiny dendrites. The size, shape, and orientation of those dendrites help determine the strength and properties of steel, aluminium, and other metals used in the production of components. To promote the understanding of solidification, it is necessary to understand the basic theory.

Solidification is defined [70] as the phase transformation from a liquid phase to one or several solid phases involving diffusion of solute and latent heat. Pure metals solidify at a single temperature. Alloys on the other hand (except in special cases such as at the eutectic composition) solidify over a temperature range during which they are in the semi-solid state.

### **2.4.1 Nucleation**

The first stage of solidification is nucleation. Nucleation occurs when a small piece of solid grows in liquid. The liquid system in transition to solid phase has to nucleate first and then undergoes subsequent growth. As the liquid changes phase into solid, heat must be lost in the process. The driving force for homogeneous nucleation is the change in Gibbs free energy, which is derived by adding the interface and volume terms, which can be written as [71, 72]:

$$\Delta G = \frac{4}{3}\Delta g r^3 \pi + 4r^2 \pi \sigma \quad 2.17$$

where  $\Delta g$  is Gibbs free energy difference between solid and liquid per unit volume,  $r$  is the radius of a nucleus, and  $\sigma$  is the solid/liquid interface energy.  $\Delta g$  is proportional to  $\Delta T$ :

$$\Delta g = -\Delta s_f \cdot \Delta T \quad 2.18$$

where  $\Delta s_f$  is the difference in the slopes of the Gibbs free energy-temperature plots of the two phases. If the solid is larger than the critical radius, further growth causes the



total energy to decrease and this allows the solid to become stable, thus, the nucleation occurs. If the solid is smaller than its critical radius, the solid prefers to re-melt to a liquid phase so that the free energy decreases. The equilibrium solidification temperature minus the original temperature below the liquidus is the undercooling ( $\Delta T$ ). Therefore this is the temperature to which the liquid form of the metal must cool before nucleation can occur.

As the size of the solid nucleus increases the Gibbs free energy also increases. When solid forms, an interface forms between the solid and the liquid. The solid/liquid interface energy  $\sigma$  is the energy per unit area of this interface. If the solid area is large, the boundary will be large so therefore the interfacial energy will be large as well. These are two types of nucleation and there will be discussed in the next sections below.

#### ***2.4.1.1 Homogeneous Nucleation***

Spontaneous nucleation, also known as homogeneous nucleation, may occur when an alloy is cooled rapidly to a temperature well below its equilibrium freezing temperature [71]. When solid forms within its own melt without the aid of foreign materials, it is said to be nucleate homogeneously [70]. Homogeneous nucleation involves creation of variously sized crystals with an interface between the solid and liquid phases. It occurs when the amount of undercooling becomes large enough to cause the formation of the stable nucleus. Undercooling is the temperature drop below the equilibrium freezing temperature at which, in practice, a metal begins to solidify [73, 74]. As the amount of undercooling is increased, the critical radius for nucleation decreases. The radius  $r^*$  which the metal system is stable at an undercooling  $\Delta T$  is given by [70];

$$r^* = -\frac{2\sigma}{\Delta g} \quad 2.19$$

The particle of radius  $r^*$  is termed the critical nucleus. Only particles larger than  $r^*$  are stable and able to grow as the free energy  $\Delta g$  decrease (see Fig. 2.16).

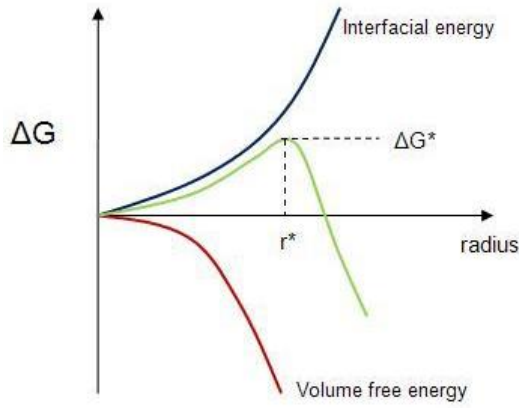


Fig. 2.16 A schematic diagram of critical radius

#### 2.4.1.2 Heterogeneous Nucleation

Due to the moderate cooling rates experienced in most metal solidification processes, large enough undercoolings for homogeneous nucleation are not in general obtained. Instead, solidification commonly commences by heterogeneous nucleation. When the melt contains solid particles such as inoculants, or is in contact with a crucible wall or oxide layer, nucleation may be facilitated as the activation energy is decreased and it is said to nucleate heterogeneously [75]. A nucleus forms on the substrate (the crucible wall or a foreign particle) as shown in Fig. 2.17. The contact angle between the foreign solid and the nucleus is  $\theta$ . This angle describes the shape of the solid on the catalyst's surface. The lower the angle of contact, the greater the area of contact and the better the adhesion. During nucleation two new interfaces are formed  $A_{LC}$  and  $A_{CS}$ .  $A_{LC}$  is the surface between the crystal and the liquid, and  $A_{CS}$  is the surface between the crystal and the substrate. The area of the original interface between substrate and liquid is reduced by  $A_{CS}$ . From the angle of contact, equilibrium pertains when

$$\sigma_{LS} - \sigma_{CS} = \sigma_{LC} \cos \theta \quad 2.20$$

where  $\sigma_{LS}$ ,  $\sigma_{CS}$ ,  $\sigma_{LC}$  are the surface energies of liquid-substrate, crystal-substrate and liquid-crystal interfaces, respectively. The critical radius  $r^*$  for heterogeneous nucleation is [72]:

$$r^* = \frac{2\sigma_{LC}T_m}{|\Delta H|(T_m - T)} \quad 2.21$$

where  $T_m$  is the melting temperature.

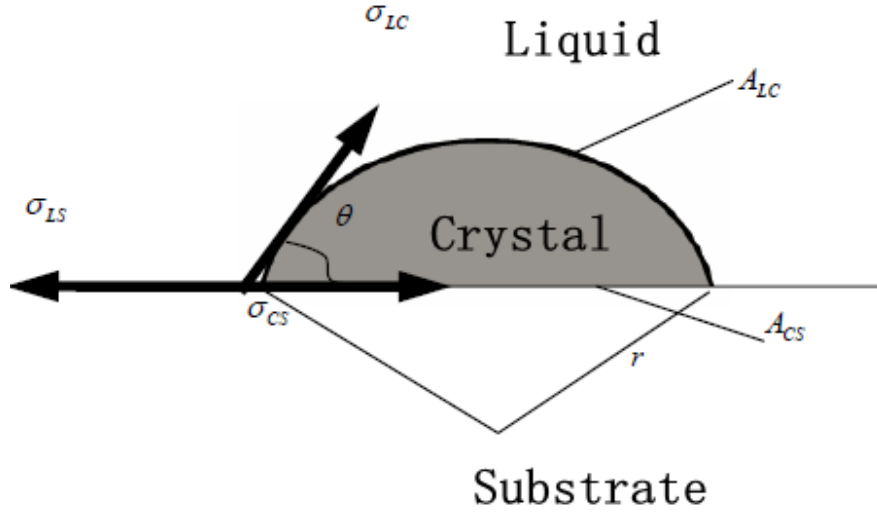


Fig. 2.17 Schematic of heterogeneous nucleation

#### 2.4.2 Nucleation Rate

The heterogeneous nucleation rate is expressed by the exponential kinetic expression [72]:

$$I_{heter} = I_{heter}^0 \exp\left(-\frac{\Delta G}{k_B T} f(\theta)\right) \quad 2.22$$

where  $k_B$  is the Boltzmann's constant,  $I_{heter}^0$  is a pre-exponential coefficient and  $T$  is temperature. The activation energy is the free energy of nucleation  $\Delta G$ .  $f(\theta)$  is a function of the contact angle  $\theta$  of the nucleus on a catalytic solid surface. When the surface is flat,  $f(\theta)$  is written as

$$f(\theta) = \frac{1}{4}(2 + \cos\theta)(1 - \cos\theta)^2 \quad 2.23$$

#### 2.4.3 Dendrite Growth

Crystal will grow from the nucleus in preferential directions according to the structure of the crystal lattice. In alloys, the primary crystal refers to the main phase that firstly solidifies. Solidification proceeds with solid growth from the solid/liquid interface. There are two possible mechanisms of growth: constrained and unconstrained.

Constrained growth occurs where the solid/liquid interface is at a lower temperature than the liquid into which it is advancing. Heat flow is therefore opposite to the growth direction, as for columnar solidification. On the contrary, unconstrained growth occurs where the solid/liquid interface is at a higher temperature than the liquid into which it is advancing, as for equiaxed solidification. In this case, heat and solute diffuse away through the liquid [70, 75]. Alloys tend to have more dendritic growth with larger solidification ranges [73]. Dendritic solidification is the most common form of solidification in castings and an example of dendrites can be seen in Fig. 2.6(a).

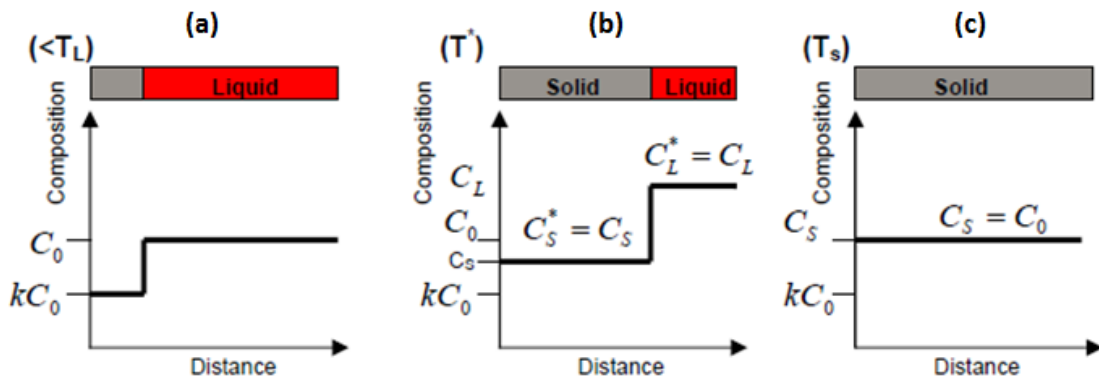
The driving force for dendritic growth, structure, and rate of solidification in pure metals is the thermal gradient of the solid/liquid interface, which is controlled by thermal diffusion. For alloys, this is controlled by the solute diffusion and is a much slower process. At high cooling rates, there is little time for solute diffusion, so large solute concentrations are present in the liquid in the interface front. Thus, larger growth undercoolings occur. Higher cooling rates may therefore produce a more dendritic structure. Rapid solidification of an alloy can lead to coring. This occurs when the primary phase and the eutectic formed during solidification have layers of progressively higher solute contents from the centre of the grain to the grain boundary. It may result in hot shortness where weak grain boundaries result in detrimental mechanical properties. Overall, in both cases, solid growth is preferential in the direction of the largest thermal gradient. Apart from thermal gradient, cooling rate and composition are also important in determining the exact dendrite morphology [75].

#### ***2.4.4 Homogenization and Solutionising***

Heating the metal to a certain temperature to allow atom diffusion, regarded as solution heat treatment, is often used to homogenise the microstructure. Homogenization can reduce the effects of microsegregation and remove the non-equilibrium state. Also it can dissolve the precipitation of excess concentrations of elements [21]. Homogenization mainly involves diffusion of alloy elements from solute-rich regions to cell centres. Primary phase particles grow when the smaller particles shrink during the homogenization process. Smaller particles have higher surface interfacial energy per unit volume than larger particles. Therefore, in order to reduce the energy content, diffusion flow occurs from the small particles to the larger ones. As a result, the small particles are dissolved and disappear while the larger ones grow still larger. This

process in which the mean radius of the average primary particle increases is called Ostwald ripening and has been described theoretically by Lifshitz and Slyozov [76] and Wagner [77]. The increasing of the primary particle size is also termed coarsening. Particle coarsening also occurs by agglomeration (or coalescence).

During dendritic solidification, many effects occur: Crystallisation, solute distribution, coarsening and inter-dendritic fluid flow etc. The complex interrelation of these effects determines the final microstructural composition, morphology, and hence the mechanical properties of the metal. The solute composition changes during the solidification in equilibrium condition are demonstrated in Fig. 2.18. The first solid begins to form at  $T_L$  and is of composition  $kC_0$ , lower in solute than the initial composition. The balance of the solute is rejected from the solid-liquid interface and diffuses into the liquid as shown in Fig. 2.18(a). At the temperature  $T^*$ , the liquid is enriched in solute and the solid denuded as shown in Fig. 2.18(b). When solidification is finished, the composition  $C_s$  equals to the initial composition  $C_0$  under equilibrium condition.



(a) At start of solidification (b) At temperature  $T^*$  (c) after solidification

Fig 2.18 Solute redistribution in equilibrium solidification [75]

## 2.5 Thermodynamic Prediction

### 2.5.1 Equilibrium Model

Equilibrium calculation uses the true Gibbs energy minimisation procedure developed by Davies (see [78]) which requires no initial estimate of the equilibrium state. The

equilibrium state of a metallurgical or chemical system can be determined by solving the following equation (with a given temperature and pressure):

$$\text{Minimise } G = \sum_{j=1}^N n_j \mu_j \quad 2.24$$

$$\text{such that } \sum_{j=1}^N a_{ij} * n_j = r_i \quad n_j \geq 0 \text{ and } i = 1, 2, 3 \dots M \leq N$$

where  $G$  is Gibbs energy;  $n_j$  is the amount in moles of species  $j$  present in the system, each chemical substance with a different phase designation being considered as a distinct chemical species;  $N$  is the number of species in the system;  $\mu_j$  is the chemical potential of species  $j$ ;  $a_{ij}$  is the number of units of component (element)  $i$  per species  $j$ ;  $M$  is the number of components in the system;  $r_i$  is the number of moles of component  $i$  in the system.

Equilibrium solidification is where the solidification proceeds under the equilibrium conditions and the solute compositions follow the lever rule, as discussed in Section 2.3.6.

### 2.5.2 Scheil Model

The ‘Scheil equation’ allows some back diffusion into the solid during isothermal increment of solidification. The composition of the liquid is then modified to a new value and this liquid then proceeds to the next isothermal step. The Scheil-Gulliver equation [79]:

$$C_S = kC_0(1 - f_S)^{k-1} \quad 2.25$$

where  $k$  is the partition coefficient. The process that physically occurs during ‘Scheil’ solidification can be envisaged as follows (Fig. 2.19). A liquid of composition  $C_0$  is cooled to a small amount below its liquidus to  $T_1$ . It precipitates out solid with a composition  $C_{S,1}$  and the liquid changes its composition to  $C_{L,1}$ . However, on further cooling to  $T_2$  the initial solid cannot change its composition owing to lack of back-diffusion and it is effectively isolated. A local equilibrium is then set up where the liquid of composition  $C_{L,1}$  transforms to a liquid of composition  $C_{L,2}$  and a solid with

composition  $C_{S,2}$  which is precipitated onto the original solid with composition  $C_{S,1}$ . Eventually, the composition of the liquid will reach the eutectic composition and final solidification will occur via this reaction. So the Scheil model is applied with five basic assumptions [75] :

- Equilibrium interface
- No back diffusion in the solid phase
- Homogenous compositions in liquid phase
- Equal densities of the solid and liquid phases
- No undercooling effect

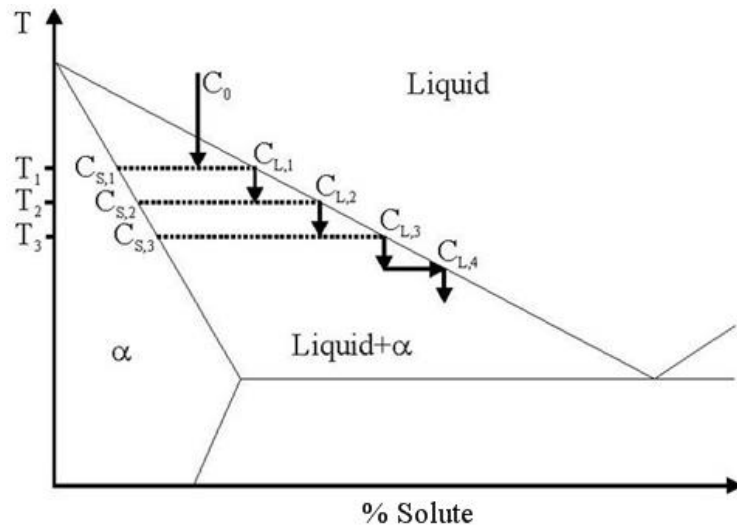


*Fig. 2.19 Schematic representation of solidification occurring under 'Scheil' conditions [80]*

Rearranging Equation 2.25 with the aid of relationships illustrated in Fig. 2.19, a dependence of liquid fraction  $f_L$ , can be indicated as follows:

$$f_L = 1 - f_S = \left(\frac{C_L}{C_0}\right)^{\frac{1}{k-1}} = \left(\frac{T_M - T}{T_M - T_L}\right)^{\frac{1}{k-1}} \quad 2.26$$

Any appearance of secondary phases can be easily taken into account in this approach with the assumption that no back-diffusion is involved. But, as the temperature step size becomes small, it provides results that are almost completely equivalent to those which would be obtained from continuous cooling.

Undercooling is important and cannot be ignored during solidification. However, it is neglected in both the equilibrium model and the Scheil model. Most complex solidification models are attempting to take the undercooling effect into consideration, but it would require more physical parameters, like viscosity, morphology and permeability etc. which are very difficult to obtain [81].

The fraction liquid is a critical parameter, both for the fundamental work and for the control of real semi-solid processing. So the curve of liquid fraction vs. temperature in an alloy is the key for semi-solid processing. Understanding the theory and prediction method for both solidification and melting is fundamental to the potential technology for alloy development and enlarging the working window in semi-solid processing.

### ***2.5.3 Thermodynamic Prediction of SSM Processability***

In order to develop alloys suitable for SSM processing, many researchers were using thermodynamic modelling packages such as Thermo-Calc software and MTDATA with special alloy databases to identify alloy compositions suitable for SSM processing. Thermodynamic modelling is a potential tool in predicting alloy compositions suitable for SSM processability. The predictions and criteria have been reviewed in Liu *et.al.* [2].

#### ***2.5.3.1 Predictions by Kazakov***

Kazakov [82] published the first examination of the SSM processability from a thermodynamic prediction point of view. Kazakov defined four critical parameters:

- (1) Temperature at which the slurry contains 50% liquid (this should be less than 585 °C to minimise pressure welding between steel tooling and the liquid aluminium);
- (2) Slope of the fraction liquid versus temperature curve at 50% fraction liquid (to minimise re-heating temperature sensitivity);
- (3) Difference between the temperature at the beginning of alpha solid solution melting and that at which the fraction liquid is 50% should be a minimum to avoid coarsening during re-heating;



(4) Slope of the fraction liquid versus temperature curve in the region where solidification is completed (Kazakov argues this slope should be relatively flat to avoid hot shortness but *Liu et al.* argue the opposite).

Kazakov used ChemSage 4.1 plus the SGTE database to generate fraction liquid versus temperature curves by thermodynamic modelling, identifying that the Al-(5-7, wt%)Si system is suitable for SSM processing based on parameter (3) above. A range of tertiary alloying elements (i.e. lithium, magnesium, zinc, copper, manganese, cerium and nickel) were selected on the basis that these should give a eutectic with aluminium and should increase strength. The results of the fraction liquid versus temperature predictions showed that only silicon, copper, magnesium, lithium and zinc substantially affect the temperature of the beginning of  $\alpha$ -Al solid solution melting. However, Kazakov did not carry out any practical experiments.

#### **2.5.3.2 Predictions by Fan and Co-workers**

Fan and co-workers [83, 84] have also used thermodynamic prediction, mapping thixoformable and rheocastable compositions onto sections through the ternary phase diagram. They have used Thermo-Calc software in combination with the AL-DATA database and MG-DATA database (Thermo-Tech Ltd., Guildford, UK) to evaluate the effect of alloying element compositions on processability and properties on the Al-Mg-Si system i.e. the 6000 series, and magnesium alloys (Mg-Al-Zn and Mg-Al-Mn). The basic aim is to examine the influence of alloy composition on liquidus temperature, solidification range, temperature sensitivity of liquid fraction, solidification path and potential for age hardening through the value of the difference between the solubility of the element in solid solution at the thixoforming temperature and the value at the ageing temperature.

They proposed that the absolute value of the slope of the solid fraction ( $f_s$ ) versus temperature curve,  $|df_s/dT|$  should be  $\leq 0.015\text{K}^{-1}$  for reasonable processability. For thixoforming, a fraction solid of 0.6 is chosen as typical for processing. For rheocasting, a fraction solid of 0.3 is identified as typical for processing. Fig. 2.20 (a) and (b) show a projection of the composition range for  $|df_s/dT| \leq 0.015$  of Al-Mg-Si alloy compositions selected for SSM processing. This is a helpful way of identifying compositions likely to be amenable for thixoforming.

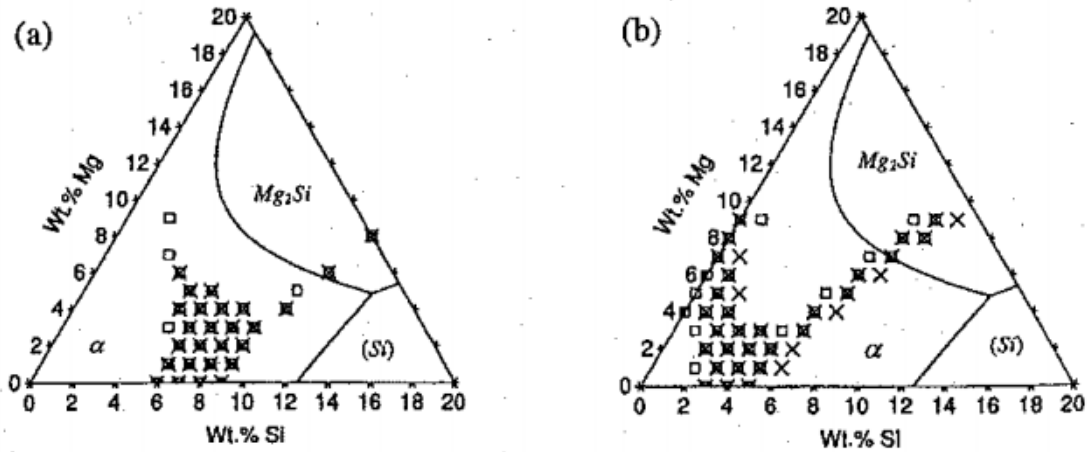


Fig. 2.20 Projections of Al-Mg-Si alloy compositions selected for SSM processing. Crosses represent the equilibrium calculation results of  $|df_s/dT| \leq 0.015K^{-1}$ , while open squares are for the Scheil mode. (a)  $f_s=0.3$ ; (b)  $f_s=0.6$  [84]

### 2.5.3.3 Predictions by Camacho

Camacho *et al.* have been investigating the potential of thermodynamic predictions for identifying amenable compositions in the Al-Zn-Mg-Cu quaternary (aluminium 7xxx) series [85]. There are two main types of wrought 7xxx series: medium strength weldable (Al-Zn-Mg) and high strength non-weldable (Al-Zn-Mg-Cu). They use a commercial software package MTDATA, with the NPL (National Physical Laboratory) alloy solution database and SGTE (Scientific Group Thermodata Europe) database.

They analysed the effect of the Zn/Mg ratio and the Zn+Mg content on the liquid fraction versus temperature in Al-Zn-Mg system and the effect of the Zn/(Mg+Cu) ratio and Zn+Mg+Cu content in the Al-Zn-Mg-Cu group. Fig. 2.21 is illustrative of the results: (a) the slopes at thixoforming liquid fractions (30%-50%) become less steep as the Zn/Mg ratio decreases at fixed Zn+Mg=6.0%, and (b) the sensitivity is lower as the Zn+Mg content increases at fixed Zn/Mg ratio 1.5. The dependence of the precipitation of the hardening phases on the Zn/(Mg+Cu) ratio and Zn+Mg+Cu content can also be predicted. Hence alloy composition thixoformability can be identified.

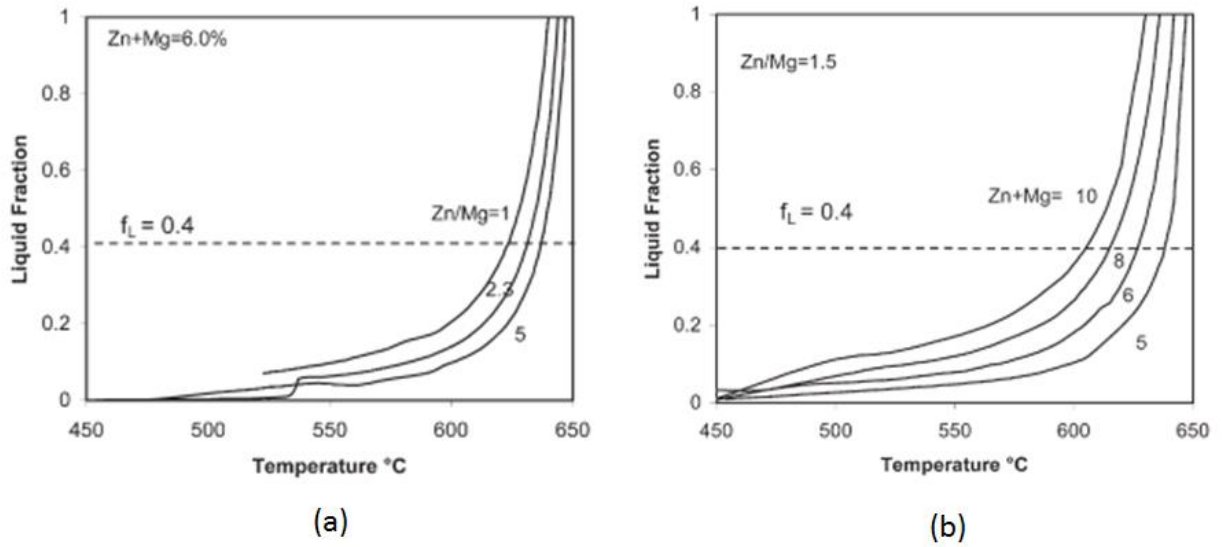
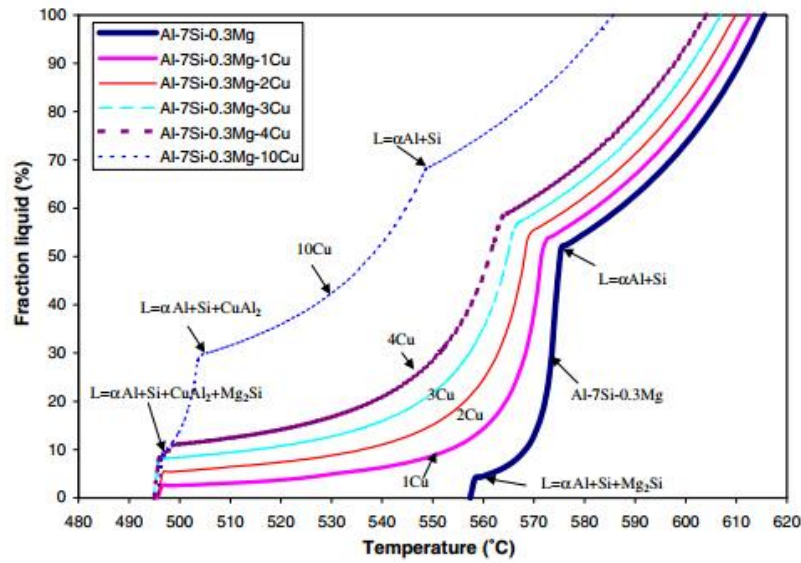


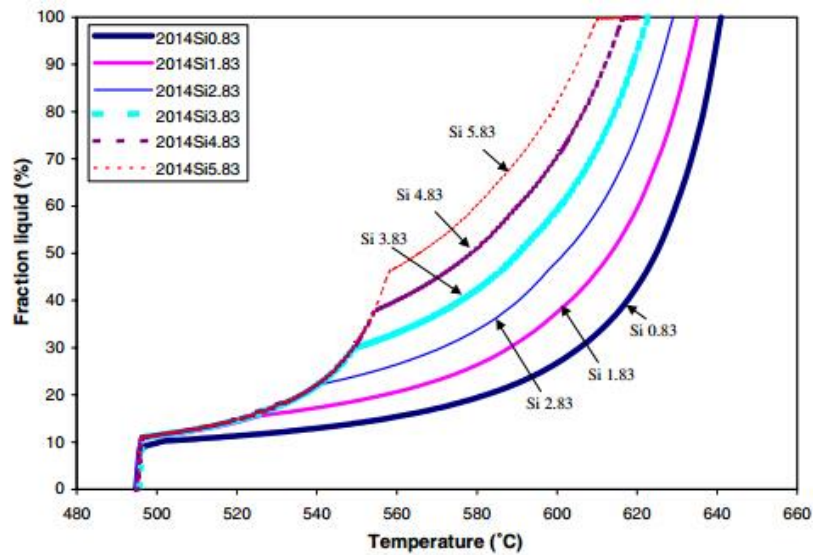
Fig. 2.21 Effect of the (a) Zn/Mg ratio, (b) the sum of Mg + Zn on the liquid fraction on liquid fraction (Scheil equation) [85]

#### 2.5.3.4 Predictions by Liu

Liu *et al.* [2] described the thermodynamic prediction of thixoformability in Al-Si-Cu and Al-Si-Cu-Mg system alloys using MTDATA packages (Scheil condition). They investigated the compositional variations, in particular the effects of added copper on alloy A356 (Al-7Si-0.3Mg, wt%) and the effect of added silicon on alloy 2014 (Al-3.91Cu-0.47Mg-0.83Si-0.29Fe-0.55Mn, wt%). The results indicated that the slopes of the curves of liquid fraction versus temperature at 40% liquid fraction become less steep and the working window between 30% and 50% liquid fraction is enlarged by adding up to 10% copper to alloy A356. The addition of silicon increases the amount of the solute enriched liquid ('knee') but decreases the solidification interval in alloy 2014 (as shown in Fig. 2.22).



(a)



(b)

Fig. 2.22 Fraction liquid versus temperature given by MTDATA/Scheil prediction for (a) A356 alloy with added Cu, (b) 2014 alloy with added silicon [2]

### 2.5.3.5 Predictions by Other Authors

Tzimas and Zavaliangos [86, 87] evaluated the processability in the semi-solid state of binary Al-Cu alloys based on the slope of the solid fraction versus temperature under equilibrium and Scheil with microsegregated condition. They suggested that the alloy SSM processability can be enhanced by using microsegregated material. This is because

for Al-Cu alloys, the homogenization time is much longer than the typical soaking time before forming and the microsegregation can retain the same level during thixoforming.

Uggowitzer and Wahlen [88] studied the eutectic  $\beta$ -phase formation in Mg-Al alloys AZ91 and AM60 during cooling from totally liquid and cooling from semi-solid state. Differential Thermal Analysis (DTA) and Thermo-Calc software with equilibrium and Scheil conditions were carried out in their research. The results showed that large amounts of brittle  $\beta$ -phase were formed in the microstructure cooling from fully liquid state and the amount of eutectic phase depended on the Al-content (12.4% for  $C_0=9\%$  Al, 6.5% for  $C_0=6\%$  Al and 2.1% for  $C_0=3\%$  Al). For cooling from semi-solid state, about 10% less eutectic phase is formed. However, there was still a significant amount of eutectic: 11.1% for  $C_0=9\%$  Al, 5.8% for  $C_0=6\%$  Al and 1.9% for  $C_0=3\%$  Al.

More recently, many works have been carried out on optimizing the database with thermodynamic prediction aiming to make it more reliable and can accurately predict the experimental results [89-94]. Overall, the new development of aluminium alloys is in process and thermodynamic calculations are a powerful tool in identifying which alloy compositions are likely to be amenable to SSM processing.

## ***2.6 Theory of Melting***

Melting rate is an important factor for semi-solid processing. The question here is what determines the kinetics of melting? Why do  $\alpha$  spheroids melt more slowly than eutectic? Where does melting first occur? One of the main purposes of this project is to develop understanding of melting. In this section, a brief description of melting theory is given.

The fundamental concept of melting is when the Gibbs free energies of solid phase and liquid phase are equal (as shown in Fig. 2.23) [95]. A perfect crystalline solid is recognized by its order and periodic lattice structure. In contrast, a liquid phase is homogeneous with randomly distributed atoms and appears as a disordered system. Hence, the melting transition can be interpreted as a breakdown of the periodic order in a system with crystal symmetry. In Fig. 2.23, at the melting temperature  $T_m$ ,  $G$  is a continuous function of pressure  $P$  and temperature  $T$  during the phase transitions, but other thermodynamic quantities (i.e. internal energy  $U$ , entropy  $S$ , volume  $V$ , and heat capacity  $C$ ) change discontinuously.

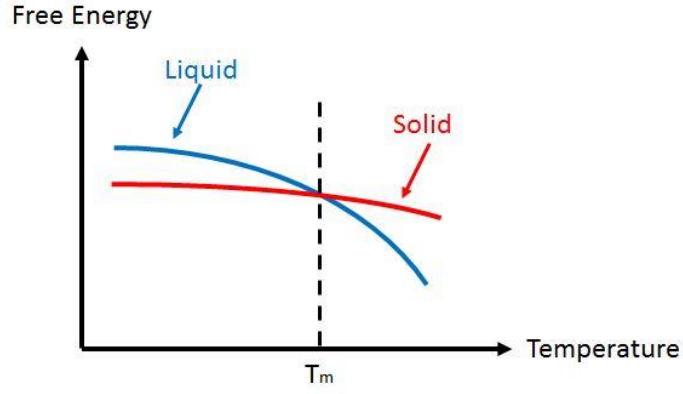


*Fig. 2.23 Variation of the Gibbs free energy of a simple atomic substance as a function of temperature*

The liquid phase entropy is higher than the solid phase at the melting temperature with the Boltzmann expression for entropy changes:

$$\Delta S_m = R \ln \left( \frac{W_l}{W_s} \right) \quad 2.27$$

where  $\Delta S_m$  is the entropy difference between the two phases,  $R$  is the gas constant,  $W_l$  is the number of independent ways of realizing the molten state and the  $W_s$  is the solid state. A number of theories of melting have been proposed treating the phenomenon as a homogeneous, bulk process, premelting etc.

### **2.6.1 Lindemann Criterion**

Lindemann [96] studied the vibration of atoms in the crystal to explain the melting transition. He assumed that melting would take place when the amplitude of thermal vibration of atoms becomes so great that direct collisions occur between neighbouring atoms, leading to the lattice instability. Lindemann obtained [97]:

$$T_m = \frac{mv^2c^2a^{*2}}{k_B} \quad 2.28$$

where  $m$  is the atomic mass,  $v$  is the frequency,  $k_B$  is the Boltzmann constant,  $c$  is the Lindemann constant and  $a^*$  is the atomic spacing.

A detailed experimental examination offered by Cho [98] found that the Lindemann parameter (the critical ratio of vibration amplitude over the interatomic distance) is

structure-dependent i.e. different for FCC, BCC and HCP metals. Furthermore numerous experiments carried out at high pressures indicate that the Lindemann model does not estimate adequately the pressure dependence of the melting temperature [99].

Nevertheless, the Lindemann criterion indicated melting could be a gradual process and is still commonly used nowadays due to its capability in predicting melting temperatures [95].

### **2.6.2 Born Criterion**

Similar to Lindemann's melting criterion, Born's theory [100] is based on the fact that liquid is different from a crystal in having zero resistance to the shear stress. Atomic distances in a solid increase as temperature rises, while the restoring force decreases due to thermal expansion. It is therefore concluded that the shear modulus of a crystal solid decreases when temperature is increasing. Born pointed out that melting occurs when the shear modulus of a crystal is zero. Later, Tallon *et al.* [101, 102] modified the Born criterion to reach better agreement with experimental results. They measured the shear moduli of various substances (metallic, organic, molecular and ionic crystals) as a function of molar volume and indicated that the solid shear modulus vanishes at the formation place of the liquid. Overall, he suggested that melting occurs when a solid can transform isothermally to a state of zero shear modulus.

Yip *et al.* [103-105] re-examine melting by computer simulations. They tested lattice stability in cases of zero external stress and arbitrary external load and indicated that Born's criteria are valid only with zero external stress. Born criteria predicted that in an ideal solid with zero pressure, melting happens as instability of the incipient lattice due to the tetragonal shear modulus vanishing. However, when a solid is under a negative pressure and undergoes pure dilatation, the lattice instability is initiated by vanishing of bulk modulus as a result of lattice de-cohesion.

### **2.6.3 Defect Induced Melting**

In the theory of liquids, the elementary mechanism of melting is connected to the formation of vacancies in solids [106, 107].

Frenkel built a vacancy model of melting in 1930 [108]. He proposed the vacancy concentration increases when heating a solid crystal. There is an instantaneous creation of “holes” (representing the passage from solid to liquid) when reached critical value. The energy needed for the formation of additional vacancies is proved by the latent heat of fusion. This model explains the observed specific heat increase at a constant pressure, which increases the thermal expansion coefficient.

Recently, Wang *et al.* [109] re-examined the role of vacancies in melting looking at vacancy migration rather than vacancy concentration. The fundamental theory is that, as a crystal is heated to the melting temperature, intense atomic migration near vacancies will be induced to an extent. Meanwhile, neighbouring atoms will decompose the vacancy. In addition, a quantitative correlation between the vacancy decomposition temperature and the kinetic instability temperature of crystals has been found. In the model, migrating atoms are defined as having the ability to exchange positions with the neighbouring vacancies. Similar to the thermal equilibrium vacancy concentration in the solid, the concentration of migrating atoms ( $C_m$ ) is expressed as:

$$C_m = \exp\left(\frac{\Delta S_m}{k} - \frac{E_m}{kT}\right) \quad 2.29$$

where  $k$  is constant,  $E_m$  is the energy barrier,  $\Delta S_m$  is the entropy change caused by vacancy formation. According to Equation 2.29, the concentration of migrating atoms increases with increasing temperature. It is suggested that when  $C_m$  reaches a critical value, vacancy decomposition occurs due to two neighbouring atoms near a vacancy possessing energies higher than  $E_m$ . Therefore, the atoms have ability to move to the vacancy. It induces destruction of the local lattice structure around the vacancy. In addition, researches show that the vacancy decomposition temperature ( $T^*$ ) is approximately equal to  $T_m^k$  of solids (shown in Fig. 2.24) [109].  $T_m^k$  is the critical temperature which is much lower than the various instability limits (i.e. the temperature where the entropy of the crystal equals that of the liquid phase, the temperature at which a shear modulus in the crystal falls to zero, the isochoric catastrophe temperature) [110]. The coincidence between  $T^*$  and  $T_m^k$  is regarded as a correlation between vacancy decomposition and the onset of melting in solids.



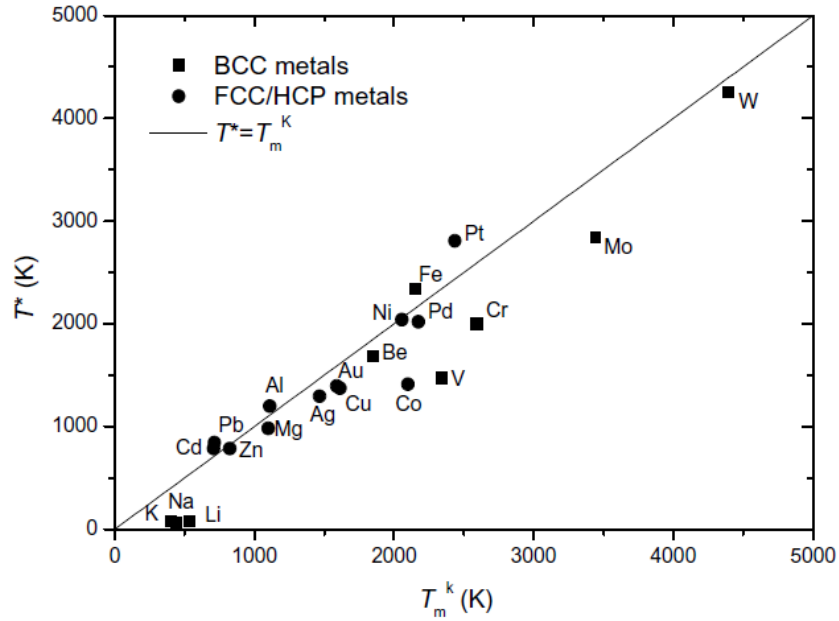


Fig. 2.24 Relationship between  $T^*$  and  $T_m^k$  for a variety of metals

Besides vacancies, interstitials have also been used in interpreting melting in what is known as the Lennard-Jones-Devonshire model [111]. In this model, melting is regarded as an order–disorder transition as a result of the change of relative atomic positions (positional melting). This simple theory of “order-disorder” transition was later generalized to the case of more realistic interaction potential between atoms, and numerical methods were applied to investigate the more complicated models [95].

In contrast to point defects, cooperative defects i.e. lattice dislocations, have been studied in the theory of melting [112-114]. These authors indicated that the total excess energy of dislocations is related to the dislocation density and temperature. Computer simulation was employed to investigate the role of dislocations in melting by Cotterill *et al.*[115, 116]. The results revealed that melting proceeds through the spontaneous proliferation of dislocation dipoles. Cotterill *et al.* concluded that melting could be caused by bifurcation instability, and liquid should be viewed as resulting from a series of cascading bifurcations.

Reviewing the previous researches on the defect effects on melting, it is conceivable that a new melting model should be advanced by considering both the concentration and the mobility of various types of defects (i.e. vacancies, interstitials and dislocations) in

solids. A key point is to understand how these defects cooperate with each other to induce the local lattice instability.

#### **2.6.4 Surface Melting**

Atoms at solid surfaces are less coordinated relative to the lattice interior. Therefore, surfaces normally have a lower thermal stability than the lattice. In reality, free surfaces of solids can act as heterogeneous nucleation sites for melting, allowing melt nucleation at surfaces below the melting temperature.

Frenken *et al.* [117] provided the first evidence of surface melting by iron shadowing and blocking measurements of the scattering of a medium energy proton beam of Pb (110). They found that the thickness of the surface liquid layer increases dramatically when the temperature approaches the melting point. Surface melting has been investigated widely in different metals. A summary of the experimental works can be found in [118-120].

Surfaces are regions of disorder and thus melting tends to initiate here. The surface is a kind of defect where atoms are loosely bound to each other when compared with perfect crystal lattice [120]. In addition, other kinds of defects exist in polycrystals, such as dislocations and grain boundaries (GB). Pre-melting on those defects has also been detected. For instance, Al GBs melt was reported to melt at 4 °C below the bulk aluminium melting temperature [121].

A detailed investigation of pre-melting at GBs and dislocations within bulk colloidal crystals using real time video microscopy is illustrated in Fig. 2.25 [122, 123]. It shows bright-field images at different temperatures (i.e. particle volume fractions) of two crystallites separated by a GB (crystallites tilted at an angle  $\theta \sim 13^\circ$  with respect to one another). In Fig. 2.25 (a), the solid and dashed lines show the GB and a partial dislocation, respectively. The GB cuts the two crystals along two different planes (the yellow line has two slopes). It is composed of an array of dislocations; the two extra planes are indicated by lines in the inset. As temperature increases, particles near the GB start to pre-melt (as in Fig. 2.25 (b)) in order to minimize the free energy, and the nearby particles undergo liquid-like diffusion (inset). In contrast, the partial dislocation that has a lower interfacial free energy than that of GBs, denoted by the dashed line, is

not affected. As temperature is increased further but not much, abrupt melting occurs along the GB as shown in Fig. 2.25 (c). At this stage, the melted region has engulfed the partial dislocation. The width of the pre-melted region increases continuously as temperature is raised. In addition to GB pre-melting, pre-melting at partial dislocations in the colloidal crystals was also clearly observed. Pre-melting from a Shockley partial dislocation was observed at a temperature (28.2°C) higher than the GB pre-melting temperature (Fig. 2.25 (d)).

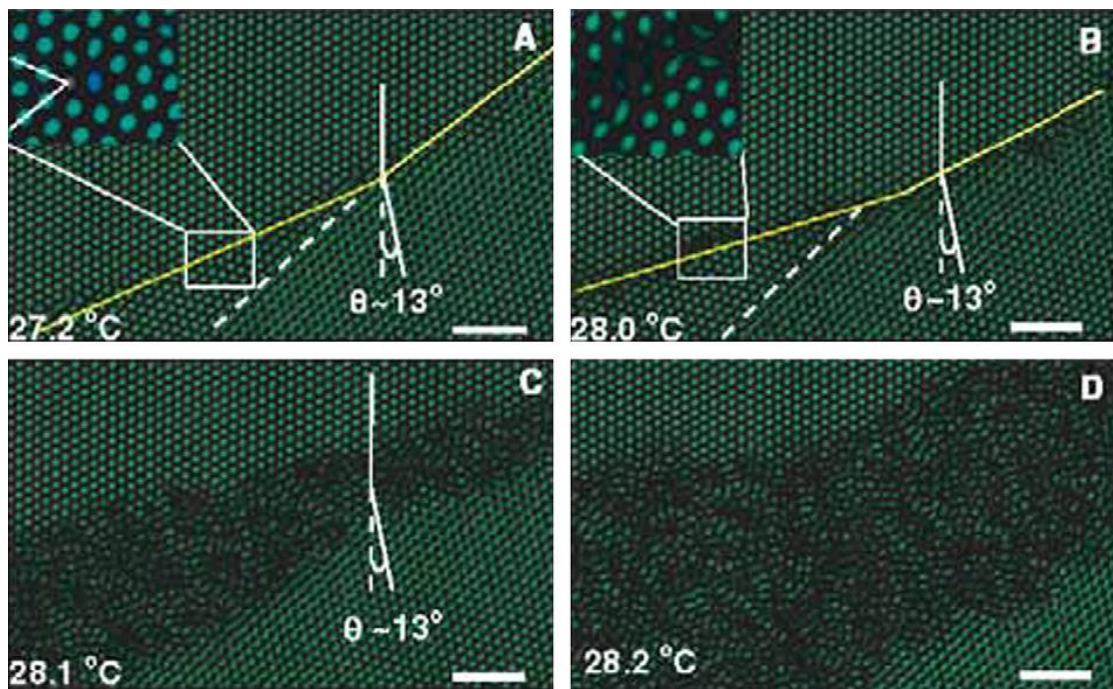


*Fig. 2.25 Pre-melting of the colloidal crystal at a grain boundary, Scale bars, 5  $\mu\text{m}$  [122]*

Melting in a real polycrystalline system is clearly quite spatially heterogeneous, with defects playing a major role in determining the regions of initial melting. Pusey [123] caught the act of melting with video microscopy as shown in Fig 2.26. Red represents the most movement; blue, the least. Before completely melting, crystalline colloids premelt along the grain boundaries (diagonal rising from left to right). Near these boundaries, the particles move rapidly and show diffusion like liquid.

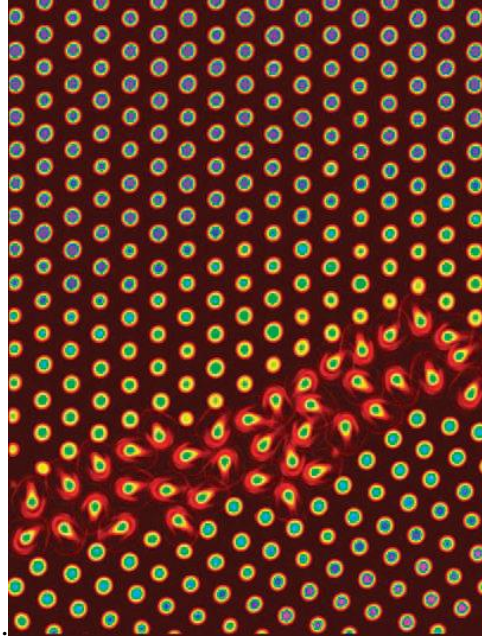


*Fig. 2.26 Caught in the act of melting [123]*

More recently, Myhra *et al.* [124] simulated the melting transition process, by means of the evolution of the amplitude field, for a polycrystalline material which is exposed to a homogeneous temperature increase, as shown in Fig. 2.27. They pointed out that melting mostly starts from the grain boundaries and moves inwards in the bulk of the individual grains. The grain boundaries in the material grow thicker with time, that is, the solid material is reduced to smaller pieces of solid material surrounded by a liquid phase.

Fig. 2.27 (a)-(d) depicts the temporal evolution of the mean amplitude field of a polycrystalline material through a melting transition induced by a homogeneous temperature increase in the system, whilst pictures (e)-(f) depict enlarged area in the same system. High values of the field parameter (yellow) indicate the crystal phase, low values (black) represent the liquid phase whilst the intermediate values (red) represent grain boundaries and other defects in the material.

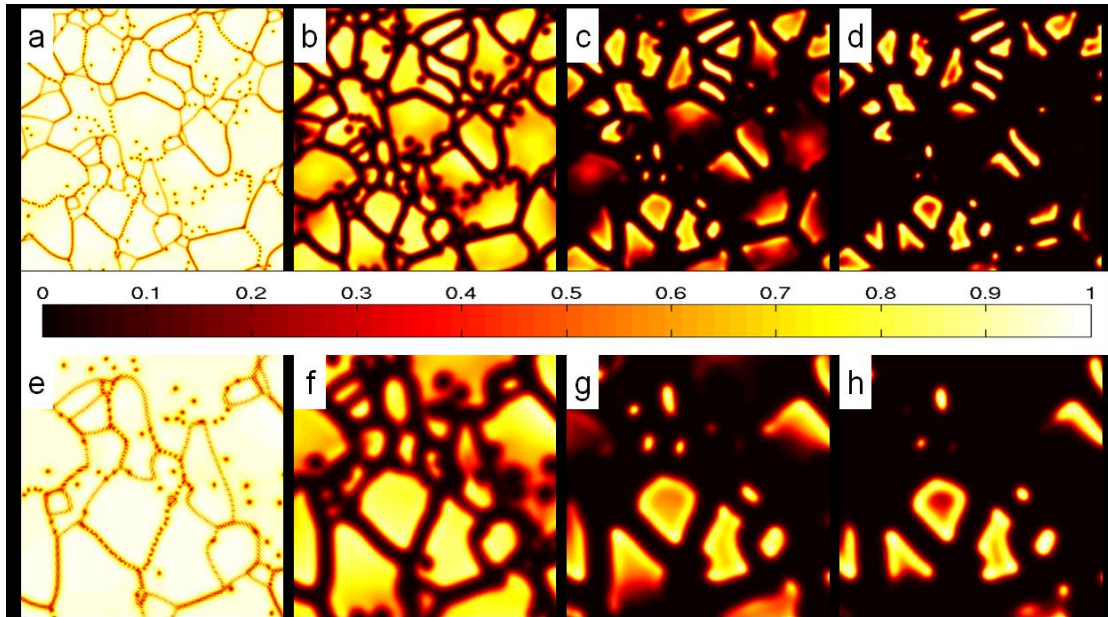


*Fig. 2.27 Simulation of melting processing [124]*

### ***2.6.5 Melting of Low Melting Phase or Impurities***

In general, if an alloy contains two or more phases, melting should begin with low melting phase or impurities. The low melting point impurities have an influence on the alloy melting temperature as well as the toughness and ductility [125].

The existing theories of melting are still far from being complete and raise new questions. Hence, in this project, developing the melting process with aluminium alloys is one the main purposes. The rate of liquid formation during re-heating is important for the semisolid processability of alloys. The heating route must be analysed to determine the heating rate in the various parts of the billet and hence predict the liquid content variation across the billet at stages in the processing. The kinetics of melting may provide a working window in time alongside the working window in temperature.

### ***2.7 Objectives of the Work***

Overall, the objectives of this project are to understand what makes an alloy suitable for SSM processing on both aspects of thermodynamics and kinetics, and to develop a prediction model for simulating the liquid fraction as a function of temperature for aluminium series alloys. Calorimeters and simulation tools were used to investigate the

liquid fraction changes during heating and cooling (as described in **Section 3.1** and **3.2** respectively).



## Chapter 3 Background of Prediction and Experiment

In this chapter, thermodynamic simulation software and the experimental techniques and instrumentation are presented. The evaluation of liquid fraction using computational methods and thermal analysis are discussed. In addition, various material characterisation techniques employed for the present study, are covered.

### *3.1 Thermodynamic Prediction*

Accurate prediction of the microstructure evolution is essential to successful materials design. In recent years, alloy design assisted by computational thermodynamics has proven to be a powerful tool for the design of materials. With efficient prediction, the experimental trial and error process can be reduced considerably. Computational thermodynamics initiated with the work of Kaufman and Bernstein [80] to develop the CALPHAD (CALculation of PHase Diagram) method in the 1970's. Nowadays, software packages such as MTDATA [126] and Thermo-Calc are well developed using the CALPHAD approximation. The importance of phase equilibria and their visual representation in the form of phase diagrams for alloy design and development is reflected in the large number of phase diagrams assessed [127]. The other crucial parameter is the kinetics. Diffusion coefficients describe the rate of flux of a particular component through a material. Combined with phase equilibrium data they enable the prediction of microstructure evolution, which is developed by Andersson and Ågren [128, 129] forming the basis of the program DICTRA (Diffusion- Controlled TRAnsformations). The scheme in Fig. 3.1 reviews how experimental data and theory are integrated in order to develop thermodynamics and diffusion mobility databases using the CALPHAD method.

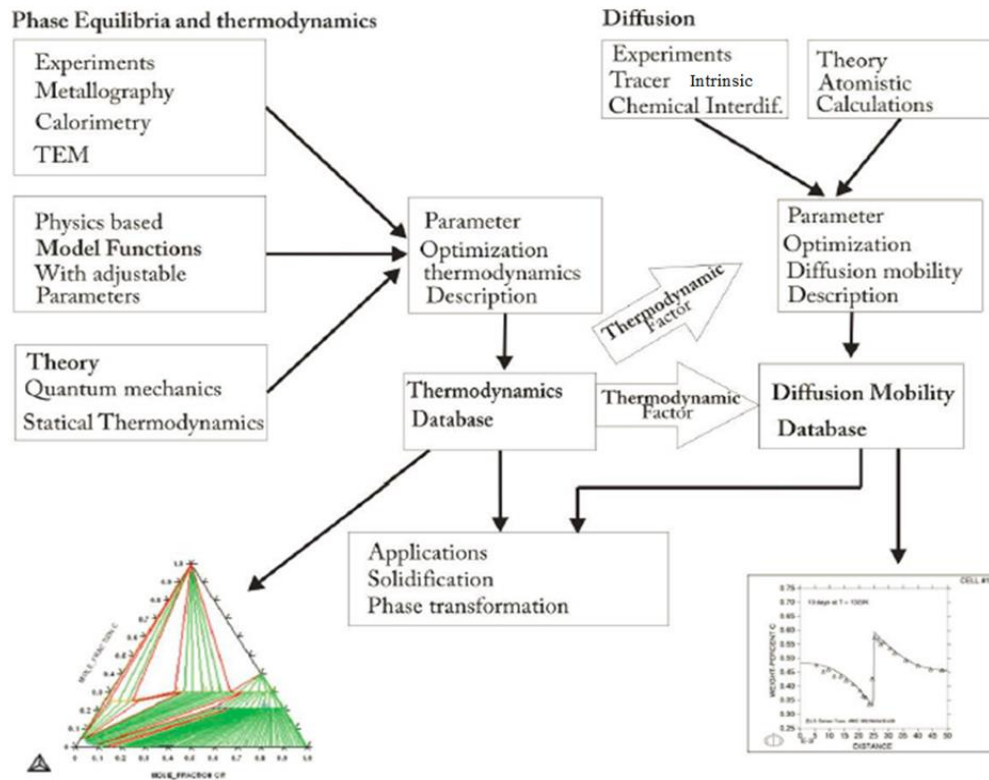


Fig. 3.1 Scheme of CALPHAD method for calculation of phase equilibrium and phase transformations [128]

In this work, the Thermo-Calc and DICTRA software will be carried out to simulate the phase transformations. Thermo-Calc and DICTRA are based on the CALPHAD method. A brief introduction to the CALPHAD modelling of thermodynamic variables in multi-component systems is given in this chapter, as well as the two software packages.

### 3.1.1 CALPHAD Modelling of Thermodynamics

Phase diagrams can provide the graphical presentation of the equilibrium state of a material as a function of temperature, pressure, and composition of the components. The heart of the CALPHAD method is the calculation of the Gibbs energy of a phase as a function of its composition temperature and pressure [130].

The modern Calphad approach is characterised by the following points [128, 131]:

- A predictive capability allows the extrapolation of thermodynamic descriptions and phase equilibrium calculation from assessed binary systems to ternary, quaternary and higher order systems.
- Identification of key experiments drastically reduces the necessary experimental effort in multicomponent systems.



- Stable and metastable phase equilibria can be calculated.
- The driving forces for all phase transformations are available.
- Local phase equilibria can be calculated, providing a numerical input to materials processing software, for example in solidification simulation or reactor modelling.
- The reading of multicomponent phase diagrams is drastically simplified by the fact that all the interesting two-dimensional sections in temperature, composition or even chemical potential can be readily calculated, plotted and read directly.

### ***3.1.2 Thermo-Calc Software***

Thermo-Calc is a powerful and flexible software and database package for all kinds of phase equilibrium, phase diagram and phase transformation calculations and thermodynamic assessments. Moreover, many types of process simulations can also be performed. It has been developed for complex heterogeneous interaction systems with strongly non-ideal solution phases [128] and can be applied to any thermodynamic system depending on the kind of database it is connected to.

The powerful applications and databases contain almost all possible types of calculations of diagrams, thermodynamic factors and most elements. In this project, Al-based databases such as TT-AL7 [132] will be used. Thermo-Calc determines the equilibrium distribution of elements resulting from crystallisation of phases. It can also calculate non-equilibrium solidification by using an implemented Scheil solidification mode. The calculation theory and equations for Thermo-Calc were described in Section 2.6.

### ***3.1.3 Diffusion-Controlled Transformations (DICTRA) Software***

Thermodynamic calculation and kinetic simulation are feasible methods in understanding material properties and processes. Software for calculation of phase diagrams and thermodynamic properties have been developed since the 1970's. Thermo-Calc, as a reliable and powerful software, has databases for all kinds of phase diagrams, phase equilibrium and phase transformation calculations. A range of selectable modules are developed to support different research purposes.

In parallel with the development of Thermo-Calc, DICTRA was developed to treat the kinetics of phase transformations including a variable function 'time'. The rate of a phase transformation is often controlled by diffusion processes. DICTRA is a software

package for diffusion simulations in multicomponent alloys with different models and applications [133]. The first version of the program DICTRA was developed in 1993 in a co-operation between the Royal Institute of Technology and the Max-Planck-Institut für Eisenforschung GmbH [134]. DICTRA is closely linked with the Thermo-Calc software, which provides all necessary thermodynamic calculations. At present a number of different models have been incorporated into the DICTRA as shown in Fig. 3.2 [128].

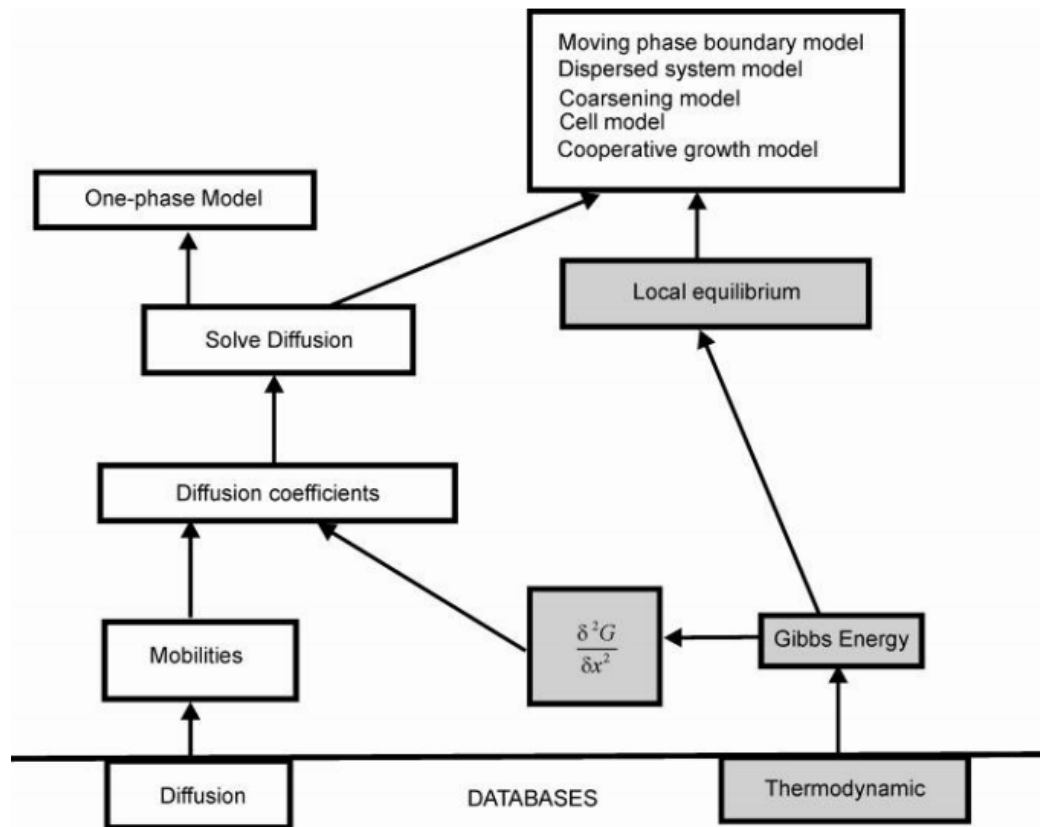


*Fig. 3.2 General structure of the DICTRA software. The grey boxes show functions supplied by Thermo-Calc, which is used as a subroutine by DICTRA [128]*

DICTRA simulations exploit databases containing data for multicomponent thermodynamics and diffusion. Diffusion coefficients are derived from the mobilities in the databases (a database that contains information about the atomic mobility of individual components in relevant phases [135]) for diffusion and thermodynamic factors from the thermodynamic databases.

The collection of models in DICTRA software has been used to simulate a range of processes. Some areas of application are [128]:

- Homogenization of alloys
- Solidification of alloys
- Single-phase model
- Moving boundary model
- Model for diffusion in dispersed systems
- Effective diffusion model
- Cell model
- Model for coarsening
- Cooperative growth model

The accuracy of DICTRA is highly dependent on database precision, however choice of geometry also makes a difference [127].

#### **3.1.3.1 Mobilities**

Generally, diffusion is based on the Fick's law, *i.e.* the movement of atoms in a concentration gradient (concentration  $c_i$  of an element  $i$  being defined as the moles per molar volume  $V_m$ ). Concentration is directly accessible by local analytical methods. In this case the kinetic parameters coupling concentration gradients with atomic fluxes are the diffusivities. From a thermodynamic point of view concentration gradients do not represent true forces. In multi-component systems this effect is common. The situation is even more complicated in the case of phases with several sub-lattices, the sub-lattices being specified by the preferential occupation of given species.

If a kinetic database is to be set up, this should not be on the basis of diffusivities. The simulation shall start with the fundamental equation relating fluxes to true thermodynamic forces. In this approach the kinetic parameters are the mobilities. This drastically reduces the number of parameters to store and so significantly decreases the complexity of the composition and temperature dependence.

Based on the absolute-reaction rate theory, the mobility contains terms related to the vacancy concentration and to the exchange rate of atoms with a vacancy. Both terms refer to thermally activated processes. Therefore, the mobility will be given the form:

$$M_k = \frac{M_k^0}{RT} \exp\left(\frac{-\Delta G_k^*}{RT}\right) \quad 3.1$$

where  $M_k^0$  denotes a frequency factor and  $\Delta G_k^*$  is a Gibbs energy barrier; both terms composition dependent. In the mobility database these terms are represented by a Redlich-Kister polynomial [136], in the same way as is done for the thermodynamic functions in the corresponding databases. For magnetic systems a magnetic factor should also be introduced.

A kinetic database has been established to cover a large number of elements and phases. It is available as MOB2.

### **3.1.3.2 Boundary Conditions**

In the numerical treatment of a single phase transformation the volume is represented by a single closed cell. The cell is subdivided into two half spaces, one for the growing phase, the other for the shrinking phase. Various geometries are possible in DICTRA, i.e. linear, cylindrical, ellipsoidal and spherical geometry. The cells are then coupled by the conditions that the total mass balance is fulfilled. Within each cell, the boundaries between regions are mobile. Within each region a phase has to be specified. The phase may be set dormant such that it appears only after a critical driving force is attained. The spatial coordinate is discretized by grid points, either equidistant or with increasing density as obtained from a geometric series [137, 138].

## **3.2 Calorimetry**

Calorimetry is a well-established measuring method that is widely used in academia as well as industry. It is used for measuring heat capacity, enthalpy changes, and for detecting the phase transitions of materials as discussed in the previous chapter. In this chapter, an overview of classic Differential Scanning Calorimetry (DSC), and a discussion of the recent Single-Pan Scanning Calorimeter (SPSC) technique will be presented.

### 3.2.1 Differential Scanning Calorimetry (DSC)

Differential Scanning Calorimetry (DSC) [139, 140] is a thermo-analytical technique in which the difference in the amount of heat required to increase the temperature of a sample and a reference is measured as a function of temperature. Both the sample and reference are maintained at nearly the same temperature throughout the experiment.

DSC is intimately related to differential thermal analysis (DTA) [141]. A schematic diagram of DSC is shown in Fig. 3.3. A DSC consists of two pans, i.e. a sample pan and a reference pan. The two pans are heated or cooled uniformly while the heat flow between the two is detected. This is done by changing the temperature at a constant rate. The advantage of DSC is that the results can be recorded quickly over a wide range of temperatures and also small samples can be tested using this technique.

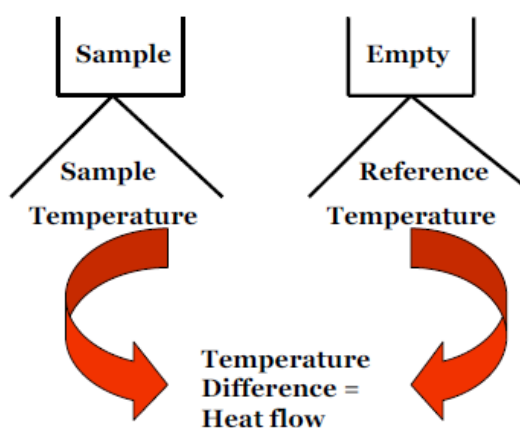


*Fig. 3.3 A schematic diagram of DSC*

There are two basic types of DSCs: 1. The power compensation DSC, 2. The heat flux DSC [142]. Both types of DSCs have two pans but the design and measuring principle differs. They both operate by scanning temperature. For power compensation DSC, the measured heat is compensated with electric energy, by increasing or decreasing the supplied heat. The reference and sample are heated together by using a split heater and extra heat is added to the sample or reference to ensure that both increase at the same rate (as shown in Fig. 3.4) [143]. This form of DSC is most commonly used in low temperature industrial applications [144]. The most common type of DSC use is heat flux DSC which will be briefly described in the next section.

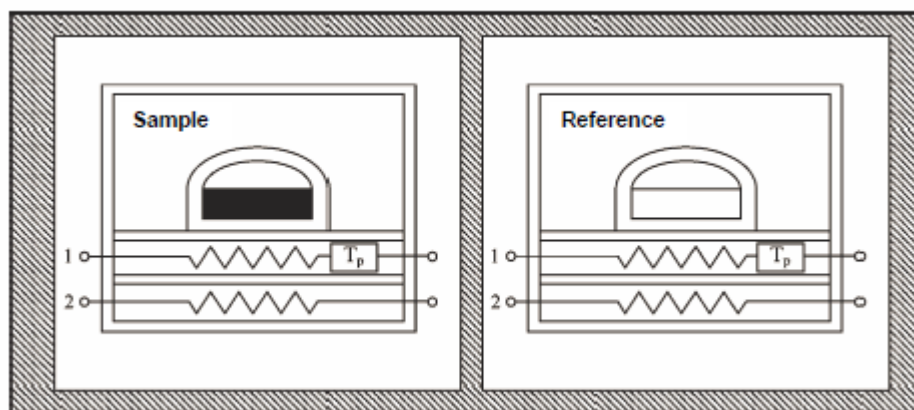
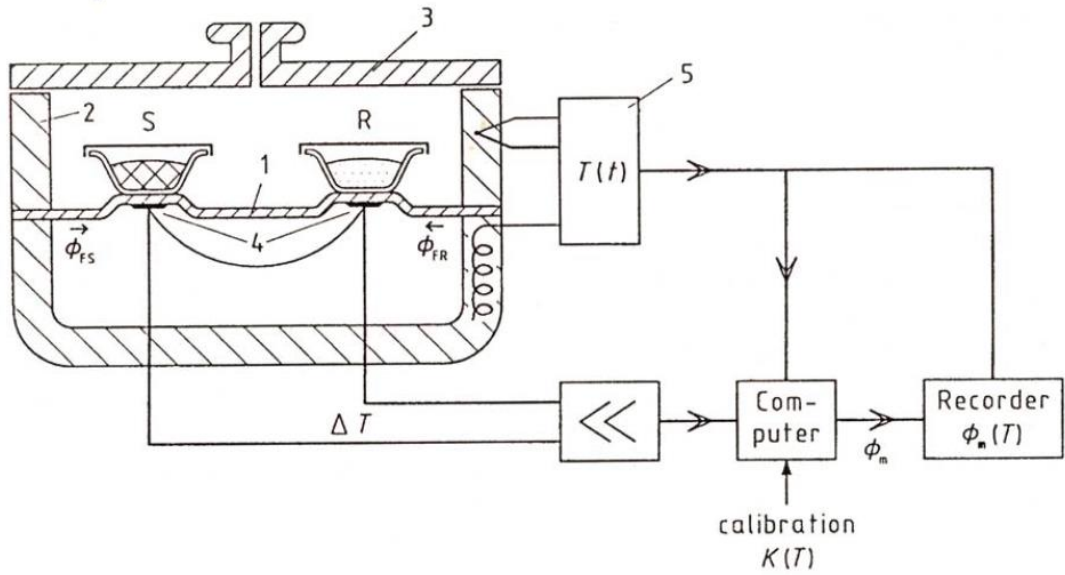


Fig. 3.4 Power compensation DSC. 1) Heating wire, 2) Resistance thermometer [143]

### 3.2.1.1 Heat Flux DSC

A schematic representation of a heat flux DSC [142] is shown in Fig. 3.5. In heat flux DSC, a defined heat exchange can be measured through a well-defined heat conduction path with a given thermal resistance. The characteristic feature of this measuring technique is that the main heat transferred from the furnace passes through a disk to the sample and the reference as shown in Fig. 3.5. The sample and reference are located symmetrically in relation to the centre of the disk. During a run, the enclosure temperature is increased or decreased at a constant rate. The temperature difference between the sample and the reference pan provides a measure of the difference in heat capacity and enthalpy change. The temperature difference  $\Delta T$  is recorded electronically as shown in Fig. 3.5. Also the difference in temperature between the sample and the reference represents heat flux to the surroundings. The temperature difference increases as the heat is applied; this shows the start of a transformation between phases. The absolute values of the thermal properties may be obtained by carrying out a run with the sample followed by a run with a calibrant of known thermal properties.



*Fig. 3.5 Heat flux DSC with disk-type measuring system [142]*

1 disk, 2 furnace, 3 lid, 4 differential thermocouple(s), 5 programmer and controller, S crucible with sample substance, R crucible with reference sample substance,  $\phi_{FS}$  heat flow rate from furnace to sample crucible,  $\phi_{FR}$  heat flow rate from furnace to reference sample crucible,  $\phi_m$  measured heat flow rate,  $K$  calibration factor.

Heat flows to the sample and the reference through the disk at a constant heating rate. The difference between the temperatures of the reference ( $T_R$ ) and furnace ( $T_F$ ) leads to a heat flux of the reference. Also the difference between the sample ( $T_S$ ) and furnace leads to a heat flux of the sample. Fig. 3.6 [5, 145] shows the heat exchange in a heat flux DSC graphically. Fig. 3.6 (a) shows the temperature of the surroundings,  $T_F$ , the temperature of the sample pan thermocouple,  $T_{SP}$ , and the temperature of the sample,  $T_S$ , plotted against time. Fig. 3.6 (b) shows the difference in sample and reference temperature ( $\Delta T_{FS} = T_F - T_S$ ;  $\Delta T_{FR} = T_F - T_R$ ) as a function of time and Fig. 3.6 (c) shows the temperature plotted as a function of the temperature difference.

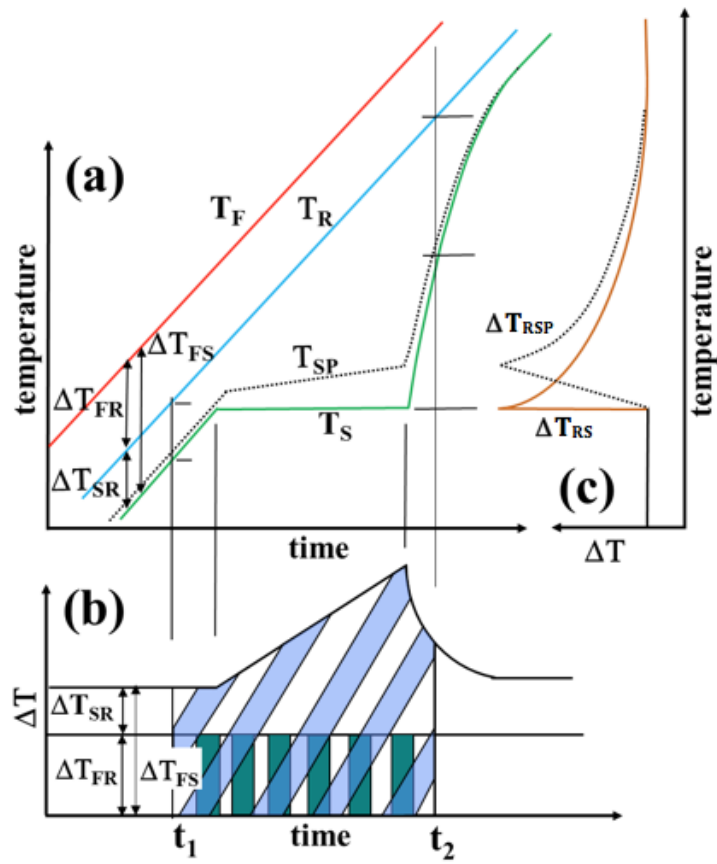


Fig. 3.6 (a) The enclosure temperature  $T_F$ , reference temperature  $T_R$  and specimen temperature  $T_S$  and temperature of the sample pan  $T_{SP}$  are plotted against time for melting a pure metal. (b) The temperature differences  $\Delta T_{FS} = T_F - T_S$  and  $\Delta T_{FR} = T_F - T_R$  plotted against time. (c) The temperature differences  $\Delta T_{RS} = T_R - T_S$  and  $\Delta T_{RSP} = T_R - T_{SP}$  plotted against time. [5, 145]

According to the equations of DSC numerical simulations [139], the shape of the curve depends strongly on the given conditions and parameters, i.e., heating rate and the thermal conductance of the sample. One objective of this project is comparing the results between DSC and SPSC. So it is necessary to make the heating conditions the same, especially the heating and cooling rate. Meanwhile, to understand the kinetics of melting of an alloy and compare with the prediction data from DICTRA, the heating rate in the experiment is very important.



### 3.2.1.2 Liquid Fraction Measurement

The development of the liquid phase with increasing temperature was calculated using the values from the DSC-measurements [139].

The evaluation of the liquid phase fraction is carried out by the application of a peak partial area integration (as seen in Fig. 3.7).

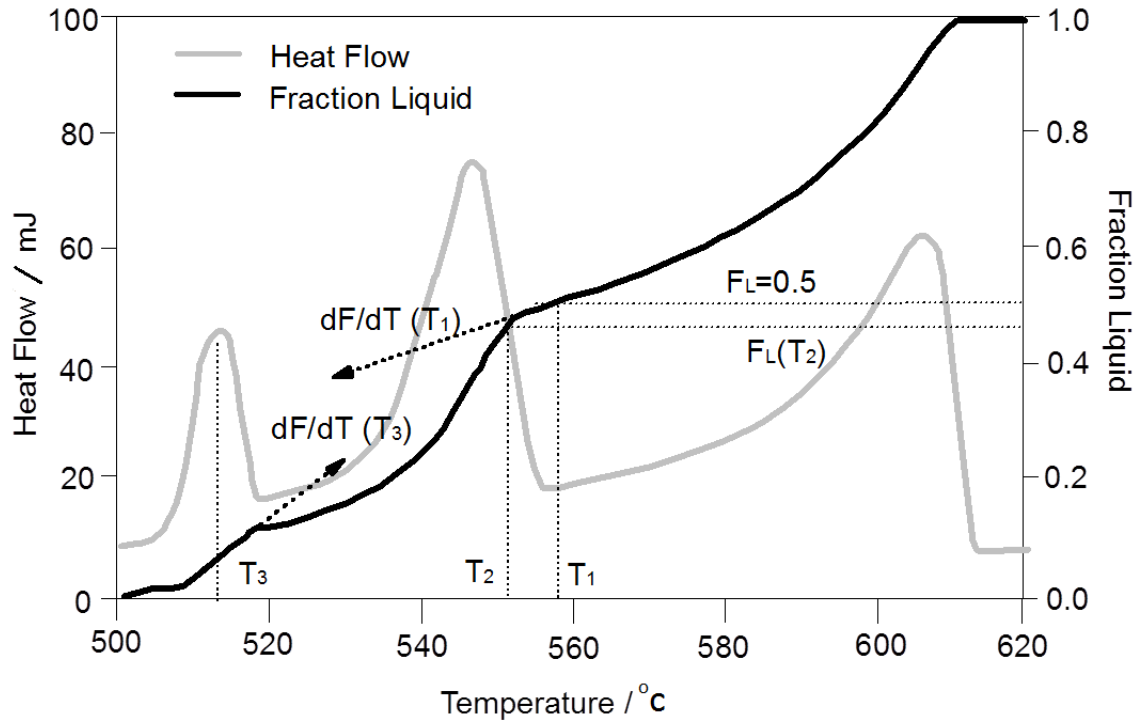


Fig. 3.7 DSC results and critical parameters for semi-solid forming (The graph shows Al-5Cu-5Si alloy) [82]

In the DSC method, the sample is heated from a temperature below solidus to a temperature above the liquidus at a fixed rate. The evolution of the heat of melting during the solid-liquid phase transformation is measured directly. The rate of evolution of the heat of melting is [146]:

$$\frac{dq}{dt} = m \left[ f_s C_{P,S} + (1 - f_s) C_{P,L} + \Delta H \frac{df_s}{dT} \right] \frac{dT}{dt} \quad 3.2$$

where  $m$  is the mass of the sample;  $C_{P,S}$  and  $C_{P,L}$  are the heat capacities of the solid and liquid phases respectively; and  $\Delta H$  is the heat of melting. Since the heating rate  $\alpha$  is

constant, the decrease of the weight solid fraction during melting can be calculated from the absorbed heat of melting. From the Equation above,

$$df_s = \frac{1}{zm\Delta H} \left( \frac{dq}{dt} \right) dT \Leftrightarrow \Delta f_s = 1 - f_s(T) = \frac{1}{zm} \int_{T_s}^T \frac{1}{\Delta H} \left( \frac{dq}{dt} \right) dT \quad 3.3$$

A usual approximation to Equation 3.3 is derived by assuming that the heat of melting is independent of the temperature and thus the composition of the solid phase and is linearly proportional to the amount of the melted alloy, i.e.:

$$f_s(T) = 1 - \frac{1}{m\Delta H} q(T) \quad 3.4$$

where  $q(T)$  is the heat absorbed from the beginning of melting until the temperature of the alloy reaches  $T$ . The whole area under the enthalpy-area curve is used to determine the melting enthalpy of the material. During DSC measurement, the typical melting peak obtained is shown in Fig. 3.8.

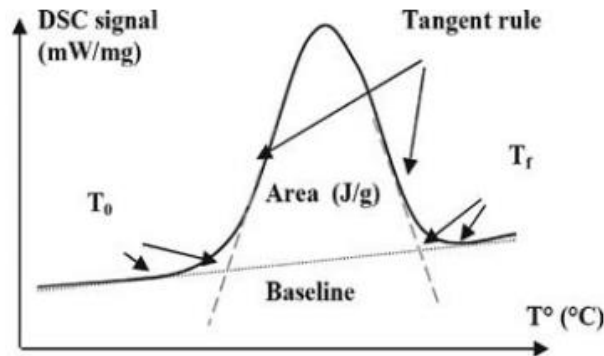


Fig. 3.8 Melting peak features [139]

The peak characteristics are:

- The changes of slope, jumps and peaks showing the thermal events (phase transformations, chemical reactions, etc.)
- The peak area is the enthalpy variation of the transformation
- The specific heat is calculated from the baseline
- Solidus-liquidus interval:  $T$  end of melting- $T$  beginning of melting ( $T_f - T_0$ )

It is often assumed that the liquid fraction is proportional to the absorbed energy during the transformation. The sample is heated until total melting. Therefore, the liquid fraction can be calculated considering the peak area of the transformation, as shown in Fig. 3.9. The characterisation of the melting peak is realised with the following parameters:

- Total area = 100% of the liquid fraction
- Beginning and end of melting

The liquid fraction at  $T_1$  ( $T_0 < T_1 < T_f$ ) is determined with the following relation:

$$\%Liquid = \frac{Area(T_1 - T_0)}{Total Area} \quad 3.5$$

where Area is the shaded area from  $T_0$  to  $T_1$ , Total area is the shaded area from  $T_0$  to  $T_f$ , as show in Fig. 3.9.

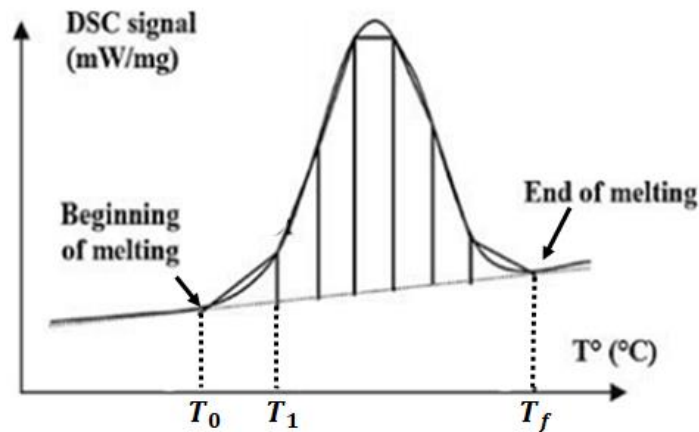


Fig. 3.9 Determination of the liquid fraction [139]

### 3.2.1.3 Problems with DSC

The apparatus measures the difference in heat flow/temperatures between the sample and the reference, and the measured difference is assumed to be proportional to the heat capacity difference between the sample and the reference. This assumption is valid when the sample is heated at a constant rate. However, when the latent heat is evolved in the sample, problems arise. It is clear from Fig 3.6 (c) that after melting  $\Delta T_{RS}$  is large because the sample temperature is rising more quickly than the reference. Although

corrections can be made, they are difficult to carry out because the various heat transfer coefficients are not completely reproducible. As a result, the problems of DSC are (1) Measured temperature difference is not proportional to the difference in heat capacity between the sample and reference; (2) the sample thermocouple doesn't measure the temperature of the sample since a large temperature difference arises between the sample and the sample thermocouple.

This effect, known as smearing, leads to significant errors in the enthalpy change and transition temperature. Although corrections can be made, they are difficult to carry out because various heat transfer coefficients within a DSC are not completely reproducible.

### ***3.2.2 Single-Pan Scanning Calorimeter (SPSC)***

#### ***3.2.2.1 Introduction***

As discussed in the above section, the two-pan DSC has a number of problems in measuring thermal properties. These problems are associated with the presence of the reference pan in the system. The reference pan is not really needed as all the information can be obtained from the temperature of the sample and the surroundings. To eliminate the problems with DSC, a new method was developed by Dong and Hunt [5] to measure heat fluxes accurately. This new apparatus is known as Single-Pan Scanning Calorimeter (SPSC) [147].

A schematic diagram of the calorimeter cell is shown in Fig. 3.10 [147]. The calorimeter cell is made of material with high conductivity. It has an outer crucible and an inner crucible. The outer crucible is thermally isolated by the furnace and has a thick wall. This ensures a constant temperature enclosure. The inner crucible is thermally isolated from the outer crucible to ensure the maximum temperature difference between the inner and outer crucibles. The large thermal resistance and the constant temperature enclosure between the sample and surroundings are the important features of the SPSC.

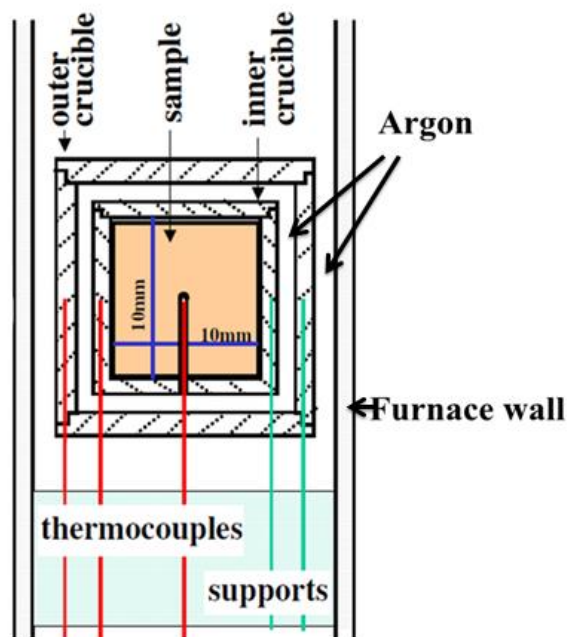


Fig. 3.10 A schematic diagram of the new calorimeter cell [147]

In DSC the sample size was chosen to minimise the smearing but in SPSC smearing is automatically eliminated so there is no disadvantage in using large samples. Three K-type thermocouples [148] were used in the SPSC. Two thermocouples were placed in the walls of the inner and outer crucibles. An additional thermocouple was placed in the centre of the sample. Typically, the sample is a machined cylinder 10mm in diameter and 10mm high. A 7mm deep hole is drilled in the centre of the sample for the thermocouple.

### 3.2.2.2 Enthalpy Calculations

The enthalpy change can be calculated by thermodynamic theory and by using a Visual Basic program. The thermocouple reading is calibrated and zero line correction made to the temperature difference measurements [149].

As the calorimeter is heated in the time period  $dt$ , the temperature of the empty inner crucible increases  $dT_E$ , the calibrant + empty increases  $dT_C$  and the sample + empty increases by  $dT_S$ . The equivalent temperature differences between the inner and outer crucible for the three cases are  $\Delta T_{DE}$ ,  $\Delta T_{DC}$  and  $\Delta T_{DS}$ . Let  $C_C$  be the change in heat substance per degree (i.e. heat capacity times mass) of the calibrant; this must be known as a function of temperature. Similarly  $C_E$  and  $C_S$  are those of the empty crucible and

sample. It should be distinguished that  $C_S$  contains any latent heat and is thus a valuable heat capacity. The heat transfer coefficient between the inner and outer crucible is defined as " $a$ " and will be a function of temperature.

The equations for the heat transfer between the inner and outer crucibles and enthalpy change within the inner crucible can be written as follow [148]:

$$\text{For the empty crucible: } a\Delta T_{DE}dt = C_E dT_E \quad 3.6$$

$$\text{For the calibrant + empty: } a\Delta T_{DC}dt = (C_C + C_E) dT_C \quad 3.7$$

$$\text{For the sample + empty: } a\Delta T_{DS}dt = (C_S + C_E) dT_S \quad 3.8$$

Eliminating  $C_E$  from equation 3.6 to equations 3.7 and 3.8 gives;

$$adt \left( \frac{\Delta T_{DC}}{dT_C} - \frac{\Delta T_{DE}}{dT_E} \right) = C_C \quad 3.9$$

and

$$adt \left( \frac{\Delta T_{DS}}{dT_S} - \frac{\Delta T_{DE}}{dT_E} \right) = C_S \quad 3.10$$

Dividing equation 3.10 by 3.9 and multiplying by  $dT_S$  gives a general expression for the rise in enthalpy of the sample  $dH_S$ .

$$C_C \left( \frac{\Delta T_{DS} - \frac{\Delta T_{DE}}{dT_E} dT_S}{\frac{\Delta T_{DC}}{dT_C} - \frac{\Delta T_{DE}}{dT_E}} \right) = C_S dT_S = dH_S \quad 3.11$$

The equation is valid as  $dT_S \rightarrow 0$  and can thus handle the latent heat of a pure material. The ratios  $\frac{\Delta T_{DE}}{dT_E}$  and  $\frac{\Delta T_{DC}}{dT_C}$  are evaluated from the empty and calibrant + empty run at the relevant temperature using the same time interval. The implication of these terms is best visualised by noting that the first is the inverse of  $\frac{dT_E}{dt} \frac{1}{\Delta T_{DE}}$  which is the rate of rise of the empty pan divided by the difference in temperature between the inner and outer crucible. The general equation is applicable for any type of function and that includes constant rate of temperature rise or constant heat flux. It should be emphasised that the

equation and the use of a central thermocouple inherently handles the de-smearing process.

### 3.2.2.3 Liquid Fraction Measurement

In DSC measurement, traditionally the liquidus temperature is determined by inspecting the intersection of the base line and the extrapolated tangent line of the heat flow peak. In the SPSC [148], combining Equation 2.13 with Equation 2.14

$$H = C_P T + L \frac{T_L - T k}{T(1-k)} \quad 3.12$$

This shows that the enthalpy does not change linearly with T. Rearranging Equation 2.13, gives:

$$T_L = T[f_L + k(1 - f_L)] \quad 3.13$$

which reveals that  $T_L$  can be determined from the measured temperature  $T$  provided that the liquid fraction  $f_L$  and partition coefficient  $k$  are known.

From the equation 2.14, if latent heat is assumed to be constant and  $C_{P \text{ solid}} = C_{P \text{ liquid}}$ , the fraction liquid can be calculated from enthalpy data, determined as follows:

$$f_L = \left[ \frac{(H - H_{\text{solidus}}) - C_P(T - T_{\text{solidus}})}{(H_{\text{liquidus}} - H_{\text{solidus}}) - C_P(T_{\text{liquidus}} - T_{\text{solidus}})} \right] \quad 3.14$$

## 3.3 X-Ray Diffraction

X-Ray Diffraction (XRD) is a widely used non-destructive technique for characterizing materials. Diffraction occurs when a wave infringes on a regular array of scattering objects, providing that the distance between the objects is of the same order of magnitude as the length of the incoming wave [150]. The scattering of the incident wave by this array leads to many scattered waves. Those could be out of phase with each other, leading to destructive interference [151]. However, when the waves are in-phase, constructive interference results in a distinct outgoing wave. This is known as Bragg's Law, after W.L. Bragg, who first proposed it. It can be simply written as:

$$2d \sin \theta = n\lambda \quad 3.15$$

where  $\lambda$  is the wavelength of the incoming wave (and its multiples  $n\lambda$ ), the spacing of the planes in the scattering array is  $d$ , and the  $\theta$  is the angle of incidence and diffraction. This is shown schematically in Fig. 3.11.

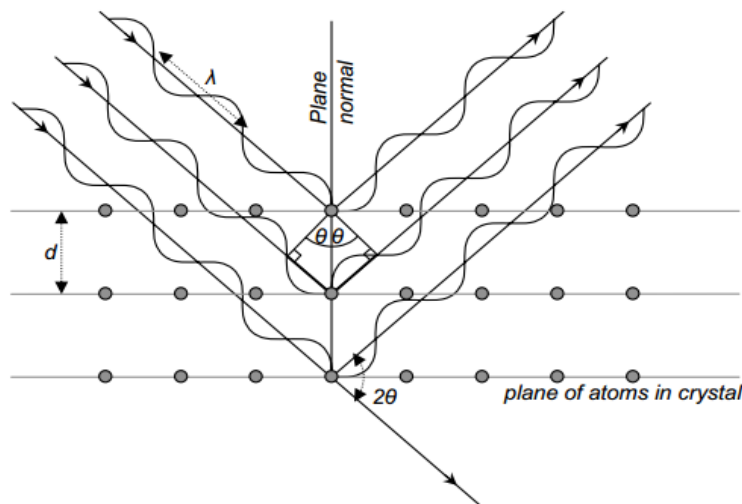


*Fig. 3.11 Diffraction of X-ray by a crystal. (Adapted from [151])*

In this study, the Powder XRD was employed. The term 'powder' means that the crystalline domains are randomly oriented in the sample. Therefore when the 2-D diffraction pattern is recorded, it gives concentric rings of scattering peaks corresponding to the various spacings ( $d$ ) in the crystal lattice. The positions and the intensities of the peaks are used for identifying the phases or structures of the material. Powder diffraction data can be collected using either transmission or reflection geometry, as shown in Fig. 3.12 below. Because the particles in the powder sample are randomly oriented, the same data will be collected from these two methods.

For data analysis, the collected diffraction data will be plotted as scattering intensity versus the scattering angle  $2\theta$  or the corresponding  $d$ -spacing. The peak positions, intensities, widths and shapes all provide important information about the structure/phase of the material. Finally, those parameters will be searched and matched in the certain databases for identification.



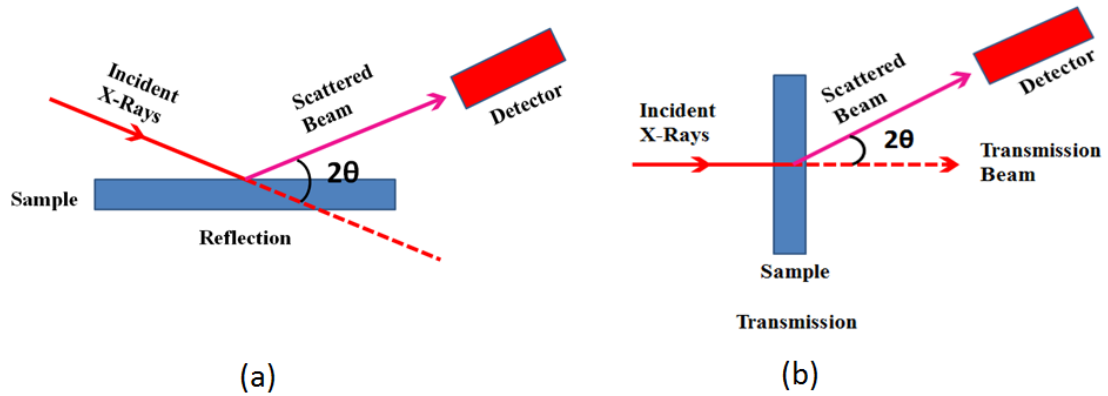


Fig. 3.12 Two collection ways of the diffraction data: (a) Reflection, (b) Transmission.

### 3.4 Vickers Hardness

Hardness testing is one of the most classic mechanical tests to obtain the strength of materials. It has the advantage of ease and speed, and requires no special specimen preparation [152]. Hardness is defined as the resistance of a material to surface penetration by an indenter under a compressive load [153]. In this study, the Vickers hardness method was employed to determine the hardness of the aluminium binary alloys. A square-based pyramid diamond indenter with a  $136^\circ$  point angle is pressed into the surface at a certain load and the diameter of the indentation is measured, as is illustrated in Fig. 3. 13

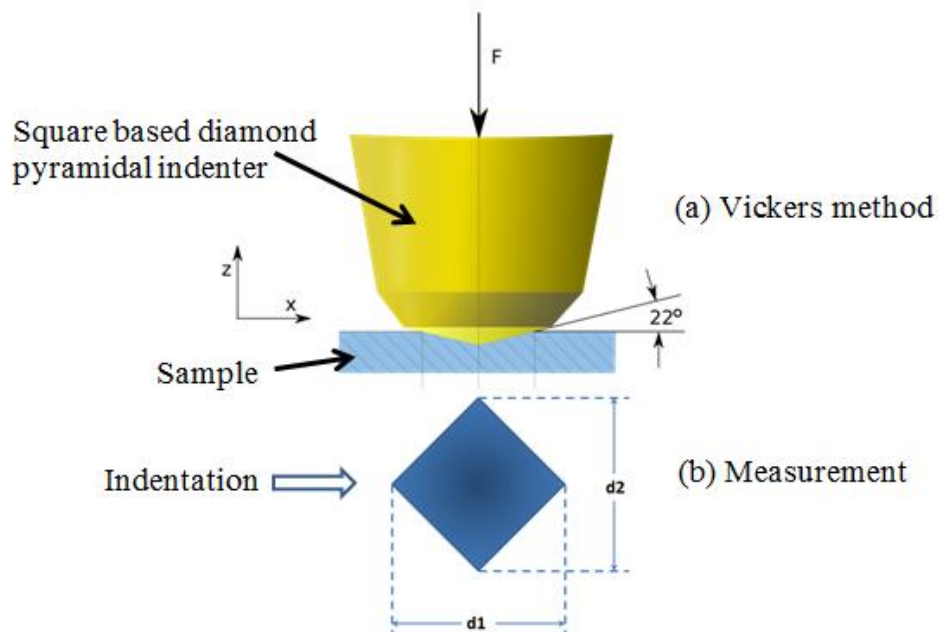


Fig. 3.13 Schematic representation of Vickers hardness test

The diagonal lengths of the resulting impression are measured by means of an optical microscope fitted with a linear measuring device, and the average of the two diagonal lengths is then converted to a hardness value. The Vickers hardness, as a function of the indenting force divided by the area of the impression, is calculated using the equation:

$$HV = \frac{2F \sin \frac{136^\circ}{2}}{d^{*2}} \cong 1854.4 \frac{F}{d^{*2}} \quad \mathbf{3.16}$$

where  $F$  is load in gram,  $d^*$  is the average diameter of the impression in  $\mu\text{m}$  (arithmetic mean of the two diagonals,  $d_1$  and  $d_2$ ). The unit is  $\text{kg/mm}^2$  but normally only the number is given.

In this work, a Mitutoyo MV-1S macro-hardness tester with a loading capacity of 1-20 kg was employed.

## Chapter 4 Experimental Procedure

### 4.1 Introduction

In this chapter, the materials, simulation methods, experimental techniques and instrumentation, including the experimental, and various material characterisation techniques employed for the present study, are covered. The experimental procedures and specimen preparation techniques for material characterisation methods are also presented.

### 4.2 As-received Materials

#### 4.2.1 Pure Aluminium

High purity (99.999%) aluminium was received from Goodfellow Cambridge Limited and was used to calibrate the temperature and enthalpy measurements of the instrument (i.e. DSC, SPSC). The chemical compositions are shown in Table 4.1.

Cu	Fe	Mg	Hg	Pd	Pt	Si	Al
0.616	0.647	1.25	<0.3	<0.1	<0.1	1.32	Bal.

*Table 4.1 Chemical compositions of pure aluminium (Unit: ppm)*

#### 4.2.2 Binary Alloys

In the first part of this project, 10 binary cast alloys were studied. These are representative of Si, Cu and Mg contents in commercial alloys used for semi-solid processing. The chemical compositions of those alloys are shown in Table 4.2. The chemical compositions were tested by inductively coupled plasma atomic emission spectroscopy (ICP-AES) in Shenyang Institute of Metal Research (SIMR). All these alloys were supplied by GRINM (General Research Institute for Nonferrous Metals, Beijing). The 10 binary alloys were manufactured by permanent mold casting without any heat treatment to a shape of rod with 20 mm in height and 80 mm in diameter.

Binary Alloys	Chemical compositions (wt%)						
	Si	Cu	Mg	Fe	Ca	Ni	Mn
Al-1Si	1.01	--	--	0.0074	0.0024	--	--
Al-5Si	5.08	--	--	0.023	0.0028	--	--
Al-12Si	11.68	--	--	0.042	<0.002	--	--
Al-18Si	17.54	--	--	0.082	0.012	--	--
Al-1Cu	--	0.98	--	--	--	0.0002	--
Al-2Cu	--	2.18	--	--	--	0.0004	--
Al-5Cu	--	4.9	--	--	--	0.0002	--
Al-0.5Mg	0.0032	<0.0005	0.42	0.0076	--	<0.0005	--
Al-3Mg	0.0040	<0.0005	2.82	0.010	--	<0.0004	0.0018
Al-5Mg	0.0028	0.0006	5.58	0.0044	--	<0.0004	0.0012

Table 4.2 Chemical compositions of 10 selected Al binary alloys (Al: Bal., analysed by ICP-AES at SIMR)

The positions of all 10 binary alloys have been labelled in different Al-based binary phase diagrams in Figs. 4.1 to 4.3 separately. Phase diagrams were calculated by Thermo-Calc with the TT-AL7 database [154].

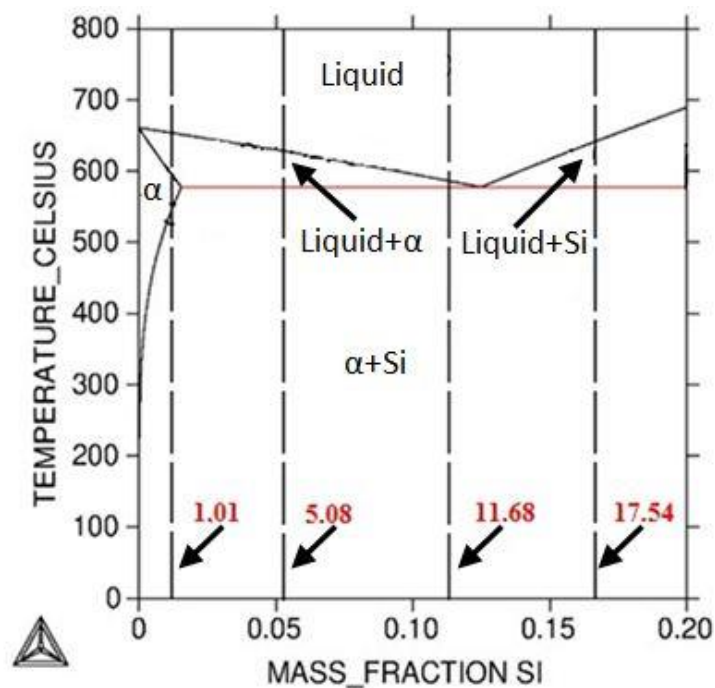


Fig. 4.1 Alloys in Al-Si binary phase diagram

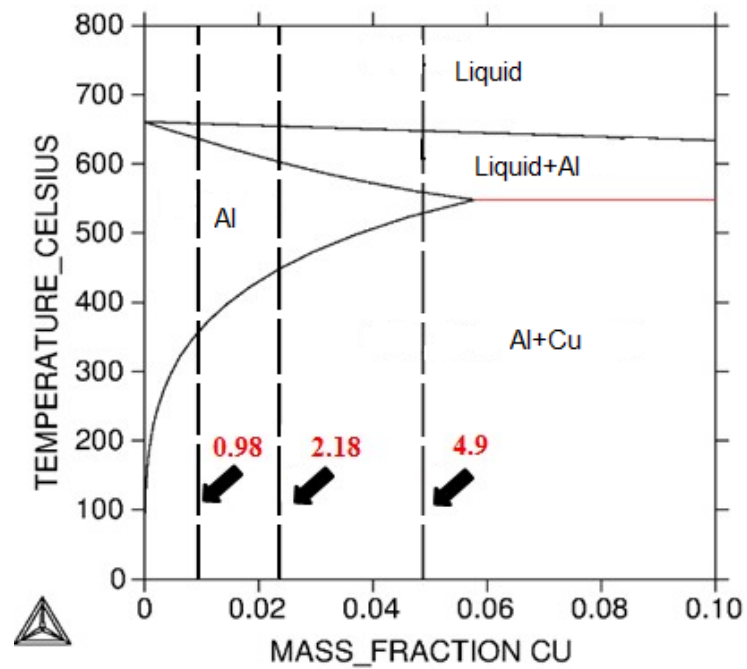


Fig. 4.2 Alloys in Al-Cu binary phase diagram

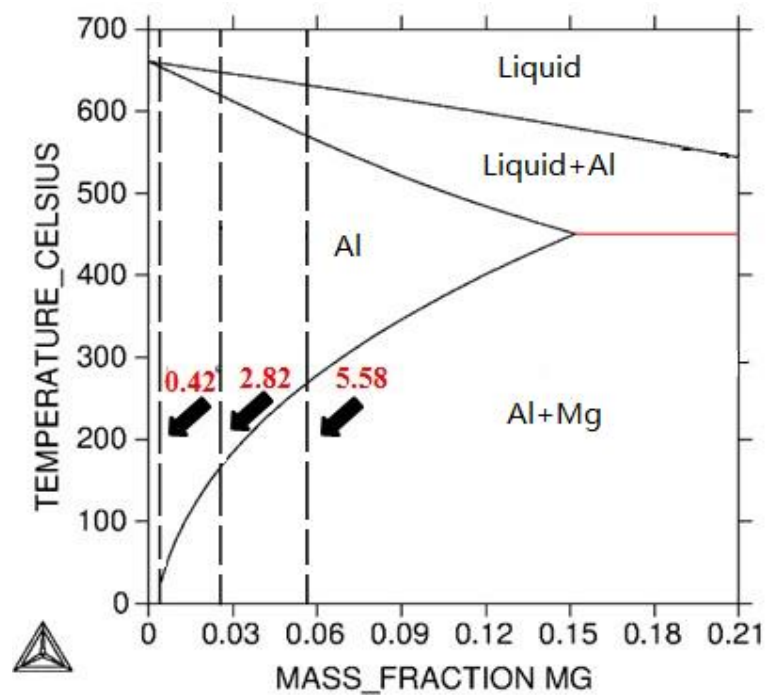


Fig. 4.3 Alloys in Al-Mg binary phase diagram

#### 4.2.3 319s Alloy and 201 Alloy

Alloy 319s is a primary version of the low-cost foundry alloy 319. The contents of elements in 319s alloy including Mn, Fe, Ni and Zn are reduced comparing with 319

alloy, while the contents of Mg increased. The mechanical properties of semi-solid cast 319s-T6 are significantly better than permanent mold cast 319-T6 [155].

Commercial 319s and 201 aluminium alloys were produced by SAG (Salzburger Aluminium Gruppe) in Austria using the MHD (Magnetohydrodynamic) stirring process to obtain the globular, semi-solid structure. The chemical compositions of the as-received alloys and the aluminium alloy (AA) standard compositions [156] are given in Table 4.3.

Alloys	Chemical compositions (wt%)							
	Cu	Si	Mg	Ti	Mn	Fe	Zn	Ag
<b>319s (actual)</b>	<b>2.95</b>	<b>6.10</b>	<b>0.37</b>	<b>0.05</b>	<b>0.02</b>	<b>0.12</b>	<b>0.02</b>	<b>--</b>
<b>319s (standard)</b>	<b>2.5-3.5</b>	<b>5.5-6.5</b>	<b>0.3-0.4</b>	<b>0.2</b>	<b>0.03</b>	<b>0.15</b>	<b>0.05</b>	
<b>319 (AA standard)</b>	<b>3.0-4.0</b>	<b>5.5-6.5</b>	<b>&lt;0.1</b>	<b>&lt;0.25</b>	<b>&lt;0.5</b>	<b>&lt;0.8</b>	<b>&lt;1.0</b>	<b>--</b>
<b>201 (actual)</b>	<b>4.80</b>	<b>0.09</b>	<b>0.25</b>	<b>0.25</b>	<b>0.29</b>	<b>0.15</b>	<b>--</b>	<b>0.70</b>
<b>201 (AA standard)</b>	<b>4.0-5.20</b>	<b>&lt;0.1</b>	<b>0.15-0.55</b>	<b>0.15-0.35</b>	<b>0.15-0.50</b>	<b>&lt;0.1</b>	<b>--</b>	<b>0.40-1.0</b>

*Table 4.3 Chemical compositions (wt%) of Alloys 319s and 201 (analysed by ICP-AES at SIMR)*

### ***4.3 Thermodynamic Prediction by Thermo-Calc and DICTRA***

Thermodynamic modelling supports the experimental work and can guide the alloy development. In this work, computational thermodynamics are applied to predict the solidification sequences of the alloys. The equilibrium and Scheil calculations were carried out using Thermo-Calc software. The solidification simulations considering diffusion kinetics were performed in DICTRA.

#### ***4.3.1 Equilibrium and Scheil Predictions by Thermo-Calc***

Thermo-Calc (Version: TCW5) software was utilised to predict the phases in both equilibrium and non-equilibrium (Scheil) freezing. Fraction liquid is a critical parameter for both fundamental work and the control of the semi-solid process. The prediction of the fraction liquid/temperature relationship is advantageous for identifying new alloy

compositions suitable for semisolid processing. The effects of added copper, silicon and magnesium on the fraction liquid were determined. The phase equilibria are calculated using thermodynamic database TT-AL7 [154] in Thermo-Calc. For each alloy, a curve of liquid fraction versus temperature was plotted.

#### 4.3.2 DICTRA Simulation

The transformation kinetics are simulated using the software DICTRA with the mobility data base MOB2 [157]. In this model a stepwise cooling is computed by taking into account the continuously changing composition of the liquid.

##### 4.3.2.1 Solidification Path Model

DICTRA simulations were performed under the model of ‘solidification path’ [133]. According to the phase diagrams in Fig.4.1-4.3, in the semi-solid state, the only phase that Al-Si binary alloy presents at equilibrium is liquid, Al (FCC) and Si. For Al-Cu and Al-Mg binary alloys, the only phases are liquid and Al (FCC). That is the reason why two different cells were designed respectively, as can be seen in Fig. 4.4.

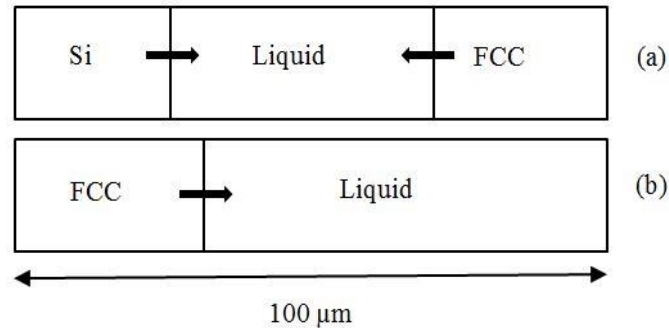


*Fig. 4.4 DICTRA cell model for simulation of solidification (a) for Al-Si binary alloys, (b) for Al-Cu and Al-Mg binary alloys*

The cooling rate was set at 3K/min and 10K/min from 700 °C to 400 °C for all binary alloys to cover the whole temperature interval between liquidus and solidus. In order to simulate solidification, FCC and silicon phase are allowed to form at the solid-liquid interface. The simulation started with homogeneously distributing alloying elements in the liquid phase with 60 linear type grid points along the cell. Then the liquid fraction/temperature relationship was plotted. Simulation codes for Al-Si, Al-Cu and Al-Mg alloys are listed in Appendix A, B and C respectively.

#### 4.3.2.2 Cell Size Impact

To include various diffusion distances and investigate the impact of cell size on the simulation of solidification of binary alloys, three cell sizes were assigned, namely, 10  $\mu\text{m}$ , 100  $\mu\text{m}$  and 1 mm. Here, we will only take the Al-5.08wt%Si alloy for demonstration. Parameter selection is described in Section 4.3.2.1. The cooling rate remains at 10K/min. Then the profiles of alloying element (Si) were plotted as well as the fraction liquid/temperature relationships.

#### 4.3.2.3 Heating and Re-heating

Melting would be most relevant to the thixo-processing rather than cooling. However, the equilibrium and Scheil mode in Thermo-Calc are for the process of solidification. Therefore, heating simulations were designed through DICTRA. However, there were hardly any reports in literature demonstrating the simulation for melting behaviour by DICTRA. In this work, a novel melting was performed with DICTRA. Both heating and re-heating procedures were carried out. Heating refers to a process of heating the sample from solid to entire liquid (i.e. solid  $\xrightarrow{1\text{K/min or } 10\text{K/min}}$  liquid), while re-heating refers to a process that the sample was quenched from liquid to solid then heating it up to totally liquid (i.e. liquid  $\xrightarrow{\text{quench}}$  solid  $\xrightarrow{1\text{K/min or } 10\text{K/min}}$  liquid)

The heating and re-heating simulations were carried out with the Al-5.08wt%Si alloy only and with the same cell structure as the ‘solidification path’ model. To simulate liquation, liquid is allowed to form at the solid-liquid interface. The heating processing was set from 500 °C to 700 °C at a heating rate of 1K/min and 10K/min and the matrix was set to solid FCC\_A1 phase with homogenously distributed Si. In the case of re-heating, the matrix was set to liquid phase and the simulation temperature started at 500°C. Therefore, at the first time step of simulation, there will be a temperature drop from liquid state to 500°C (equivalent to the quench), followed by given heating rate (1K/min and 10K/min) ramp to 700°C. The liquid fraction/temperature relationships were plotted for comparison. Simulation code for the heating is shown in Appendix D and Appendix E is for the re-heating.



#### ***4.3.2.4 Element Composition Profiles at one Specific Temperature***

In this work, the simulations were performed for nominal global compositions. The microsegregation of the elements can be directly plotted as composition profiles versus distance. In order to track the evolution of diffusion along the time axis, the microsegregation profiles of alloying elements were plotted at several specific temperatures.

#### ***4.3.3 Diffusion Coefficients of Si, Cu and Mg in FCC(Al) and Liquid(Al) Phases***

Diffusion is a fundamental and critical factor to understand many important phenomena. Among the various diffusion coefficients (self-diffusion, impurity diffusion, intrinsic diffusion, and chemical diffusion coefficients), the impurity diffusion coefficient is most crucial. It is defined as the diffusion of a solute in a solvent at an extremely small concentration. In DICTRA simulation, back-diffusion in the solid by using impurity diffusion coefficients determines the spatial profiles of elements. Apart from the practical importance, impurity diffusion coefficient describes atomic mobility in DICTRA. The impurity coefficients for elements in both solid and liquid can be studied. In this work, the impurity diffusion coefficient is calculated by the Arrhenius equation:

$$D = D_0 \exp\left(\frac{-Q}{RT}\right) \quad 4.1$$

where  $D_0$  is the Temperature-independent pre-exponential ( $\text{cm}^2/\text{s}$ );  $Q$  is the activation energy ( $\text{J/mol}$ ),  $T$  denotes the absolute temperature ( $\text{K}$ ); and  $R$  is the gas constant ( $=8.31441 \text{ J} \cdot \text{mol}^{-1} \cdot \text{K}^{-1}$ ).

The atomic radii are [158]:

Elements	Atomic radius (pm)
Cu	145
Si	111
Mg	145
Al	118

*Table 4.4 The Atomic radii of Cu, Si, Mg and Al*

In the FCC(Al) [159]:

Elements	$D_0$ (cm <sup>2</sup> /s)	Q (J/mol)	Temp. range (K)
Cu	0.645	136.0E+3	594-928
Si	2.48	137.0E+3	753-893
Mg	1.24	130.4E+3	667-928

*Table 4.5 Tracer impurity diffusion coefficients in FCC Al*

In the liquid(Al) [160]:

Elements	$D_0$ (cm <sup>2</sup> /s)	Q (kJ/mol)
Cu	1.06E-3	24.0
Si	1.34E-3	30
Mg	0.99	71.6

*Table 4.6 Tracer impurity diffusion coefficients in liquid Al*

#### **4.4 Heat Treatment for Alloy 319s and Alloy 201**

Homogenization heat treatment was employed to study the microsegregation and dissolution of copper phases for thixoformed alloys 319s and 201. Both of the alloys were heat treated at 500 °C for 72 hours (3 days) and quenched into water to freeze the microstructures. The reason for choosing 500 °C for the solutionising temperature is that the Al-Cu eutectic reacts around 510 °C for both alloys and too low a temperature will inhibit diffusion too much.

#### **4.5 Experimental Investigation by SEM**

In the present study, a Field Emission Gun Scanning Microscope (FEGSEM), FEI Sirion 200 fitted with a Princeton Gamma Technology Avalon EDX system was used. The specimens were cut from the centre of aluminium alloys and mounted in electrically conducting phenolic resin at 180 °C and 15 KN using a Struers LaboPress-3 mounting press. The mounted specimens were prepared as the following grinding and polishing procedures on the Struers TegraPol-21 grinder and polisher (Table 4.7).

	Stage	Suspension	Coolant	Duration(min.)
Step 1	Plane Grinding	Sandpaper P600	Water	2
Step 2	Plane Grinding	Sandpaper P1200	Water	3
Step 3	Fine Grinding	9 micron diamond	Oil based	3
Step 4	Polishing	3 micron diamond	Oil based	3
Step 5	Polishing	1 micron diamond	Oil based	10
Step 6	Final Polishing	0.25 micron diamond	Colloidal silica	10

*Table 4.7 The grinding and polishing procedures used for metallographic specimen preparation*

The suitable polishing clothes are used for the suspensions. After final polishing, the specimens were thoroughly washed with ethanol and dried without etching.

#### **4.6 Experimental Investigation by TEM**

A JEOL 2100 Transmission Electron Microscopy (TEM) with a maximum operating voltage of 200 kV and equipped with a Princeton Gamma Technology Avalon EDX system is the platform for investigating the precipitate phases in alloy 319s. TEM samples were prepared in the following procedures:

1. 2.5-3 mm thin sheets of specimens were cut from the alloy by means of a water-lubricated slitting wheel. Then the sheets were mounted with crystal bond wax onto a sample holder for grinding, and ground with 1200 grit SiC paper from the both top and bottom surfaces on the polishing machine at a speed of 150 rpm to ~100-120  $\mu\text{m}$  thickness. The discs were dissolved off the holder in acetone.
2. TEM discs in 3 mm diameter were punched from the thinned sheets of specimens.
3. The discs were thinned with a South Bay model tripod polisher, which is typically used for wedge polishing in TEM sample preparation (Fig. 4.5). The disc was glued on the glass rod, which is one of the feet of the tripod polisher. The tripod polisher was then placed face down onto a grinding wheel with 6, 3 and 1  $\mu\text{m}$  diamond films. The disc was first polished to 6  $\mu\text{m}$  surface finish for 3 minutes and then to 3  $\mu\text{m}$  surface for 5 minutes. Finally, it was finished with 1  $\mu\text{m}$  surface with water until a sign of disc damage was observed on the edges.

The 1  $\mu\text{m}$  polishing stage took 30-40 minutes depending on the initial thickness of the discs. The disc was dissolved off the stub in acetone. The final thickness of the disc is estimated to be 10-15  $\mu\text{m}$  (approximately, as it cannot be measured accurately). After all these stages, the thinned discs were ion-beam milled.

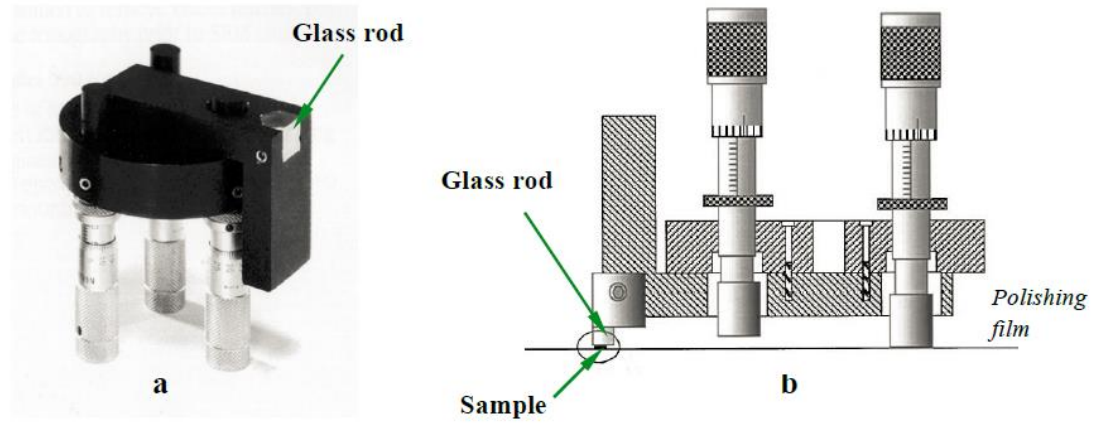


*Fig. 4.5 (a) Image of the tripod polisher used, (b) Schematic of tripod polishing [161]*

4. For the final step, in order to obtaining electron transparent areas, the dimpled discs were ion-milled with a Gatan Precision Ion Beam Polishing System (PIPS). Ion milling, as a sputtering process, leads to the material erosion knocking off the atoms of the sample as a result of the interaction between the ions from a cathode and the disc [162]. The polishing process was under argon atmosphere as shown in Fig. 4.6 for perforation polishing. The ion milling was set with  $6^\circ$  angle ( $\theta$ ), 3.5 KeV gun voltage and 3 rpm rotational speed of the disc were initially used. The total operation time varied between 5 and 7 hours depending on the thickness of the dimpled discs in the centre. To avoid the formation of steep edges around the perforation, the operating voltage was decreased from 6 keV to 4 keV, then 2 keV to 1keV in 40 minutes intervals after milling the disc for 7 hours at the initial milling parameters.

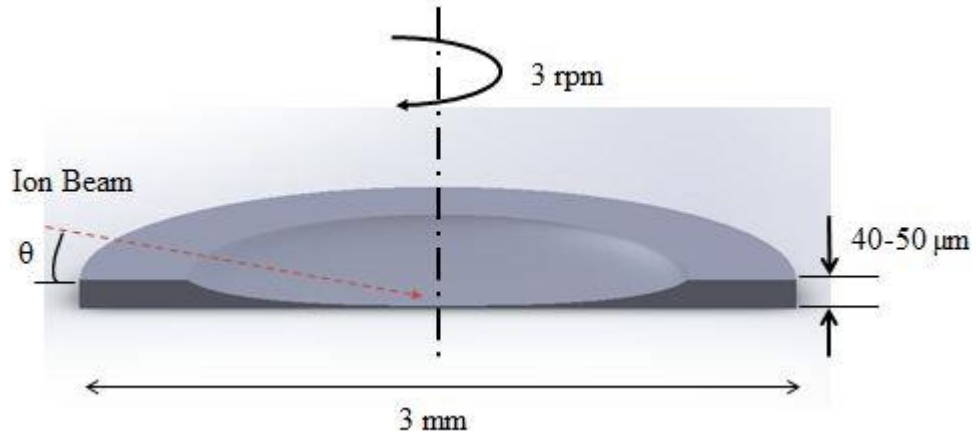


*Fig. 4.6 Cross section through a dimpled TEM disc showing incidence of ion beams during ion milling.*

#### **4.7 Experimental Investigation by XRD**

X-Ray Diffraction (Bruker D8 Advance with DaVinci, and equipped with a LynxEye Linear Position Sensitive Detector and a 90-position autosampler) was employed for investigation of the crystalline parameters of 319s alloy. Both as-received and heat treated specimens were analysed.

The instrument runs the DIFFRACplus software suite, which includes EVA [163] for search/match and phase identification, and TOPAS [164] for whole powder pattern decomposition and quantitative Rietveld analysis. Specimens were fragmented to disc with 8mm in diameter, 1mm in height (as shown in Fig. 4.7) with grinding under sandpaper P800.

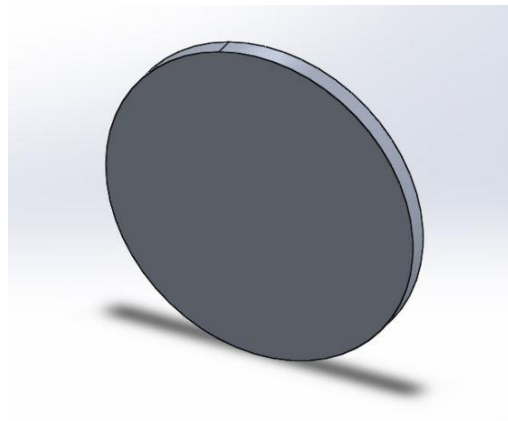


*Fig. 4.7 XRD specimen, 8mm in diameter, 1mm in height*

#### ***4.8 Thermal Analysis by DSC***

Differential scanning calorimetry was performed on a NETZSCH 404 DSC in an argon-controlled environment. The high-purity  $\text{Al}_2\text{O}_3$  pan was used as the reference material.

In order to investigate the sample mass and ramp rate effects on DSC, aluminium binary alloys were processed into two sizes: 4.5mm in diameter and 3mm in height, ~110mg on average; a small piece around 20mg. The standard heating rates in the DSC are 3K/min and 10K/min respectively. The samples were heated to 700°C at 10K/min (or 3K/min) and then cooled to 30°C at the same rate. All samples were put in an  $\text{Al}_2\text{O}_3$  pan with an  $\text{Al}_2\text{O}_3$  lid. Argon was fed through the system at a flow rate of 35ml/min to minimize oxidation of the samples. Three repetitions were carried out for each sample under each condition. A high reproducibility was obtained. The base lines were obtained by the output of the empty sample crucible measurements. The evaluation of the liquid phase fraction is carried out by the application of peak partial area integration. The measurement of the reaction temperature was determined by examining the intersection of the baseline and the extrapolated tangent line of the heat flow peak.

For 319s and 201 alloys, the specimens were cut from the centre of the as-received alloys and the masses were around 20mg. The samples were heated to 720°C at 3K/min and then cooled to 30°C at the same rate, followed by a second repetition of the same route (called 2<sup>nd</sup> heating).

#### ***4.9 Thermal Analysis by SPSC***

With the SPSC a 10K/min cooling rate cannot be achieved. Therefore, the calorimetrical measurements were carried out using a constant heat flux mode by controlling the temperature difference between the inner and outer crucible at  $\pm 6\text{K}$  on cooling, with a heating and cooling rate of about  $3.0 \pm 0.1 \text{ K/min}$  before any melting and solidification occurs. In this work, pure sapphire was used for calibration of latent heat and pure Al was used for the calibration of temperature. All the samples were machined into cylinders 10mm in diameter and 10mm in height. A hole of 1.0mm in diameter and about 6mm in depth was drilled into the bottom for the central thermocouple. After machining, the samples were cleaned in an ultrasonic cleaner using alcohol to remove dirt and oil from the sample surface. The samples were then rinsed with water and dried.

Those alloy samples were weighed and usually had a mass of approximately 2.2 g. The bottom head of the calorimeter was pulled down (see Fig. 3.11) and samples were fitted into the inner crucible. In order to provide a pure argon atmosphere during the experiments, argon was flushed through the furnace before the experiment starts for 20 min. The diagrammatic sketch of SPSC sample is show in Fig. 4.8.

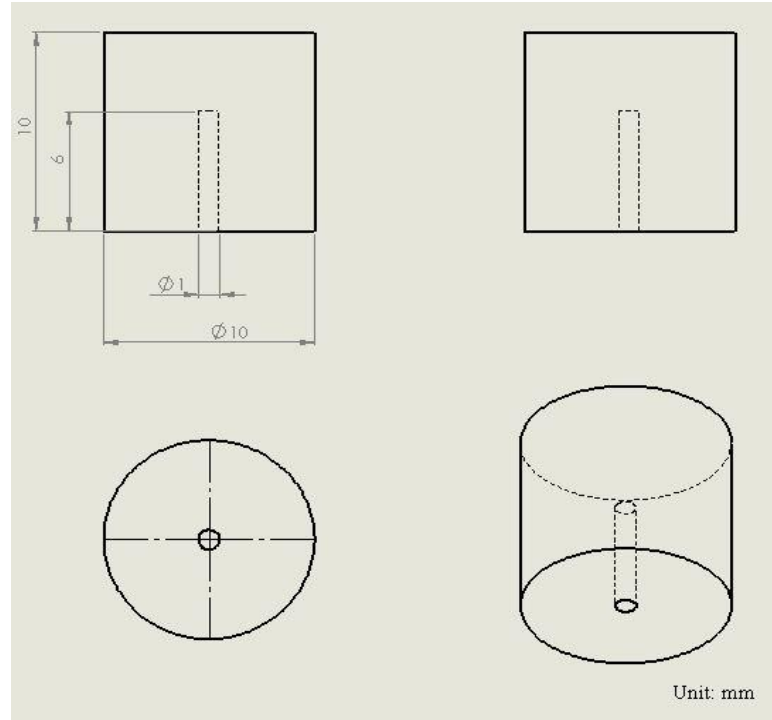


*Fig. 4.8 Diagrammatic sketch of SPSC sample*

#### **4.10 Hardness Testing**

All as-received 10 binary alloys were sectioned, mounted, ground using 600 and 1000 grit silicon carbide papers and polished with a 9  $\mu\text{m}$  diamond paste. Vickers hardness tests were performed with a Mitutoyo MVK-G1 Vickers hardness tester under the conditions of 10 kgf load, 10 seconds load time, and 50  $\mu\text{m}/\text{sec}$  loading speed. Although a load of 20 kgf is generally accepted as industrial standards for macro hardness testing, 10 kgf was used in the present study due to the limitation of optical microscope lens fitted with the machine of the testing machine. 20 indentations were conducted along the longitudinal cross-section of each sample.

## **Chapter 5 Results**

### ***5.1 Introduction***

In this chapter, the results obtained during this project are presented. Firstly, in section 5.2, the microstructure characterizations and hardness properties of as received alloys are presented. In section 5.3, the thermodynamic simulations for the 10 binary alloys including the comparison between Thermo-Calc and DICTRA predictions are illustrated. Section 5.4 shows the DSC tracing signal curves and the integrated liquid fraction as a function of temperature results for the 10 binary alloys. In section 5.5, the SPSC results for 10 binary alloys are presented. Then in section 5.6, comparison between prediction of liquid fraction versus temperature and experimental results from DSC and SPSC is described in details. Finally, in sections 5.7 and 5.8, the characterization of the dissolution of copper phases in 319s and 201 alloys using both calorimetry and electron microscopy is discussed.

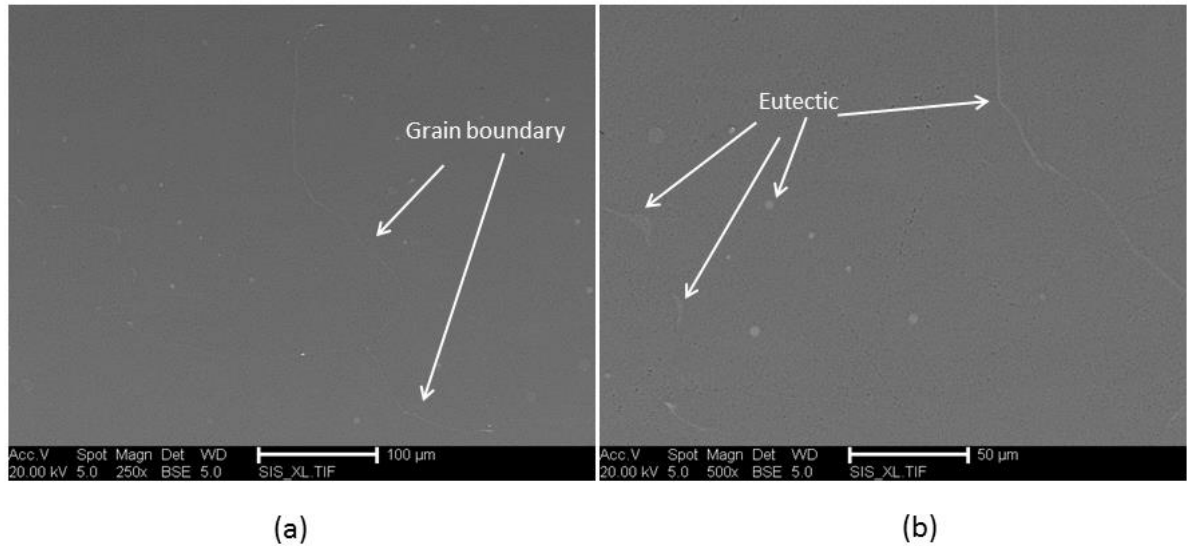
### ***5.2 Starting Materials for Thermal Analysis***

#### ***5.2.1. Microstructures***

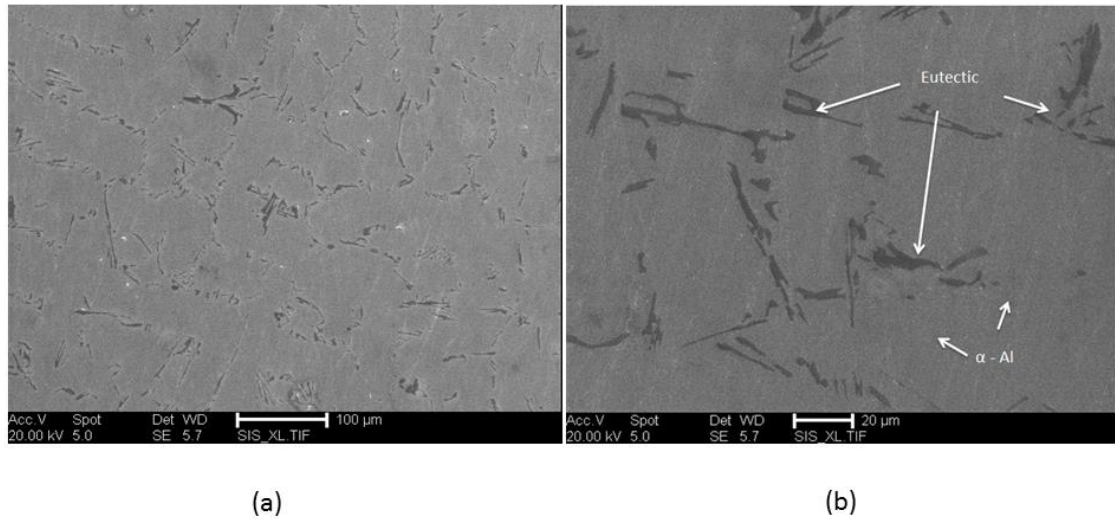
##### ***5.2.1.1 Al-Si Binary Alloys.***

The aluminium binary alloys for SEM are all un-etched. Fig. 5.1 shows the SEM back scattered electron image of as-received Al-1.01wt%Si alloy. The small white particles representing Al-Si precipitates are scattered randomly in the visual field. In Fig. 5.1(a), several long grain boundaries can be seen. These grain boundaries are composed of Al-Si eutectic phases. Due to the small amount of the silicon, the average size of eutectic particles is about 2  $\mu\text{m}$ . Most of the eutectic particles are spheroidal and only a few of them are elongated, which can be found in on the left hand side of Fig. 5.1(b).



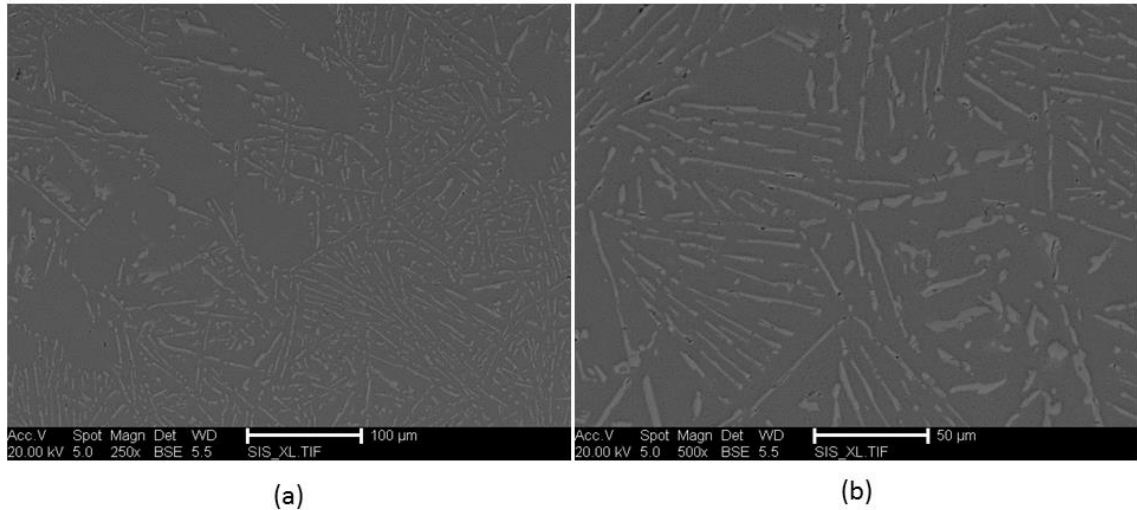


*Fig. 5.1 SEM back scattered electron image of Al-1.01wt%Si alloy*



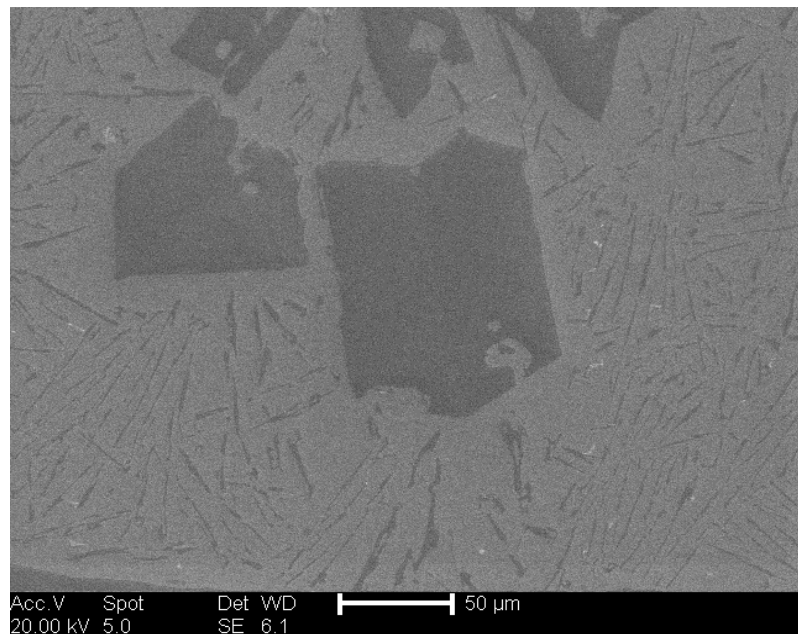
*Fig. 5.2 SEM secondary electron image of Al-5.08wt%Si alloy*

Fig. 5.2 shows the typical SEM secondary electron image of Al-5.08wt%Si alloy. It is obvious from Fig. 5.2 that the microstructures of the Al-Si samples consist of two distinguishable phases. The matrix phase is ( $\alpha$ -Al) phase, grey phase. In contrast, the second phase is in a form of eutectic phase particles, dark phase. In Fig. 5.2(a), it is clear that the eutectic phases are located on the  $\alpha$ -Al boundaries. The average grain size of the (Al) phase is found equivalent to 55  $\mu$ m, which is much finer than the Al-1.01wt%Si alloy.



*Fig. 5.3 SEM back scattered electron image of Al-11.68wt%Si alloy*

Nearly eutectic (12.6 wt% in literature) microstructures of Al-Si are shown in Fig. 5.3. There is more eutectic phase than in the Fig. 5.2 with silicon percentage increasing. As 11.68wt%Si is below the eutectic point (12.6wt %) of Al-Si binary alloys, in the low magnification image (Fig. 5.3(a)), several relatively large (Al) phases can be seen. The eutectic phase is needle-like and thinner than that in Al-5.08wt%Si alloy.



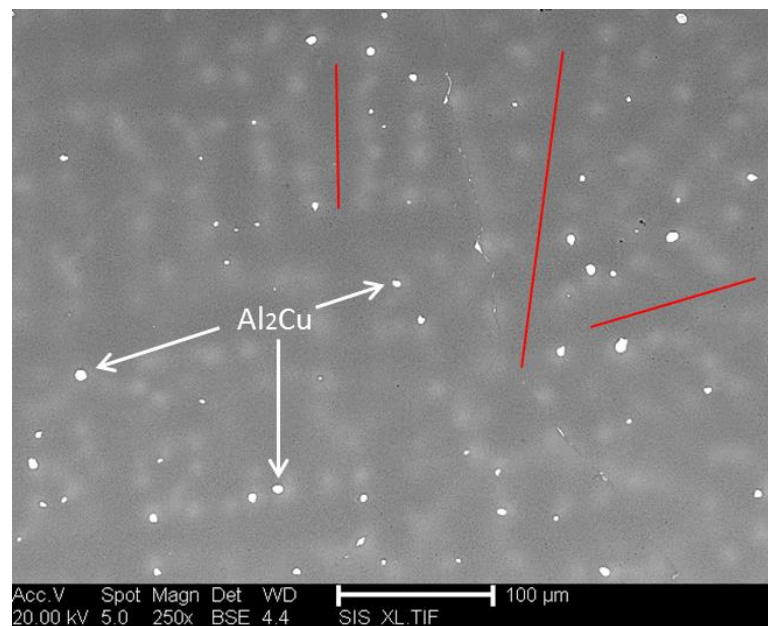
*Fig. 5.4 SEM secondary electron image of Al-17.54wt%Si alloy*

With the fraction of silicon growing, the percentage of silicon phase ascends, especially for hypereutectic alloy. Fig. 5.4 shows the microstructure of Al-17.54wt%Si hypereutectic alloy. A huge silicon block can be observed with diameter of about 85 μm,

which is the primary Si particle. The primary silicon phase is surrounded by Al-Si eutectic phases. The microstructure of the alloy generally depends on the nucleation and cooling rates during solidification. The morphology of primary silicon crystals depends considerably on solidification parameters such as cooling rate and temperature gradient. Generally, the cast microstructure of the hypereutectic Al-Si alloy consists of coarse and segregated primary silicon crystals along with the needle like eutectic phases.

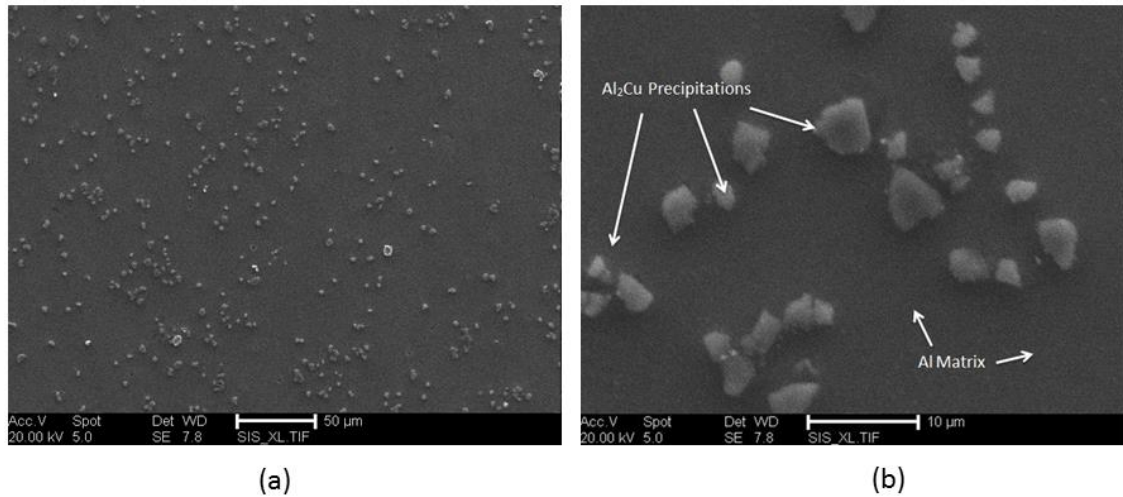
#### 5.2.1.2 Al-Cu Binary Alloys

Fig. 5.5 shows the SEM back scattered electron image of Al-0.98wt%Cu alloy. Clearly, few white  $\text{Al}_2\text{Cu}$  ( $\theta$ ) particles are located on the boundaries, which are light grey. The long (Al) dendrites can be seen in dark grey and the directions of the dendrites are marked with red lines. The average size of the  $\text{Al}_2\text{Cu}$  particles is about 4  $\mu\text{m}$ .



*Fig. 5.5 SEM back scattered electron image of Al-0.98wt%Cu alloy*

For Al-2.18wt%Cu binary alloy, the amount of precipitation of  $\theta$  phase in Fig. 5.6 is increased compared with Al-0.98wt%Cu alloy. However, the average size of particles is still about 4  $\mu\text{m}$ . The precipitates are small and block-like, which is similar with Al-0.98wt%Cu alloy.



*Fig. 5.6 SEM secondary electron image of Al-2.18wt%Cu alloy*

The microstructures of Al-4.9wt% Cu alloy are shown in Fig. 5.7. Again, the  $\text{Al}_2\text{Cu}$  ( $\theta$ ) phase is in white. The difference is the  $\text{Al}_2\text{Cu}$  ( $\theta$ ) phases are more complex (shown in Fig. 5.7(b)) elongated and rib-like phases. In addition, the second phase particle ( $\theta$  phase) is found to be larger and coarser.

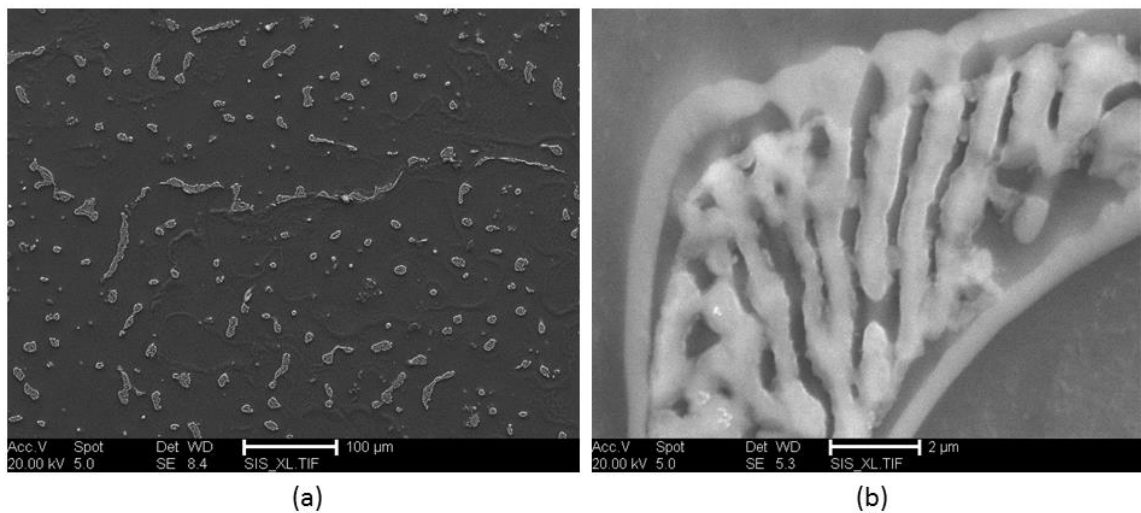


*Fig. 5.7 SEM secondary electron image of Al-4.9wt%Cu alloy*

### **5.2.1.3 Al-Mg Binary Alloys**

The SEM back scattered electron images of Al-5.58wt%Mg binary alloy are shown in Fig. 5.8. The dark particles in Fig. 5.8(a) are second phase particles,  $\beta$  phase ( $\text{Al}_3\text{Mg}_2$ ). In high magnification, several small dark particles can be seen in Fig. 5.8(b). Due to the lack of accuracy of EDX on these particles, an area analysis was carried out on the whole area in Fig. 5.8(b). The results showed that there is about 4.5wt% Mg within this

area. A conclusion can be drawn that the magnesium is dissolved in the (Al) phase matrix and can hardly be distinguished because those two elements have very close contrast under electron scanning. The microstructures of Al-0.42wt%Mg and Al-2.82wt%Mg are very similar with Fig. 5.8(b) and there is scarcely any dark  $\beta$  phase ( $\text{Al}_3\text{Mg}_2$ ) in the vision field under SEM analysis.

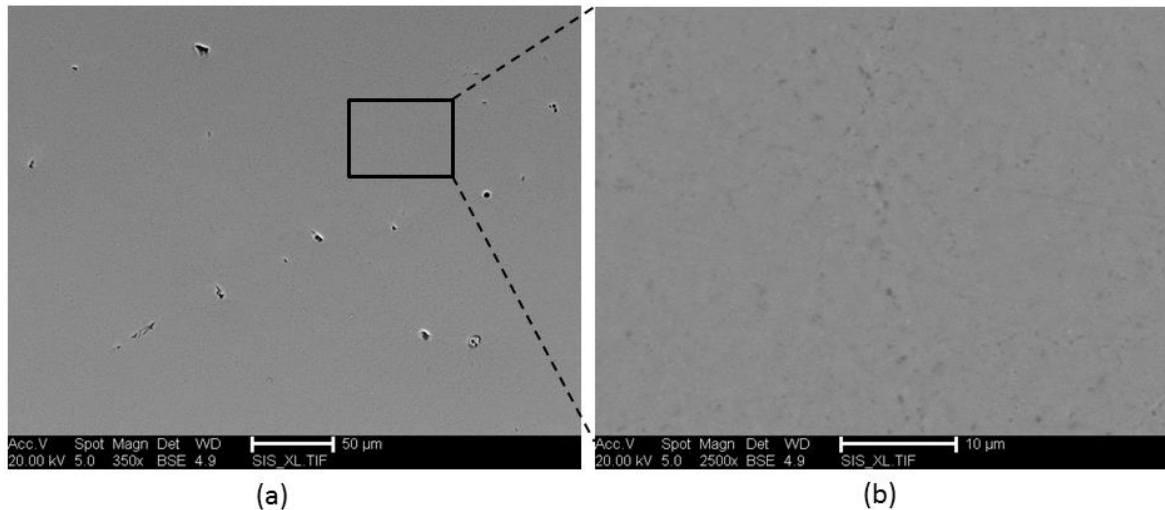


*Fig. 5.8 SEM back scattered electron image of Al-5.58wt%Mg alloy*

### **5.2.2 Hardness Properties**

Micro-hardness was measured 20 times and an average result was calculated for each sample. Fig. 5.9 plots the Vickers hardness values versus the alloying element weight percentage for the 10 aluminium binary alloys. High purity (99.999%) cast aluminium was carried out for reference.

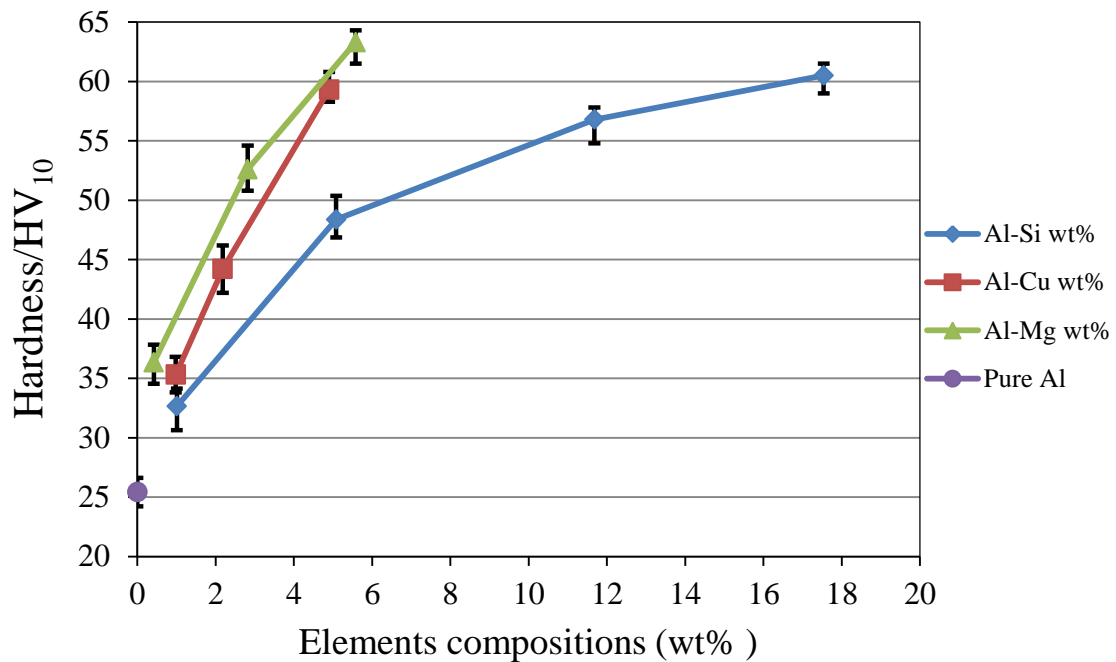


*Fig. 5.9 The Vickers hardness values versus the compositions of alloying elements in Al based binary alloys*

Hardness increases as the alloy element compositions increase. As for Al-Si binary alloys, the hardness for Al-1.01wt%Si alloy is 32 which is 7 HV<sub>10</sub> higher than the pure aluminium. With the silicon increasing, the hardness raises up to 61 for hypereutectic alloy Al-17.54wt%Si. However, the slope of hardness decreases for the part of silicon profiles above the eutectic point (12.6 wt%). The difference could be attributed to eutectic phase, rather than the primary silicon phase, being the major phase contributing to the hardness property, which was confirmed with FEGSEM. However, the values are lower than in Table 2.1. Though the samples are all prepared by casting, there are still some uncertain parameters during the casting processing, i.e. cooling rate, mold materials etc. The possible differences in purity, solidification conditions and the surface preparation of the test pieces also can influence the results.

Al-0.98wt%Cu alloy has a hardness of 3 HV<sub>10</sub> higher than the Al-1.01wt%Si alloy and 10 HV<sub>10</sub> higher than pure aluminium. It was increased to 52 HV<sub>10</sub> for Al-2.18wt%Cu and 63 for Al-4.9wt%Cu respectively and showed a linear HV<sub>10</sub>–wt% relation. So with the rising in copper content, the increase of Al<sub>2</sub>Cu phase leads to a harder alloy than the  $\alpha$ -Al phase, as shown in the microstructures. The increasing matrix hardness due to solid solution hardening can also improve the machinability of alloys [165].



For Al-Mg binary alloys, although the  $\alpha$ -Al phase takes a large percentage of the structure,  $\text{Al}_3\text{Mg}_2$  phase is still an active phase as it can strengthen the alloy's hardness. The green symbols in Fig. 5.9 representing for Al-Mg binary alloy were above the other two curves, which indicates that the hardness of Al-Mg binary alloy are higher than both Al-Si and Al-Cu alloys in the same composition. The hardness values are in good agreement with ref [38]. Mg is also a powerful solid solution strengthener.

The as-received 10 binary alloys were permanent mold casted without any heat treatment. When compared on a longitudinal scale in Fig. 5.9, the Al-Si binary alloys have the lowest hardness while the Al-Mg binary alloys have the greatest hardness values. However, certain heat treatments are normally carried out for alloys in commercial use. The relationships presented here will be changed.

### ***5.3 Prediction Results***

In this section, the calculation results of equilibrium and Scheil will be described firstly, following by the DICTRA studies. In the DICTRA results section, the results of impacts of parameters i.e. cell size and cooling rate, will be shown. Finally, a comparison between the non-kinetic calculations and diffusion kinetics simulations will be discussed.

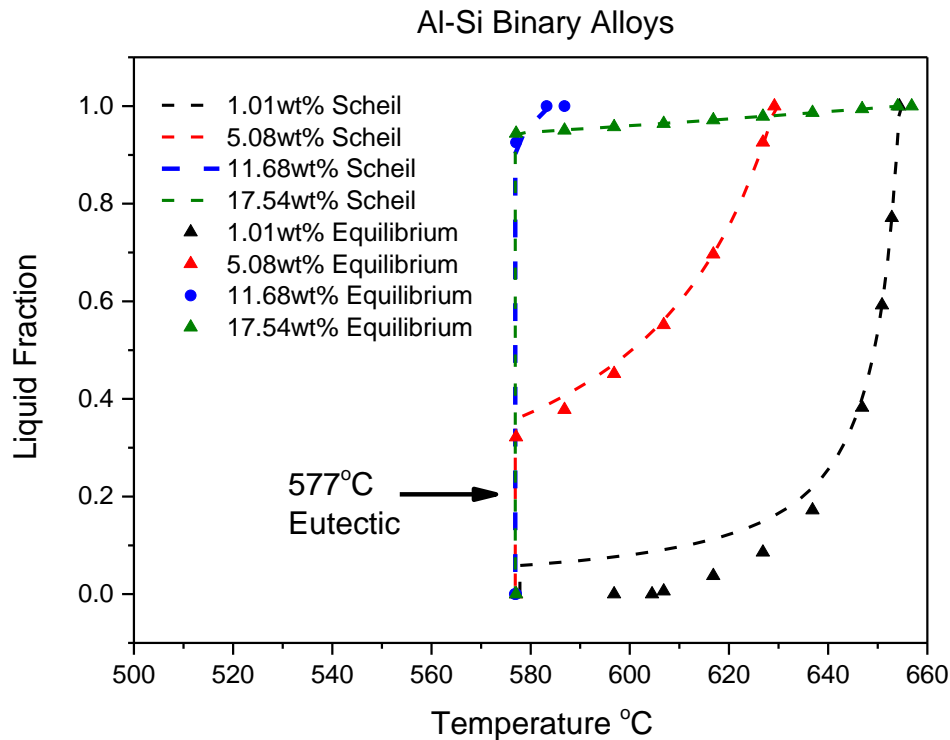
#### ***5.3.1 Equilibrium and Scheil Calculations by Thermo-Calc***

Fig. 5.10 shows the liquid fraction/temperature relationships under both equilibrium and Scheil conditions with the increasing silicon weight percentage in Al-Si binary alloys. The equilibrium data are illustrated by symbols and the Scheil results are shown by dash-lines. The Al-Si eutectic temperature is 577 °C and the Si composition for the eutectic point is about 12.6 wt%. All curves end at the eutectic temperature except the Al-1.01wt%Si under equilibrium condition. This is because the solidus line for the 1.01wt% silicon in Al-Si phase diagram (Fig. 4.1) is higher than eutectic temperature.

At the eutectic temperature, the maximum liquid fraction points increase as the silicon composition increases. The eutectic phases are about 32% for Al-1.01wt%Si alloy, 92% for Al-11.68wt% Si alloy and 95% for Al-17.54wt%Si alloy, respectively. For hypoeutectic alloys, the liquidus temperature decreases as the silicon content increases. However, the liquidus temperature for Al-17.54wt%Si alloy is slightly higher than the

Al-1.01wt%Si alloy. Those are in good agreement with the phase diagram liquidus lines in Fig. 4.1.

When comparing equilibrium data with the Scheil curves, a higher temperature ( $\geq 577^{\circ}\text{C}$ ) is needed to reach the same liquid fraction with equilibrium condition.



*Fig. 5.10 Comparison of different silicon compositions under equilibrium and Scheil condition as a relationship of liquid-fraction vs. temperature*

Fig. 5.11 shows the liquid fraction/temperature relationships under both equilibrium and Scheil conditions with the increasing copper content for Al-Cu binary alloys. The solidus temperatures under Scheil mode for all the three alloys are the same ( $548^{\circ}\text{C}$ ). However, the solidus temperature under equilibrium condition increases with copper added and all are greater than for the Scheil curves. The slopes of curves are slightly steeper at 40% fraction liquid with less copper additions. Under the Scheil condition, the eutectic percentage for alloys increases with copper compositions ascending, which is 1% for Al-0.98wt%Cu alloy, 2% for Al-2.18wt%Cu alloy and 6% for Al-4.9wt%Cu alloy. Similarly with Al-Si binary alloys, the curves below 50% fraction liquid with equilibrium mode contain less liquid fraction at the same temperature than for the Scheil.



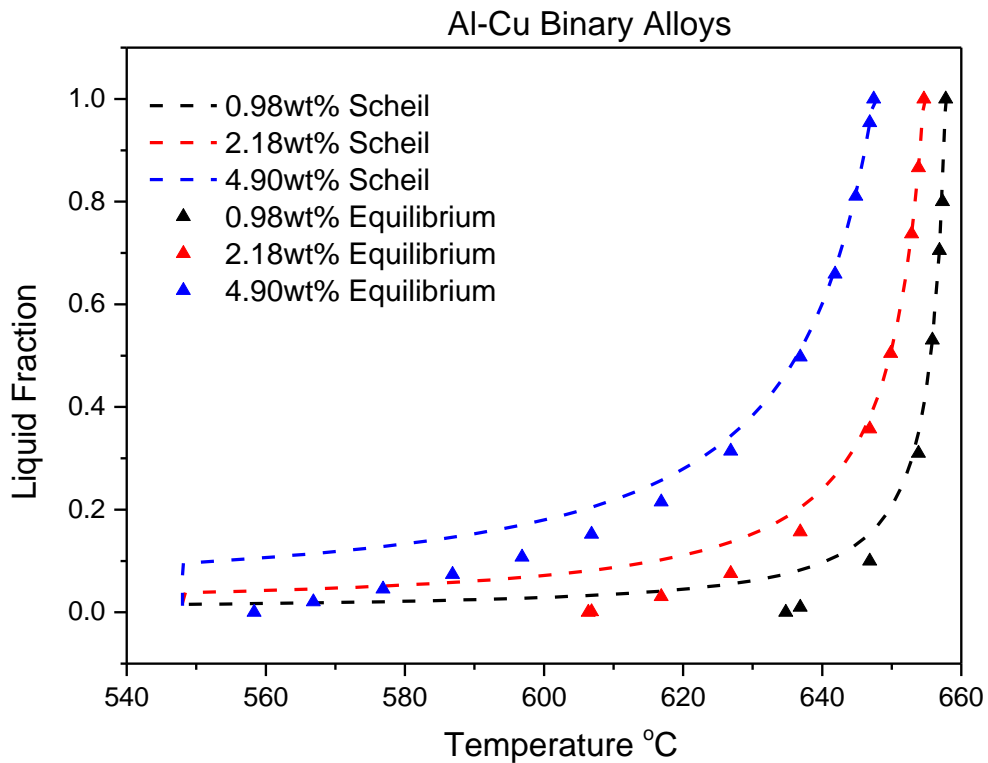


*Fig. 5.11 Comparison of different copper compositions under equilibrium and Scheil condition as a relationship of liquid-fraction vs. temperature*

The results with different magnesium compositions with both equilibrium and Scheil condition as a relationship of liquid-fraction vs. temperature are shown in Fig. 5.12. It should be noticed that the temperature interval between liquidus and solidus temperatures is enlarged significantly with Scheil mode in comparison with equilibrium. The solidus temperature for both Al-2.82wt%Mg and Al-5.58wt%Mg alloys in Scheil mode is 450 °C. However, according to the lever rule calculation, the solidus temperature is 615 °C for Al-2.82wt%Mg alloy and 570 °C for Al-5.58wt%Mg alloy respectively. The differences are about 165 °C and 120 °C respectively.

In addition, in the same way as for Al-Cu binary alloys, a conclusion can be made that aluminium alloys with added magnesium can reduce liquidus temperature and solidus temperature. The slopes of curves decrease at 40% fraction liquid with magnesium content increase.

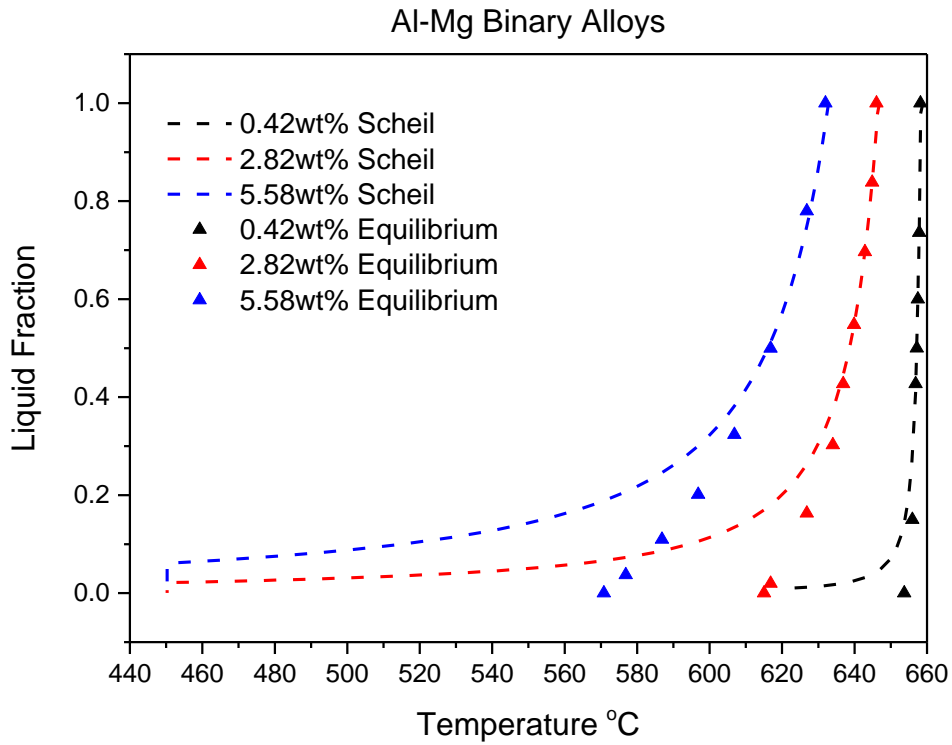


*Fig. 5.12 Comparison of different magnesium compositions under equilibrium and Scheil condition as a relationship of liquid-fraction vs. temperature*

### 5.3.2 DICTRA Simulation Results

#### 5.3.2.1 Diffusion Coefficients of Si, Cu and Mg in FCC(Al) and Liquid(Al) Phases

The simulation with DICTRA is a diffusion controlled solidification process. It is necessary to know the diffusion coefficients of alloying elements in different matrixes.

Fig. 5.13 shows the calculated tracer impurity diffusion coefficients as a function of temperature in the liquid and FCC solid phases of Al. The diffusion coefficients increase significantly with the temperature increase in solid. Copper has the lowest diffusion ability in Al solid phase while the magnesium may diffuse quicker than both silicon and copper in the FCC Al phase.

In the liquid phase (Fig. 5.13(a)), the tracer impurity diffusion coefficients of silicon are higher than that of copper, but neither change too much when temperature changes. The diffusion coefficients of magnesium show a slightly increase with the temperature rising and are much higher than those of copper and silicon. When compared with the

coefficients in solid and liquid, the results show the coefficients are about 10000 times higher in the liquid phase.

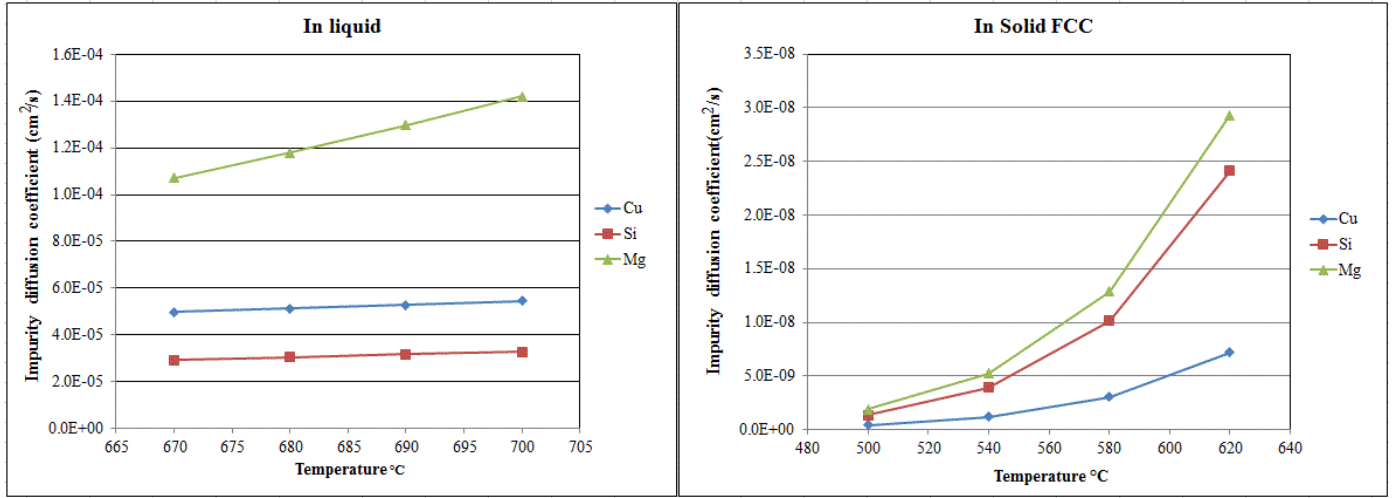


Fig. 5.13 Tracer impurity diffusion coefficients in (a) liquid(Al) and (b) in FCC(Al) for Cu, Si, Mg

### 5.3.2.2 Cell Size Impact

In order to make sure the cell size was designed accurately for current simulations, three different cell lengths (1mm, 100 $\mu$ m and 10 $\mu$ m) were tested with Al-5.08wt% Si alloy. Fig. 5.14 shows the simulation results (fraction liquid/temperature relationships) for 10K/min cooling rate of three different sizes. It is obvious that the curve (pink line) of 1mm cell size is far away from the others. The green line, which is for the 10 $\mu$ m cell size, is very close to the equilibrium data. As expected, results for the 100 $\mu$ m cell size lies between the two extremes.

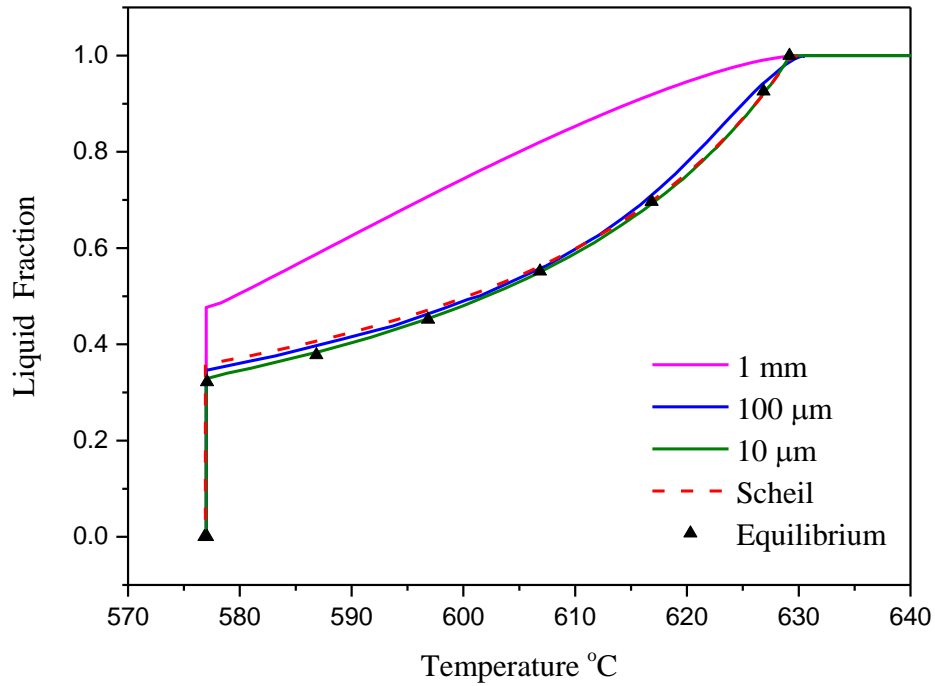


Fig. 5.14 Comparison of DICTRA solidification simulation with different cell sizes (1mm, 100  $\mu\text{m}$  and 10  $\mu\text{m}$ ) for alloy Al-5.08wt% Si with 10K/min cooling rate

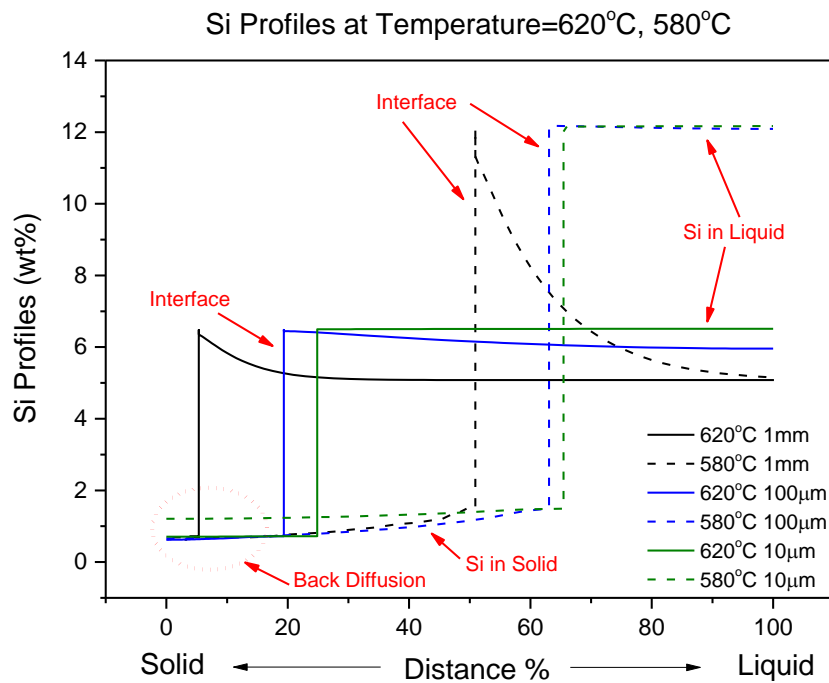


Fig. 5.15 Solidification simulation using DICTRA for Al-5.08wt%Si, Si composition profiles for the time steps under different cell sizes (1mm, 100  $\mu\text{m}$  and 10  $\mu\text{m}$ ) with 10K/min cooling rate

The microsegregation of the elements can be directly plotted as composition profiles versus distance (Fig. 5.15). The distance in percentages was carried out for comparison. The liquid phase was set as matrix, which is shown on the right side of the interface line. The other side represents solid phase. Since the solidification begins at 700 °C and the cooling rate is 10K/s, the 620 °C represents 8 seconds and the 580 °C represents 12 seconds.

At 620 °C, for 1mm cell size, the distribution of silicon is the same with initial profiles (5.08wt%) after 30 distance% in liquid phase. When comparing between the 100µm and 10µm sized cells, the result of the 10µm size simulation shows the silicon content is distributed more homogeneously than that of 100µm size. This indicates that the 10 µm size cell is too small for diffusion to be significant in controlling the process and that is the reason why the results for 10 µm size are very close to equilibrium data in Fig.5.14. At 580 °C, the characteristic diffusion length is less than 1mm for the 1mm cell size simulation. The silicon profile in solid phase for size 10µm is much higher as the back diffusion is more significant on the smaller scale. The interface for the size of 100µm is on the left of 10µm's interface, illustrating that the liquid fraction at 580 °C of the 100µm size cell is higher than that of the 10µm size cell. This conclusion can be seen in Fig. 5.14 as well.

As the 1mm size is too large for the simulation of 10K/min cooling rate, a much lower cooling rate of 1K/min has been carried out to study the cooling rate effect in the simulation. Here, a demonstration of the cooling rate effect is shown in Fig. 5.16. It shows a DICTRA solidification simulation with different cooling rates, i.e. 10K/min, 1K/min, of 1mm cell size for alloy Al-5.08wt% Si. It can be seen that the curve for 1K/min cooling is slightly above the Scheil mode. Comparing with the 10K/min curve, the 1K/min goes back to the Scheil as expected. This is because the low diffusion driving force in the low cooling rate contributes to more time for diffusion. As a result, the phenomenon that Si profile is same with initial composition at liquid phase in Fig. 5.15 (black lines), which, has disappeared. In addition, the 1K/min curve in Fig. 5.15 is above the Scheil curve, which is still not reliable. It is because the Scheil condition assumes no back diffusion in the solid phase and homogeneous composition in liquid phase, which is an extreme condition for solidification. Curves with diffusion in both

solid and liquid phases should lie between Scheil and equilibrium curves (two extremes). In addition, the 100 $\mu\text{m}$  cell size suits the phase size in microstructure.

In conclusion, by comparing different cell sizes for simulation, 100 $\mu\text{m}$  cell size was selected for DICTRA simulation.

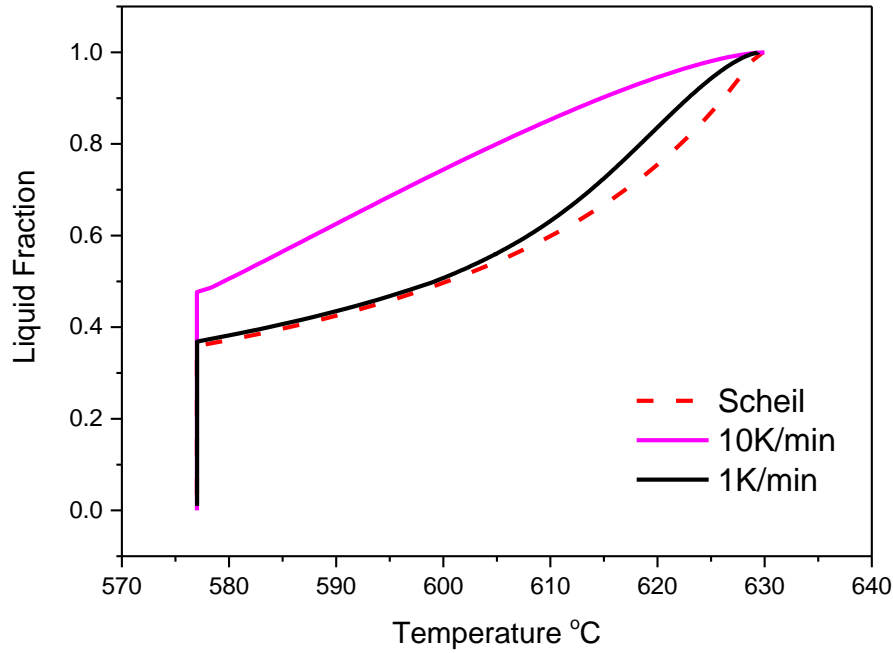


*Fig. 5.16 Comparison of DICTRA solidification simulation with different cooling rates (10K/min, 1K/min) of 1mm cell size for alloy Al-5.08wt% Si*

### **5.3.2.3 Element Composition Profiles at one Specific Temperature**

The element profiles during simulations were investigated with the DICTRA solidification path model with a 100 $\mu\text{m}$  cell size. Taking alloy Al-5.08Si for example, Fig. 5.17 shows the Si composition profiles at 620 °C and 580 °C at different cooling rates. In the solid phase, back diffusion takes place when the interface is moving. In the liquid phase, as the diffusion is much faster than in the solid phase, the Si composition profiles are more uniform. The vertical interfaces for 3K/min lie to the right hand side of those with 10K/min cooling rate and in the solid, phases are below those for 10K/min indicating that the alloy with the higher cooling rate will have a slightly higher liquid fraction at the same temperature.

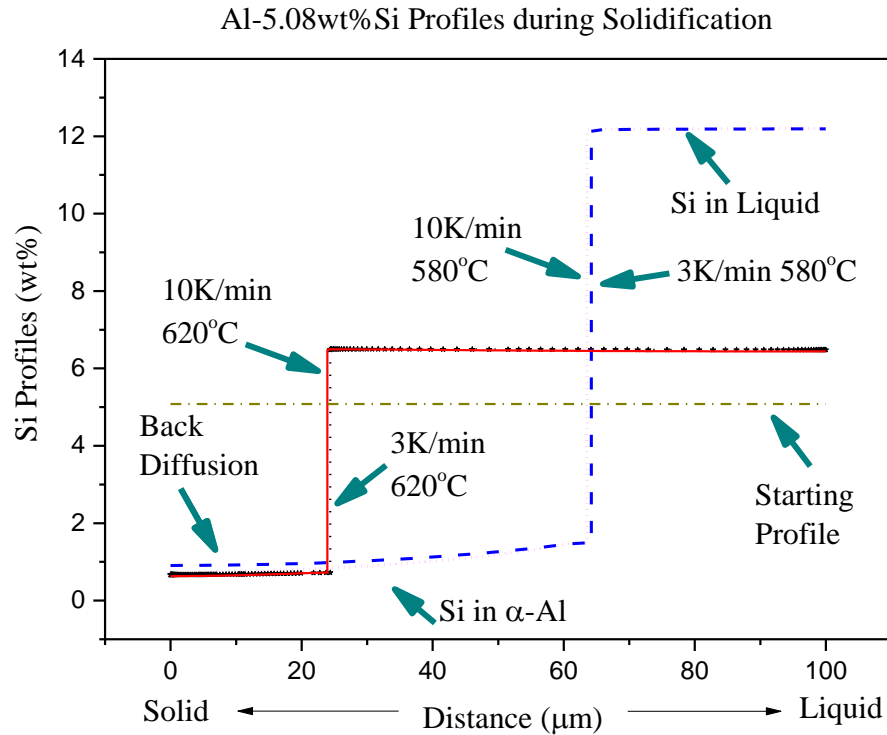


Fig. 5.17 Solidification simulation of Al-5.08wt%Si using DICTRA: Si composition profiles at 620 °C and 580 °C under different cooling rates (3K/min, 10K/min), cell size: 100 μm

#### 5.3.2.4 Liquid Fraction Calculated by DICTRA

Fig. 5.18 shows the simulation results for 3K/min and 10K/min cooling rates for Al-1.01wt%Si alloy respectively by DICTRA, together with the equilibrium and Scheil results. For the left hand part of the graph, it can be seen that the DICTRA results lie between the equilibrium and Scheil curves. For the right hand side, the lines coincide. The DICTRA curve with the higher cooling rate is closer to Scheil curve. This means that at a given temperature an alloy with Scheil mode can achieve a relatively higher liquid fraction. With DICTRA prediction, at a given temperature, a higher cooling rate gives a higher liquid fraction than with a lower cooling rate. In addition, the lowest liquid fraction is obtained under the equilibrium condition. The differences are however small. The equilibrium data ends at 596 °C rather than the eutectic temperature 577 °C. This is true with the phase diagram. As one of the assumptions for Scheil is that no back diffusion happens in solid phase, the solidus temperature for Scheil shifts to 577 °C, 19 °C lower than the equilibrium curve.

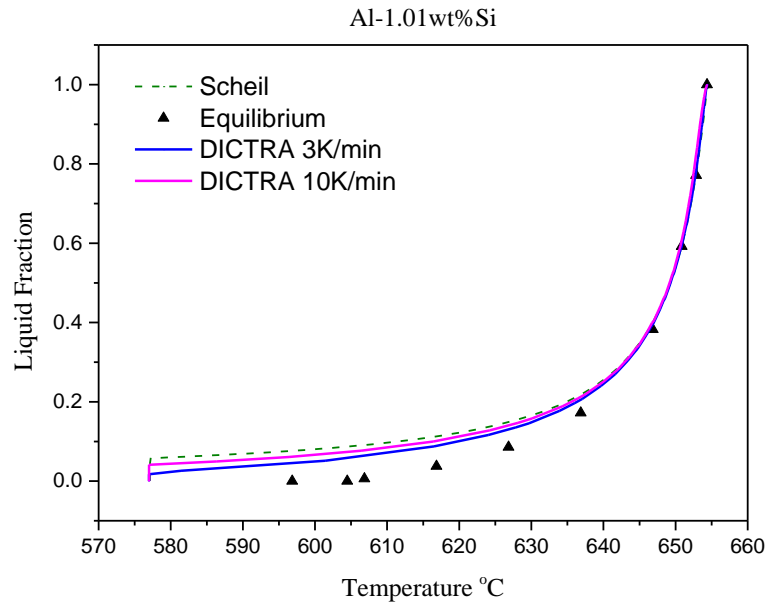


Fig. 5.18 Comparison between DICTRA solidification simulation results (with 3K/min, 10K/min cooling rate) and equilibrium & Scheil data as a relationship of liquid-fraction vs. temperature for Al-1.01wt%Si alloy

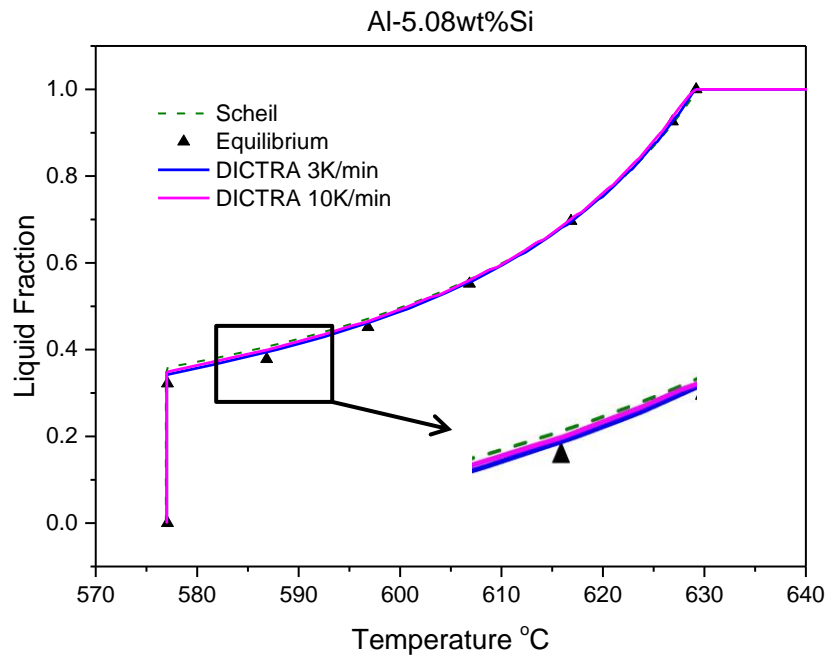
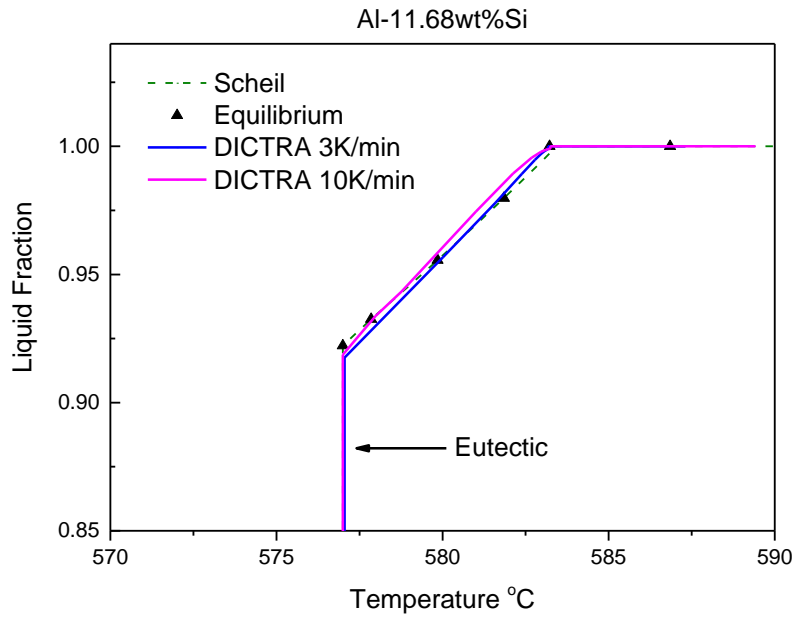
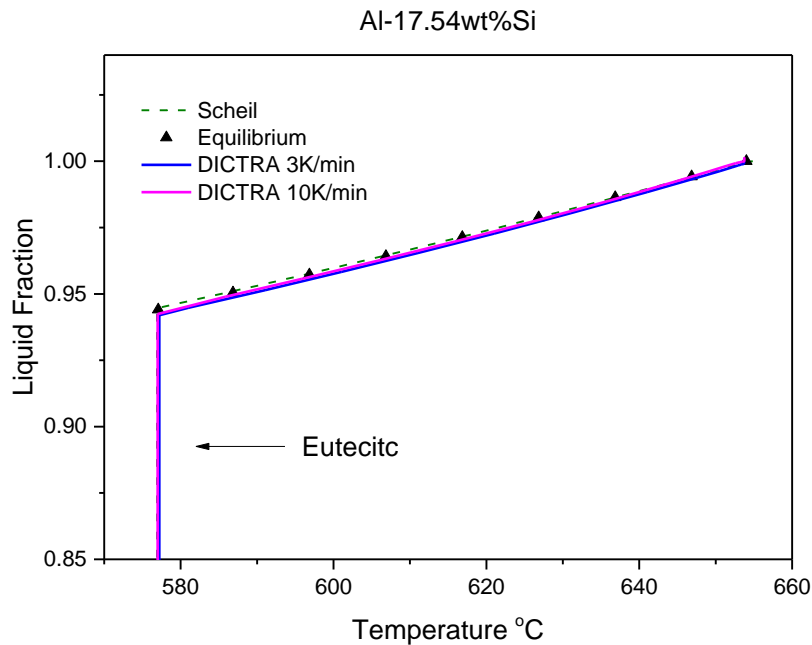


Fig. 5.19 Comparison between DICTRA solidification simulation results (with 3K/min, 10K/min cooling rate) and equilibrium & Scheil data as a relationship of liquid-fraction vs. temperature for Al-5.08wt%Si alloy





*Fig. 5.20 Comparison between DICTRA solidification simulation results (with 3K/min, 10K/min cooling rate) and equilibrium & Scheil data as a relationship of liquid-fraction vs. temperature for Al-11.68wt%Si alloy*



*Fig. 5.21 Comparison between DICTRA solidification simulation results (with 3K/min, 10K/min cooling rate) and equilibrium & Scheil data as a relationship of liquid-fraction vs. temperature for Al-17.54wt%Si alloy*

Figs 5.19 to 5.21 show the DICTRA simulation results and the thermo-prediction results respectively. At the *Liquid*  $\rightarrow$   $\alpha$ -Al formation state (above 577 °C), the DICTRA data of both 3K/min and 10K/min lie between the two extremes. All curves end at the eutectic reactions. The liquid-fraction values at the eutectic points are showing an order: Scheil>10K/min>3K/min>Equilibrium.

Fig. 5.22 to Fig. 5.24 show the simulation results under 3K/min and 10K/min cooling rates by DICTRA, together with the Equilibrium and Scheil results for Al-Cu binary alloys. Again, same conclusions can be made with the Al-Si alloys. The DICTRA curves lies between the Scheil curve and equilibrium data. The curve with 10K/min cooling rate is closer to Scheil curve than the 3K/min one. The knee at the 547 °C represents the reaction  $\text{Liquid} \rightarrow \alpha\text{-Al} + \text{Al}_2\text{Cu}$ . Therefore, with the weight percentage of copper increasing, the more liquid fraction can be obtained for a given temperature.

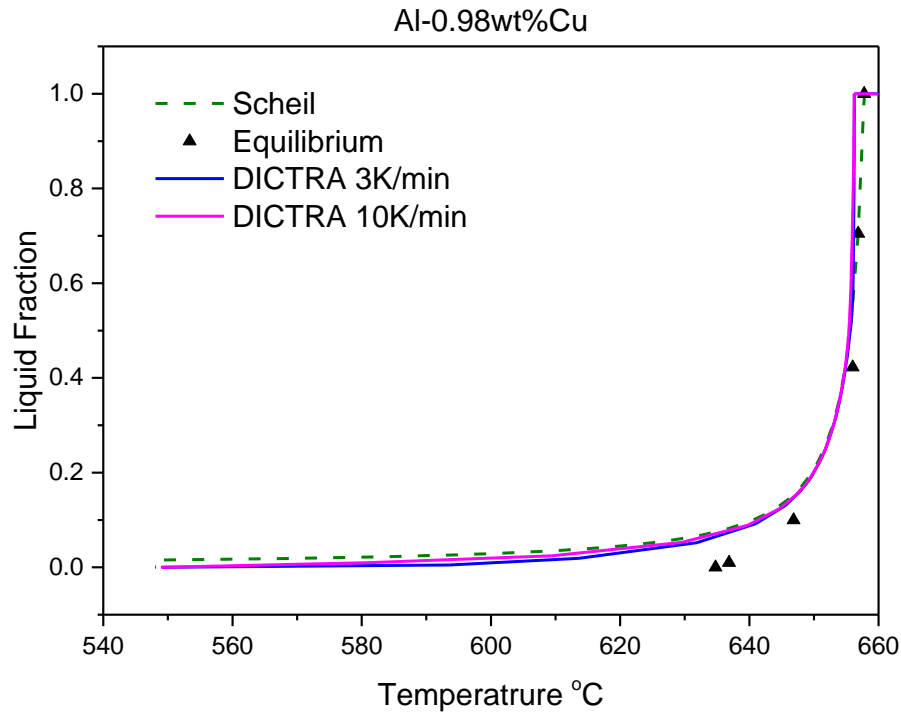


*Fig. 5.22 Comparison between DICTRA solidification simulation results (with 3K/min, 10K/min cooling rate) and equilibrium & Scheil data as a relationship of liquid-fraction vs. temperature for Al-0.98wt%Cu alloy*

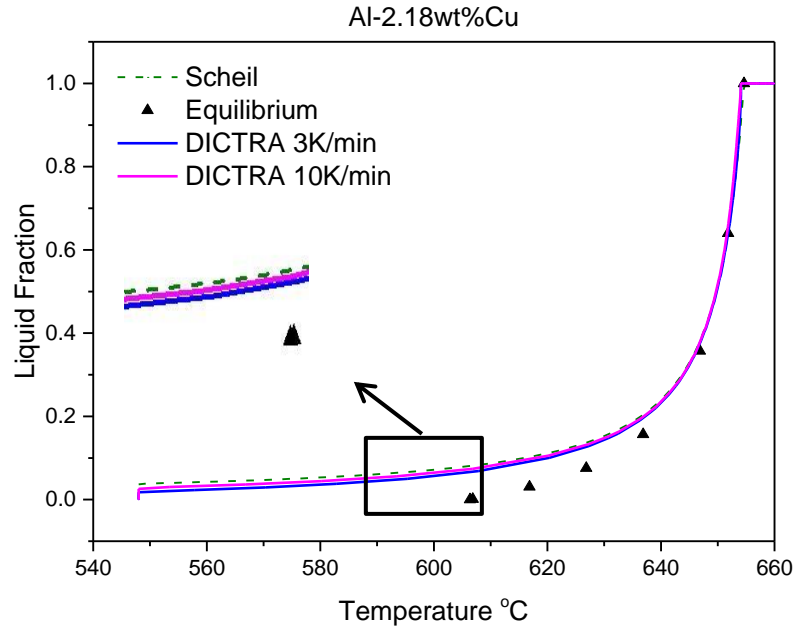


Fig. 5.23 Comparison between DICTRA solidification simulation results (with 3K/min, 10K/min cooling rate) and equilibrium & Scheil data as a relationship of liquid-fraction vs. temperature for Al-2.18wt%Cu alloy

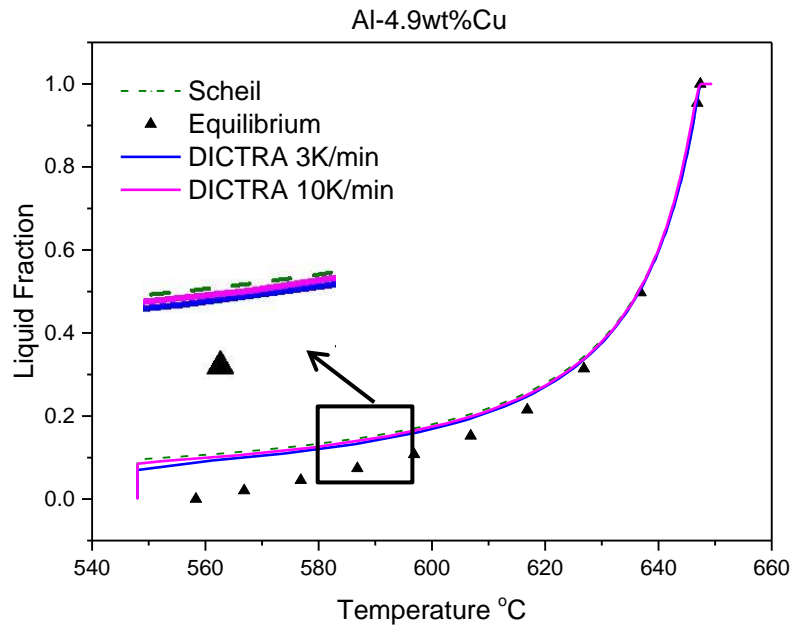
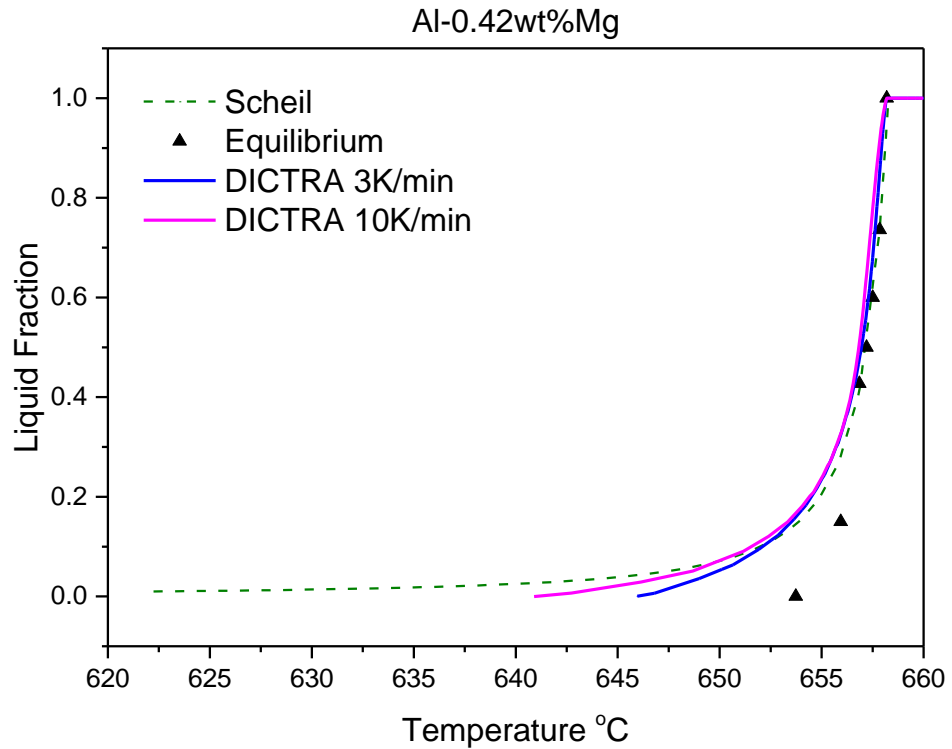
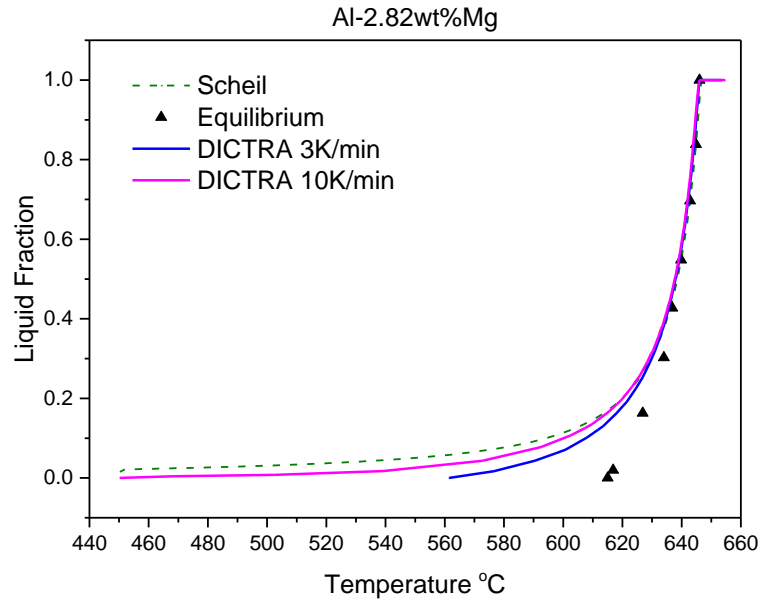


Fig. 5.24 Comparison between DICTRA solidification simulation results (with 3K/min, 10K/min cooling rate) and equilibrium & Scheil data as a relationship of liquid-fraction vs. temperature for Al-4.9wt%Cu alloy

Fig. 5.25 to Fig. 5.27 show the simulation results under 3K/min and 10K/min cooling rates by DICTRA, together with the equilibrium and Scheil results for Al-Mg binary alloys. The solidification equation for Al-Mg binary alloys is Liquid  $\rightarrow$   $\alpha$ -Al +  $\text{Al}_3\text{Mg}_2$  at 450 °C. In Fig. 5.25 and Fig. 5.26, it should be noticed that the solidus temperatures of DICTRA curves are higher than Scheil but lower than equilibrium data. This may be because the coefficients of diffusion for Mg are relatively high in both solid and liquid Al. Low cooling rates and small amount of Mg in alloys result in a fast diffusion of Mg during solidification. In addition, when the cooling rate is reduced, the temperature interval between liquid and solid for Al-0.42wt%Mg and Al-2.82wt%Mg is reduced as well.



*Fig. 5.25 Comparison between DICTRA solidification simulation results (with 3K/min, 10K/min cooling rate) and equilibrium & Scheil data as a relationship of liquid-fraction vs. temperature for Al-0.42wt%Mg alloy*



*Fig. 5.26 Comparison between DICTRA solidification simulation results (with 3K/min, 10K/min cooling rate) and equilibrium & Scheil data as a relationship of liquid-fraction vs. temperature for Al-2.82wt%Mg alloy*

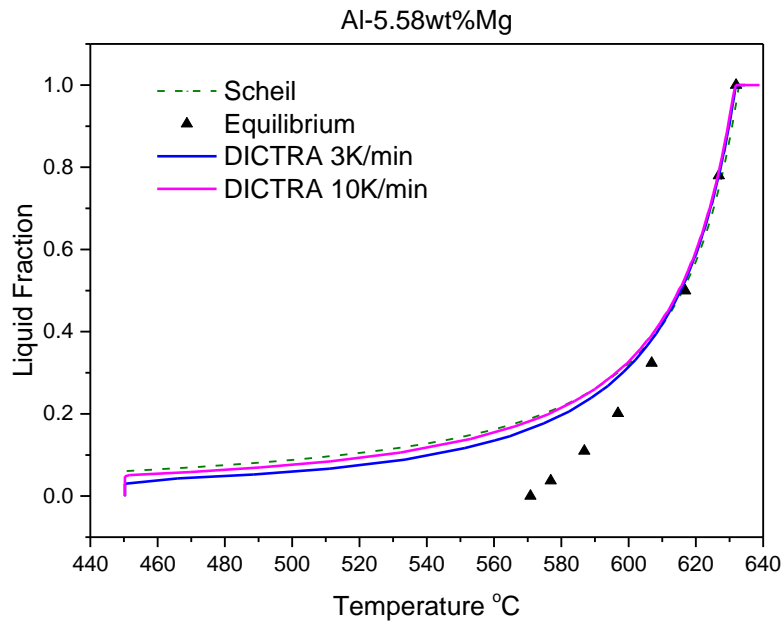


*Fig. 5.27 Comparison between DICTRA solidification simulation results (with 3K/min, 10K/min cooling rate) and equilibrium & Scheil data as a relationship of liquid-fraction vs. temperature for Al-5.58wt%Mg alloy*

### 5.3.2.5 Heating and Re-heating

The simulation results of heating and re-heating using DICTRA for Al-5.08wt%Si alloy with two cooling rates, 1K/min and 10K/min, are shown in Fig. 5.28. As can be seen, the re-heating simulation results show a good match with Scheil data above eutectic temperature. There is a liquid fraction drop at the beginning of melting (which in effect is for cooling) for re-heating (blue curves) because the matrix of remelting simulation was set as liquid phase. However, for the heating simulation with 1K/min, the curves start from 0 to 1 smoothly without a eutectic reaction. The heating at 10K/min stops at about 0.3 fraction liquid with a temperature of 629 °C. However, the reason is unknown.

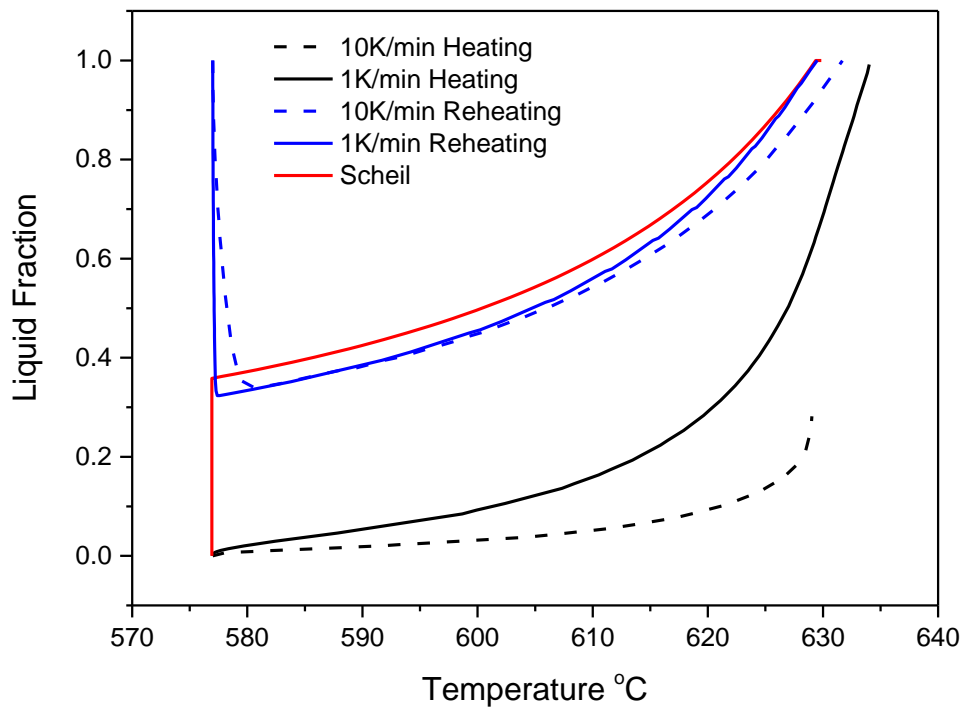


*Fig. 5.28 Heating and re-heating simulations using DICTRA of Al-5.08Si alloy as a relationship of liquid fraction/temperature*

The Si composition profiles are plotted for the different time steps during heating and re-heating simulation in Fig. 5.29 and Fig. 5.30 respectively. As can be seen in Fig. 5.29, with the temperature going up, the interface moves to the left with a dramatic composition drop in the liquid phase (comparing the red curve with the blue curve in Fig. 5.29). At the 630 °C, the Si profiles become equivalent in both liquid and solid phase, only left with an interface position at about 68  $\mu\text{m}$  distance.

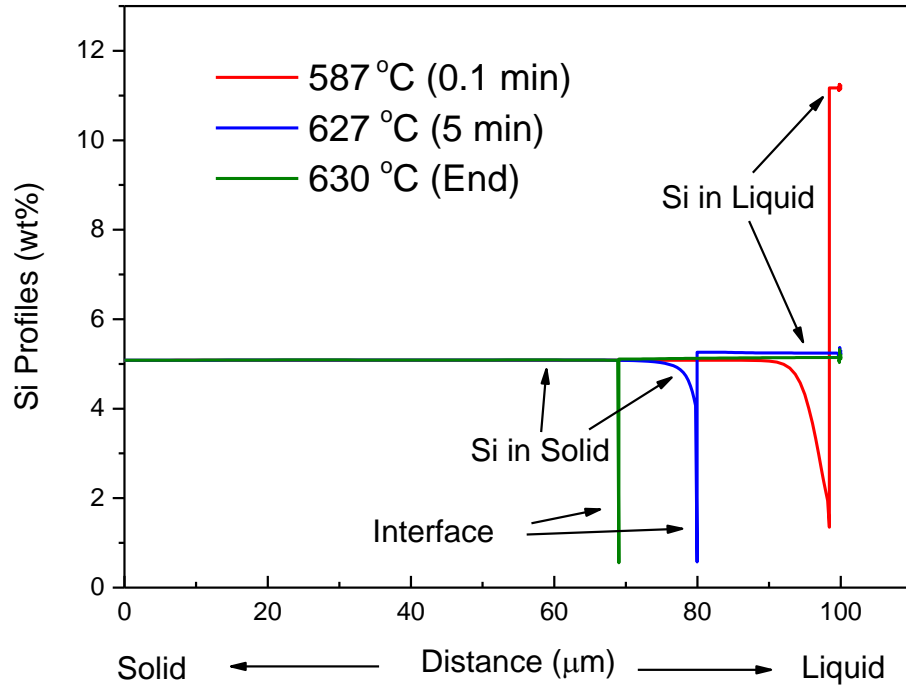


*Fig. 5.29 Si composition profiles of DICTRA simulation with 10K/min heating for Al-5.08wt%Si alloy at different temperatures*

However, there are huge differences for re-heating simulations. In Fig 5.30, the red curve is for the very beginning of remelting simulation. The solid-liquid interface was pulled from the distance at 100 $\mu$ m to the solid side at the beginning and then the interface was moving properly during the temperature increase. This might be because the matrix is liquid and the driving force of interface relies on the diffusion in liquid rather than in solid for heating. During the re-heating, the Si profiles in the liquid phase increase significantly while in the solid phase it stays at around 1.5 wt%. Finally, the composition of silicon is homogenous in 100% liquid with an original composition of 5.08wt%.

Though the curves for re-heating (blue lines in Fig. 5.28) are close to Scheil, it cannot be acceptable for simulation melting behaviour by DICTRA.

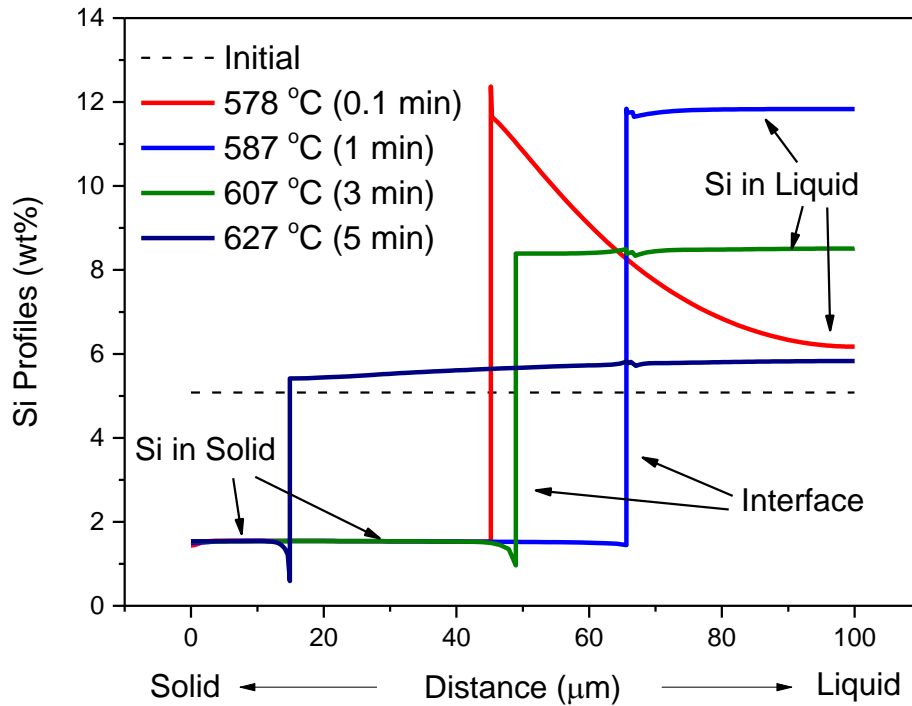


Fig. 5.30 Si composition profiles of DICTRA simulation with 10K/min re-heating for Al-5.08wt%Si alloy at different temperatures

## 5.4 Thermal Analysis by DSC

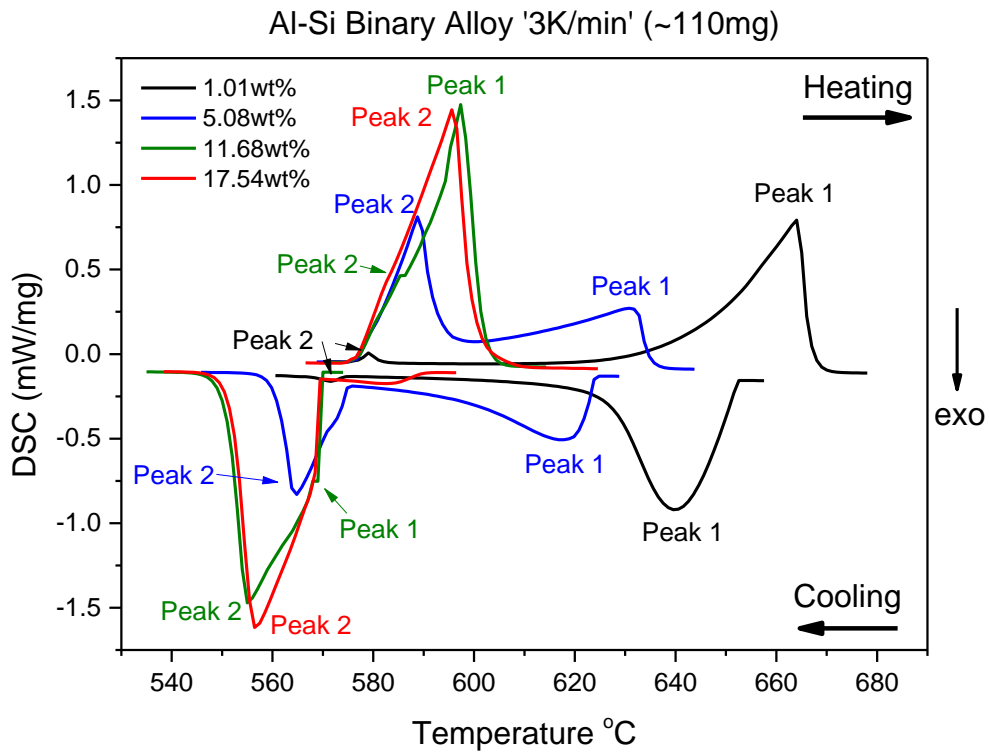
### 5.4.1 DSC Traces Results

Two sample sizes (~110mg and ~2mg) and two scanning rates (3K/min and 10K/min) were selected for the DSC experiments. Fig. 5.31 to Fig. 5.33 show the 3K/min with ~110mg mass sample results. Fig. 5.34 to Fig. 5.36 show the 3K/min with ~20mg mass sample results. Finally, Fig. 5.37 to Fig. 5.39 show the 10K/min with ~110mg mass sample results.

Fig. 5.31 shows the DSC traces for melting and solidification of as-received Al-Si binary alloys at a heating/cooling rate of 3K/min. For hypoeutectic Al-Si binary alloys, there are two phases i.e.  $\alpha$ -Al and Al-Si eutectic. In the DSC trace of Al-1.01wt%Si alloy, Al-5.08wt%Si alloy and Al-11.68wt%Si alloy, there are two reaction peaks in both melting and solidification. Peak 1 at high temperature represents Liquid  $\rightarrow$   $\alpha$ -Al reaction and peak 2 at the low temperature represents the eutectic reaction. As shown in the Fig. 5.31, the eutectic reaction peak (black peak 2) for Al-1.01wt%Si alloy is much smaller than peak 2 (blue) of Al-5.08wt%Si alloy. The simple reason for this is the

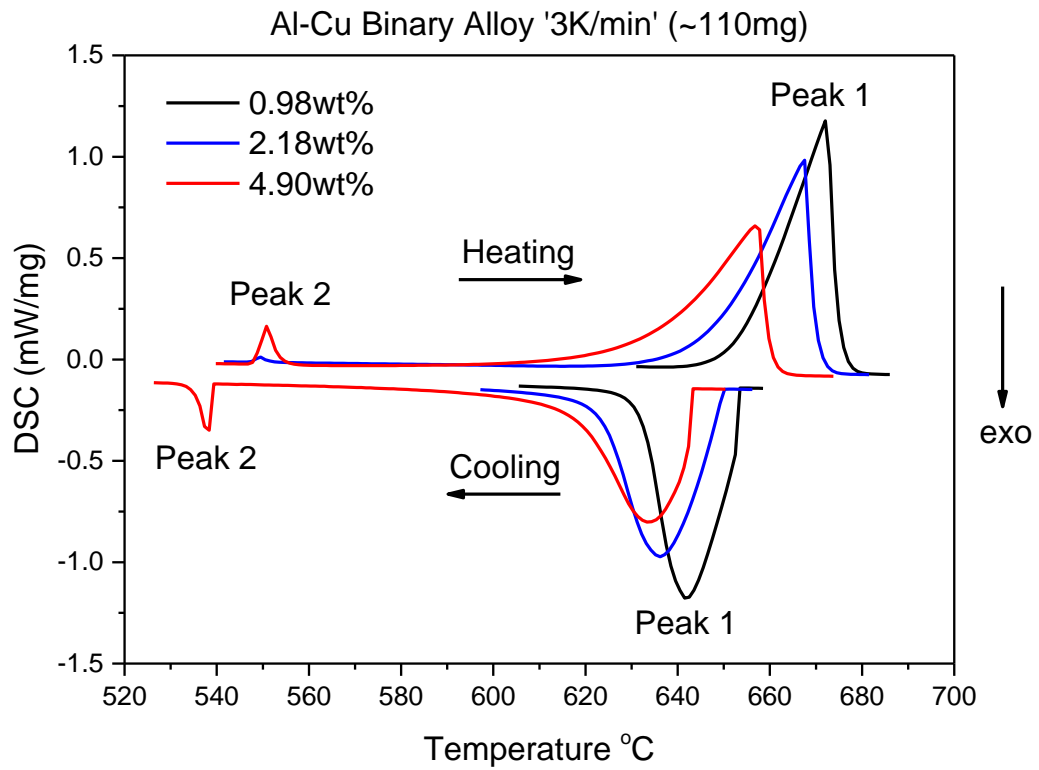


amount of eutectic phases in the structure. However, for Al-11.68wt% Si alloy, due to the very close compositions to the eutectic, peak 2 (green) merge with peak 1 on the DSC traces and just appears as a shoulder on peak 1. For hypereutectic alloy, i.e. Al-17.54wt%Si, there is only one peak on the DSC traces, which represents the eutectic reaction.



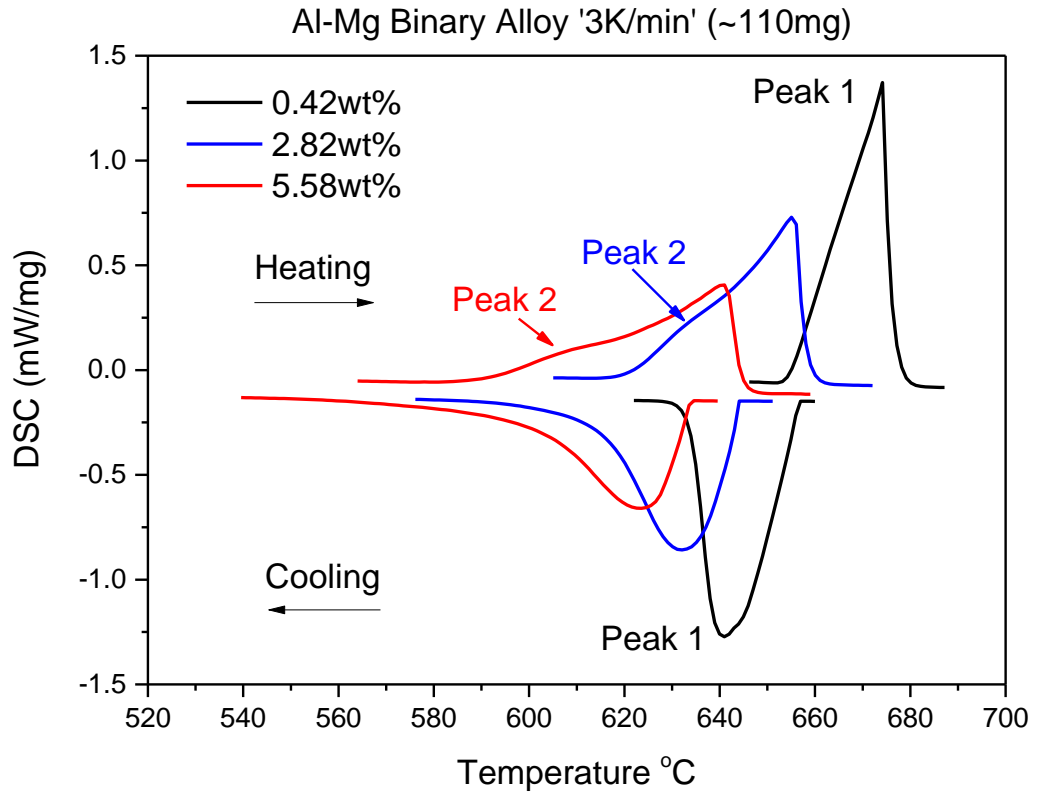
*Fig. 5.31 DSC curves vs. temperature under 3K/min for Al-Si alloys (sample mass: ~110mg)*

Fig. 5.32 shows the DSC traces for melting and solidification of as-received Al-Cu binary alloys at a heating/cooling rate of 3K/min. For Al-Cu binary alloys, the equation of solidification is: Liquid  $\rightarrow$   $\alpha$ -Al + Al<sub>2</sub>Cu. For Al-0.98wt% Cu alloy, the amount of copper is too small to be detected in DSC. Therefore, there is only one peak starting at 643 °C on melting and 653 °C on solidification. For Al-2.18wt%Cu and Al-4.9wt%Cu, two peaks show on the DSC traces. Peak 1 represents the reaction of Liquid  $\rightarrow$   $\alpha$ -Al and peak 2 represents the reaction of eutectic. With added copper, peak 2 (Al<sub>2</sub>Cu phase) is broader and higher, meanwhile, the peak position of  $\alpha$ -Al reaction moves to a lower temperature.



*Fig. 5.32 DSC curves vs. temperature under 3K/min for Al-Cu alloys (sample mass: ~110mg)*

Fig. 5.33 shows the DSC traces for melting and solidification of as-received Al-Mg binary alloys at a heating/cooling rate of 3K/min. According to the phase diagram of Al-Mg binary alloy, the equation of solidification should be: Liquid  $\rightarrow$   $\alpha$ -Al + Al<sub>3</sub>Mg<sub>2</sub>. Similarly to the Al-0.98wt%Cu alloy, in the traces of DSC, only one main peak was detected for heating and cooling for Al-0.42wt%Mg alloy due to the small amount of Mg. The peak 2 for reaction of Al<sub>3</sub>Mg<sub>2</sub> phases is found together with the Liquid  $\rightarrow$   $\alpha$ -Al reactions for Al-2.82wt% Mg and Al-5.58wt%Mg alloys. In addition, the added magnesium can increase the alloys' melting temperature.



*Fig. 5.33 DSC curves vs. temperature under 3K/min for Al-Mg alloys (sample mass: ~110mg)*

Fig. 5.34 to Fig. 5.36 show the DSC traces for melting and solidification of as-received aluminium binary alloys at a heating/cooling rate of 3K/min with small samples (average sample masses of 20mg±1mg). Compared with the DSC traces in Fig 5.31 to 5.33, the shapes of these peaks and the initial melting/solidification points remain the same but the peak areas become narrower and taller in the experiments with small samples. This is because the small mass of samples makes the heat release or absorption (in effect heat transfer) easier and the signal of DSC is divided by the sample mass. This is in good agreement with ref [142].

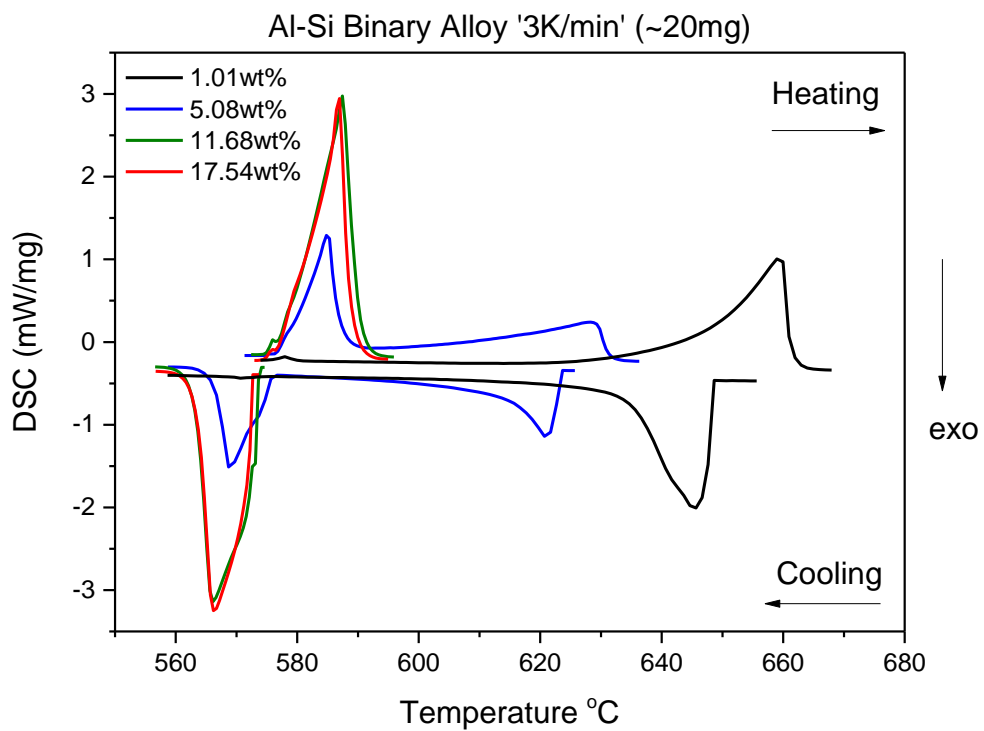


Fig. 5.34 DSC curves vs. temperature under 3K/min for Al-Si alloys (sample mass: ~20mg)

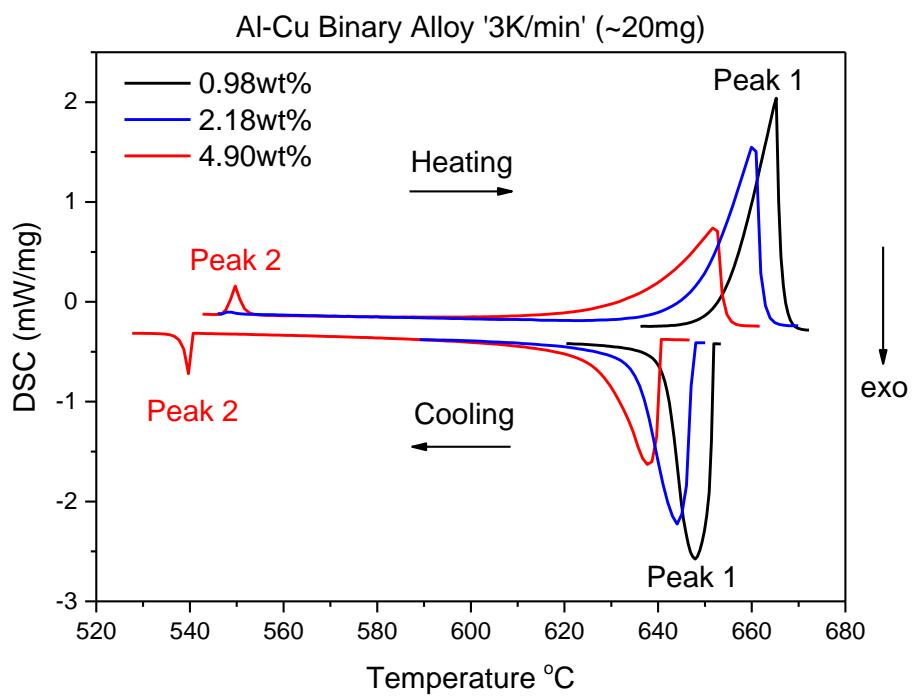
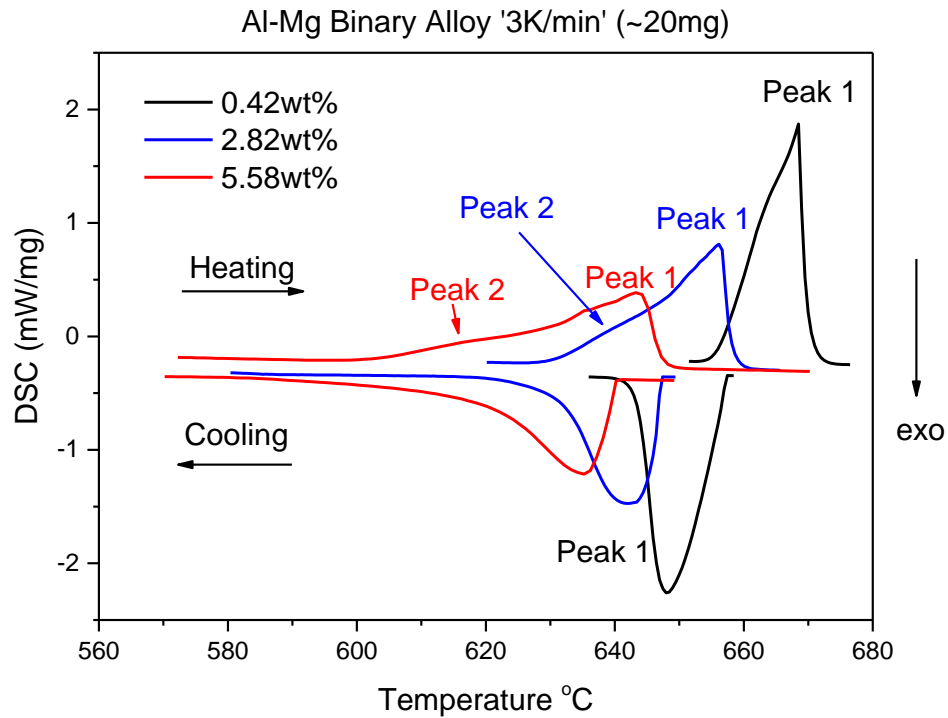


Fig. 5.35 DSC curves vs. temperature under 3K/min for Al-Cu alloys (sample mass: ~20mg)



*Fig. 5.36 DSC curves vs. temperature under 3K/min for Al-Mg alloys (sample mass: ~20mg)*

Fig. 5.37 to Fig. 5.39 show the DSC traces for melting and solidification of as-received aluminium binary alloys at a heating/cooling rate of 10K/min with an average sample mass of  $110\text{mg} \pm 2\text{mg}$ . When compared with the DSC traces with 3K/min heating/cooling rate but the same sample mass, the peaks under of 10K/min rate are broader and higher. Taking Al-0.42wt%Mg alloy for example, the top peak point of 10K/min rate is at (675 °C, 2.6 mW/mg) and (672 °C, 1.3 mW/mg) for 3K/min rate. The beginning melting points are the same at 653 °C but the end temperature points for the peak area under 10K/min is 710 °C and 680 °C for the 3K/min measurement. The increase with heating rate on the curve of DSC has increased the solidus-liquidus interval for measured alloys.



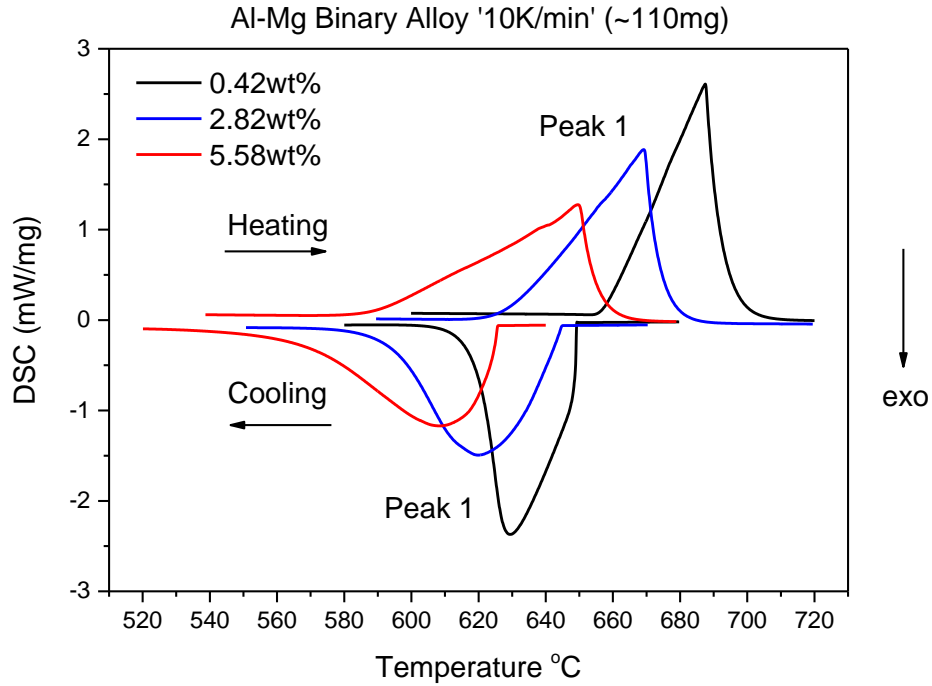


Fig. 5.39 DSC curves vs. temperature under 10K/min for Al-Mg alloys (sample mass: ~110mg)

#### 5.4.2 Calculated Liquid Fraction by DSC

Fig. 5.40 to Fig. 5.49 show the liquid fraction vs. temperature calculated from DSC data for these 10 binary alloys. The liquid fraction was calculated through the integration method for the peaks in the DSC traces curves. Generally, the trend for the experimental curves in the upper part of the graphs follows the order (from left hand side to right hand side):

DSC 10K/min cooling → DSC 3K/min cooling → DSC 3K/min cooling (small sample) → DSC 3K/min heating (small sample) → DSC 3K/min heating → DSC 10K/min heating.

The influence of heating (cooling) rate on the DSC curves for alloys is shown by the fact that the processing window between the fraction liquid 30% and 50% is wider for 10K/min heating (cooling) rate than for 3K/min (i.e. the slope of the curve is steeper for 3K/min). The solidus temperatures for alloys on the DSC heating curves are the same for every alloy. For the Al-5.08wt%Si alloy, the knee (shown in Fig. 5.41) at the

eutectic point is smoother in the DSC 10K/min heating (cooling) rate curve than in the 3K/min one.

The DSC measurement is controlled with a constant heating (cooling) rate. Increasing the heating rate results in a broader peak and a higher onset temperature when the DSC signal is plotted versus temperature [142]. In addition, the liquidus-solidus temperature range for the high heating (cooling) rate is wider than for a low rate. As a result, the curve for the 10K/min heating (cooling) rate on DSC is lying on the right (left) hand side of the curve for the 3K/min heating (cooling) rate.

With a higher mass sample, the rate at which a sample can absorb or release heat is slower than for a low mass sample. This leads to a broader peak for the large mass sample when plotting versus temperature but the onset temperature for solidification will not vary provided the heating (cooling) rate is the same [142]. This is consistent with the fact that the curve for the DSC 3K/min heating (cooling) rate with small sample mass is lying to the left (right) hand side of the curve for the DSC 3K/min with the large sample.

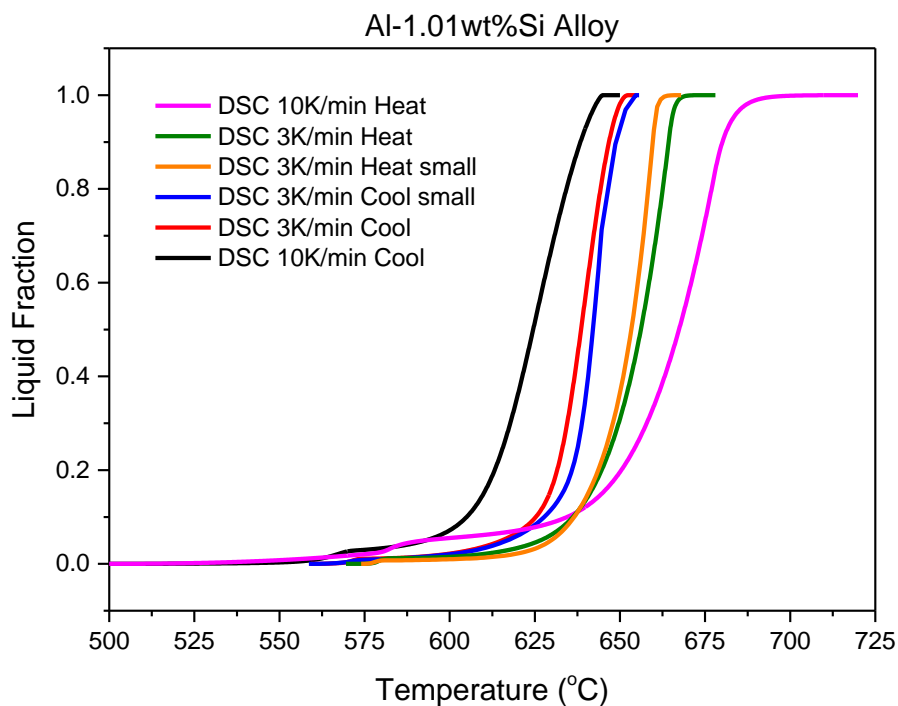


*Fig. 5.40 Liquid fraction vs. temperature calculated from DSC data for Al-1.01wt%Si alloy ('small' means small samples for DSC, i.e. the 20mg sample)*



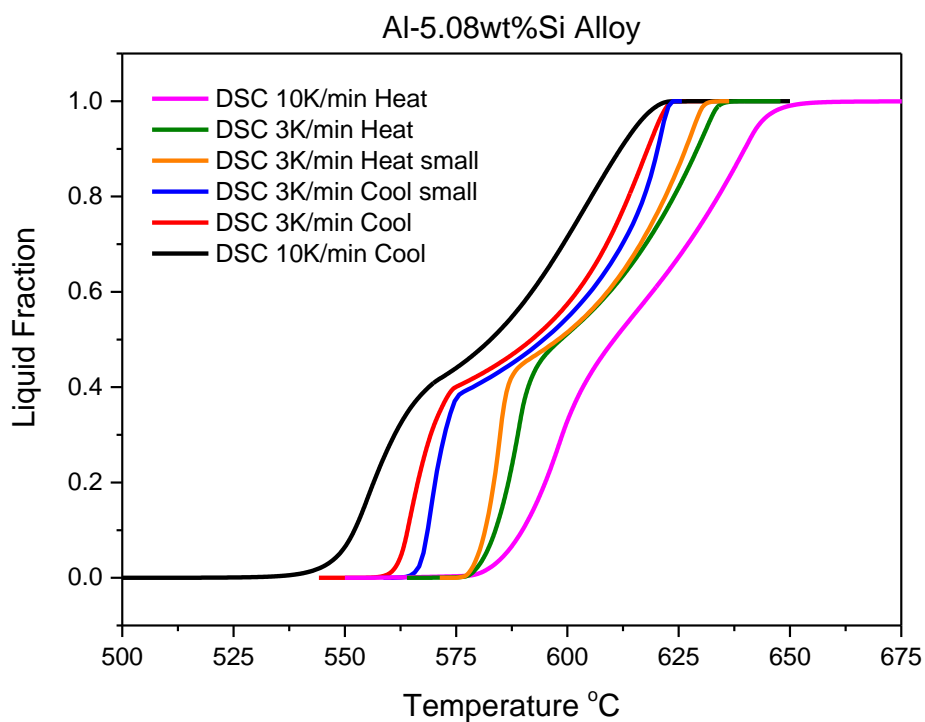


Fig. 5.41 Liquid fraction vs. temperature calculated from DSC data for Al-5.08wt%Si alloy ('small' means small samples for DSC, i.e. the 20mg sample)

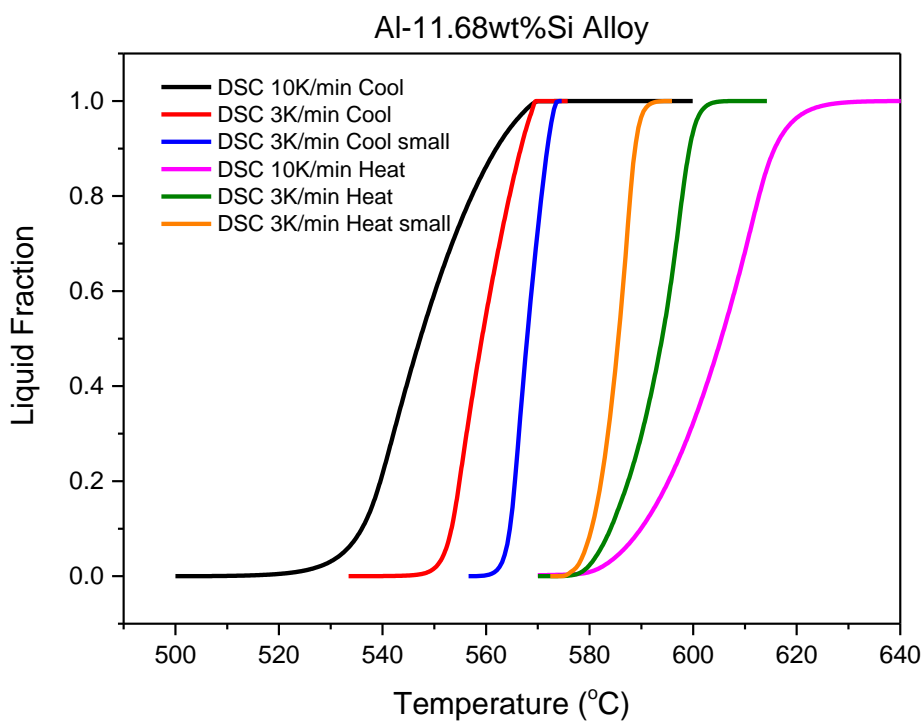


Fig. 5.42 Liquid fraction vs. temperature calculated from DSC data for Al-11.68wt%Si alloy ('small' means small samples for DSC, i.e. the 20mg sample)

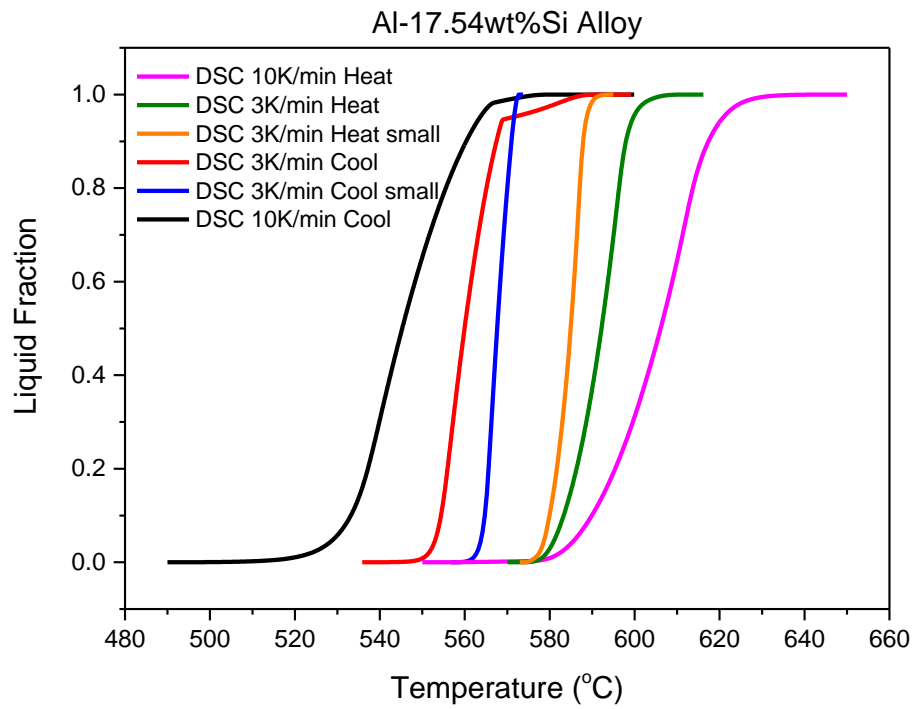


Fig. 5.43 Liquid fraction vs. temperature calculated from DSC data for Al-17.54wt%Si alloy ('small' means small samples for DSC, i.e. the 20mg sample)

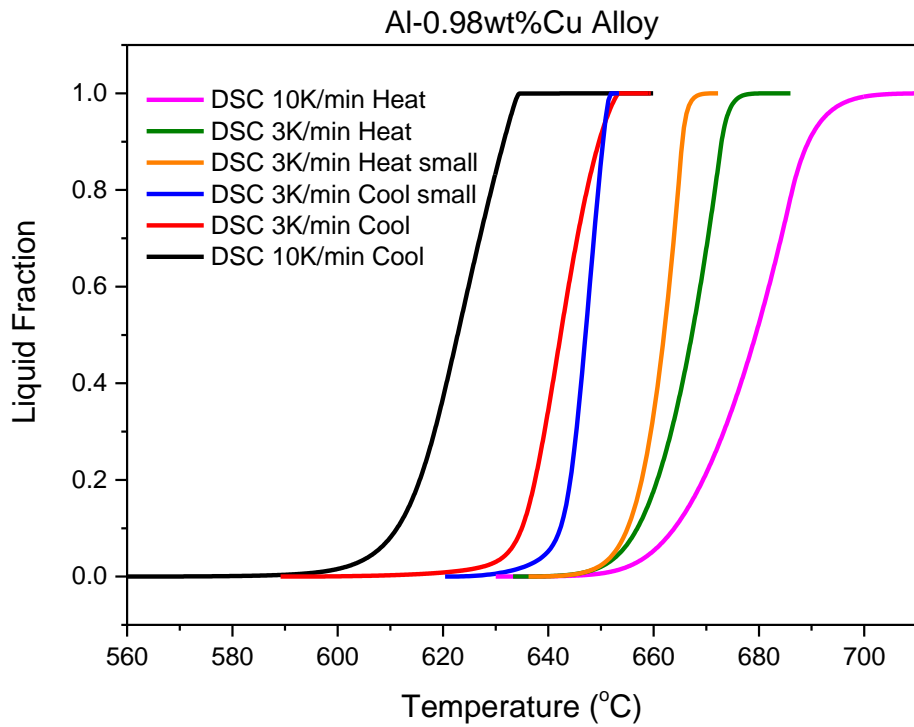


Fig. 5.44 Liquid fraction vs. temperature calculated from DSC data for Al-0.98wt%Cu alloy ('small' means small samples for DSC, i.e. the 20mg sample)

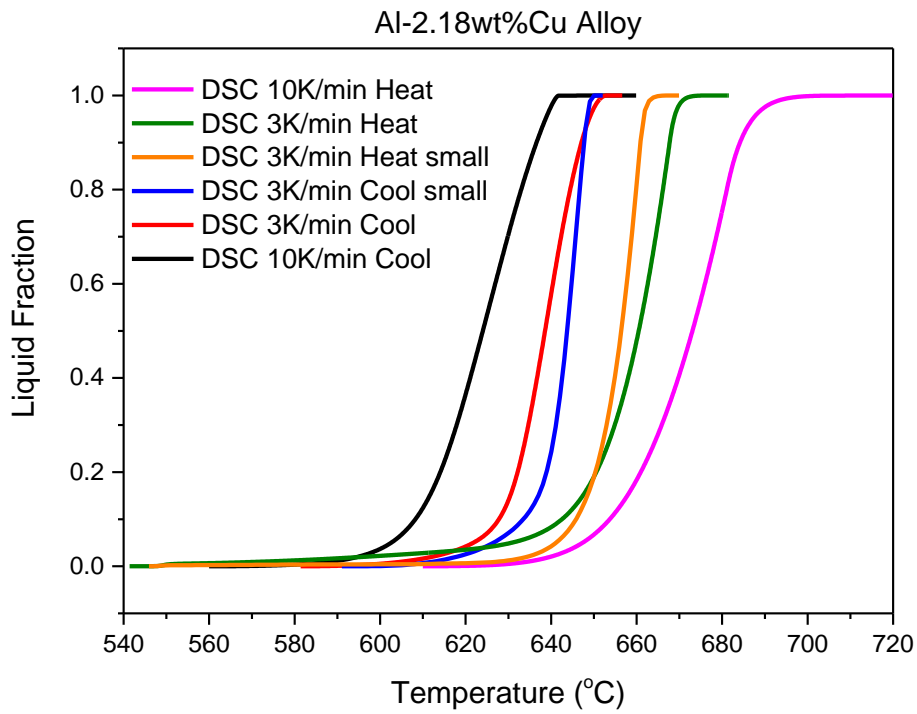


Fig. 5.45 Liquid fraction vs. temperature calculated from DSC data for Al-2.18wt%Cu alloy ('small' means small samples for DSC, i.e. the 20mg sample)

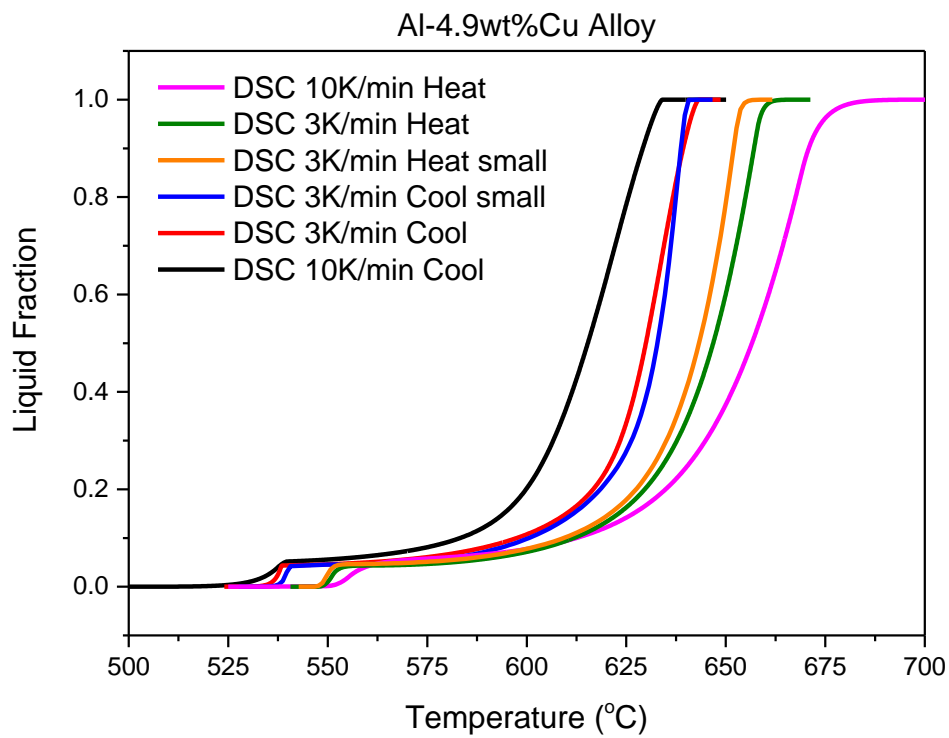


Fig. 5.46 Liquid fraction vs. temperature calculated from DSC data for Al-4.9wt%Cu alloy ('small' means small samples for DSC, i.e. the 20mg sample)

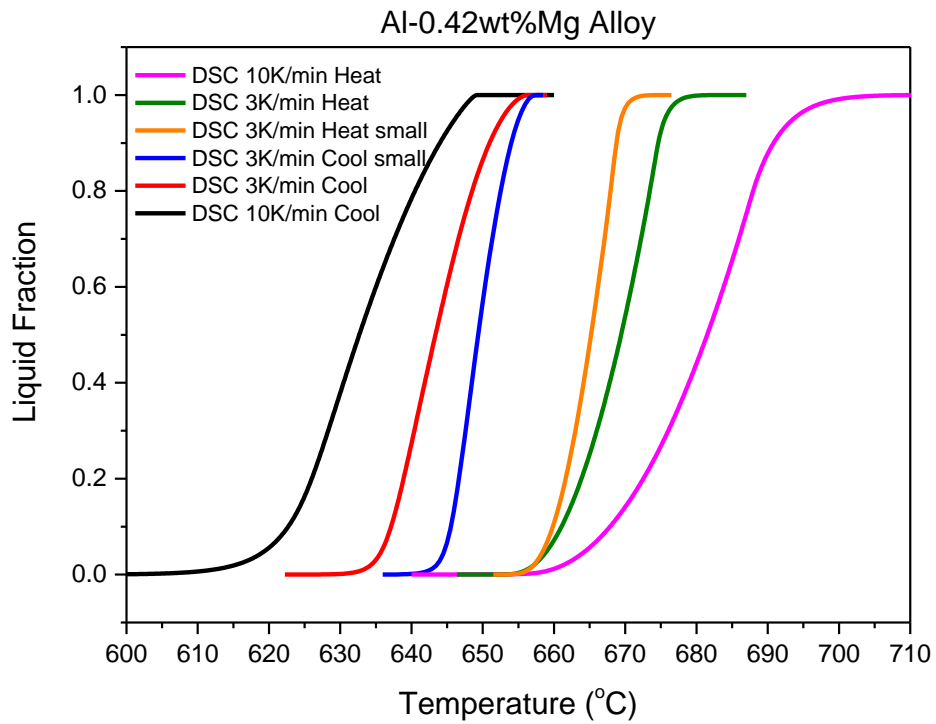


Fig. 5.47 Liquid fraction vs. temperature calculated from DSC data for Al-0.42wt%Mg alloy ('small' means small samples for DSC, i.e. the 20mg sample)

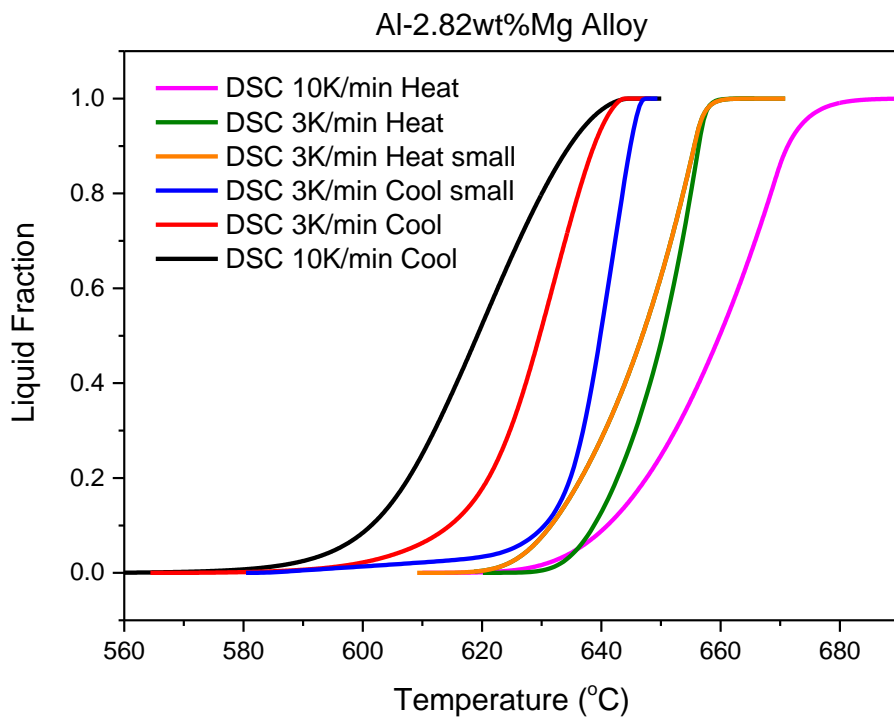
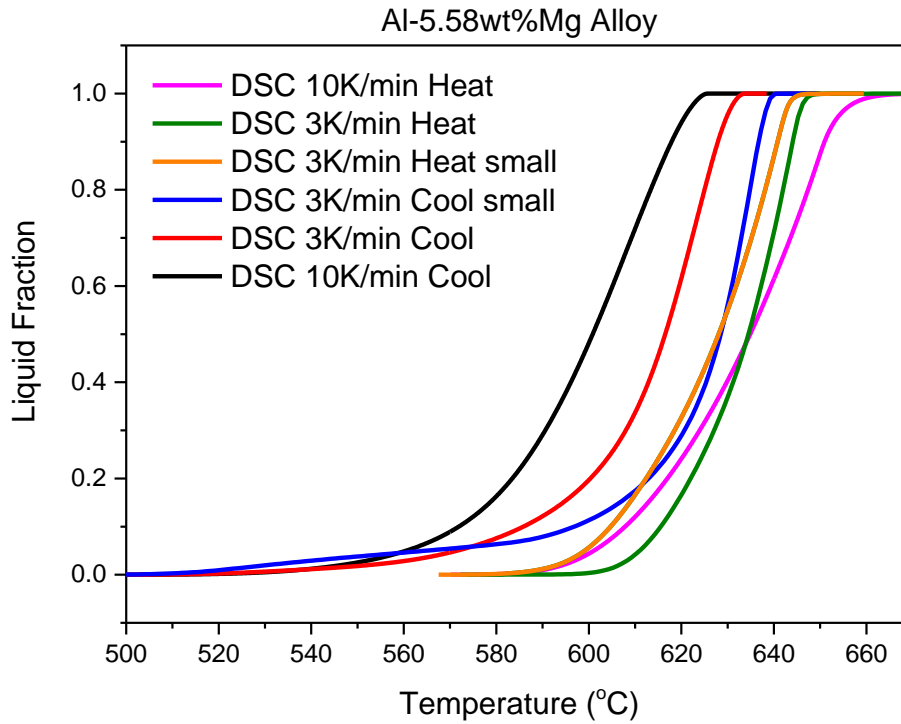


Fig. 5.48 Liquid fraction vs. temperature calculated from DSC data for Al-2.82wt%Mg alloy ('small' means small samples for DSC, i.e. the 20mg sample)



*Fig. 5.49 Liquid fraction vs. temperature calculated from DSC data for Al-5.58wt%Mg alloy ('small' means small samples for DSC, i.e. the 20mg sample)*

Table 5.1 and 5.2 are the summarised measurement of liquidus and solidus temperature data from the DSC experiments and the thermo-prediction results. Generally, the solidus-liquidus temperature range under 10K/min is larger than 3K/min for both experiments and predictions. The solidus-liquidus temperature range is also enlarged by adopting higher sample mass with DSC. This is significant because many semi-solid processes are using DSC for guidance.

The solidus-liquidus intervals of DICTRA simulations are between the equilibrium and Scheil data for Al-Cu and Al-Mg alloys. As the eutectic reaction occurs on Al-Si alloys, the DICTRA results of solidus-liquidus temperature range are coincide with the Scheil results.

In addition, the solidus-liquidus intervals of DICTRA and Scheil predictions for Al-2.82wt%Mg and Al-5.58wt%Mg alloys are much higher than the DSC results. This is because the Scheil calculation indicated that the reaction of  $\text{Al}_3\text{Mg}_2$  phase is at 450 °C, but due to the small amount of Mg and the sensitivity of DSC, it was not detected in the experiments. However,  $\text{Al}_3\text{Mg}_2$  was confirmed by the SEM analysis in Fig. 5.8.

The temperatures at 30% and 50% liquid fraction and the semi-solid temperature range (30% -50% liquid fraction) are listed in Table 5.3 and Table 5.4 respectively. In general, the semi-solid temperature range is enlarged by higher heating/cooling rate and larger sample mass with DSC. The semi-solid temperature ranges by DICTRA are between the equilibrium and Scheil results. In addition, there is no cooling rate effect (i.e. 3K/min and 10K/min) on semi-solid temperature range in DICTRA simulations (for 100 $\mu$ m cell size). However, the semi-solid temperature ranges are slight different between DSC results and predictions.

*Table 5.1 Solidus and liquidus temperatures determined by DSC curves for aluminium binary alloys, compared with Thermo-Calc (equilibrium and Scheil) and DICTRA results, 's' means small sample~20mg*

Binary Alloys	Solidus (°C)										Liquidus (°C)									
	DSC						Thermo-Calc		DICTRA		DSC						Thermo-Calc		DICTRA	
	Heat			Cool							Heat			Cool						
	3K/min 's'	3K/min	10K/min	3K/min 's'	3K/min	10K/min	Equilibrium	Scheil	3K/min	10K/min	3K/min 's'	3K/min	10K/min	3K/min 's'	3K/min	10K/min	Equilibrium	Scheil	3K/min	10K/min
Al-1.01wt%Si	578	578	579	568	567	558	604	577	577	577	660	666	683	652	652	645	654	654	654	654
Al-5.08wt%Si	579	579	580	562	561	546	577	577	577	577	630	637	646	624	624	623	629	629	629	629
Al-11.68wt%Si	579	579	580	560	551	533	577	577	577	577	592	602	619	570	570	569	583	583	583	583
Al-17.54wt%Si	579	579	580	560	552	530	577	577	577	577	590	600	620	590	590	579	654	654	654	654
Al-0.98wt%Cu	653	653	655	640	632	608	635	548	548	548	668	676	691	654	654	635	658	658	658	658
Al-2.18wt%Cu	549	549	550	635	630	517	606	548	548	548	661	670	686	653	653	642	655	655	655	655
Al-4.90wt%Cu	548	548	550	537	535	522	558	548	548	548	653	660	674	642	642	634	647	647	647	647
Al-0.42wt%Mg	655	655	658	640	634	619	654	622	646	641	670	676	693	656	656	649	658	658	658	658
Al-2.82wt%Mg	622	622	626	629	613	594	615	450	450	560	657	658	674	644	644	645	646	646	646	646
Al-5.58wt%Mg	589	589	592	590	587	567	571	450	450	450	643	646	656	632	632	626	632	632	632	632

*Table 5.2 Solidus-liquidus temperature ranges for aluminium binary alloys, 's' means small sample~20mg*

Binary Alloys	Solidus-liquidus temperature range (°C)									
	DSC						Thermo-Calc		DICTRA	
	Heat			Cool						
	3K/min 's'	3K/min	10K/min	3K/min 's'	3K/min	10K/min	Equilibrium	Scheil	3K/min	10K/min
Al-1.01wt%Si	82	88	104	84	85	87	50	77	77	77
Al-5.08wt%Si	51	58	66	62	63	77	52	52	52	52
Al-11.68wt%Si	13	23	39	10	19	36	6	6	6	6
Al-17.54wt%Si	11	21	40	30	38	49	77	77	77	77
Al-0.98wt%Cu	15	23	36	14	22	27	23	110	110	110
Al-2.18wt%Cu	112	121	136	18	23	125	49	107	107	107
Al-4.90wt%Cu	105	112	124	105	107	112	89	99	99	99
Al-0.42wt%Mg	15	21	35	16	22	30	4	36	12	17
Al-2.82wt%Mg	35	36	48	15	31	51	31	196	196	86
Al-5.58wt%Mg	54	57	64	42	45	59	61	182	182	182

*Table 5.3 Temperatures at 30% and 50% liquid fractions determined by DSC curves for aluminium binary alloys, compared with Thermo-Calc (equilibrium and Scheil) and DICTRA results, 's' means small sample~20mg*

Binary Alloys	Temperature at 30% liquid fracion (°C)										Temperature at 50% liquid fracion (°C)									
	DSC						Thermo-Calc		DICTRA		DSC						Thermo-Calc		DICTRA	
	Heat			Cool							Heat			Cool						
	3K/min 's'	3K/min	10K/min	3K/min 's'	3K/min	10K/min	Equilibrium	Scheil	3K/min	10K/min	3K/min 's'	3K/min	10K/min	3K/min 's'	3K/min	10K/min	Equilibrium	Scheil	3K/min	10K/min
Al-1.01wt%Si	648	650	658	639	635	618	643	642	643	643	653	656	667	642	638	625	649	649	649	649
Al-5.08wt%Si	588	589	599	573	569	561	577	577	577	577	599	600	611	595	592	585	600	601	601	601
Al-11.68wt%Si	584	590	599	567	556	542	577	577	577	577	585	594	605	568	559	547	577	577	577	577
Al-17.54wt%Si	583	589	600	566	557	540	577	577	577	577	585	592	606	568	560	545	577	577	577	577
Al-0.98wt%Cu	660	663	673	645	639	618	654	653	653	653	662	667	680	647	643	623	656	655	655	655
Al-2.18wt%Cu	653	655	666	641	635	618	646	644	644	644	657	661	673	644	638	624	653	650	650	649
Al-4.90wt%Cu	635	638	645	626	623	606	626	622	624	624	643	647	657	632	630	615	637	636	636	636
Al-0.42wt%Mg	663	666	676	648	640	628	655	642	655	655	665	670	682	649	644	633	657	647	657	657
Al-2.82wt%Mg	641	645	652	637	625	612	634	629	630	629	647	652	660	640	630	618	639	638	638	637
Al-5.58wt%Mg	621	624	627	620	608	591	605	597	598	597	628	633	636	628	617	601	617	616	615	615

*Table 5.4 Semi-solid temperature ranges for aluminium binary alloys, 's' means small sample~20mg*

Binary Alloys	Semi-solid (30%-50% liiquid fraction) temperature range (°C)									
	DSC						Thermo-Calc		DICTRA	
	Heat			Cool						
	3K/min 's'	3K/min	10K/min	3K/min 's'	3K/min	10K/min	Equilibrium	Scheil	3K/min	10K/min
Al-1.01wt%Si	5	6	9	3	3	7	6	7	6	6
Al-5.08wt%Si	11	11	12	22	23	24	23	24	24	24
Al-11.68wt%Si	1	4	6	1	3	5	0	0	0	0
Al-17.54wt%Si	2	3	6	2	3	5	0	0	0	0
Al-0.98wt%Cu	2	4	7	2	4	5	2	2	2	2
Al-2.18wt%Cu	4	6	7	3	3	6	7	6	6	5
Al-4.90wt%Cu	8	9	12	6	7	9	11	14	12	12
Al-0.42wt%Mg	2	4	6	1	4	5	2	5	2	2
Al-2.82wt%Mg	6	7	8	3	5	6	5	9	8	8
Al-5.58wt%Mg	7	9	9	8	9	10	12	19	17	18



## 5.5 Thermal Analysis by SPSC

### 5.5.1 SPSC Study with Pure Aluminium

The SPSC overcomes the “smearing” effect and the measured raw data (temperature vs. time) with the temperature difference between the inner and outer crucible at  $\pm 6\text{K}$  is shown in Fig. 5.50. The temperature variation during melting and solidification was very small. The undercooling occurs when solidification starts, as circled in Fig. 5.50.

In order to study the scanning rate effect on the SPSC results, a larger temperature difference between the inner and outer crucible at  $\pm 12\text{K}$  was applied. These temperature differences correspond to a heating and cooling rate of  $8.5 \pm 0.1\text{K/min}$ . Very good reproducibility was obtained. The measured enthalpies (calculated by Equation 3.11) of pure Al obtained at the two different heat fluxes are shown in Fig. 5.51. It can be seen that there is very little difference between these enthalpy curves for the different rates, except for a small difference in the enthalpy step at the beginning of solidification. This is because the as-expected undercooling occurs during freezing.

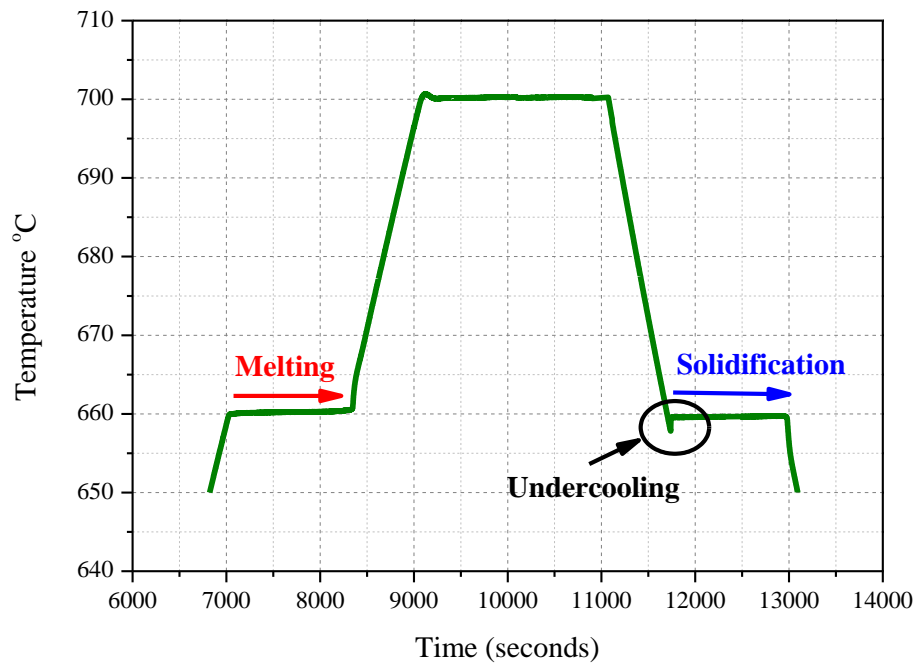
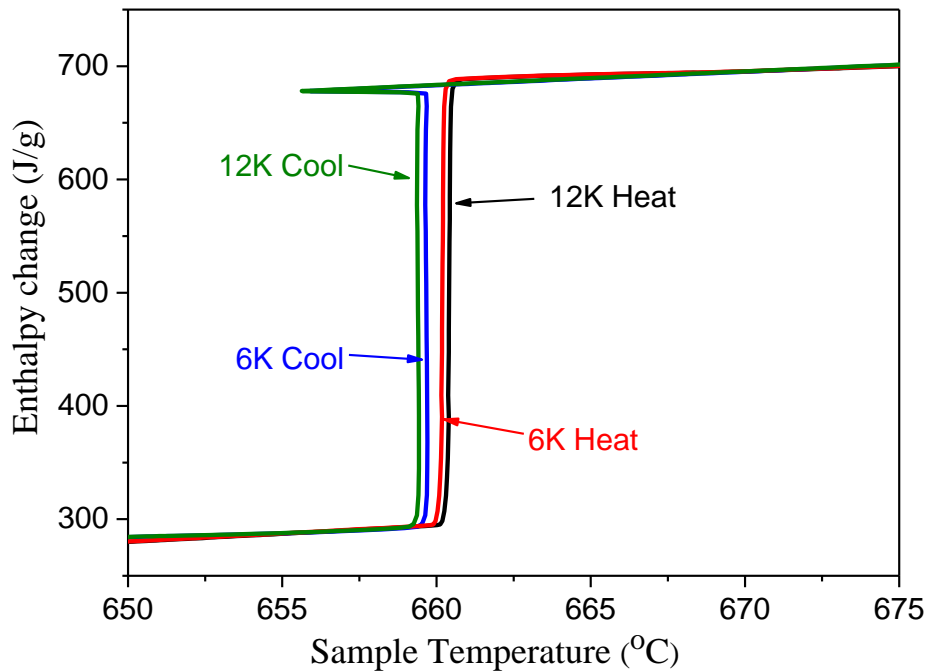


Fig. 5.50 Measured sample temperature versus time for pure Al with SPSC



*Fig. 5.51 Measured enthalpy curve for pure Al, for the temperature differences at  $\pm 6K$  and  $\pm 12K$  with SPSC*

The liquid fractions were calculated by Equation 3.14 and were plotted versus temperature in Fig. 5.52. The results give a constant temperature line when pure aluminium is melting or solidifying because it is measuring exactly the sample's temperature. There is only a  $0.1\text{ }^{\circ}\text{C}$  difference in melting temperature between the two scanning rates, i.e.  $3K/min$  and  $8.5K/min$ . This is a significant result in comparison with DSC.

There is a difference of about  $0.2\text{ }^{\circ}\text{C}$  between heating and cooling curves with same scan rate. This difference is associated with the undercooling phenomenon which is the driving force for nucleation.

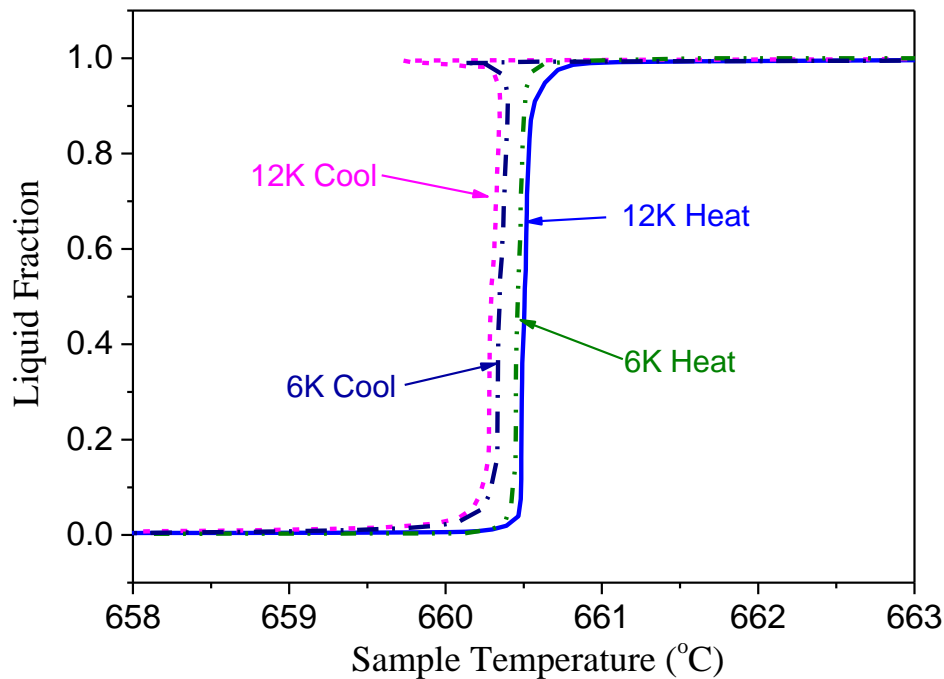


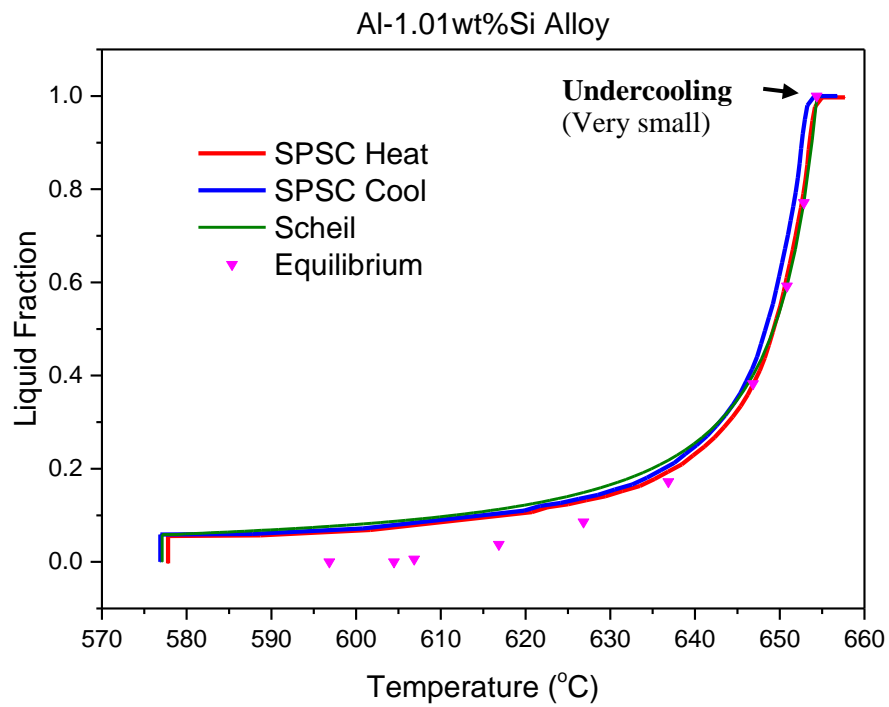
*Fig. 5.52 Calculated liquid fraction as a function of temperature for pure Al from SPSC experimental results*

### **5.5.2 Calculated Liquid Fraction by SPSC**

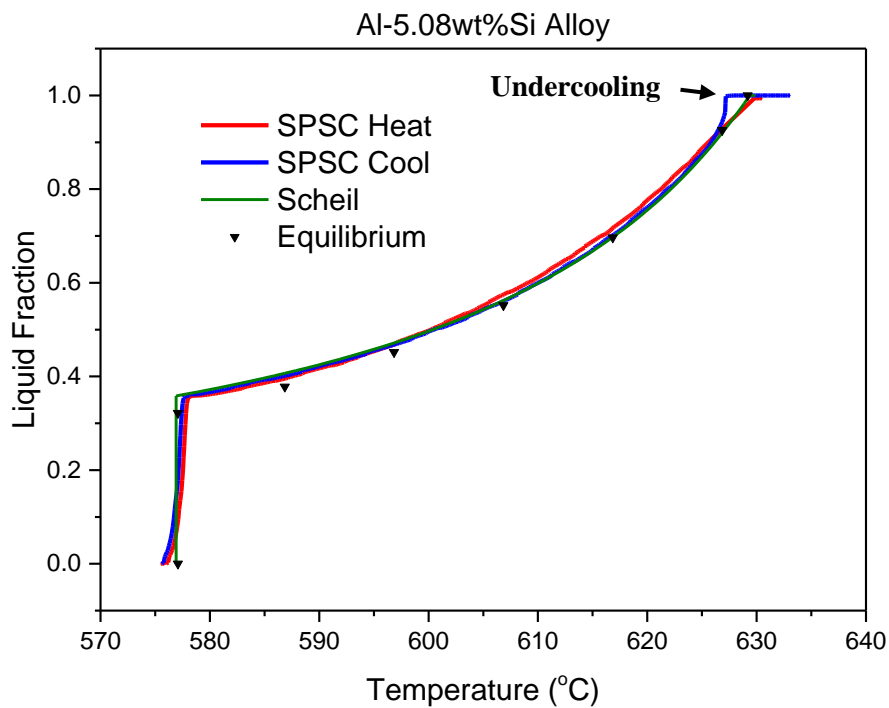
The calculated liquid fraction versus temperature results for 10 binary alloys by SPSC are presented from Fig 5.53 to Fig. 5.62 respectively.

Fig. 5.53 to Fig. 5.56 show the SPSC results for Al-Si binary alloys. It can be seen that the SPSC results are close to the Scheil curves. As the thermodynamics doesn't consider the undercooling effect, there is a temperature drop at the beginning of solidification, which can be seen clearly at the top of blues curves.

In Fig 5.55, the nucleation undercoolings for  $\alpha$ -dendrite and eutectic solidification are clearly shown on the liquid fraction curves. The undercoolings in Al-Si binary alloys increase with silicon content, suggesting that the addition of Si increases the undercooling for nucleation.



*Fig. 5.53 Liquid fraction vs. temperature calculated from SPSC data for Al-1.01wt%Si alloy*



*Fig. 5.54 Liquid fraction vs. temperature calculated from SPSC data for Al-5.08wt%Si alloy*

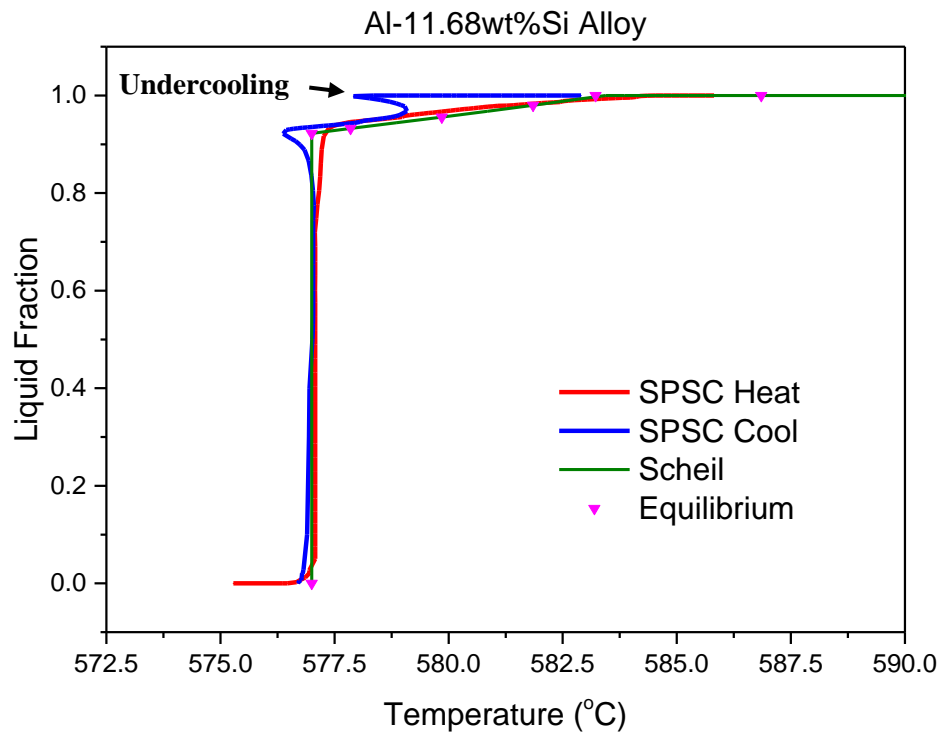


Fig. 5.55 Liquid fraction vs. temperature calculated from SPSC data for Al-11.68wt%Si alloy

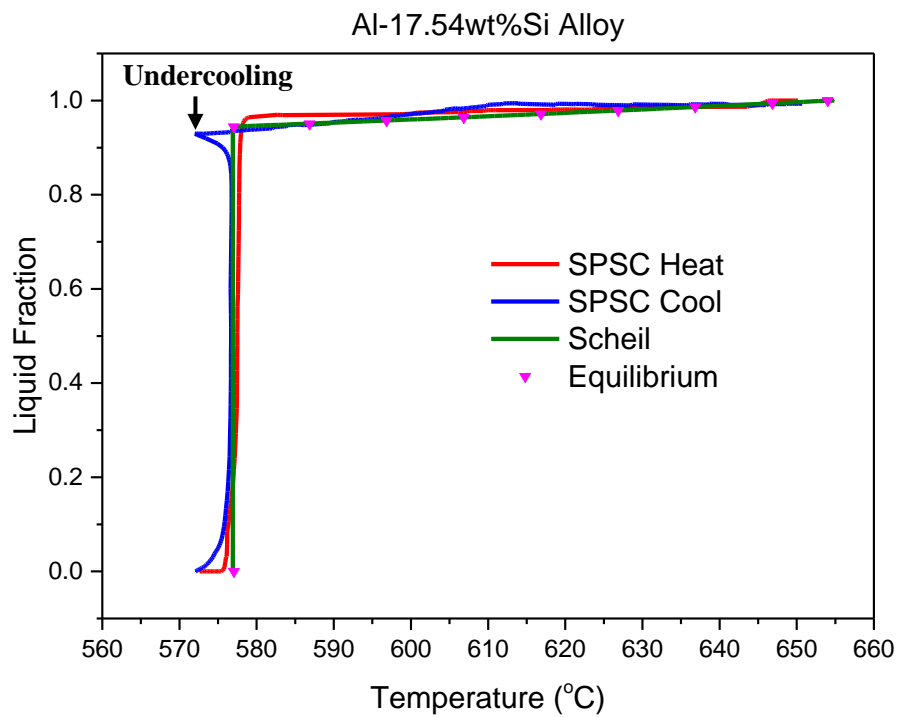
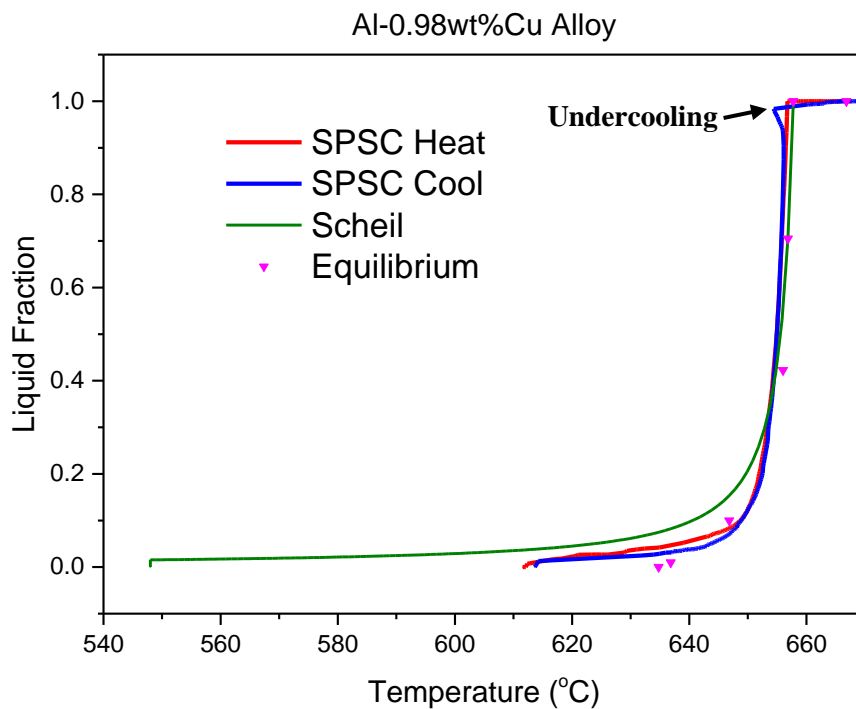


Fig. 5.56 Liquid fraction vs. temperature calculated from SPSC data for Al-17.54wt%Si alloy

Fig. 5.57 to Fig. 5.59 show the SPSC results for Al-Cu binary alloys. Generally, the undercoolings for nucleation in Al-Cu binary alloys increase with the Cu content. In Fig. 5.57, the SPSC results are close to the equilibrium curve rather than the Scheil one. The solidification finished at around 612 °C, which is much higher than the Scheil result (548 °C) but lower than the equilibrium data (635 °C). It might be because the small amount of copper has been dissolved into the matrix during heating or formed small Al<sub>2</sub>Cu eutectic phases during cooling without getting temperature variations.

For the Al-2.18wt%Cu alloy in Fig. 5.58, the SPSC results show large differences between 10%-30% fraction liquid compared to the predictions. The result show lower copper eutectic fractions than the predictions and the liquid fraction is 15% lower for SPSC data at 640 °C compared to the Scheil curve. The reason is uncertain.

The SPSC results of Al-4.9wt%Cu alloy show similar problems with the Al-2.18wt%Cu alloy. Measurement by SPSC shows lower liquid fraction by 13% than the Scheil prediction. In addition, the liquidus temperature measured by SPSC for Al-4.9wt%Cu alloy is slightly lower than the equilibrium and Scheil calculations. This could be because there were variations of the weight percent of copper in the specimen for SPSC.



*Fig. 5.57 Liquid fraction vs. temperature calculated from SPSC data for Al-0.98wt%Cu alloy*

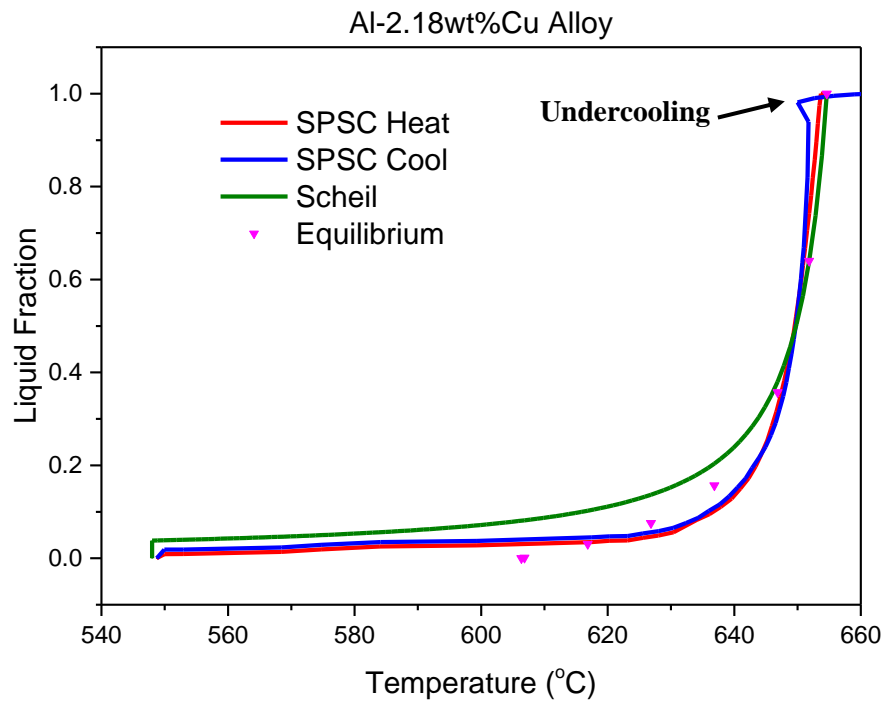


Fig. 5.58 Liquid fraction vs. temperature calculated from SPSC data for Al-2.18wt%Cu alloy

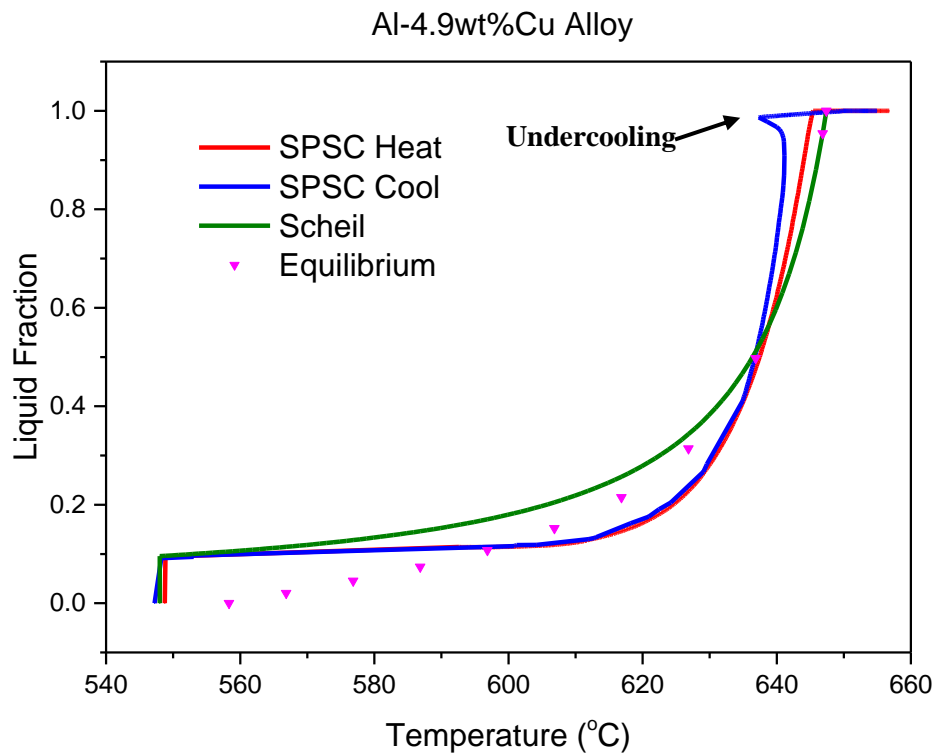
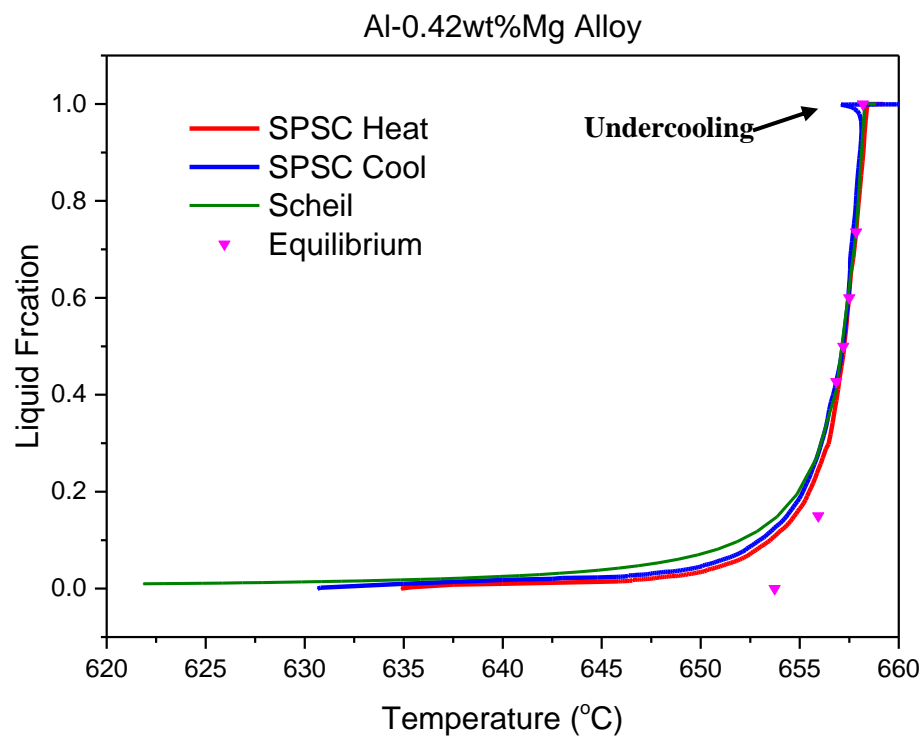


Fig. 5.59 Liquid fraction vs. temperature calculated from SPSC data for Al-4.9wt%Cu alloy

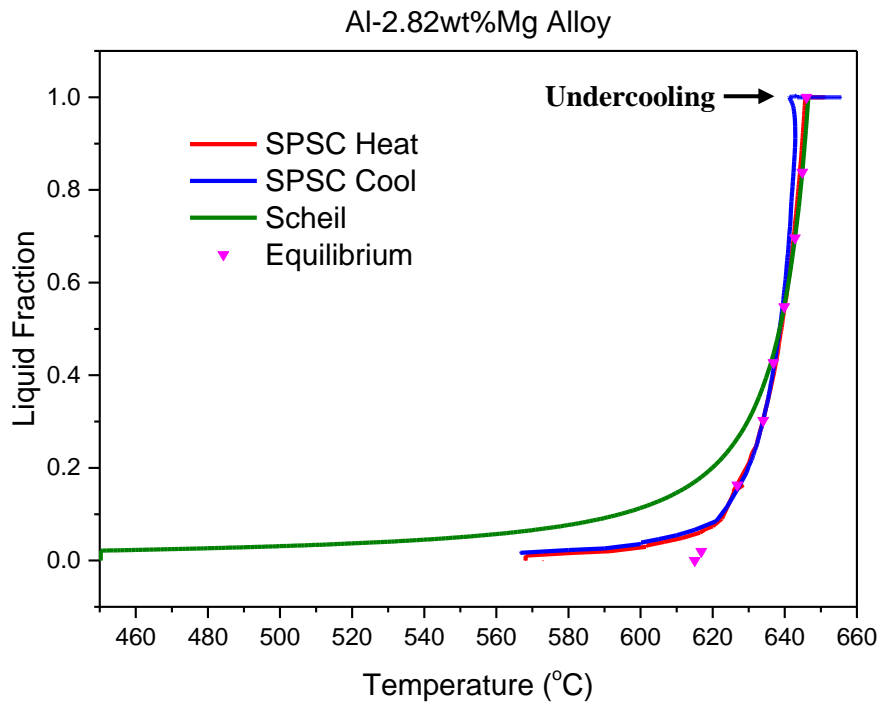
Fig. 5.60 to Fig. 5.62 show the SPSC results for Al-Mg binary alloys. It can be seen that the SPSC results are lying between the Scheil and equilibrium curves. With Mg addition, the undercoolings for nucleation in Al-Mg binary alloys increased.

It should be noticed that the solidus temperatures measured by SPSC for Al-Mg binary alloys are much higher than the Scheil predictions. This is in very good agreement with DSC results. It is suggested that the eutectic reaction for Al-Mg binary alloys (Mg contents below 5wt%) at 450 °C predicted by Scheil for alloy could not be measured by calorimetry.



*Fig. 5.60 Liquid fraction vs. temperature calculated from SPSC data for Al-0.42wt%Mg alloy*





v

*Fig. 5.61 Liquid fraction vs. temperature calculated from SPSC data for Al-2.82wt%Mg alloy*

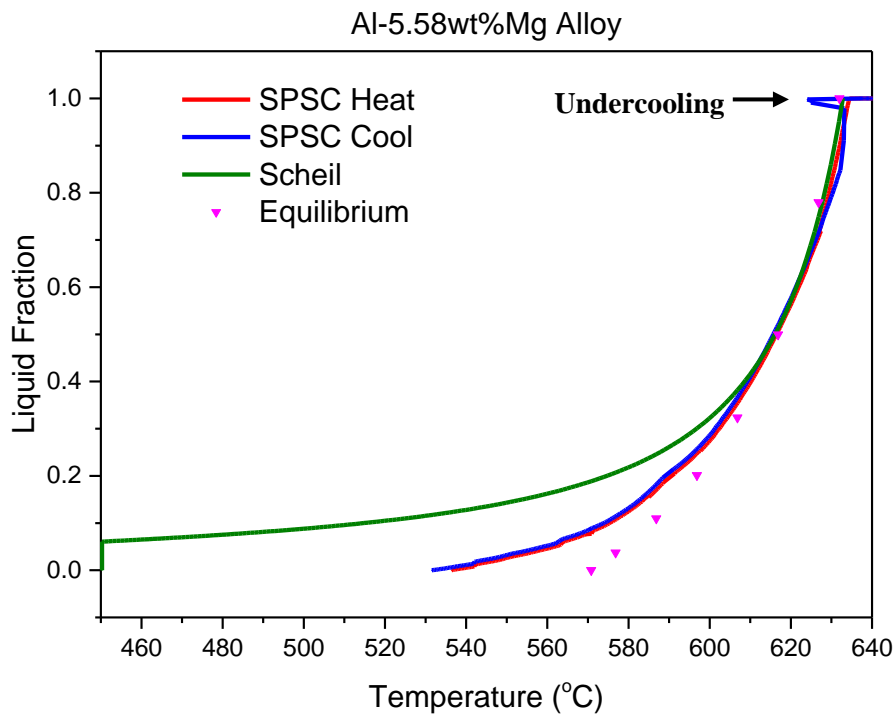


*Fig. 5.62 Liquid fraction vs. temperature calculated from SPSC data for Al-5.58wt%Mg alloy*

## 5.6 Comparison between Predictions and Experiments

In this section, comparison between predictions results and experimental results are illustrated for the 10 binary aluminium alloys.

Fig. 5.63 to 5.66 show the liquid fraction-temperature relationships from DSC and SPSC data for Al-Si series binary alloys together with the prediction curves for equilibrium and Scheil condition and DICTRA simulations. The liquid fraction has been estimated from both heating and cooling curves. From DICTRA prediction, at a given temperature, higher cooling rate gives just slightly higher liquid fraction than with a lower cooling rate. The lowest liquid fraction is obtained under equilibrium conditions in the 30-50% liquid range. The inset in Fig. 5.63 shows the difference between equilibrium and SPSC Cool to be ~0.04, which could be significant in processing terms. Fig. 5.63 shows that the SPSC heating and cooling curves are very close together and, although the SPSC cannot achieve 10K/min cooling, the curves for 10K/min are expected to be very close to these because SPSC operates via the constant heat flux mode.

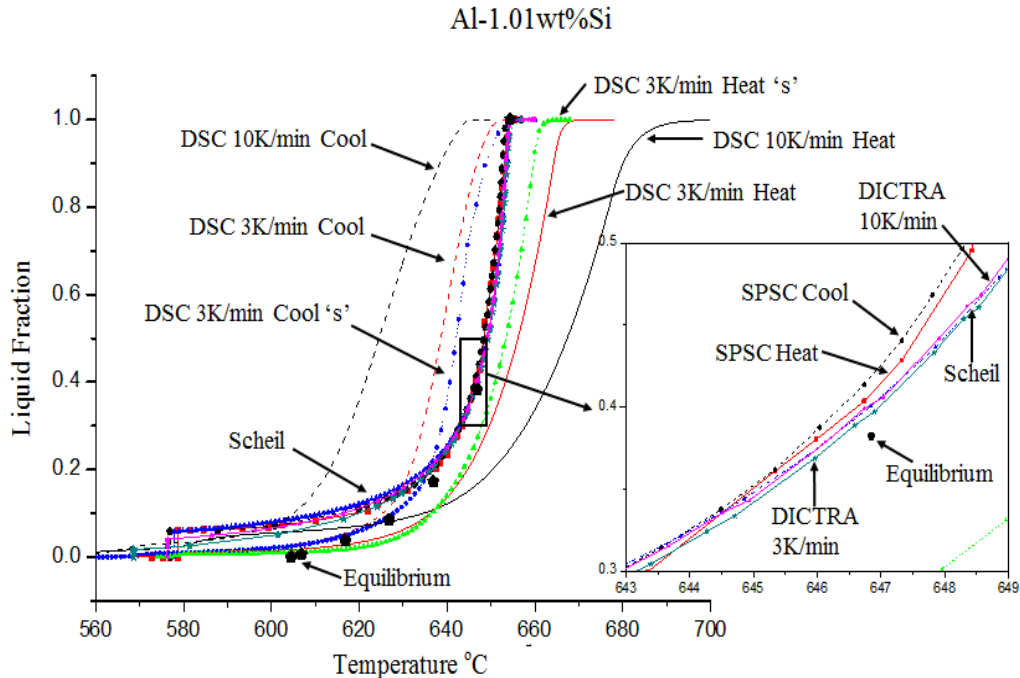


Fig. 5.63 Liquid fraction as a function of temperature from SPSC & DSC for Al-1.01wt%Si alloy, together with prediction curves. ('s' means small samples for DSC, i.e. the 20mg sample)

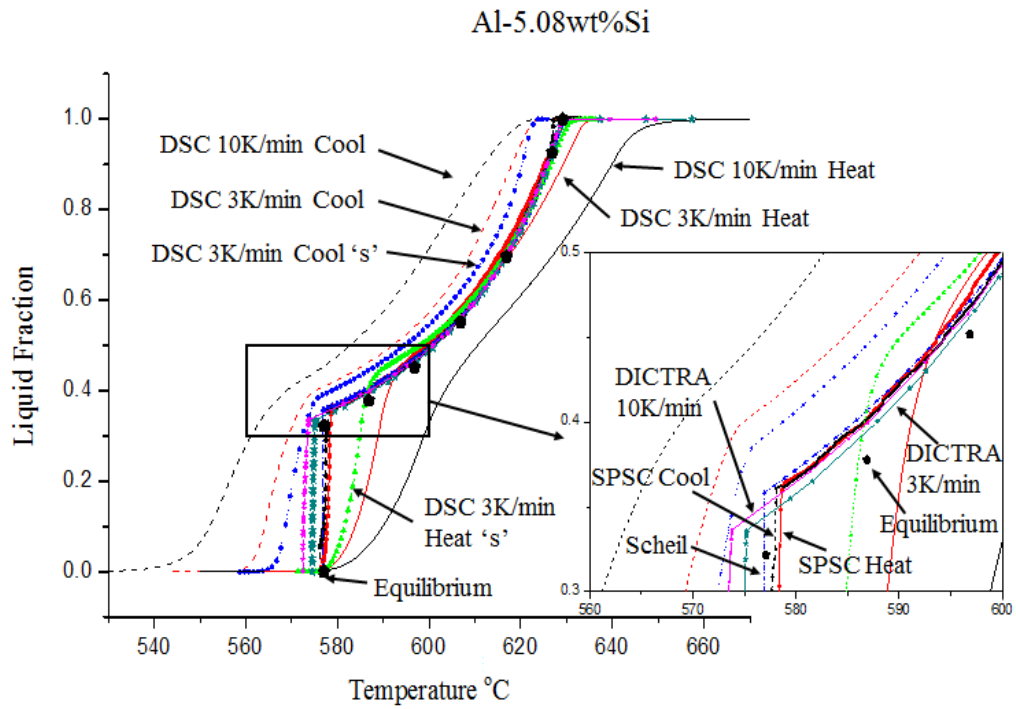


Fig. 5.64 Liquid fraction as a function of temperature from SPSC & DSC for Al-5.08wt%Si alloy, together with prediction curves. ('s' means small samples for DSC, i.e. the 20mg sample)

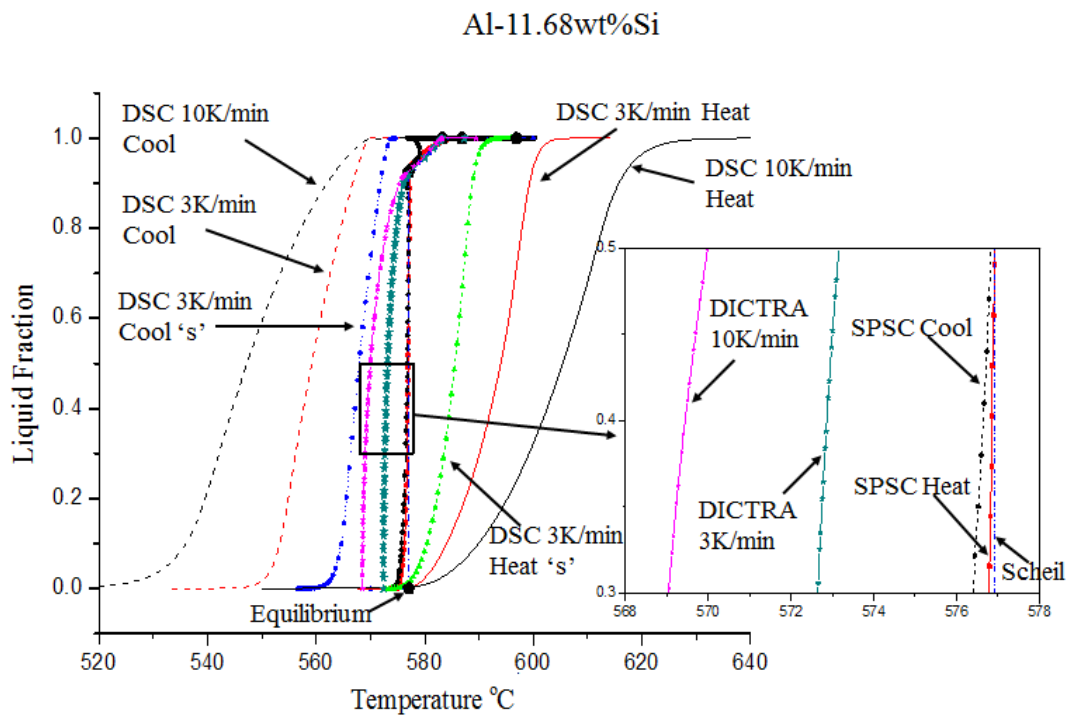


Fig. 5.65 Liquid fraction as a function of temperature from SPSC & DSC for Al-11.68wt%Si alloy, together with prediction curves. ('s' means small samples for DSC, i.e. the 20mg sample)

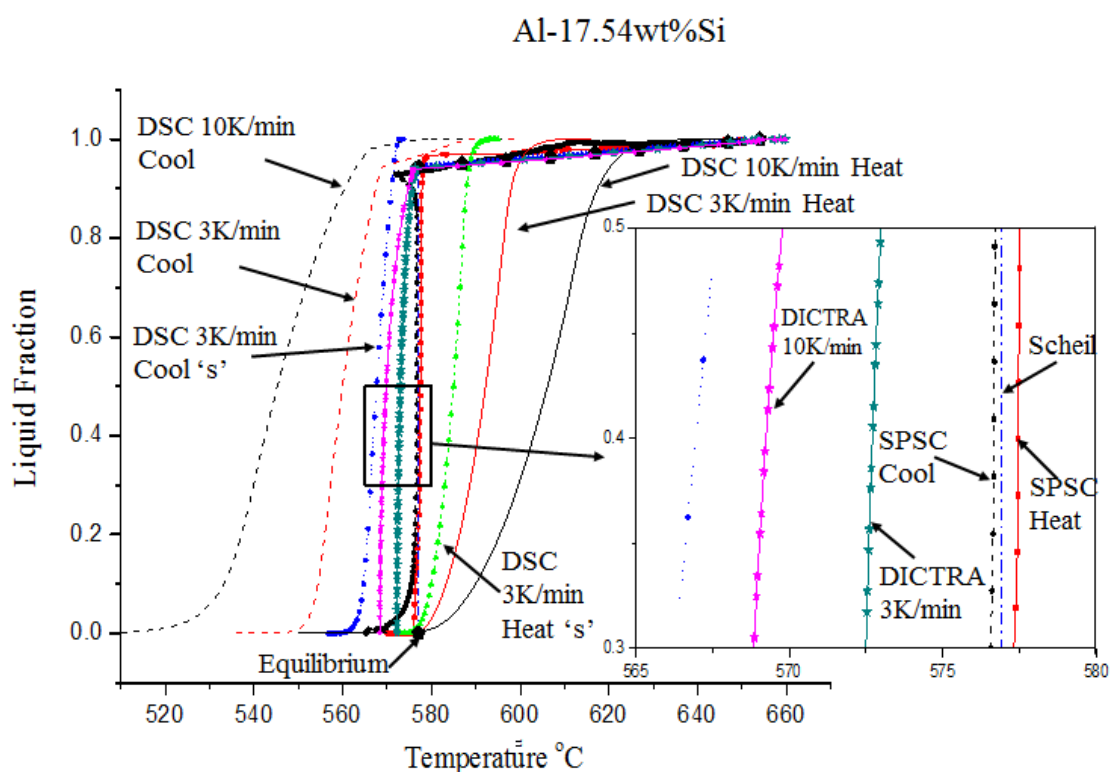


Fig. 5.66 Liquid fraction as a function of temperature from SPSC & DSC for Al-17.54wt%Si alloy, together with prediction curves. ('s' means small samples for DSC, i.e. the 20mg sample)

The influence of heating (cooling) rate on the DSC curves for alloys is shown by the fact that the processing window between the fraction liquid 30% and 50% is wider for 10K/min heating (cooling) rate than for 3K/min (i.e. the slope of the curve is steeper for 3K/min). The solidus temperatures for alloys on the DSC heating curves are the same for every alloy. For the Al-5.08wt%Si alloy, the knee (shown magnified in Fig. 5.64) at the eutectic point is smoother in the DSC 10K/min heating (cooling) rate curve than in the 3K/min. In addition, the knee on the DSC heating curves is associated with more liquid (~44%) than the DSC cooling (~38%), SPSC (~36%) and Scheil (~36%) curves.

Fig 5.67 to Fig 5.69 show the liquid fraction/temperature relationships calculated by DSC and SPSC data for Al-Cu series binary alloys together with the prediction curve. The same conclusions of the curve positions can be made for Al-Si alloys. As for Al-0.98wt% Cu alloy, the solidus temperatures of DSC heating are much higher than the prediction data, which is 547 °C. The reason is that the limited copper compositions are hard to detect, which can be found in Fig 5.32, Fig 5.35 and Fig5.38. For the alloy Al-4.9wt%Cu, as can be seen in Fig 5.69, the  $\text{Al}_2\text{Cu}$  phase reaction points have lower

liquid fraction than the Scheil condition. It is about 6% for DSC results and 11% liquid for Scheil.

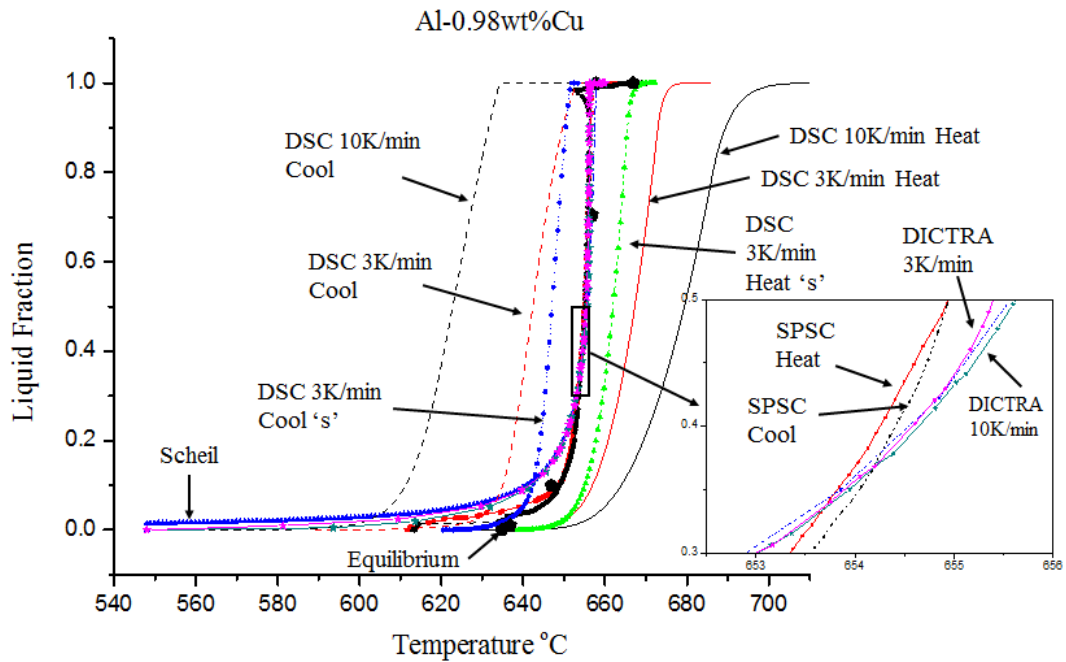


Fig. 5.67 Liquid fraction as a function of temperature from SPSC & DSC for Al-0.98wt%Cu alloy, together with prediction curves. ('s' means small samples for DSC, i.e. the 20mg sample)

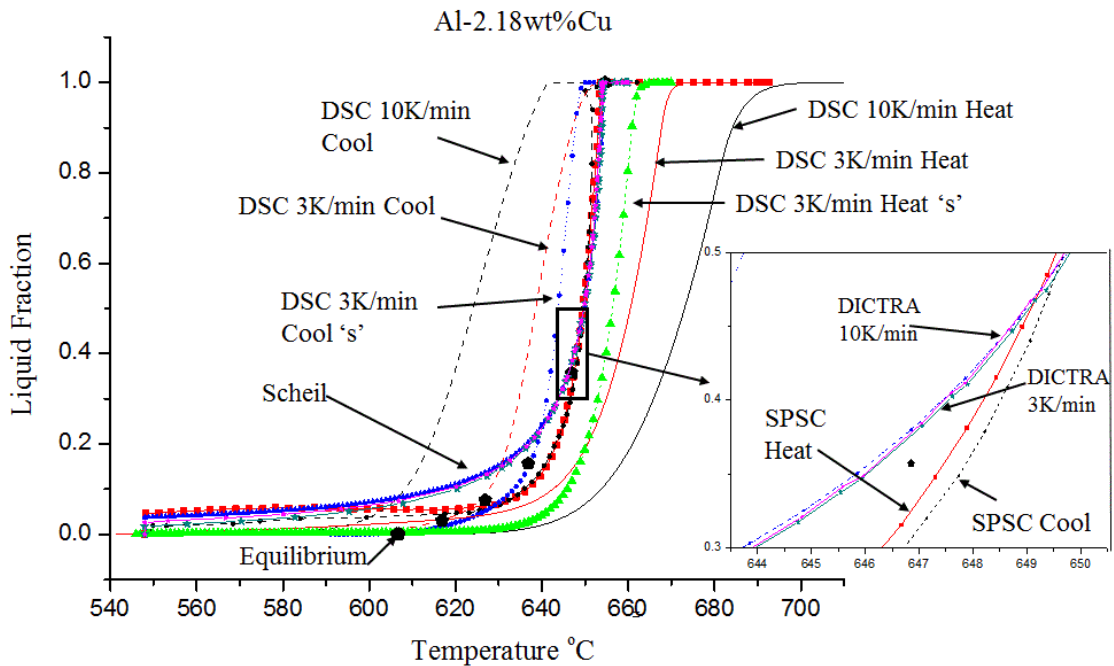


Fig. 5.68 Liquid fraction as a function of temperature from SPSC & DSC for Al-2.18wt%Cu alloy, together with prediction curves. ('s' means small samples for DSC, i.e. the 20mg sample)

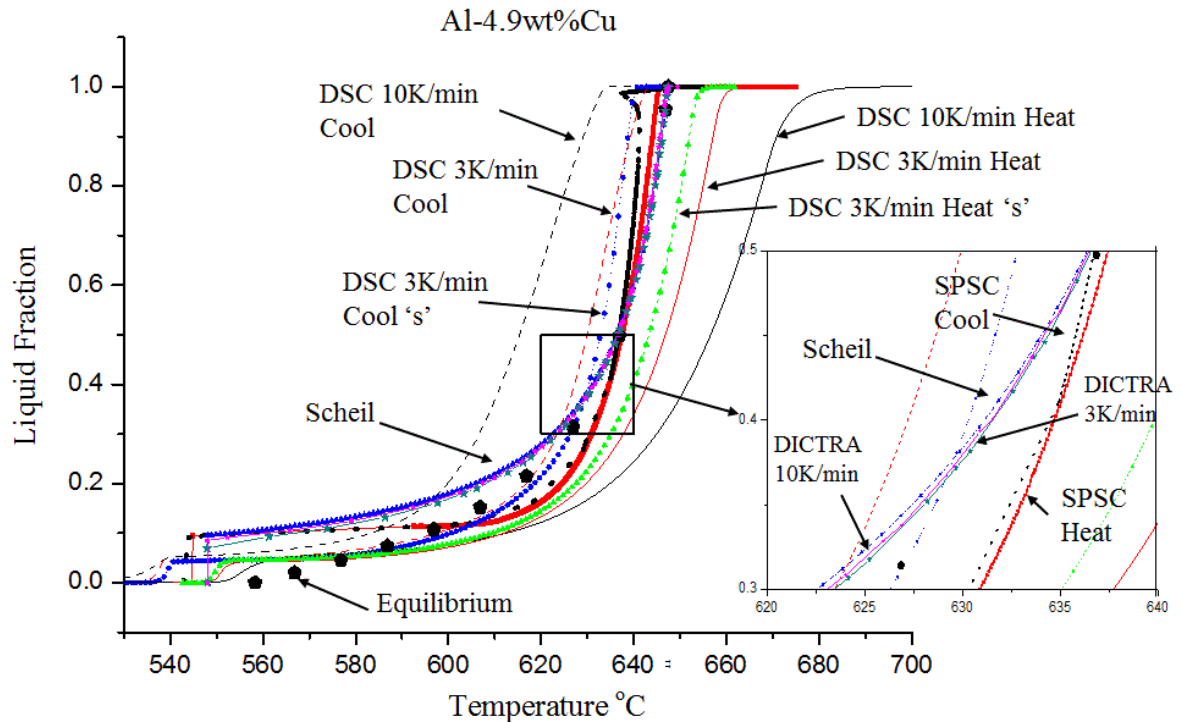


Fig. 5.69 Liquid fraction as a function of temperature from SPSC & DSC for Al-4.9wt%Cu alloy, together with prediction curves. ('s' means small samples for DSC, i.e. the 20mg sample)

Fig. 5.70 to Fig. 5.72 show the liquid fraction/temperature relationships calculated by DSC and SPSC data for Al-Mg series binary alloys together with the prediction curve. Again, the same trend of the curves positions as the Al-Si and Al-Cu alloys can be observed. As described in the Fig. 5.24, Fig. 5.27 and Fig. 5.30, the melting starting points for Al-2.82wt%Mg and Al-5.58wt%Mg are higher than 450 °C of the Scheil condition.

The general trend for the experimental curves in the upper part of the graphs is of the following order (from left hand side to right hand side): DSC 10K/min cooling → DSC 3K/min cooling → DSC 3K/min cooling (small sample) → SPSC cooling → SPSC heating → DSC 3K/min heating (small sample) → DSC 3K/min heating → DSC 10K/min heating. The prediction curves are close to the SPSC results.

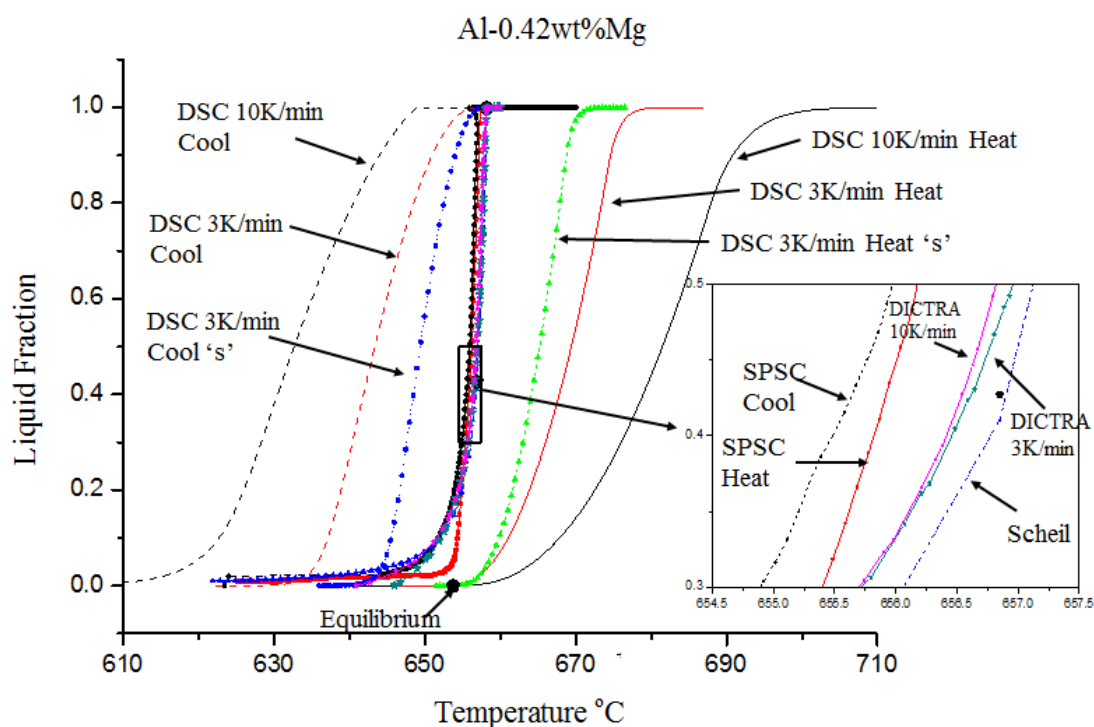


Fig. 5.70 Liquid fraction as a function of temperature from SPSC & DSC for Al-0.42wt%Mg alloy, together with prediction curves. ('s' means small samples for DSC, i.e. the 20mg sample)

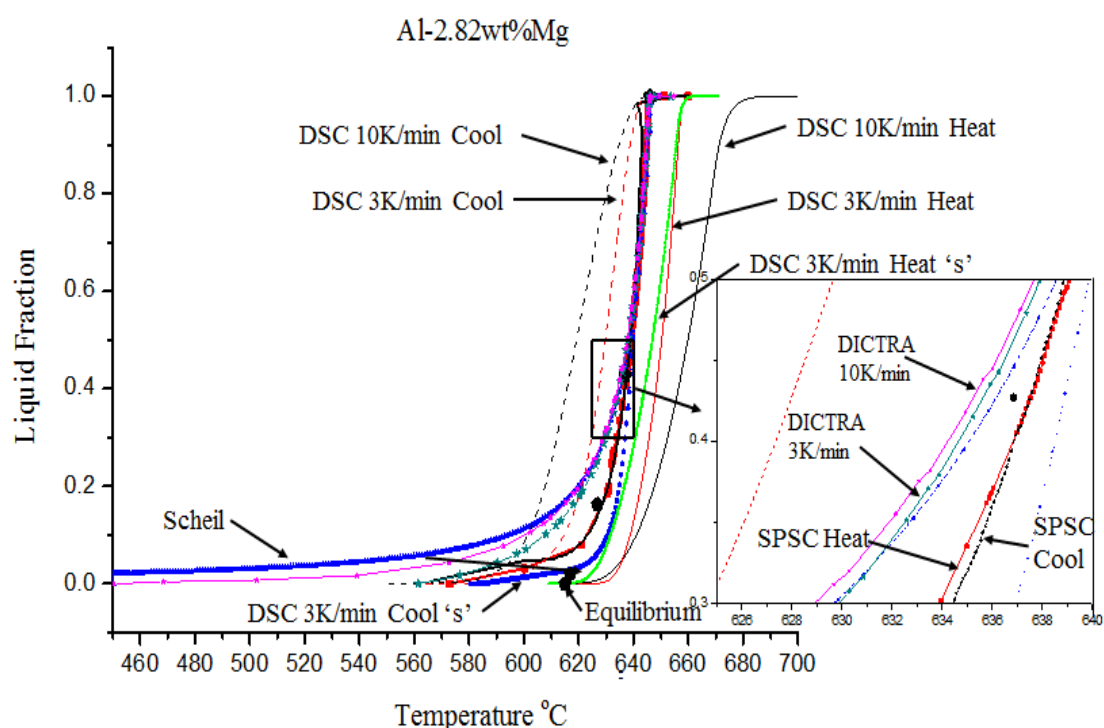


Fig. 5.71 Liquid fraction as a function of temperature from SPSC & DSC for Al-2.82wt%Mg alloy, together with prediction curves. ('s' means small samples for DSC, i.e. the 20mg sample)

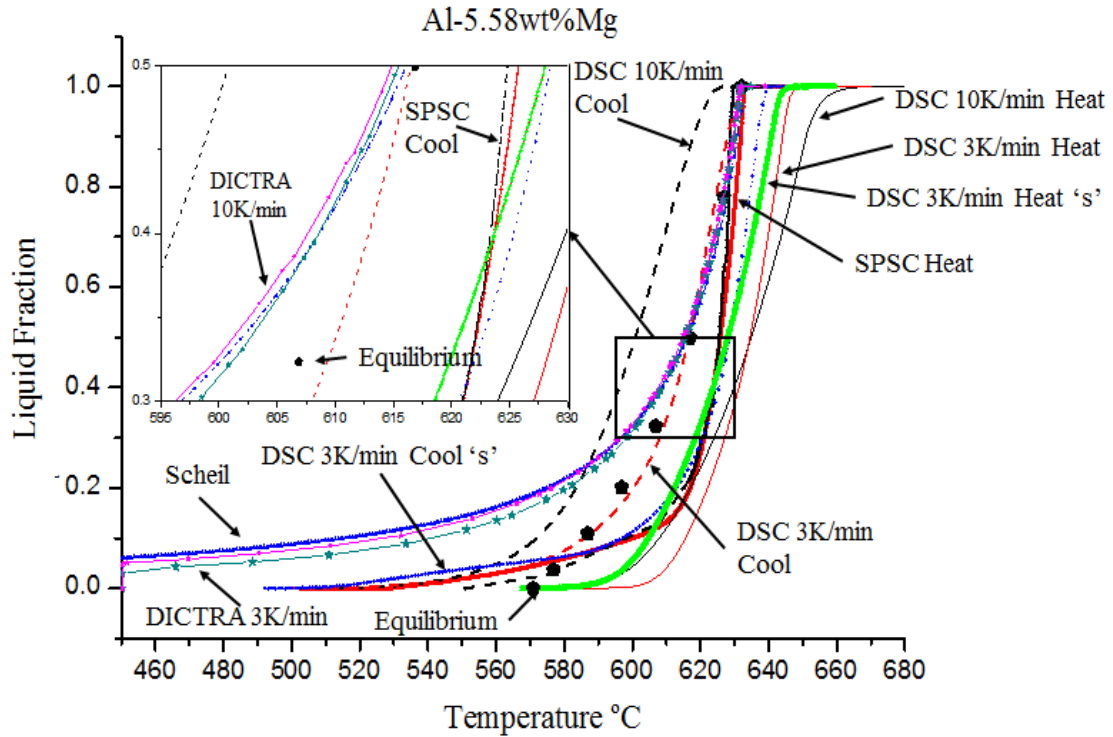


Fig. 5.72 Liquid fraction as a function of temperature from SPSC & DSC for Al-5.58wt%Mg alloy, together with prediction curves. ('s' means small samples for DSC, i.e. the 20mg sample)

## 5.7 Study of 319s Alloy

### 5.7.1 Determination of the Dissolution from DSC Traces

The results of DSC trace curves and calculated liquid fraction vs. temperature for 319s alloy are shown in Fig. 5.73. The second heating means the sample was heated from 30 °C just after the first cooling. As the sample was completely melted and then controlled by DSC constant cooling rate, it can be regarded as a slow solidification process. As seen, the melting curves show four temperature arrests but only three for the cooling curve. The peaks 1, 2 and 4 are correspondent with the following reactions (solidification) [31]:

Reactions

---

1. Liq.  $\rightarrow$   $\alpha$ -Al

---

2. Liq.  $\rightarrow$  Al +  $\text{Al}_{15}(\text{FeMn})_3\text{Si}_2$

---

Liq.  $\rightarrow$  Al + Si +  $\text{Al}_5\text{FeSi}$

---

4. Liq.  $\rightarrow$  Al +  $\text{Al}_2\text{Cu}$  + Si +  $\text{Al}_5\text{Mg}_8\text{Cu}_2\text{Si}_6$

---



Peak 3 was not reported in previous literatures. Thermodynamic calculations performed with the Thermo-Calc software show that this could be the  $\text{Al}_5\text{Mg}_8\text{Cu}_2\text{Si}_6$  phase. Gupta et al. [166] also suggested that the  $\text{Al}_5\text{Mg}_8\text{Cu}_2\text{Si}_6$  phase could be insoluble at solution temperatures as high as 530 °C in Al-Si-Cu-Mg alloys with relatively low silicon contents.

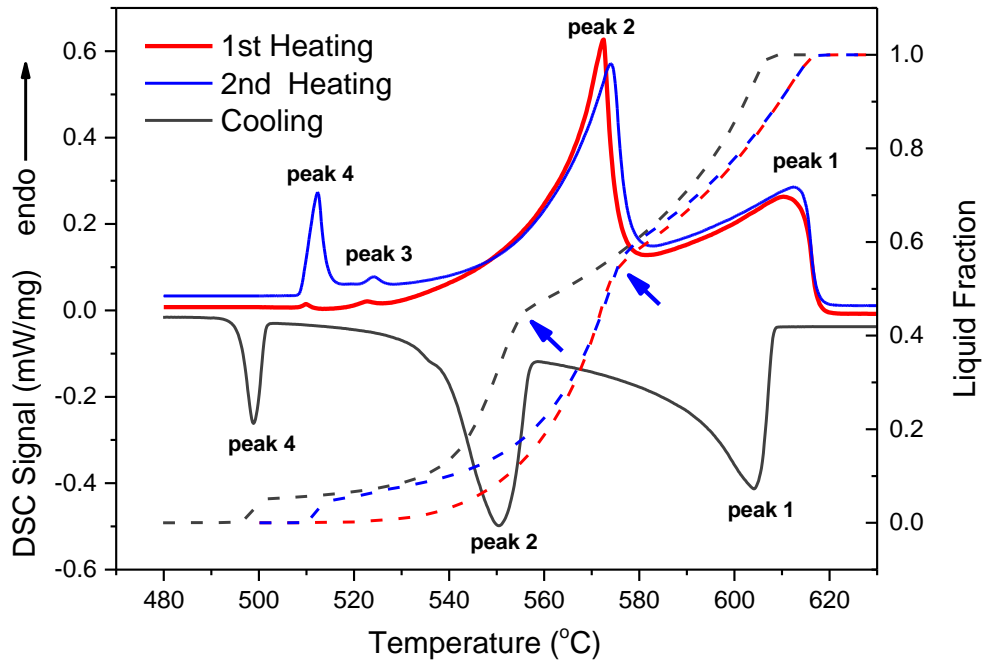


Fig. 5.73 Measured DSC signal range vs. temperature and calculated liquid fraction vs. temperature for 319s alloy with rate 3K/min (solid line is DSC curve and dash line is liquid fraction)

Undercooling leads to a temperature lag and as a consequence, all the critical temperatures of reactions are shifted to lower values. The parameters calculated from melting and cooling curves are summarised in Table 5.5. It is suggested that the  $\text{Al}_2\text{Cu}$  phase may undergo dissolution in the  $\alpha\text{-Al}$  matrix until the melting temperature of the  $\text{Al}_2\text{Cu}$  phase at 510 °C [35, 167]. It is clear that peak 4 increases on the 2<sup>nd</sup> heating curve comparing with the 1<sup>st</sup> heating curve. This is because in the initial structure (which is supplied in a state ready for semi-solid processing), the  $\alpha\text{-Al}$  phase is globular and all the  $\text{Al}_2\text{Cu}$  phases are distributed finely in the grain boundaries. After slow solidification, the  $\text{Al}_2\text{Cu}$  phase together with polynary eutectic phases forms a blocky-

like phase. The dissolution of  $\text{Al}_2\text{Cu}$  phase in a semi-solid structure is much easier than in a blocky structure.

The disappearance of peak 3 can also be seen on the cooling curve in Fig. 5.73. Each reaction needs a driving force, which is the undercooling for the solidification. The results indicate that the 3K/min cooling rate may create a large undercooling for the nucleation of small amount of the polynary eutectic phase.

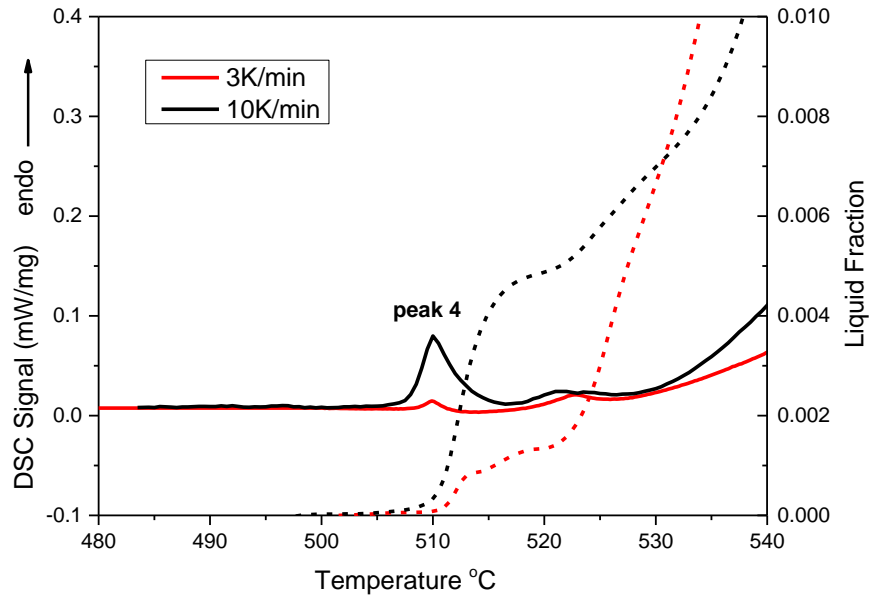
Reaction peak	Melting start	Melting end	Melting range	Solidification start	Solidification end	Solidification range
1	575.7	617.3	41.6	609.2	555.7	53.5
2	556.4	575.7	19.3	555.7	537.1	18.6
3	521.7	526.6	4.9	-	-	-
4	510.2	515.5 (1 <sup>st</sup> ) 511.8 (2 <sup>nd</sup> )	5.3 (1 <sup>st</sup> ) 1.6 (2 <sup>nd</sup> )	501.4	496.1	5.3

*Table 5.5 Temperatures ( °C) for reaction peaks calculated from DSC melting and cooling curves for 319s alloy*

As for the calculated liquid fraction versus temperature, it is obvious that the ‘knee’ (arrows in Fig. 5.73) for heating occurs at 9% more liquid fraction and 20 °C higher than for the cooling curve. Moreover, the fraction of the  $\text{Al}_2\text{Cu}$  phase and the polynary eutectic phases at low temperature was strongly impacted by the structure status of the sample. The importance of the sample conditions and DSC routes is clear. As in SSM processing, the sensitivity of liquid fraction between 30% and 50% is a key parameter [2], and DSC is commonly used as an analysis method, therefore the DSC results should be treated with care.

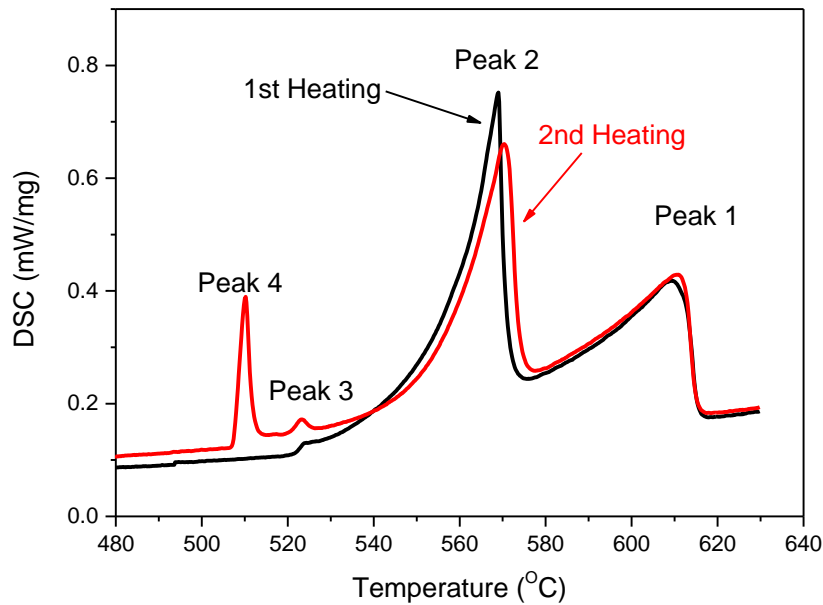
In consequence, the heating rate should be chosen carefully as the higher heating rate will lead to the peaks overlapping [142]. Ref [37, 168] suggested that the intermetallic phase (peak 3) could be dissolved during heating and the peak will be lowered with low heating rate (<10K/min). So a 10K/min heating rate was adopted and the peak was recorded in Fig. 5.74. Though the peak will increase with higher heating rate for the same sample [142], the calculated liquid fraction in Fig. 5.74 indicates that additional 0.4%  $\text{Al}_2\text{Cu}$  phases were observed under higher heating rate. It was in good agreement

with the dissolution of the  $\text{Al}_2\text{Cu}$  phase when pre-heating and will lower the DSC peak. However, overall the research [169] suggested that the 10K/min rate under DSC may offer less accuracy than 3K/min rate compared with the predicted results.



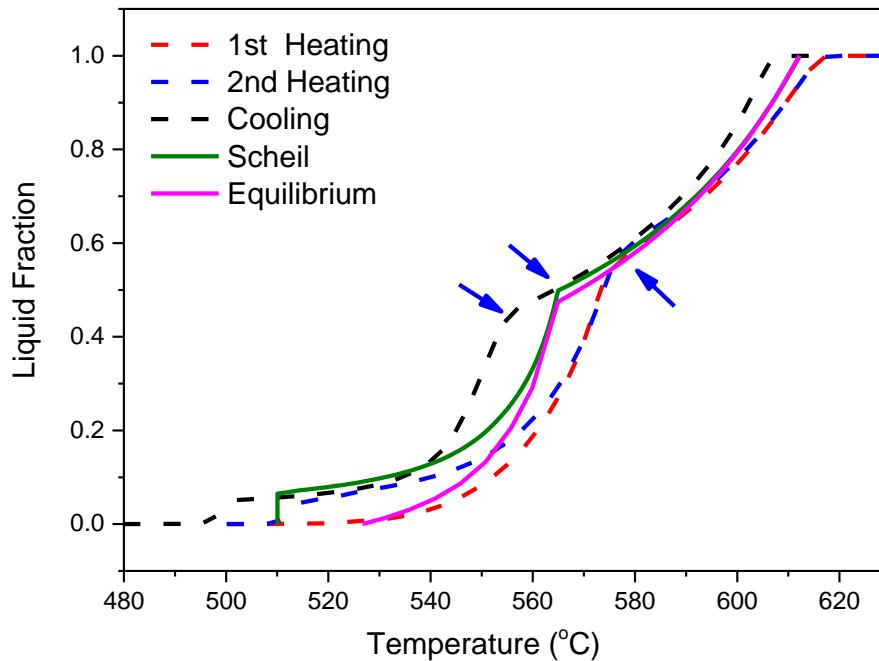
*Fig. 5.74: Measured DSC signal range vs. temperature and calculated liquid fraction vs. temperature for 319s alloy with heating rate 3K/min and 10K/min from semi-solid state (solid line is DSC curve and dash line is liquid fraction)*

Fig. 5.75 shows the DSC trace curves for 3K/min heating on the heat treated 319s alloy. It can be seen that there is no peak 4 on the 1<sup>st</sup> heating curve but a big one on the 2<sup>nd</sup> heating curve. It indicates that the copper phase has been more or less dissolved into the matrix after heat treatment. However, there is a small peak 4 on the 1<sup>st</sup> heating curve in Fig. 5.73 for the as-received 319s alloy, suggesting that the thixoformed alloy is nearly homogenised but not completely as the alloy was heat treated at 500 °C for 72 hours.



*Fig. 5.75 Measured DSC signal range vs. temperature for 319s alloy after heat treatment with heating rate 3K/min*

Fig. 5.76 compares the liquid fraction-temperature relationships from DSC for 319s alloy together with the prediction curves for equilibrium and Scheil condition. It can be seen that the DSC results lack agreement with the prediction results. The ‘knee’ on the prediction curves is between the cooling and heating curves. This is because the constant scan rate will result in an inaccurate reaction peak and calorimetry measurement should be under constant heat flux mode rather than constant scan rate. It is worth noticing that the 1<sup>st</sup> heating curve in Fig. 5.76 is close to the equilibrium curve at the solidus temperature. On the contrary, the 2<sup>nd</sup> heating and cooling are close to the Scheil curve. This indicates that the copper phases are more or less dissolved into the matrix homogeneously in the thixoformed status. The SSM processing can be regarded as a procedure for obtaining homogeneous structure for cast alloys.



*Fig. 5.76 Calculated liquid fraction vs. temperature from DSC (3K/min) for 319 alloy (~20mg), together with Scheil and lever rule calculations*

### 5.7.2 SPSC Analysis

Fig. 5.77 shows the SPSC trace for the alloy 319s in a relationship of sample temperature versus time. There are three inflection points on the heating and cooling processes respectively. As the SPSC uses the same heat flux mode, the inflection point indicates a reaction occurs. According to the temperature of the inflection points, the 1<sup>st</sup> one should be  $\text{Al}_2\text{Cu}$  phase, the 2<sup>nd</sup> one is the main eutectic reaction of  $\text{Al-Si}$  phase. The 3<sup>rd</sup> one should be the reaction of the  $\alpha\text{-Al}$  phase.

Fig. 5.78 shows the calculated liquid fraction as a function of temperature curves obtained from SPSC and prediction data. There are two inflection points on the Scheil curve. The one on the 50% liquid fraction represents  $\text{Liquid} \rightarrow \alpha\text{-Al} + \text{Si}$  and the other one on the 7% fraction liquid represents  $\text{Liquid} \rightarrow \alpha\text{Al} + \text{Si} + \text{Al}_2\text{Cu} + \text{Al}_5\text{Mg}_8\text{Cu}_2\text{Si}_6$ . The eutectic reaction on equilibrium condition contains less liquid than Scheil. However, there is only one inflection point on the equilibrium curve at the liquid fraction of 47%. The liquidus-solidus interval decreased from 140 °C in Scheil to 110 °C in equilibrium. The SPSC results are very close to the equilibrium curve. However, the measured Si

eutectic reaction from SPSC is higher than the predictions. In addition, the 'knee' is also higher than the predictions in terms of liquid fraction.

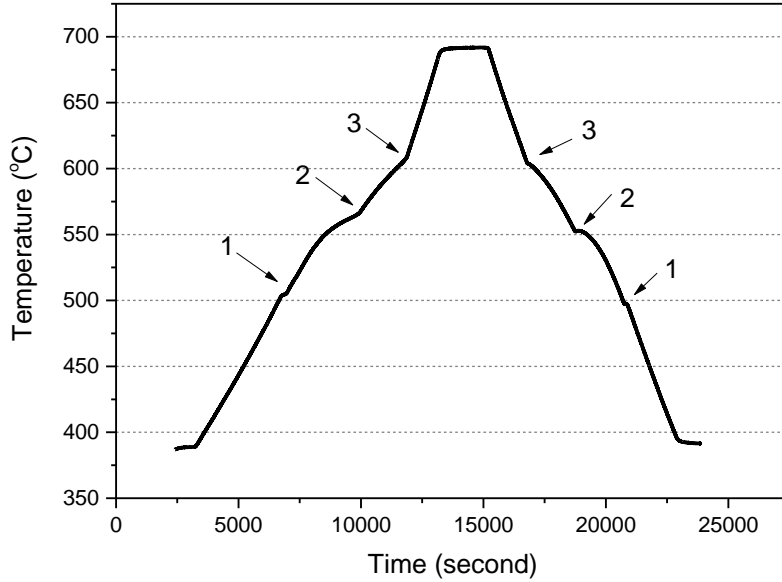


Fig. 5.77 The SPSC curves during heating and cooling in a relationship of sample temperature-time for 319s alloy (3K/min before any melting and solidification occurs)

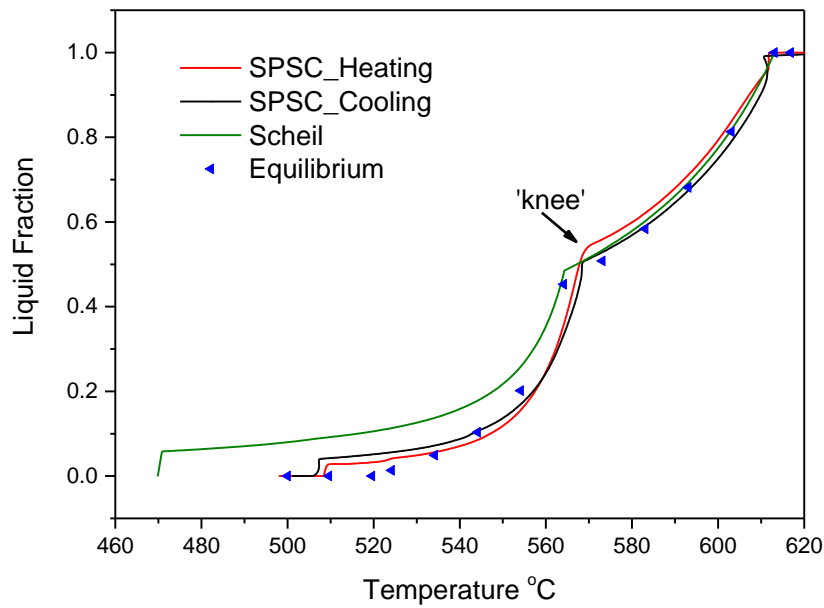


Fig. 5.78 Comparison of Liquid-Fraction as a function of temperature of SPSC for 319s alloy, together with prediction curve of Scheil mode and Equilibrium mode

### 5.7.3 XRD Analysis

The XRD results for 319s alloys with different statuses are illustrated from Fig. 5.79 to Fig. 5.81. The peaks marked red stands for the primary  $\alpha$ -Al phase, blue for Si phase and green for  $\text{Al}_2\text{Cu}$  phase. Other multi-component phases were not observed in the XRD test.

In general, the green peaks in the Fig. 5.80 are more obvious than the other two results. Though in XRD results, the position and counts for the peaks only suggest that a phase exists but not the evidence for phase fraction. It could be an indication that the  $\text{Al}_2\text{Cu}$  phase in the sample after DSC test could be easily observed by EDX. In other words, the  $\text{Al}_2\text{Cu}$  phase is becoming relatively larger after DSC test. In addition, the green peaks in Fig. 5.81 are extremely weak, which would be consistent with effective solutionising.

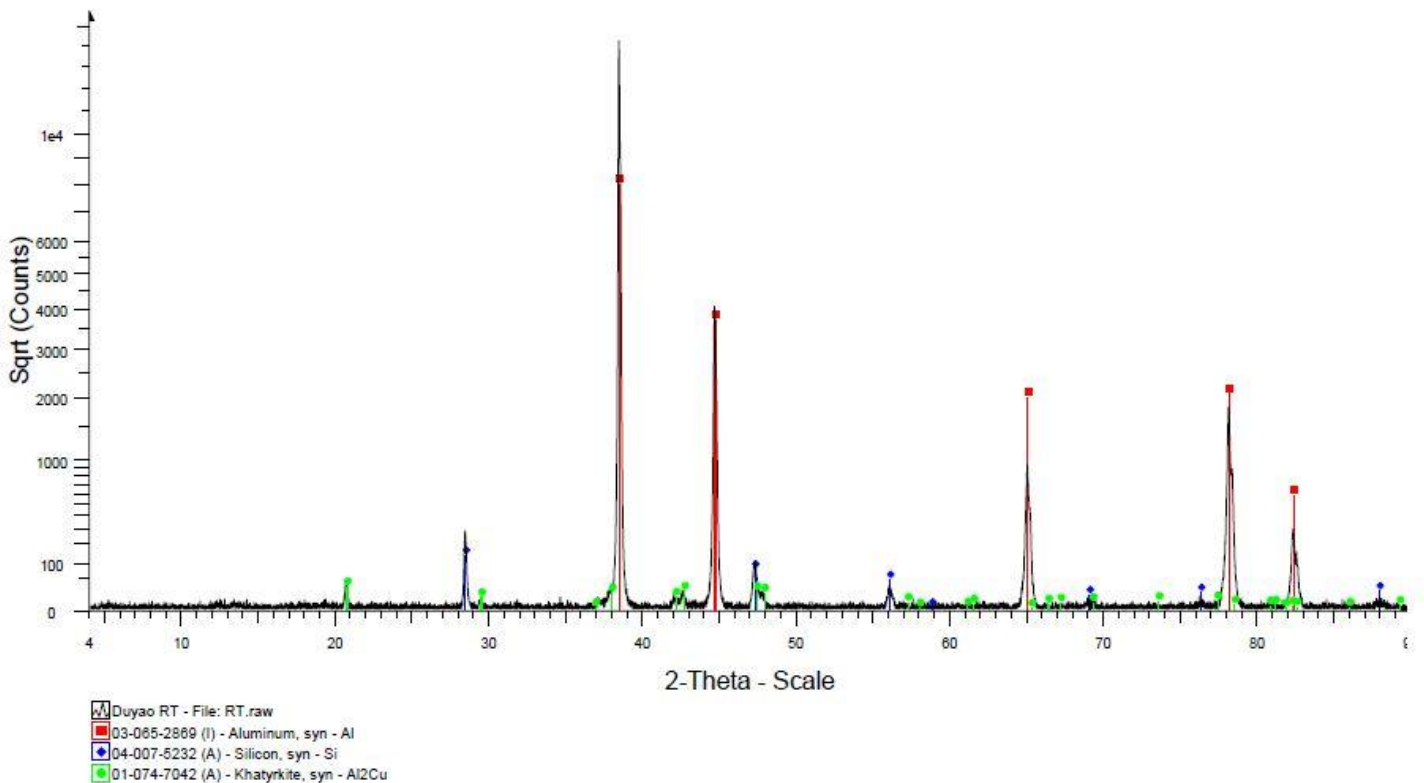


Fig. 5.79 XRD results for as received (Thixoformed) 319s alloy

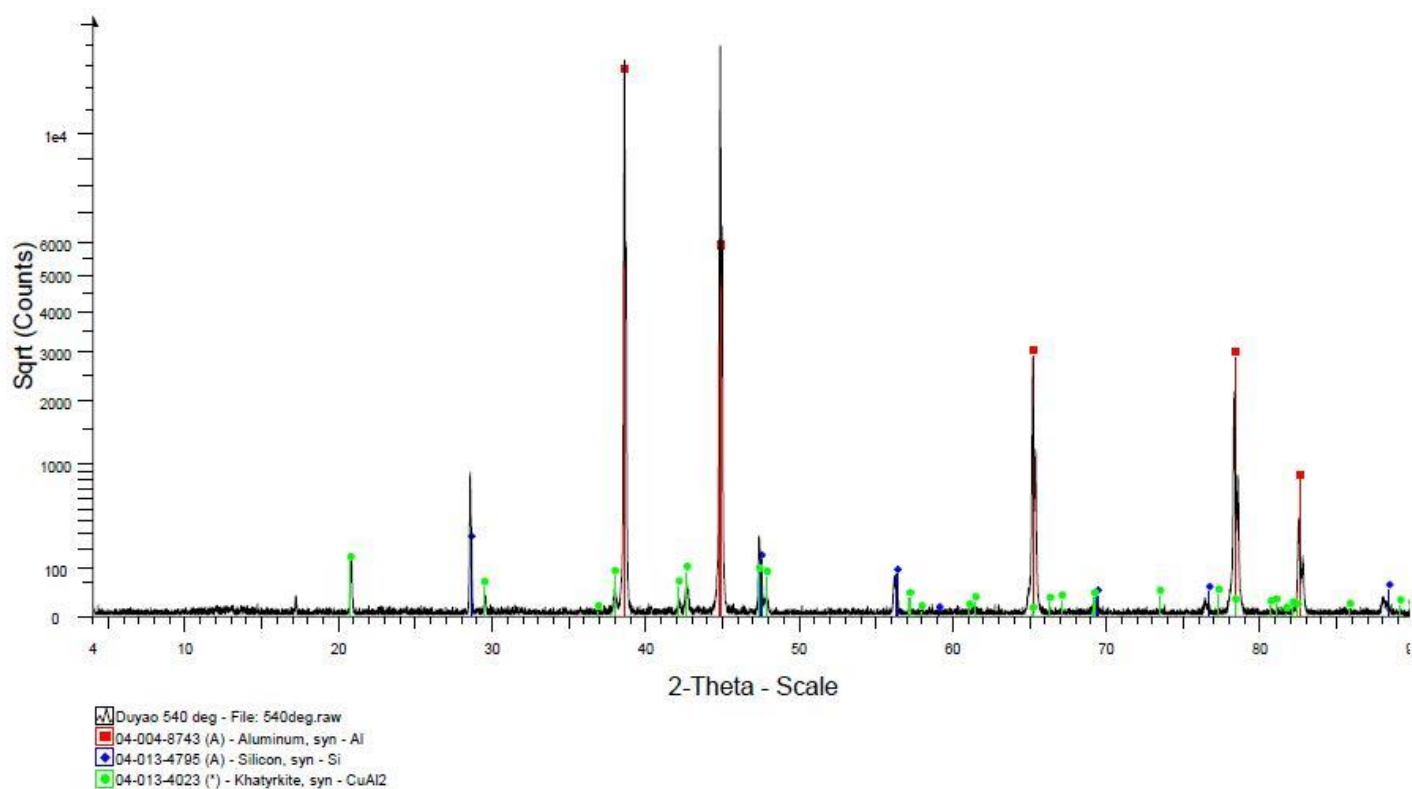


Fig. 5.80 XRD results for 319s alloy after DSC test

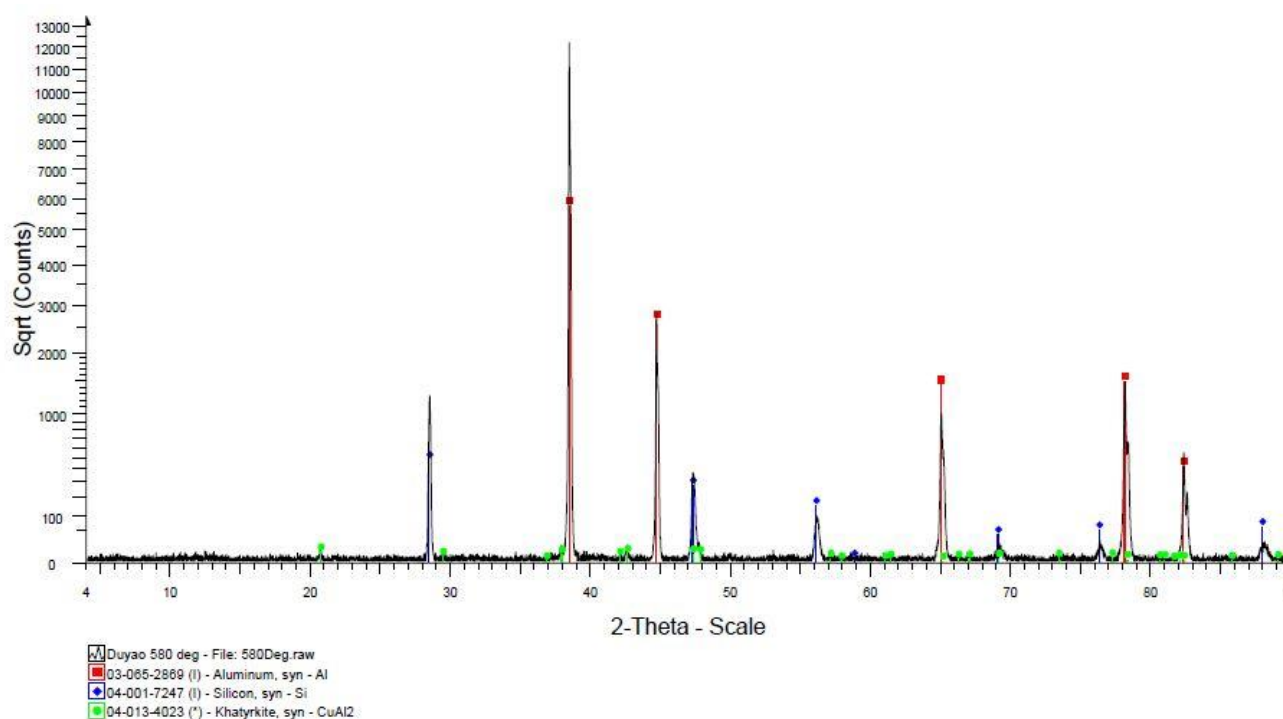
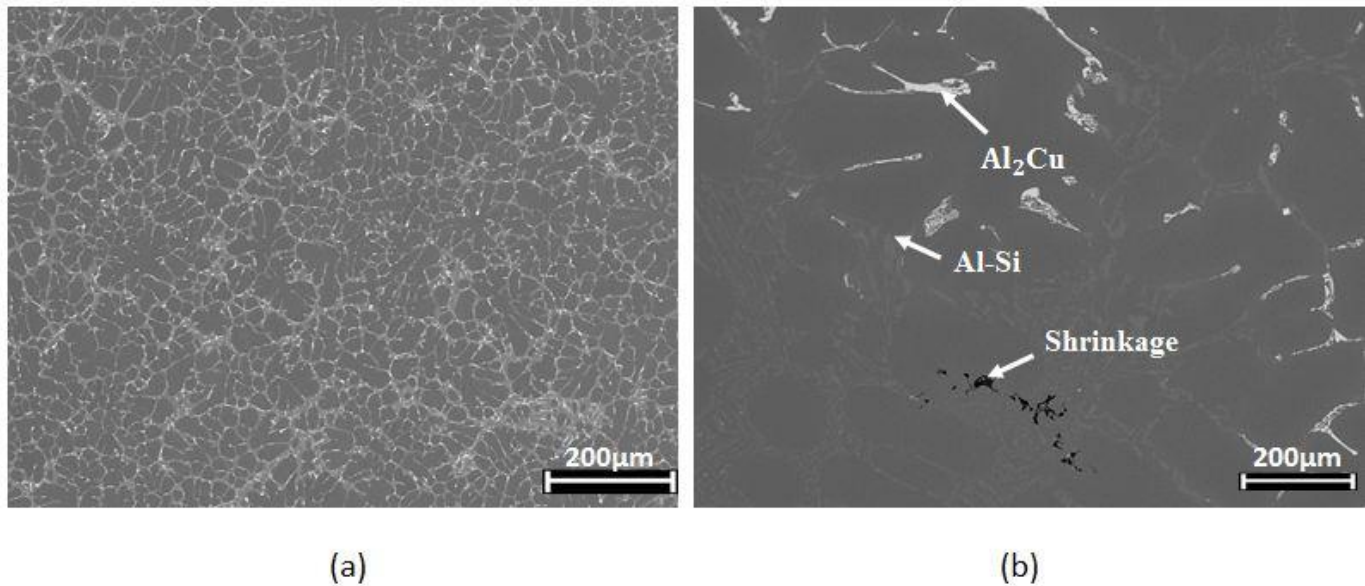


Fig. 5.81 XRD results for 319s alloy after heat treatment at 500 °C for 72 hours



#### 5.7.4 Microstructures

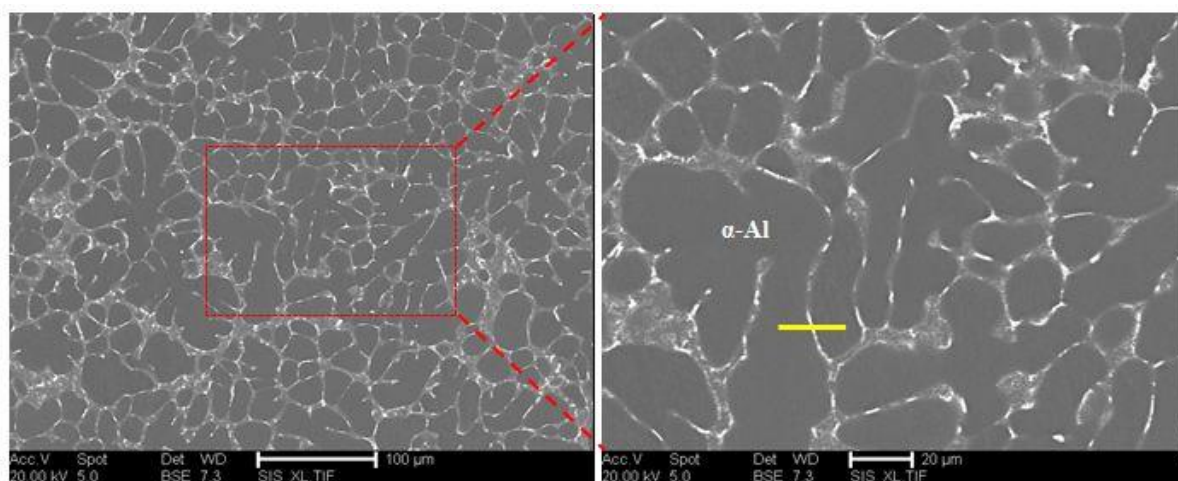
Microstructures for 319s alloys in thixoformed state and after DSC test are illustrated in Fig. 5.82. It can be seen that the fine and spheroidal microstructure becomes a microstructure with coarse and large secondary phases after DSC slow cooling. In addition, there are some shrinkages in the slow cooling microstructure. The Al-Si and Al<sub>2</sub>Cu phases are separated in Fig. 5.82(b).



*Fig. 5.82 SEM back scattered images of the 319s alloy: (a) as thixoformed, (b) after DSC test (3K/min with ~20mg sample)*

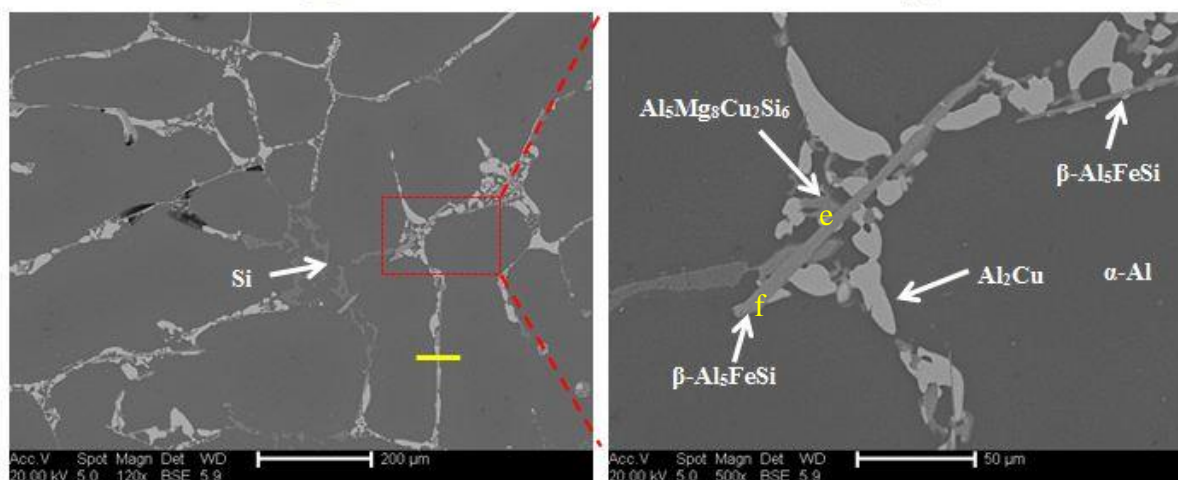
Microstructures and EDX analysis of a rich copper phase area of 319s alloy are shown in Fig. 5.83. Fig. 5.83(a, b) show the as-received thixoformed structure of 319s alloy, in which the aluminium matrix is globular. The silicon phase and copper phase are seen mainly as fine and evenly distributed in the grain boundaries, covering the aluminium globules. After the DSC test, i.e., slow solidification, the microstructure (copper-rich area) turns out to be a typical cast microstructure, shown in Fig. 5.83(c, d). Compared to Fig. 5.83(a) and (c), it is obvious that the copper phase is getting much coarser and block-like. A high magnification micrograph, Fig. 5.83(d), shows the details of the polynary phases in junction with Al<sub>2</sub>Cu phase. The needle shaped  $\beta$  phase and the Al<sub>5</sub>Mg<sub>8</sub>Cu<sub>2</sub>Si<sub>6</sub> are formed along with the Al<sub>2</sub>Cu phase. The intermetallics are identified in phase calculations (Thermo-Calc) and in ref [31, 34, 35]. However, those polynary phases are barely distinguished in the thixoformed microstructure. Relating to the DSC

heating curves, it is in good agreement with the changes in peak 4 in Fig. 5.73. Fine and evenly distributed  $\text{Al}_2\text{Cu}$  phase can be easily dissolved into the matrix. The results of EDX quantitative line analysis across a grain and grain boundaries are given in Fig. 5.83(g, h). It is obviously that the microsegregation in the SSM state is much weaker than that after slow solidification structure.



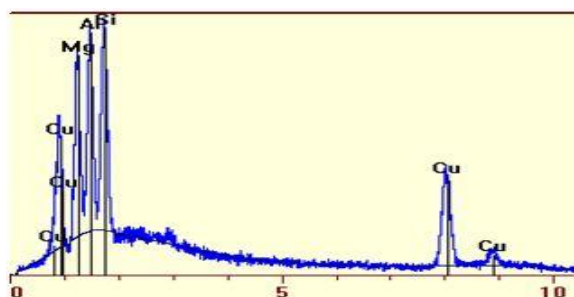
(a)

(b)

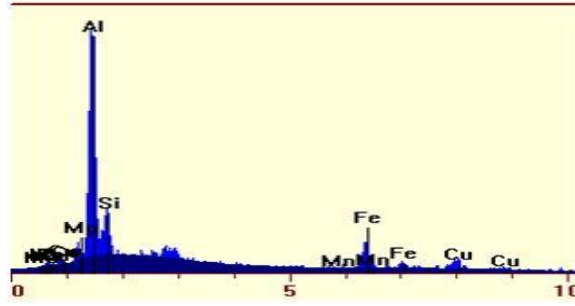


(c)

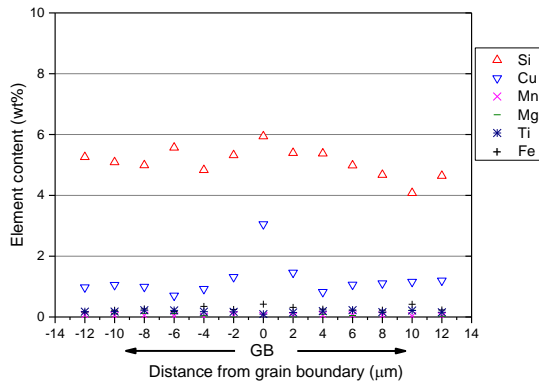
(d)



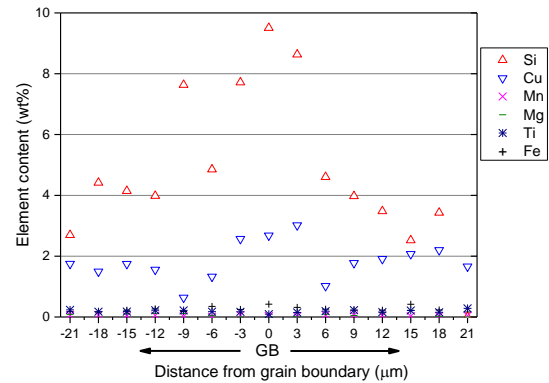
(e)



(f)



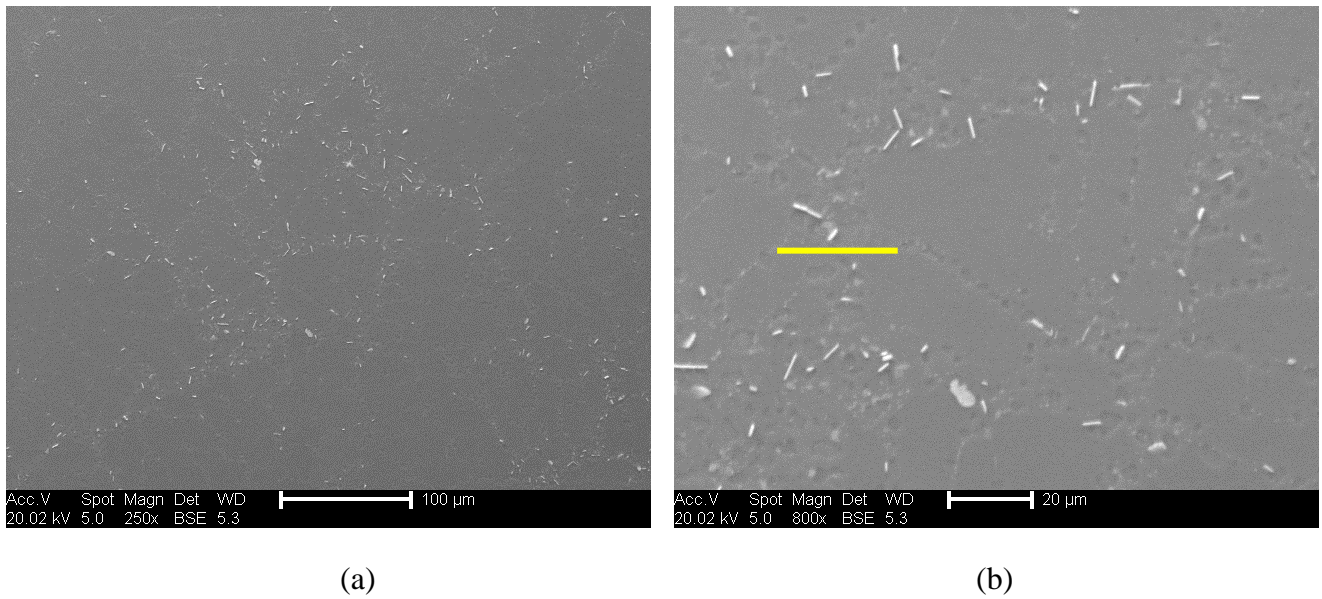
(g)



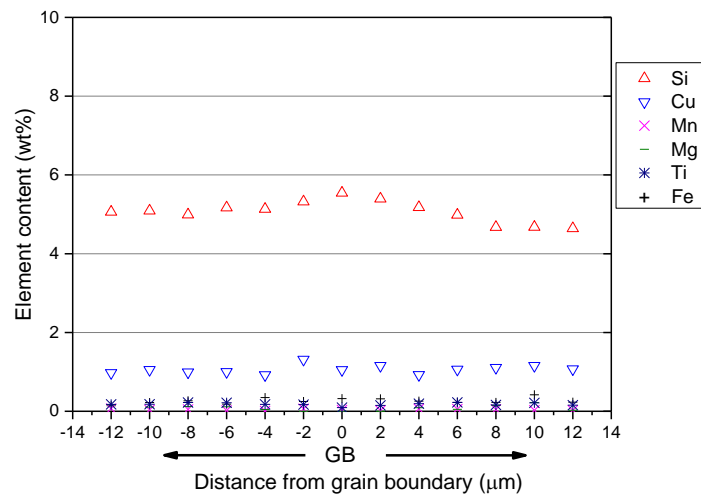
(h)

Fig. 5.83 Microstructures and EDX analysis of the 319s alloy: (a) as-received, (b) high magnification micrograph showing grain boundaries, (c) after DSC test (d) high magnification micrograph showing the intermetallic compounds, (e) EDX spectrum for  $Al_5Mg_8Cu_2Si_6$ , (f) EDX spectrum for  $\beta-Al_5FeSi$ , (g) line analysis across a grain boundary in (b), (h) line analysis across a grain boundary in (c)

Fig. 5.84 shows the microstructures in the 319s alloy after heat treatment. Compared to Fig. 5.83(a, b), it is clear that the bright phases present on boundaries have disappeared. Instead, there are few needle-like white copper particles and the average dendrite size of the matrix has not changed. Fig. 5.85 shows the results of EDX quantitative line analysis across a boundary labelled in Fig. 5.84(b). It can be seen that the distribution of alloying elements is more uniform than in the as-thixoformed alloy (in Fig. 5.83(g))



*Fig. 5.84 SEM back scattered electron image of the 319s alloy after heat treatment at 500 °C for 72hours, (b) high magnification micrograph showing grain boundaries*



*Fig. 5.85 line (marked as yellow) analysis results across a grain boundary in Fig. 5.84(b)*

The presence of multi-component phases was also investigated with TEM imaging. The sample is the as-thixoformed 319s alloy. Fig. 5.86 represents the  $\text{Al}_5\text{Mg}_8\text{Cu}_2\text{Si}_6$  particle. The particles are hexagonal and around 45nm in diameter. The electron diffraction patterns show that the  $\text{Al}_5\text{Mg}_8\text{Cu}_2\text{Si}_6$  particle belongs to be hexagonal crystal system. The measured interplanar spacing is 8.98 Å. In the ASM book [7], the lattice parameter

for the  $\text{Al}_5\text{Mg}_8\text{Cu}_2\text{Si}_6$  phase is  $a=10.32$  and  $b=4.05$ . The calculated interplanar spacing is  $8.94 \text{ \AA}$ .

A zigzag shape of the  $\text{Al}_8\text{Mg}_3\text{FeSi}_6$  particle was found by TEM as shown in Fig. 5.87. The measured interplanar spacings are  $4.06 \text{ \AA}$  and  $3.06 \text{ \AA}$ . It is in hexagonal type and the lattice parameter is  $a=6.63$ ,  $c=7.94$  [7]. The calculated interplanar spacing is  $5.74 \text{ \AA}$  (100),  $4.06 \text{ \AA}$  (110) and  $3.06 \text{ \AA}$  (11-1). The  $\text{Al}_8\text{Mg}_3\text{FeSi}_6$  phase was not predicted by Thermo-Calc, however in ref [34, 35], they indicated that adding magnesium to A319 alloy Al-Si alloys converts eutectic  $\text{Al}_2\text{Cu}$  and acicular  $\beta\text{-Al}_5\text{FeSi}$  phases to  $\text{Al}_5\text{Cu}_2\text{Mg}_8\text{Si}_6$  and Chinese script  $\text{Al}_8\text{Mg}_3\text{FeSi}_2$  phases, respectively.

Fig. 5.88 shows the TEM image of a small and round  $\text{Al}_2\text{Cu}$  phase adjacent to the  $\text{Al}_8\text{Mg}_3\text{FeSi}_2$  phase. The size is around 130nm in diameter.

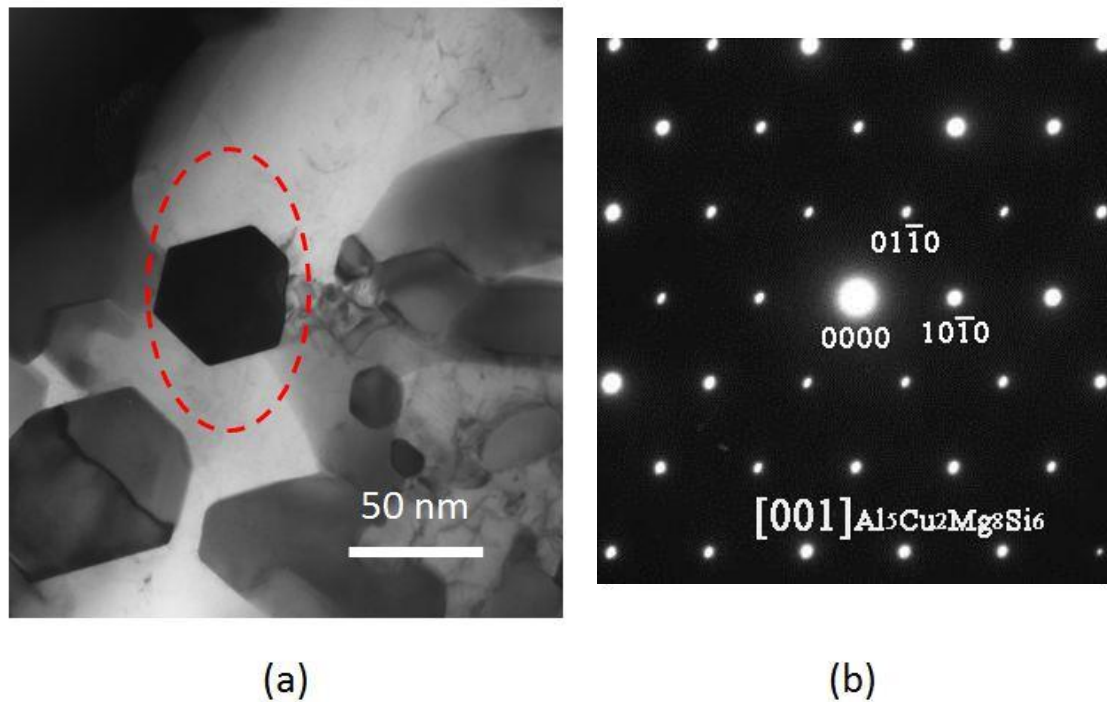
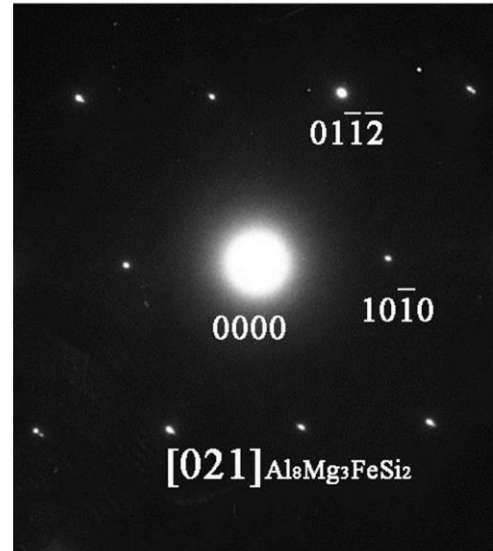


Fig. 5.86 (a) TEM image of the composites indicating the  $\text{Al}_5\text{Mg}_8\text{Cu}_2\text{Si}_6$  nanoparticles  
(b) the electron diffraction patterns for the  $\text{Al}_5\text{Mg}_8\text{Cu}_2\text{Si}_6$





(a)



(b)

Fig. 5.87 (a) TEM image of the composites indicating the  $\text{Al}_8\text{Mg}_3\text{FeSi}_2$  particle (b) the electron diffraction patterns for the  $\text{Al}_8\text{Mg}_3\text{FeSi}_2$  particle

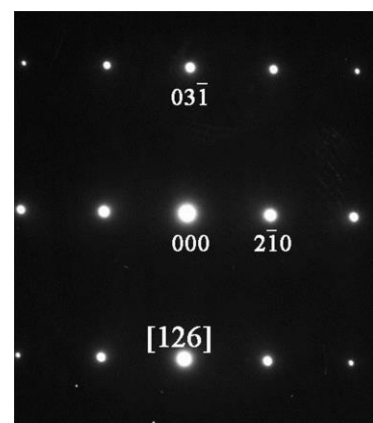
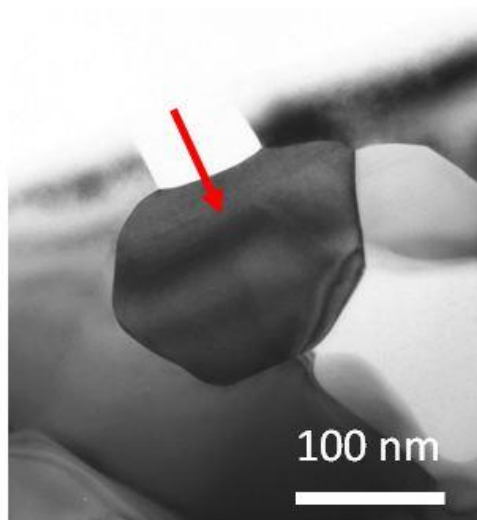


Fig. 5.88 TEM image of the composites indicating the  $\text{Al}_2\text{Cu}$  particle

## 5.8 Study of 201 Alloy

### 5.8.1 Determination of the Dissolution from DSC Traces

Fig. 5.89 shows the DSC trace curves and calculated liquid fraction vs. temperature for 201 alloy and the temperatures for the reactions are summarized in Table 5.6. The peak 1', 2', and 3' are correspondent to the following reactions (solidification) according to ref [31], respectively:

Reactions	Suggested Temperature ( °C)
1'. Liq. $\rightarrow$ $\alpha$ -Al	652
Liq. $\rightarrow$ Al + Al <sub>6</sub> (MnFeCu)	649
2'. Liq. + Al <sub>6</sub> (MnFeCu) $\rightarrow$ Al + Al <sub>20</sub> Mn <sub>3</sub> Cu <sub>2</sub>	617
3'. Liq. $\rightarrow$ Al + Al <sub>2</sub> Cu + Al <sub>20</sub> Mn <sub>3</sub> Cu <sub>2</sub> + Al <sub>7</sub> FeCu <sub>2</sub>	525

It is clear that the peak 3' is increased on the 2nd heating curve indicating the same dissolution phenomenon as with the Al<sub>2</sub>Cu phase with 319s alloy. The peak 3' is weaker on 1<sup>st</sup> heating than the 2<sup>nd</sup> heating. The calculated liquid fraction as a function of temperature shows a slight difference between 30% to 50% liquid fraction regardless of the undercooling thermo-lag. However, it is obvious that there is a 5% liquid fraction difference at the solidus temperature for the 1<sup>st</sup> heating curve due to the differences from reaction 3'. That means at most 5% copper phases have been dissolved in the matrix in the thixoformed structure.

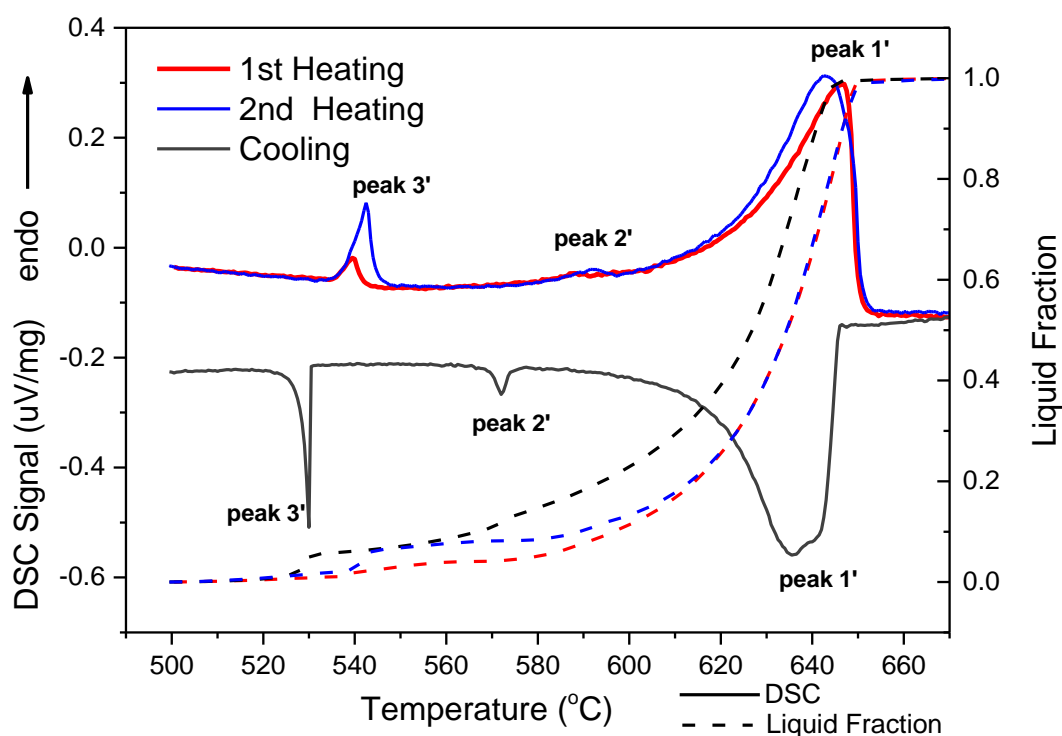


Fig. 5.89 Measured DSC signal range vs. temperature and calculated liquid fraction vs. temperature for 201 alloy with rate 3K/min

Reactions peak	Melting start	Melting end	Melting range	Solidification start	Solidification end	Solidification range
1'	616.5	652.6	36.1	645.4	617.6	27.8
2'	585.6	597.1	11.5	574.6	569.4	5.2
3'	536.0 (1 <sup>st</sup> ) 536.0 (2 <sup>nd</sup> )	542.2 (1 <sup>st</sup> ) 545.4 (2 <sup>nd</sup> )	6.2 (1 <sup>st</sup> ) 8.7 (2 <sup>nd</sup> )	530.6	527.4	3.2

Table 5.6 Temperatures ( °C) for reaction peaks calculated from DSC melting and cooling curves for 201 alloy

Fig. 5.90 shows the DSC trace curves for 3K/min heating on heat treated 201 alloy. It can be seen that the peak 3' on the 1<sup>st</sup> heating curve is weak (similar to the peak in Fig. 5.89). Unlike the disappeared Al<sub>2</sub>Cu phase peak of 319s alloy in Fig. 5.75, the copper phase reaction can still be observed with DSC after heat treatment for 201 alloy.



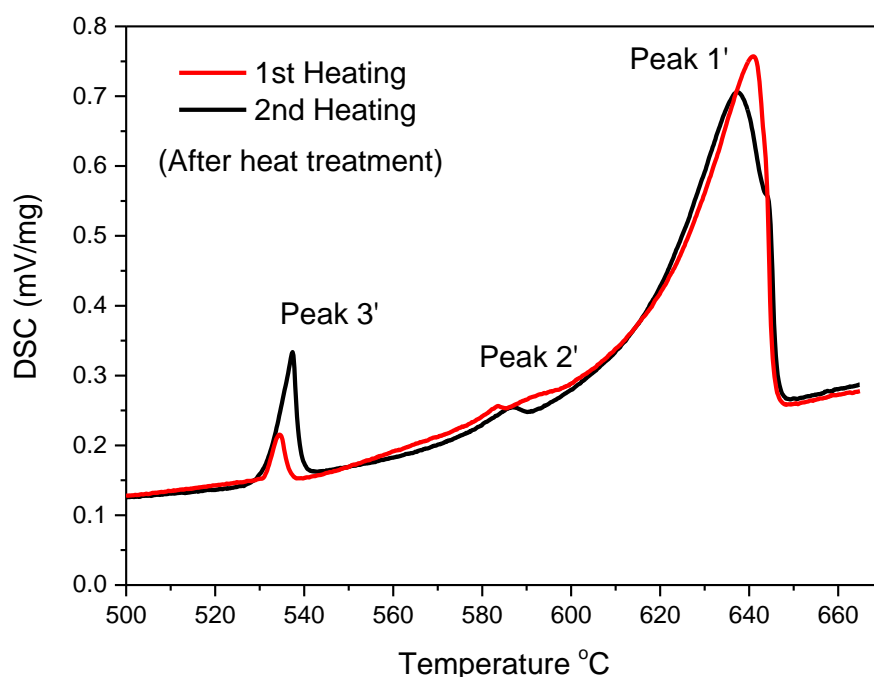
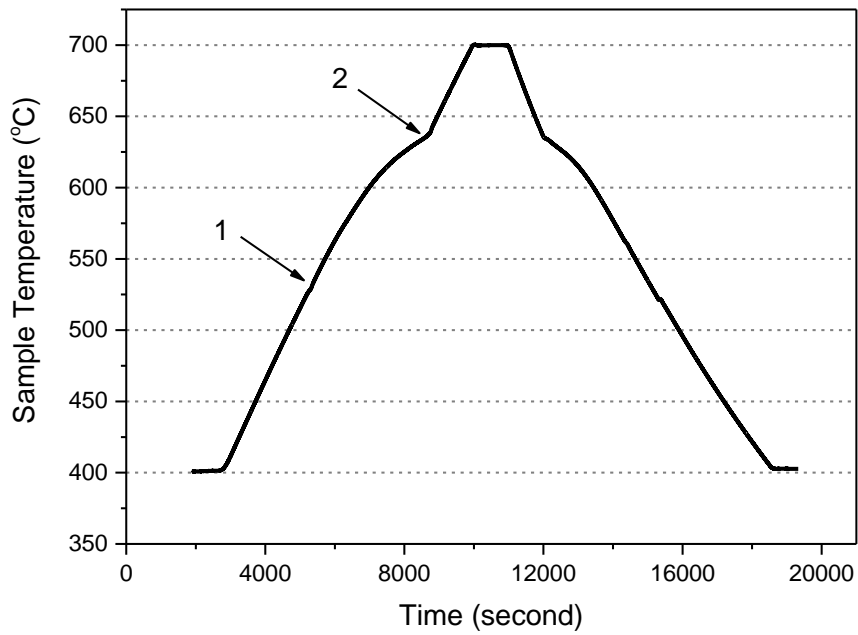


*Fig. 5.90 Measured DSC signal range vs. temperature for 201 alloy after heat treatment with heating rate 3K/min*

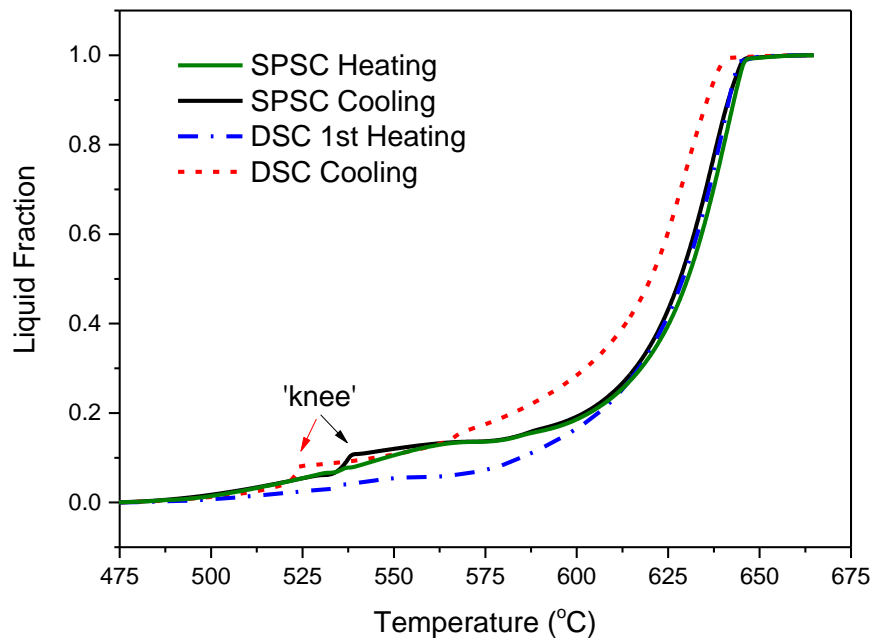
### 5.8.2 SPSC Analysis

Fig. 5.91 shows the SPSC trace for the alloy 201 as sample temperature vs time. There are two inflection points on the heating and cooling process respectively. According to the temperature of the inflection points, the 1<sup>st</sup> one is the melting beginning point which is the reaction of the  $\text{Al}_2\text{Cu}$  phase. The 2<sup>nd</sup> one is the end of the primary  $\alpha\text{-Al}$  phase reaction. However, there is no clear demarcation point between  $\alpha\text{-Al}$  and  $\text{Al}_2\text{Cu}$  reactions.

Fig. 5.92 shows the calculated liquid fraction from SPSC data for the 201 alloy at heating/cooling rate of 3K/min. It can be seen that there is an  $\text{Al}_2\text{Cu}$  phase reaction peak at about 535 °C on cooling curve. However, the heating curve is smooth at 560 °C. The two curves are very close above 570 °C. Compared to the liquid fraction calculated by DSC results, the SPSC data show good agreement with the 1<sup>st</sup> heating curve when the liquid fraction is higher than 20%. However, the ‘knee’ ( $\text{Al}_2\text{Cu}$  eutectic phase) on SPSC cooling curve has higher temperature than for the DSC cooling curve.



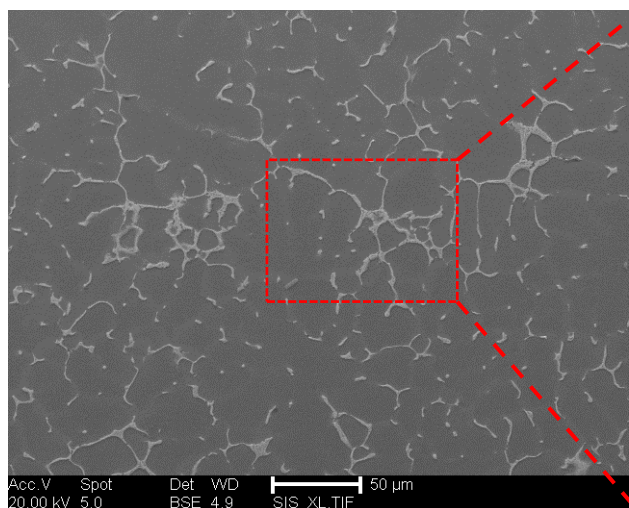
*Fig. 5.91 The SPSC curves during heating and cooling in a relationship of sample temperature-time for 201 alloy (3K/min before any melting and solidification occurs)*



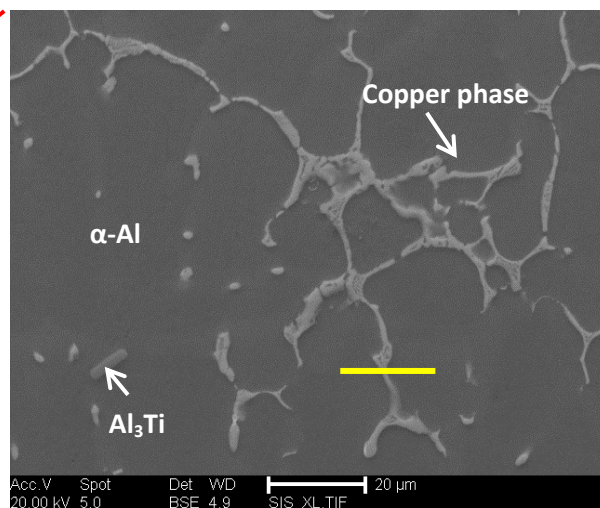
*Fig. 5.92 Calculated liquid fraction as a function of temperature from SPSC (3K/min, ~2.1g mass) and DSC (3K/min, ~20mg mass) for 201 alloy*

### 5.8.3 Microstructures

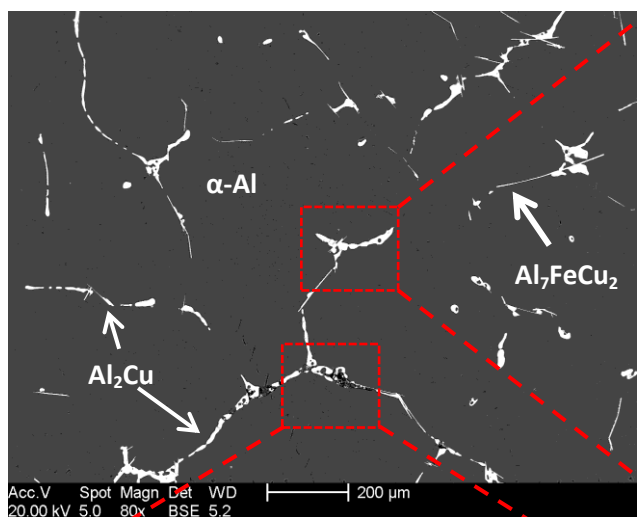
Similar to the 319s alloy, the microstructure of 201 alloy after the DSC test shows expected coarse copper phases and stronger microsegregation (Fig. 5.93). It can be readily seen in Fig. 5.93 (d, e) that the intermetallic compounds ( $\text{Al}_{20}\text{Mn}_3\text{Cu}_2$  and  $\text{Al}_7\text{FeCu}_2$ ) grow closely associated with  $\text{Al}_2\text{Cu}$  phase, which relates to the increased peak 3' on the 2nd heating curve (Fig. 5.89). The acicular  $\text{Al}_7\text{FeCu}_2$  phase in Fig. 5.93 (c, d) is clearly observed along the  $\text{Al}_2\text{Cu}$  phase. The black and round  $\text{Al}_{20}\text{Mn}_3\text{Cu}_2$  phases are surrounded by the secondary copper phases. These two intermetallic phases were identified in ref [31] and in phase calculations (Thermo-Calc), also confirmed by the EDX quantitative analysis in Fig. 5.93 (f, g). Two line analyses across the grain boundaries were shown in Fig. 5.93 (i, j) respectively. The content of Cu increases in the region of the boundary due to the intermetallic phases associated with it. The average Cu content in as-thixoformed is lower than for the slowly cooled 201 alloy. This result shows that most Cu concentrates at globule boundaries in thixoformed 201 alloy, forming a coarse eutectic phase.



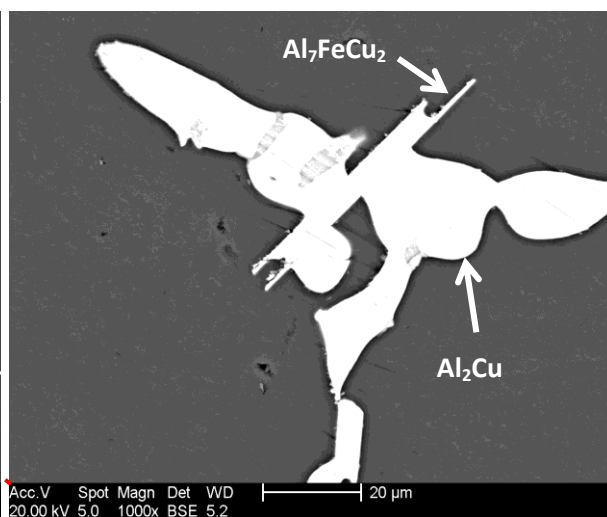
(a)



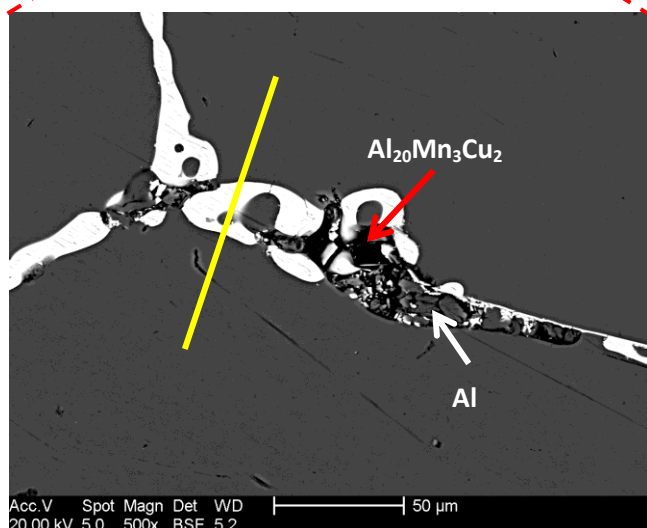
(b)



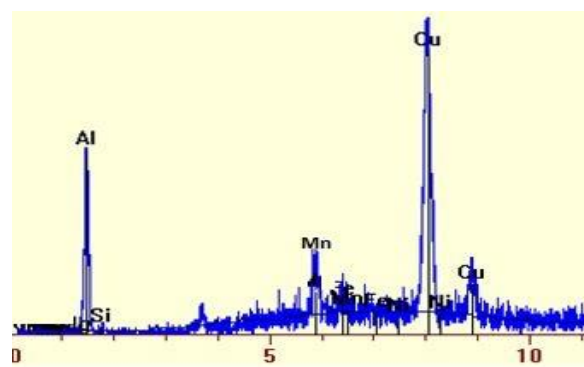
(c)



(d)



(e)



(f)

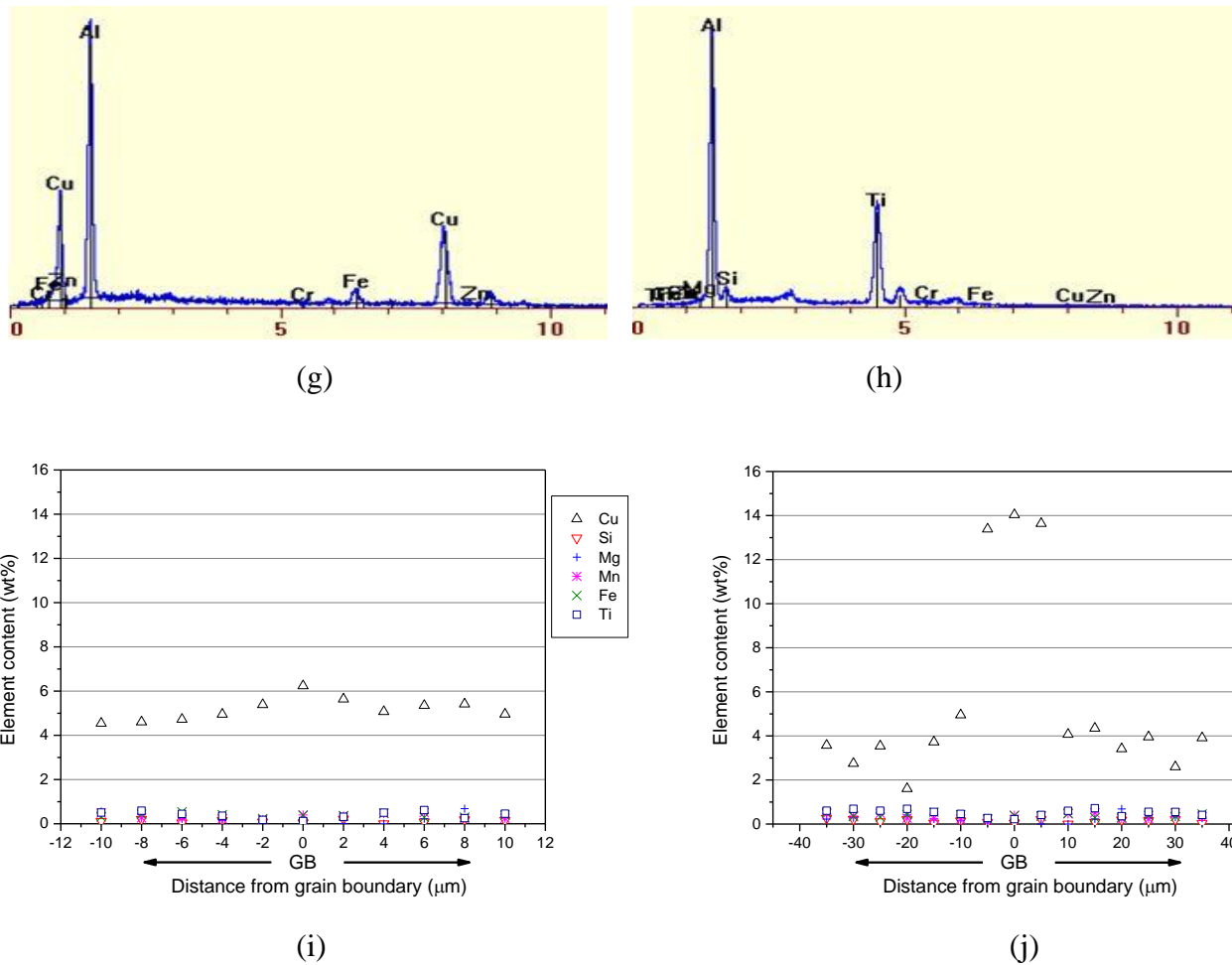
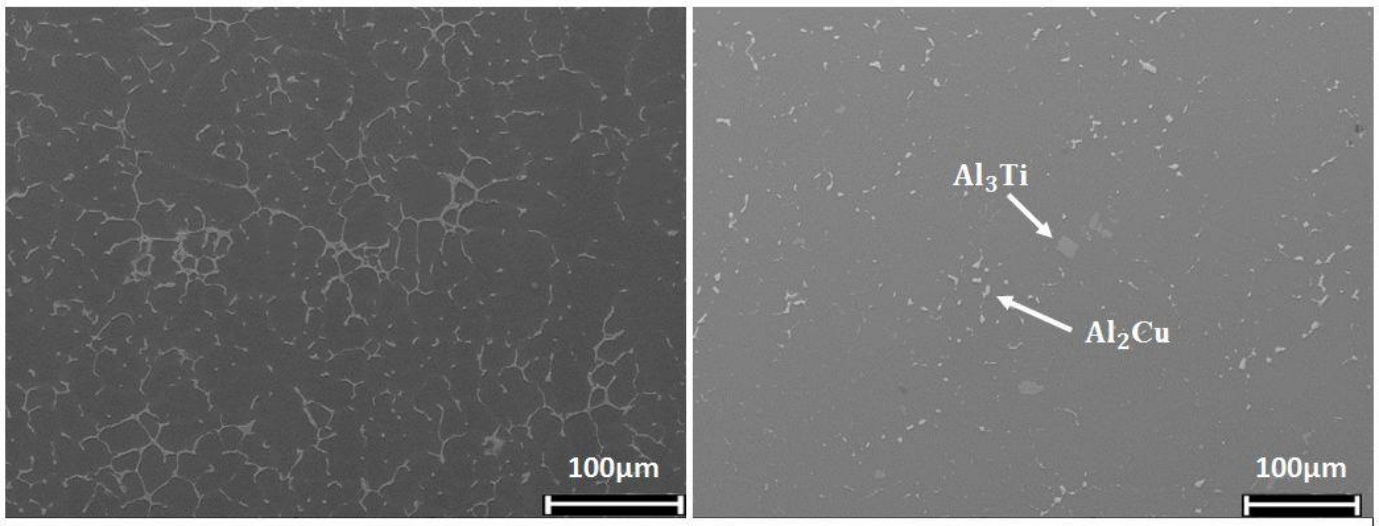


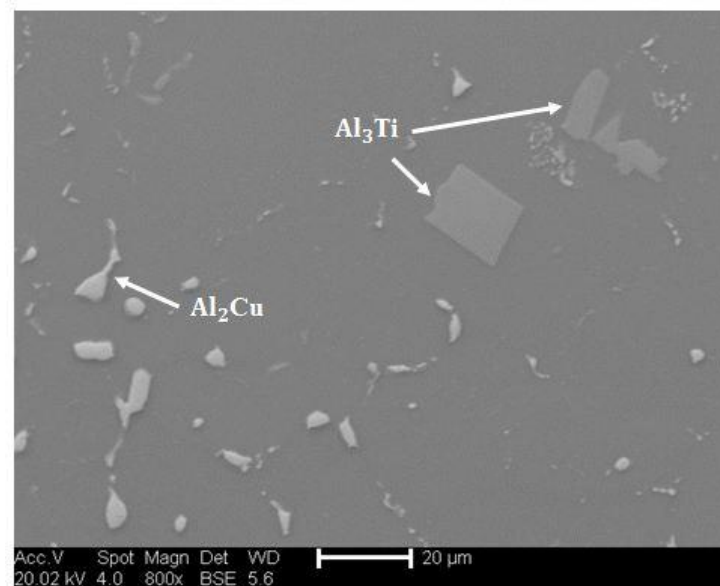
Fig. 5.93 Microstructures and EDX analysis of the 201 alloy: (a) as-received, (b) high magnification micrograph showing grain boundaries and  $\text{Al}_3\text{Ti}$  particles, (c) after DSC test (d) high magnification micrograph showing the  $\text{Al}_7\text{FeCu}_2$  particle, (e) high magnification micrograph showing the  $\text{Al}_{20}\text{Mn}_3\text{Cu}_2$  particle, (f) EDX spectrum for  $\text{Al}_{20}\text{Mn}_3\text{Cu}_2$  phase (g) EDX spectrum for  $\text{Al}_7\text{FeCu}_2$  phase, (h) EDX spectrum for  $\text{Al}_3\text{Ti}$  phase, (i) line analysis across a grain boundary in (b), (j) line analysis across a grain boundary in (e)

Fig. 5.94 is a general view of the microstructure of 201 alloy after 72 hours solution treatment at  $500^\circ\text{C}$ , revealing the almost complete dissolution of the  $\text{Al}_2\text{Cu}$  phase, although a few particles are still observed in the matrix. At the same time, it is also worth noting that, during the process of dissolution, the  $\text{Al}_3\text{Ti}$  particles are still block-like.



(a)

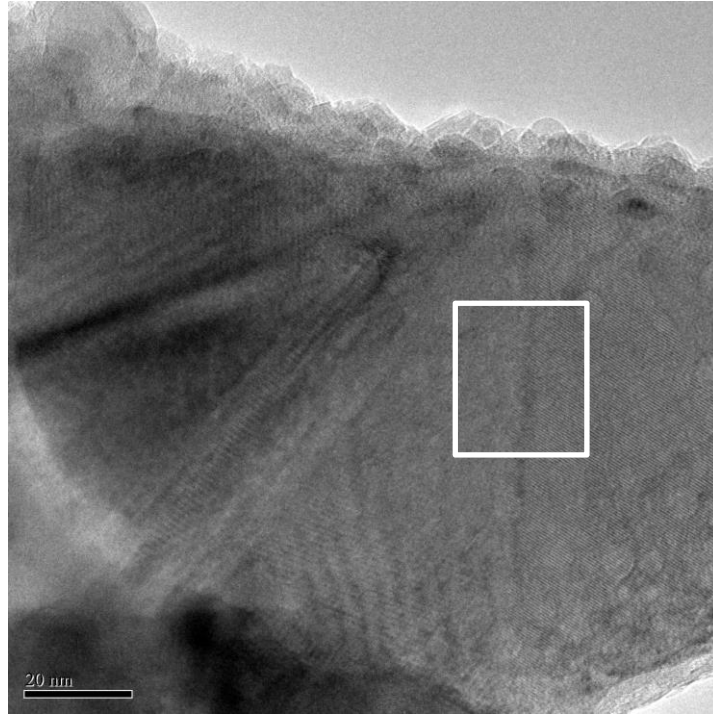
(b)



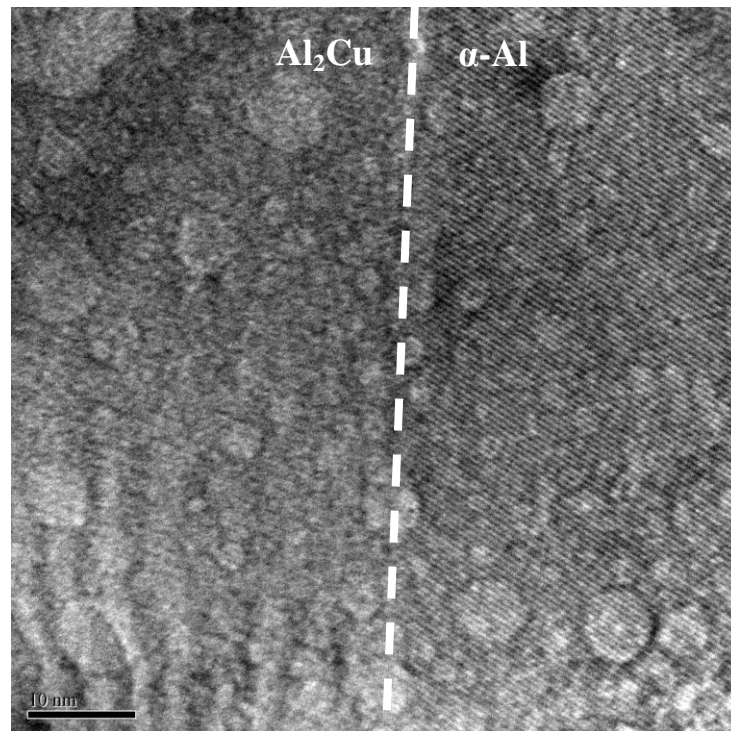
(c)

*Fig. 5.94 SEM back-scattered electron image of the 201 alloy: (a) as-thixoformed, (b) after heat treatment at 500 °C for 72 hours, (c) high magnification micrograph of (b) showing  $\text{Al}_2\text{Cu}$  and  $\text{Al}_3\text{Ti}$  particles*

Fig. 5.95 shows a very high magnification image of the bonding between the matrix and the  $\text{Al}_2\text{Cu}$  phase marked with a white square in Fig. 5.95(a). The figure also reveals the Al and  $\text{Al}_2\text{Cu}$  lattice fringes.



(a)



(b)

*Fig. 5.95 High magnification TEM image of the 201 alloy (as-thixoformed without heat treatment) boundaries of primary  $\alpha$ -Al and  $\text{Al}_2\text{Cu}$  phases*

#### 5.8.4 Predictions by Thermo-Calc

The calculated liquid fraction versus temperature curves for 201 alloy (without Ag) with lever rule and Scheil condition are shown in Fig. 5.96 to Fig. 5.98 respectively. It should be noticed that the  $\text{Al}_{20}\text{Mn}_3\text{Cu}_2$  phase was not predicted in the Scheil mode (Fig. 5.97) but was in equilibrium mode (Fig. 5.96). However,  $\text{Al}_{20}\text{Mn}_3\text{Cu}_2$  particles were found in the microstructure analysis. Other non-primary phases, i.e.  $\text{Al}_7\text{FeCu}_2$  and  $\text{Al}_2\text{Cu}$  were both observed in predictions and experiments. The absence of  $\text{Al}_{20}\text{Mn}_3\text{Cu}_2$  in Scheil curve could lead a weak agreement with experimental results in terms of liquid fraction. Fig. 5.98 shows the comparison between equilibrium and Scheil curves. In theory, the experimental curves should lie between the two extremes. As the Thermo-Calc database does not include the Ag element, there could be slight different in predictions when adding Ag into the system.

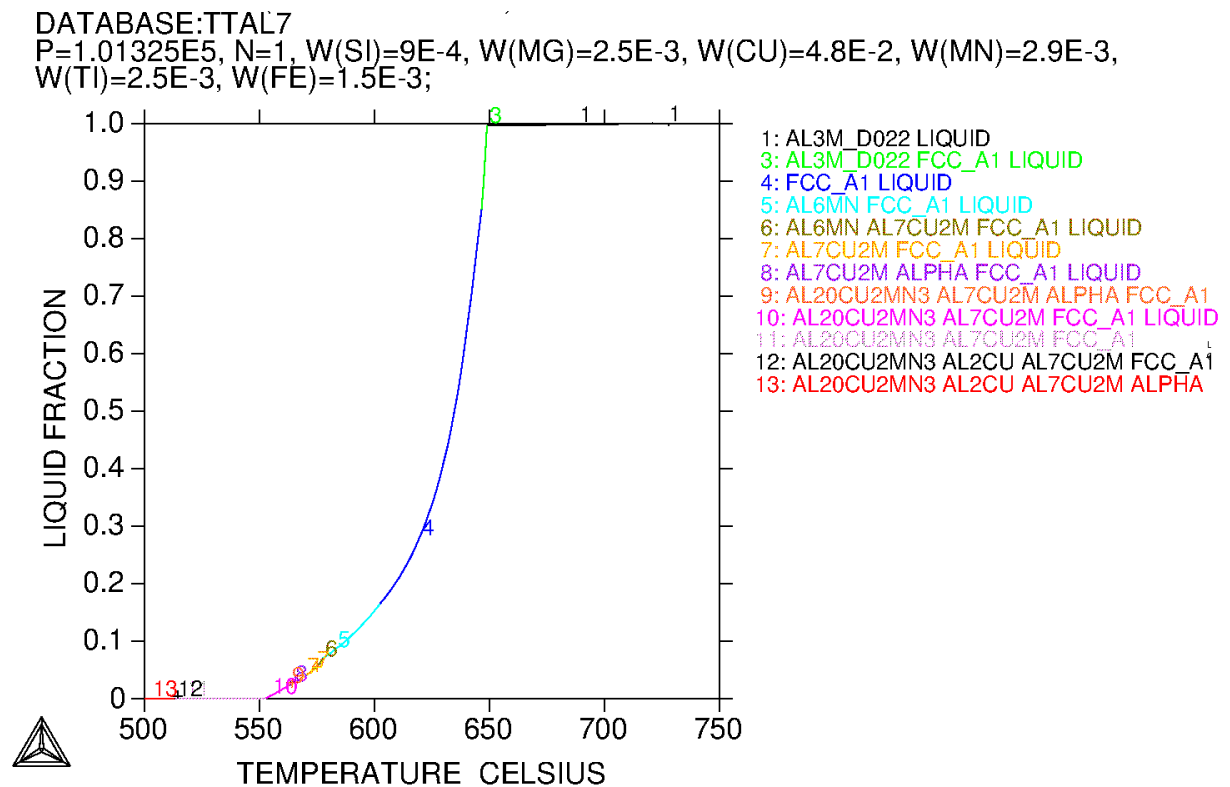


Fig. 5.96 Predicted liquid fraction vs temperature curves for 201 alloy (without Ag),  
Equilibrium



DATABASE:TTAL7

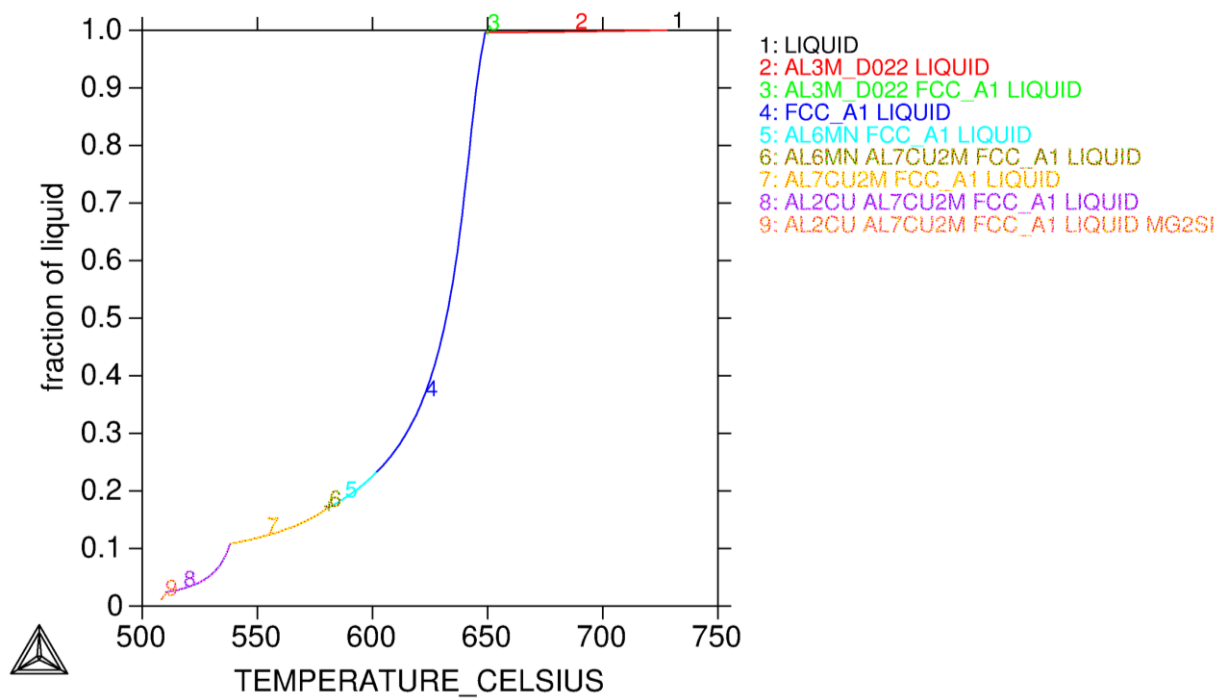


Fig. 5.97 Predicted liquid fraction vs temperature curves for 201alloy (without Ag), Scheil

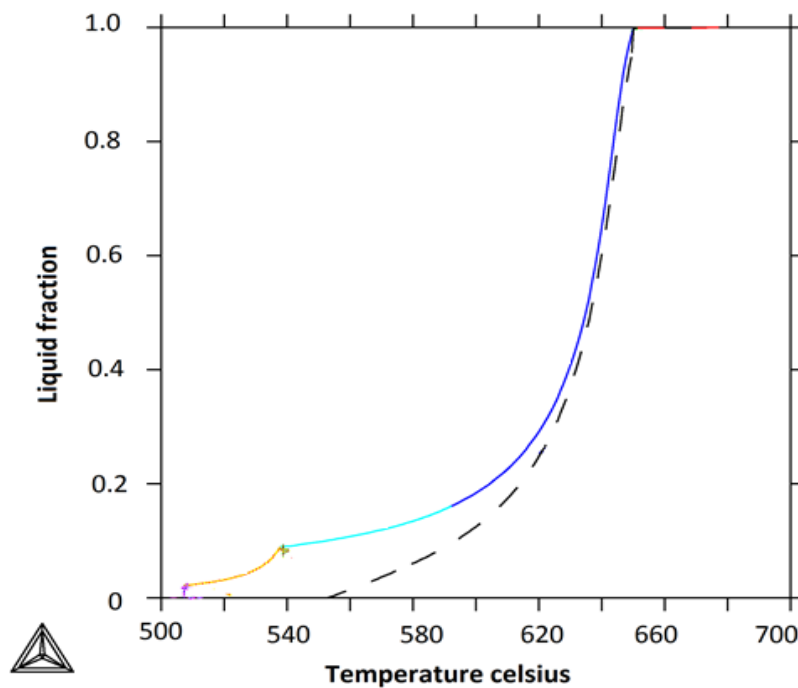


Fig. 5.98 Predicted liquid fraction vs temperature curves for 201alloy (without Ag), dash line is equilibrium curve and solid line is Scheil curve

## Chapter 6 Discussion

### *6.1 Effects of Alloy Elements on Microstructures*

The results of SEM microscopy indicated the presence of  $\alpha$ -Al dendrites and eutectic silicon phase in the case of Al-1.01wt%Si, Al-5.08wt%Si and Al-11.68wt% Si samples (Fig. 5.1 to Fig. 5.3). In addition, the amount of eutectic phases grows with Si content increasing, as well as the average eutectic size. In the case of hypereutectic as-casted Al-17.54wt%Si alloy, the results of microstructural characterization (see Fig. 5.4) indicated the presence of primary silicon (Si) and eutectic silicon phases. The primary Si exhibited the blocky morphology while the eutectic silicon exhibited the needle shaped morphology. The size of the eutectic Si was, however, found to be comparatively larger when compared to the hypoeutectic alloys. The presence of these phases is in accordance with the equilibrium microstructural phases predicted by the binary Al-Si phase diagram (see Fig. 2.1).

As for Al-Cu binary alloys, the  $\theta$ -Al<sub>2</sub>Cu phase can be found in the microstructure (Fig. 5.5 to Fig. 5.7). With the copper content increasing, the sizes of the  $\theta$ -Al<sub>2</sub>Cu phase are rising from  $\sim 3\mu\text{m}$  to  $\sim 15\mu\text{m}$ . The hardness increase of those alloys in Fig. 5.9 was due to the coarse  $\theta$ -Al<sub>2</sub>Cu phases. As no aging process was applied to those alloys, the  $\theta'$  phases are hardly found in the microstructure.

Few dark  $\beta$  particles (Al<sub>3</sub>Mg<sub>2</sub>) were found in Al-5.58wt%Mg alloy as shown in Fig. 5.8. Undoubtedly, with the Mg content increasing, the  $\beta$  phase fraction increases. However, the  $\beta$  phase is hardly seen in the Al-0.42wt%Mg alloy and the Al-2.82wt%Mg alloy due to the small amount and the similar contrast between Al and Mg under electron images.

### *6.2 Effects of Alloy Elements on Hardness*

It may be observed that the hardness improves by adding alloy elements. For Al-Si alloy, the hardness increases because as the amount of silicon in the alloy grows, the size, shape and distribution of silicon particles in the cast structures increase. Al-Cu alloys are age-hardening alloys [31]. The hardness values are strongly dependent on the aging treatment. In this work, all the tested Al-Cu alloys were received from die cast without age hardening. The changes in the structure are reflected on the hardness results. With

the composition of Cu increasing, the  $\text{Al}_2\text{Cu}$  phases become relatively larger in the structure which causes the hardness to rise.

According to the Al-Mg binary phase diagram, the phases of low compositions Mg are  $\alpha$ -Al phase and  $\text{Al}_3\text{Mg}_2$  phases. Based on the results in Fig. 5.9, it could be concluded that the Al-Mg binary alloys have higher hardness values than other alloys with the same content of copper or silicon alloying elements from permanent mode casting but without heat treatment.

### ***6.3 Simulations of Aluminium Binary alloys***

#### ***6.3.1 Equilibrium and Scheil by Thermo-Calc***

Computational thermodynamic calculations were carried out by Thermo-Calc for Al binary alloys with actual chemical compositions. The equilibrium calculation was based on the lever rule while the Scheil model was applied with five basic assumptions [75]:

- Equilibrium interface
- No back diffusion in the solid phase
- Homogenous compositions in liquid phase
- Equal densities of the solid and liquid phases
- No undercooling effect

In reality, however, the diffusion of the solute in both solid and liquid exists and therefore, the calculated liquid fraction versus temperature curve should lie between the equilibrium and Scheil modes. The prediction of liquid fraction versus temperature curves under equilibrium and Scheil mode for Al-Si binary alloys are shown in Fig. 5.10. During heating, alloys are expected to start with the melting of the eutectic phase, then followed by that of the  $\alpha$ -Al phase, in which case the temperature immediately above the eutectic point must be reached to initiate stable melting. As the composition increases from 1.1wt% to 11.68wt%, the eutectic content in the corresponding alloy increases. For melting, a very minor change in the temperature can cause all the eutectic to become liquid. For semi-solid processing, a higher variation in temperature and controllable transformation is needed to produce liquid in the semi-solid material. For alloys Al-1.01wt% and Al-5.08wt%Si, a low eutectic fraction (~8%, ~38% respectively) at the eutectic temperature (577 °C) is observed. However, Al-11.68wt%Si and

17.54wt%Si alloys possess a higher amount of liquid (almost 95%) at the eutectic temperature. The sensitivity of liquid fraction versus temperature is  $\infty$ . This could cause the billet to collapse and make it difficult to operate on the semi-solid product.

For Al-Cu binary alloys (Fig. 5.11), the addition of copper causes  $Al_2Cu$  phases to form. As the temperature rises, the  $Al_2Cu$  phases will be the first to melt, followed by the  $\alpha$  phase. The ‘knees’ on the curves in the graph represent the onset of the  $\alpha$  phase melting. However, under equilibrium condition, there is no knee on the curves and the slope is steeper than that in Scheil below the 40% liquid fraction. This is simply because the lever rule assumes the diffusions in both liquid and solid are  $\infty$ . For semi-solid processing using these alloys, the process window should be above 545 °C due to the lower sensitivity it elicits. However, in this case, the amount of solid formed is more than 80%. The ideal situation of 50% liquid requires a great effort in control. The main component in these alloys is the solid solution  $\alpha$  phase. Aluminium with high copper content possesses poor final mechanical properties as well as poor corrosion resistance [21]. In conclusion, the alloys with a high concentration of copper would not be suggested.

Another alloy system that has been studied is the Al-Mg binary system, as shown in Fig. 5.12. In this case, again, the liquid fraction-temperature relationship presents the same problem with Al-Cu binary alloys. A large amount of Mg is needed to reproduce the semi-solid ‘knee’. In thixoforming procedures, melting begins with the  $Al_3Mg_2$  precipitates, usually at the grain boundaries, followed by the melting of the  $\alpha$  phase. As shown in Fig. 5.12, these alloys present a steep slope at the liquid fraction of 40% to 50%, leading to the aforementioned difficulties in control during the process.

### ***6.3.2 DICTRA Simulation vs. Scheil and Equilibrium Mode***

#### ***6.3.2.1 Differences between DICTRA and Thermo-prediction***

The simulations of solidification at different cooling rates (3K/min, 10K/min) using DICTRA are illustrated in comparison to the equilibrium prediction results from Fig. 5.18 to Fig. 5.27. Generally, the DICTRA results show a high consistency with the Scheil results. The regular pattern can be drawn that the DICTRA results with 3K/min are close to the equilibrium curves while the results with 10K/min are close to the Scheil curves. Unlike calculations with the Scheil approach or the equilibrium approach,

solid or back diffusion cannot be treated without assumptions regarding the micro-geometry of the liquid plus solid region and the time evolution of the fraction liquid. During primary solidification, it is common to assume a plate, cylindrical or spherical geometry for dendrite (arms) to allow the treatment of diffusion in the solid in one dimension. The back diffusion can be seen in the Si microsegregation profiles in Fig. 5.17.

In the relationship of liquid-fraction vs. temperature, the DICTRA simulation curves lie between the two extremes as expected. The mobility data used by this work is listed in the ref [170-173] for Al-Si alloys, ref [170, 173, 174] for Al-Cu alloys and ref [170, 173, 175] for Al-Mg alloys.

#### ***6.3.2.2 Cell Size Impact on DICTRA Simulation***

The impact of cell size on the simulation was studied with Al-5.08wt%Si alloy. From the results, the obvious conclusion to be made is that 100 $\mu$ m is the most suitable simulation cell size for Al-5.08wt%Si alloy, which can also be proved by the dendrite size in microstructure.

The cell size set for the simulation should be the approximate secondary dendrite arm spacing. Since the mass transfer across the phases is less effective, the cell size may decide the diffusion length. Indeed, it can be seen from the Si profile graph in Fig. 5.15, the result of the 10 $\mu$ m size simulation shows a more homogenous silicon distribution than that of the 100 $\mu$ m size one, which means 10 $\mu$ m is too small for the diffusion to take place. The simulation under 10 $\mu$ m is more like the equilibrium solidification as the size is limited, making the element always distributed homogeneously. As for the size of 1mm, the distribution of silicon equals to the initial composition at 30 distance% for 620 °C and 70 distance% for 580 °C in liquid phase, which means that the cell size is too large for the characteristic diffusion length. Only with the cell size of 100 $\mu$ m, simulation results show the proper distribution of elements rather than that of equilibrium or Scheil.

#### ***6.3.2.3 Heating Behaviour Simulations by DICTRA***

In contrast to the solidification process, the melting process is rarely studied. Simulations of melting behaviour were performed using DICTRA. It shows the huge

differences of diffusion in different matrix (Fig. 5.28). The diffusion coefficients based on FCC and liquid (Fig. 5.13) are responsible for the differences of melting and remelting results. However, when compared with the DSC results, the remelting results above eutectic temperature are closer to experimental data. Hallstedt [176] studied the melting behaviour of the tool steel X210CrW12 (Fe–2w%C–12w%Cr–0.8w%W) from a diffusion controlled simulation using the DICTRA software. His result showed that the melting starts considerably above the equilibrium solidus in a homogenised material. However, no clear reason was given in his paper.

#### ***6.4 The Experimental Results vs. Prediction Results***

The relationships of liquid fraction versus temperature were calculated through integration method with DSC data, as shown from Fig. 5.40 to Fig. 5.49. The DSC is controlled to a constant heating (cooling) rate. The influence of the heating rate is illustrated in Fig. 6.1. Increasing the heating rate results in a broader peak and a higher onset temperature when the DSC signal is plotted versus temperature. In addition, the liquid fraction was calculated by the integration of the peak area, so, the liquidus-solidus temperature range for the high heating (cooling) rate is wider than for a low rate. As a result, the curve for the 10K/min heating (cooling) rate on DSC is lying on the right (left) hand side of the curve for the 3K/min heating (cooling) rate. The main reason for this phenomenon is that with a higher heating, the solute cannot be redistributed rapidly over a short time interval to obtain areas with a composition suitable for melting

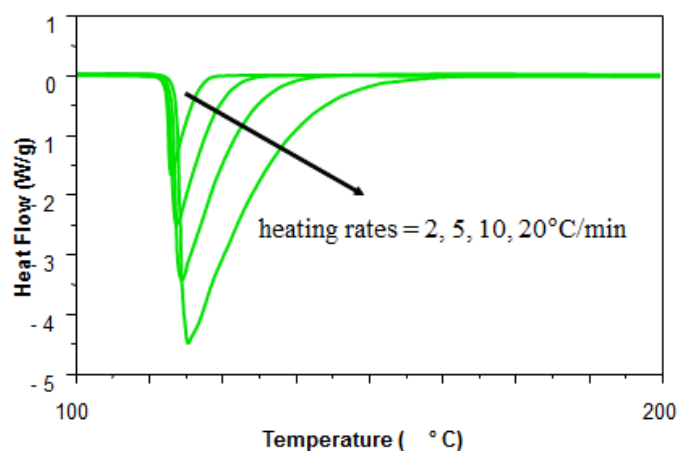


*Fig. 6.1 A schematic diagram of the influence on heating rate of DSC*

The influence of sample mass on DSC traces is illustrated in Fig. 6.2 [142]. With a higher mass sample, the rate at which a sample can absorb or release heat is slower than for a low mass sample. This leads to a broader peak for the large mass sample when plotting versus temperature but the onset temperature for solidification will not vary provided the cooling rate is the same. This is consistent with the fact that the curve for the DSC 3K/min heating (cooling) rate with small sample mass is lying to the left (right) hand side of the curve for the DSC 3K/min with the large sample.

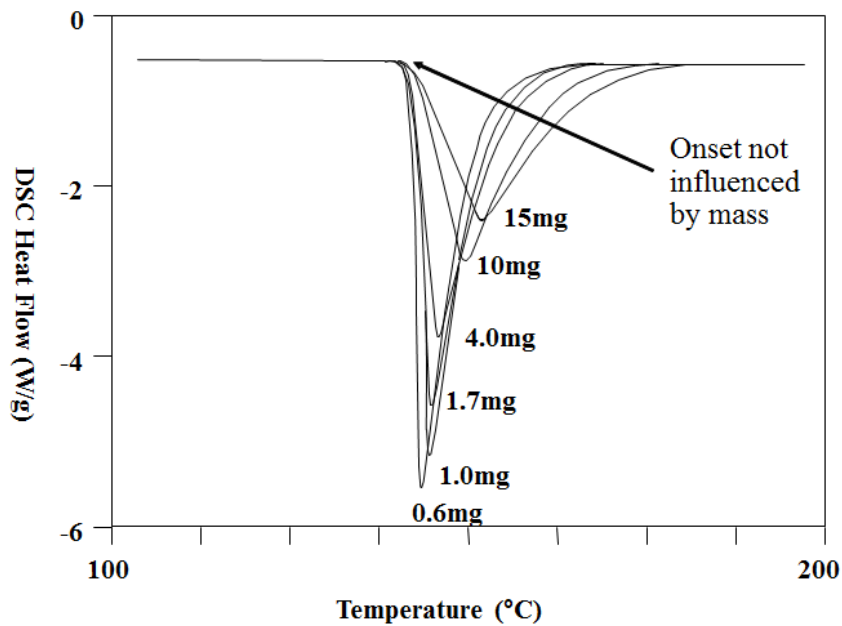
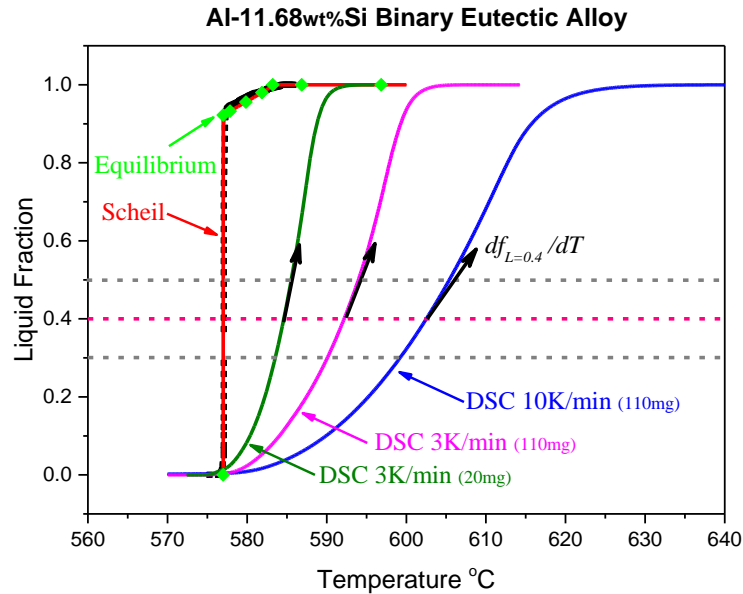


Fig. 6.2 A schematic diagram of the influence on sample mass of DSC [142]

The DSC is controlled to the ramp rate and the DSC curves change significantly due to the influence of the sample mass and the heating rate, which affects the liquid fraction versus temperature. For the DSC with two pans, to minimize errors, it is generally recognized that small samples and low heating/cooling rates must be used when latent heat is evolved, as described in Section 3.2.1.1 (Fig. 3.7) and Section 3.2.1.3. Even when samples are small the errors have been reduced but not eliminated. Taking the near eutectic Al-Si binary alloy (Al-11.68wt%Si) for example, Fig. 6.3 shows the calculated liquid fraction versus temperature by heating curves from DSC with predictions from Thermo-Calc. It can be seen that the liquid fraction sensitivity ( $df_{L=0.4}/dT$ ) is decreased with the sample mass and heating rate increasing. However, the prediction curves show that the  $df_{L=0.4}/dT = \infty$  with both equilibrium and Scheil.



*Fig. 6.3 Calculated liquid fraction versus temperature by heating curves from DSC with predictions from Thermo-Calc for Al-11.68wt%Si alloy*

The DSC is controlled to the scanning rate, while the SPSC is using a constant heat flux mode and can eliminate the smearing effect in a conventional DSC and the exactly sample temperature has been measured. The liquid fraction as a relationship of temperature curves calculated by SPSC for the 10 binary aluminium alloys are illustrated from Fig. 5.53 to Fig. 5.62. It could be concluded that the SPSC results are closer to the prediction results than DSC curves even with the relatively large sample size associated with SPSC.

During SPSC test, the temperature difference between the inner and outer crucibles is kept constant. The temperature variation during melting and solidification is very small and the measurements do not vary significantly with heating rate. These advantages for SPSC make it measuring the exactly sample temperature. As a result, the calculated liquid fraction during melting/solidification agreed well with the prediction results from Thermo-Calc coupled with thermodynamic database.

The comparison between prediction results and experimental results are represented from Fig 5.63 to Fig. 5.72. It can be seen that the DSC results are significantly different from those in the SPSC and the DICTRA simulation predictions. The influence of heating (cooling) rate on the DSC curves for alloys is shown by the fact that the



processing window between the fraction liquid 30% and 50% is wider for 10K/min heating (cooling) rate than for 3K/min (i.e. the slope of the curve is steeper for 3K/min). The solidus temperatures for alloys on the DSC heating curves are the same for every alloy. For the Al-5.08wt%Si alloy, the knee (shown magnified in Fig. 5.64) at the eutectic point is smoother in the DSC 10K/min heating (cooling) rate curve than in the 3K/min. In addition, the knee on the DSC heating curves is associated with more liquid (~44%) than the DSC cooling (~38%), SPSC (~36%) and Scheil (~36%) curves. The next challenge is to investigate how far the DICTRA simulation can be relied on for practical processing.

Overall, the key finding in comparison between the predictions and experiments is that the results from the SPSC are very close to the DICTRA predictions. The DICTRA predictions are based on a solidification route rather than melting (which would be more appropriate for at least some forms of semi-solid processing). In practice in semi-solid processing, the heating route must be analysed to determine the heating rate in the various parts of the billet and hence predict the liquid content variation across the billet at stages in the processing.

## ***6.5 Process Window***

Process window is defined as a collection of process parameters that allow materials to be manufactured and to operate under desired specifications [177]. In semi-solid processing, the process window is related to a stage between the solidus and the liquidus of a metallic alloy. Semi-solid processing from a solid state starting point (thixoforming) is normally carried out with between 30% and 50% liquid as it leads to an optimum slurry viscosity and a good die filling property [47, 54, 178]. Inspired by Curle's work [3, 4] and in order to isolate the role of time for aluminium pure metal and hence to illustrate an analysis which can be applied to alloys in due course, the liquid fraction sensitivity to temperature  $(df_L/dT)_{f_L=0.4}$  and the liquid fraction sensitivity to time  $(df_L/dt)$  will be evaluated for the processing route. The thixoforming route will be focused on (where it is the range between 30% and 50% liquid which is of concern) but the analysis has parallels for other semisolid processing routes such as rheocasting.

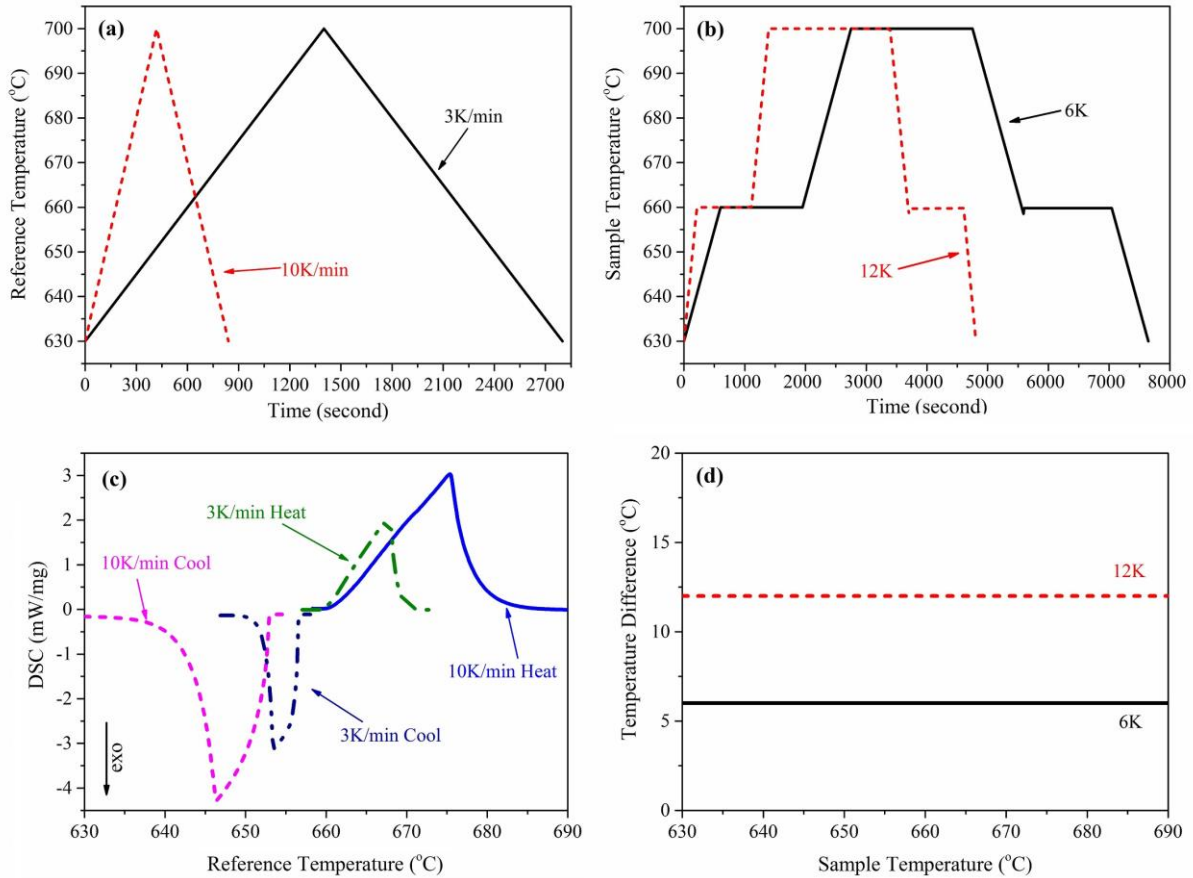


*Fig. 6.4 (a) Measured reference temperature versus time for pure Al with DSC (b) Measured sample temperature versus time for pure Al with SPSC, (c) Measured DSC signal (heat flow) versus reference temperature for pure Al, (d) Measured temperature difference (heat flow) versus sample temperature for pure Al with SPSC, showing maintenance of steady-state condition during melting and solidification to ensure the high accuracy in enthalpy measurement in SPSC*

The DSC traces for melting and solidification of pure aluminium are shown in Fig. 6.4(a,c). Although pure aluminium has a fixed melting point at 660.34 °C, the measured DSC signal shows that melting and freezing occur over a range of temperature, a 10K range for 3K/min and a 20K range for 10K/min. This was termed as the “smearing” effect by Hähne et al [142]. The smearing effect was further quantitatively analysed by Dong and Hunt [5, 148] and they revealed that during melting and freezing, a large temperature difference occurs between the sample and the sample thermocouple, i.e. the sample thermocouple doesn’t measure the sample temperature correctly during melting and freezing. This is particularly true for metals and alloys because extremely high solidification interface velocities (in order of mm/s) were measured even with temperature differences from the melting point of a few hundredths of a degree [179,

180]. The “smeared” DSC signals have commonly been used to study solidification kinetics and ironically the “smeared” signals provide better-looking but wrong figures in kinetic analysis. The SPSC overcomes the “smearing” effect and the measured raw data (temperature vs. time) with the temperature difference between the inner and outer crucible at  $\pm 6\text{K}$  and  $\pm 12\text{K}$  is shown in Fig. 6.4(b). The temperature variation during melting and solidification was very small. Steady state temperature differences have been obtained through melting and solidification for high accuracy enthalpy measurement, as shown in Fig. 6.4(d).

The measured enthalpy changes during melting and solidification for pure aluminium obtained by DSC and SPSC is shown in Fig. 6.5. It can be seen that there is very little differences among these enthalpy curves for the different rates for SPSC, except for a small difference in the enthalpy step at the beginning of solidification. This is because the as-expected undercooling occurs during freezing. However, the enthalpy measured by DSC shows large differences between different scan rates, which is not correct.

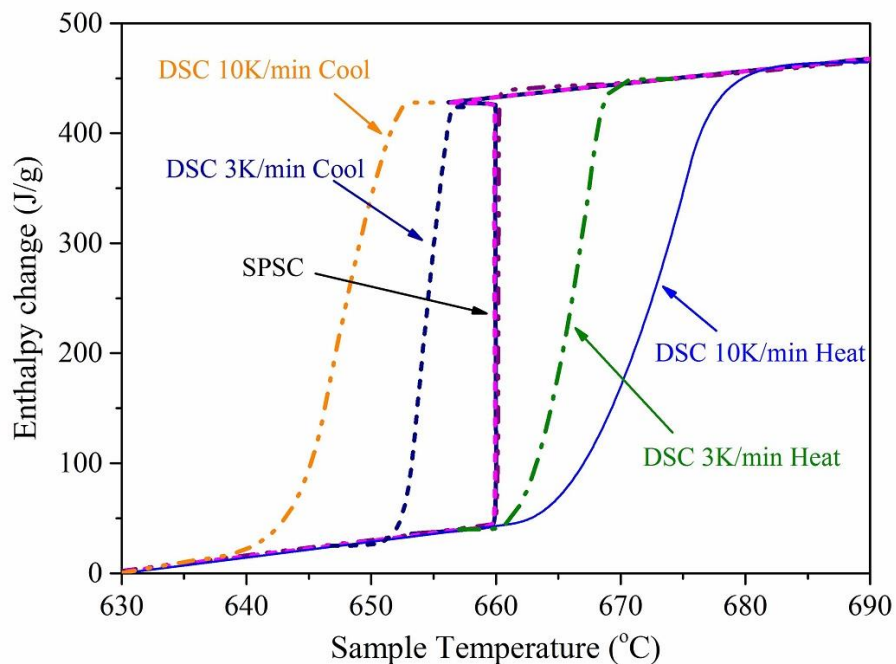


*Fig. 6.5 Measured enthalpy changes versus temperature by DSC and SPSC for pure Al*

The liquid fraction versus temperature curves calculated from the DSC and SPSC results are shown in Fig. 6.6. As can be seen in Fig. 6.6(a), the DSC curves vary significantly with changes in heating rate. However, this is not a proper reflection of

reality because the measured temperature is the reference pan temperature rather than the sample temperature. The SPSC (Fig. 6.6(b)), in contrast, gives a constant temperature line when pure aluminium is melting or solidifying because it is measuring exactly the sample's temperature. Liquid fraction sensitivity to temperature can be defined from the slope (Fig. 6.6(a)) of the liquid fraction versus temperature curve as  $(df_L/dT)_{f_L}$ .

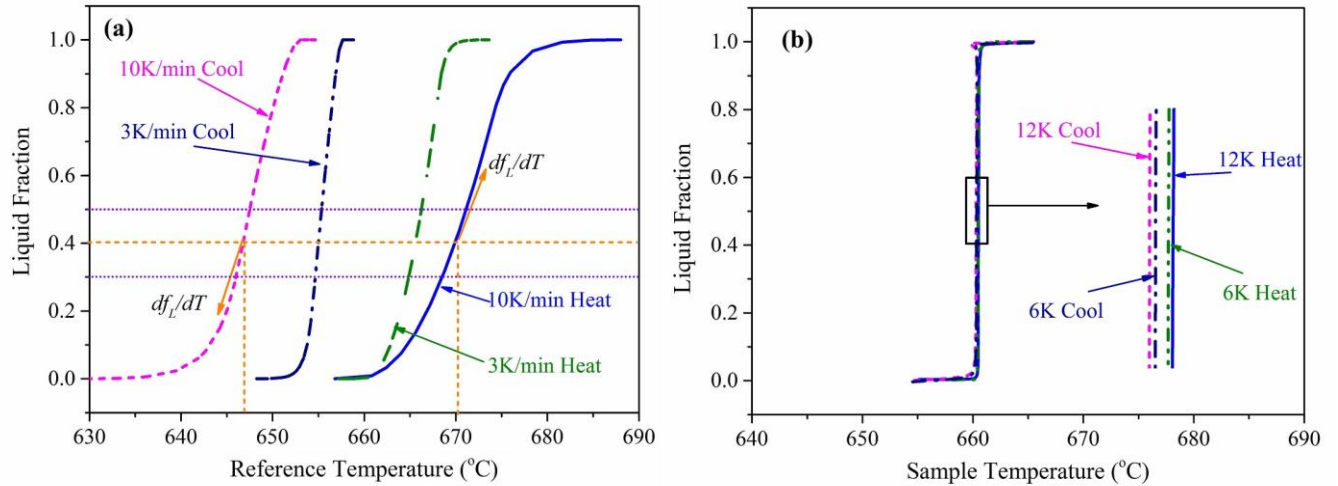


Fig. 6.6 Calculated liquid fraction as a function of temperature (a) DSC, (b) SPSC, for pure Al.

When taking time into consideration, the calculated liquid fraction as a function of time for pure aluminium with SPSC for the temperature difference at  $\pm 6K$  is shown in Fig. 6.7. It can be seen that the vertical curves in Fig. 6.6(b) becomes curves with slopes about  $\pm 3$  seconds per % liquid. The results indicated 2.10g pure aluminium needs about 1200 seconds to be totally melted under the set condition ( $\sim 240s$  to transition the 30%-50% liquid temperature range).

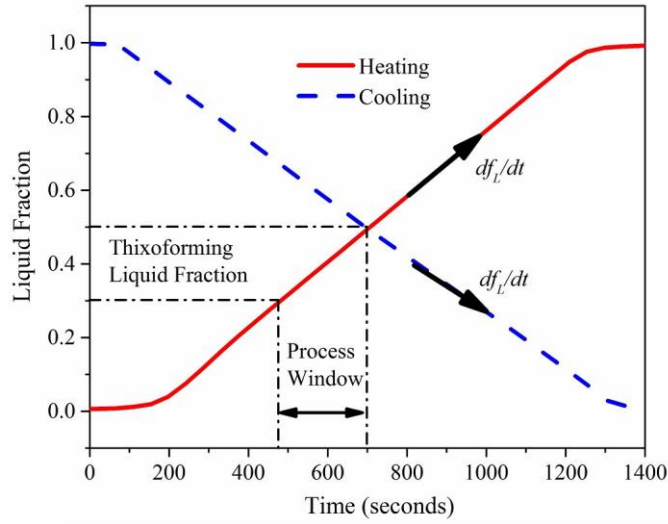


Fig. 6.7 Process window calculated using liquid fraction as a function of time for pure Al with SPSC for the temperature difference between inner and outer crucible at  $\pm 6K$ .

The liquid fraction sensitivity to temperature  $(df_L/dT)_{f_L=0.4}$  and the liquid fraction sensitivity to time  $(df_L/dt)_{f_L=0.4}$  for both DSC and SPSC are listed in Table 6.1. The sensitivity declines with an increase of the heating/cooling rate for DSC. However, the liquid fraction sensitivity to temperature for the SPSC result is infinity because the melting/solidification temperature variation for pure aluminium is almost zero.

Sensitivity	DSC				SPSC	
	10K/min Heat	10K/min Cool	3K/min Heat	3K/min Cool	3K/min Heat	3K/min Cool
$(\frac{df_L}{dT})_{f_L=0.4} \cdot (K^{-1})$	0.11	-0.12	0.26	-0.28	$+\infty$	$-\infty$
$(\frac{df_L}{dt})_{f_L=0.4} \cdot (min^{-1})$	1.10	-1.20	0.78	-0.84	+0.05	-0.05

Table 6.1: Calculated liquid fraction sensitivity to temperature/time for DSC and SPSC

As DSC is controlled to a constant heating/cooling rate, the time is proportional to the temperature during melting and solidification. As a result, the sensitivity to time  $(df_L/dt)_{f_L=0.4}$  equals the sensitivity to temperature  $(df_L/dT)_{f_L=0.4}$  times the heating/cooling rate. For SPSC, the liquid fraction sensitivity to time (Fig. 6.7) drops from  $\infty$  to  $\sim \pm 0.05 min^{-1}$ . The decreased liquid fraction sensitivity to time can open a process window for semi-solid processing.

In practice in semi-solid processing, it is impossible to heat/cool a billet at a constant rate when melting or solidification occurs. Instead, there is a holding time in the semi-solid state [17], where the thermo-arrest occurs. As Fig. 6.7 shows, the melting or solidification does not happen instantaneously. The diffusion time during phase transformations is dependent on the amount of heat flux. Therefore, the liquid fraction sensitivity to time can be controlled through the heat flux. The process window can be enlarged when a lower heat flux ratio is applied depending on the mass of sample. Thus the liquid fraction sensitivity to time at 40% liquid fraction must be analysed, and is a substantive criterion for identifying the process window for semi-solid processing. Semi-solid processing can occur even for materials lacking a temperature interval between the solidus and the liquidus (e.g. pure binary eutectics and pure metals) because of the kinetics of melting/solidification. However, the temperature window is practically much more preferable to time window because time is hard to control in practice.

## ***6.6 Dissolution of Al<sub>2</sub>Cu Phase in 319s and 201 Alloys***

The dissolution of copper phases, especially the Al<sub>2</sub>Cu phase, was investigated using DSC. The differences between melting the copper intermetallic phases from SSM processing state and re-solidification state have been observed relating the dissolution of the Al<sub>2</sub>Cu phase with endothermic peaks during DSC runs. As can be seen from the results in Sections 5.7 and 5.8, the microsegregation of copper in the SSM alloys (319s and 201) is much weaker than in the normal cast alloys and it leads to lower liquid fraction values calculated through the integration method from DSC results. Copper phases can be dissolved into matrix up to 0.4 % below melting temperature under 3K/min heating rate when compared with 10K/min heating rate for the 319s alloy.

Dissolution of the eutectic (Al+Al<sub>2</sub>Cu) takes place at temperatures close to the final solidification temperature of the alloy (i.e. 500 °C). The copper phases have been significantly dissolved into matrix at the solution heat treatment temperature of 500 °C for 72 hours compared with the as thixoformed alloys.

Fine and equiaxed dendrites are distributed uniformly in the structure of the thixoformed alloy. After melting and slow cooling, coarsened phases and large dendrites were

observed. Intermetallic phases have been observed through SEM and TEM image analysis but not with the XRD results, as the intermetallic phase are too small in scale.

As a side issue, computational thermodynamic calculations were carried out by Thermo-Calc for 319s alloy with actual chemical compositions and for 201 alloy without the Ag element. Similar to the previous study of binary alloys, the SPSC results are close to the predication while the DSC curves enlarged the window between 30 % and 50% fraction liquid.

Overall, the liquid fraction values for copper phase calculated from DSC data are lower for thixoformed state than for the slow solidified state. The DSC ramp rate should be carefully selected as higher heating rate can prevent dissolution of the intermetallic phase during heating but will overestimate liquid fractions.

## Chapter 7 Conclusions

In this study, the binary aluminium alloys based on Al-Si (Al-1.01wt% Si, Al-5.08wt%Si, Al-11.68wt%Si, Al-17.54wt%Si), Al-Cu (Al-0.98wt%Cu, Al-2.18wt%Cu, Al-4.9wt%Cu) and Al-Mg (Al-0.42wt%Mg, Al-2.82wt%Mg, Al-5.58wt%Mg) systems and thixoformed 319s (Al-Si-Cu-Mg) and 201 (Al-Cu) alloys, were examined via thermodynamic simulations (Thermo-Calc, DICTRA) and experimental thermo-analysis (DSC, SPSC) as well as microstructure examination with FEGSEM, TEM and XRD techniques. The following conclusions can be drawn;

- 7.1** The hardness properties are improved by adding alloying elements (up to 17.54wt% Si, up to 4.9wt% Cu and up to 5.58wt% Mg) for permanent mold cast aluminium binary alloys.
- 7.2** The added copper, magnesium and silicon (up to 5.08wt %) can reduce the steep rate of fraction liquid vs. temperature curves and enlarge the temperature window between 30% and 50% fraction liquid from both the equilibrium and Scheil mode.
- 7.3** The cell size of 100 $\mu$ m is suitable for DICTRA solidification (with cooling rate 3K/min and 10K/min) simulations of tested alloys, while a 10 $\mu$ m cell is too small for diffusion driving force and a 1mm cell is too long for the characteristic diffusion length.
- 7.4** The curves on DICTRA solidifications simulation predict the same pattern with DSC results. With DICTRA prediction, at a given temperature, higher cooling rate gives just slightly higher liquid fraction than a lower cooling rate. The lowest liquid fraction is obtained under equilibrium conditions in the 30-50% liquid range.
- 7.5** The slopes of the curves of fraction liquid vs. temperature at 40% fraction liquid become less steep and the liquid fraction sensitivity to temperature between 30 % and 50% is enlarged by higher heating/cooling rate and larger sample size on DSC. The DSC results are sensitive to the ramp rate and sample mass because the measured temperature is the reference pan temperature rather than the sample temperature.



**7.6** The SPSC results of relationship of fraction liquid-temperature are closer to the prediction results than the DSC curves even with relatively large sample size used in SPSC. In addition, it is better to use Scheil than equilibrium for prediction because Scheil fits better to SPSC data.

**7.7** Process window has been redefined as the liquid fraction sensitivity to time for SSM processing. It can be a significant criterion for identifying the process window for SSM processing. The process window can be enlarged when a lower heat flux ratio is applied. Thus, the liquid fraction sensitivity to time at 40% liquid fraction must be analysed. Though the role of time in determining the process window is scientifically important, the temperature window is better than the time window because time is hard to control in practice in SSM processing. The heating/cooling route must be analysed to determine the melting/solidification in various parts of the billet and hence to predict the liquid content variation across the billet at stages in the processing.

**7.8** DSC was successfully used to observe the differences of melting  $\text{Al}_2\text{Cu}$  phase between semi-solid state and slow solidification state in 319s and 201 aluminium alloys. The microsegregation of copper in the SSM alloys is much lower than the normal cast alloys and it leads to lower liquid fraction values calculated through the integration method from DSC results. Copper phases can be dissolved into matrix up to 0.4 % before melting temperature under 3K/min heating rate when compared with 10K/min heating rate for 319s alloy. The DSC scan rate should be carefully selected as higher heating rate can avoid dissolution of the intermetallic phase during heating but will overestimate liquid fractions.

## **Chapter 8 Further Work**

### **8.1 Predictions**

Predictions of liquid fraction versus temperature taking into account both thermodynamic and kinetics of diffusion were compared to experimental results and a very similar pattern was obtained. However, there was some inconsistency between the predictions and experiments. The long term aim is to gain confidence in prediction with software packages which will reduce trial and error. In current project, the next challenge is to investigate how far the DICTRA simulation can be relied on for practical processing. In addition, simulation of melting will be a further step because melting would be most relevant to the thixo-processing.

### **8.2 Thermodynamic Analysis**

Binary aluminium alloys were selected for fundamental studies of two different calorimeters, i.e. SPSC and DSC. More reliable results were obtained from SPSC than DSC. Further work should concentrate on the thermodynamic analysis of commercial alloys by SPSC to determine the SSM processing route. Also, SPSC results would be important to compare with simulations.

### **8.3 Determination of Actual Liquid Fraction**

Enthalpy was used to evaluate the liquid fraction during thermo-analysis assuming that the latent heat is constant for liquid and solid. However, liquid content varies across the billet at stages in the practical processing. Therefore, further work needs to concentrate on the evaluation of liquid content in various parts of the billet during practical processing. In this case, a heating component should be further designed along with the in situ X-ray Computed Tomography (CT) to investigate the liquid content in various parts of the billet in processing and hence to predict the processing route.

### **8.4 Alloy Design**

The effect of the alloying elements on the liquid fraction evolution during solidification and melting was studied in this work. As the experimental results obtained from SPSC are very close to predictions, it is necessary and efficient to investigate phases in

equilibrium and Scheil in new compositions before any experiments. Promising compositions will be selected for further development for practical processing.

### **8.5 Thixoforming**

The time sensitivity of liquid fraction can be a significant criterion for identifying the process window for SSM processing. This parameter may offer many possibilities for future research on SSM processing of high performance alloys where there is a narrow solidus-liquidus temperature interval. The processing parameters, e.g. die design, heating/cooling route, spheroid morphology control etc. will be investigated. Additionally, heat treatment needs further development to achieve the high properties for SSM processed alloys.

## References

- [1] H.V. Atkinson, Semisolid processing of metallic materials, *Materials Science and Technology*, 26 (2010) 1401-1413.
- [2] D. Liu, H.V. Atkinson, H. Jones, Thermodynamic prediction of thixoformability in alloys based on the Al–Si–Cu and Al–Si–Cu–Mg systems, *Acta Materialia*, 53 (2005) 3807-3819.
- [3] U.A. Curle, H. Möller, J.D. Wilkins, Shape rheocasting of high purity aluminium, *Scripta Materialia*, 64 (2011) 479-482.
- [4] U.A. Curle, H. Möller, J.D. Wilkins, Shape rheocasting of unmodified Al–Si binary eutectic, *Materials Letters*, 65 (2011) 1469-1472.
- [5] H.B. Dong, J.D. Hunt, A novel single-pan scanning calorimeter, measurement of thermophysical properties of metallic alloys, *Journal of Thermal Analysis and Calorimetry*, 64 (2001) 341-350.
- [6] S. Shankar, Y. Riddle, M. Makhlof, Eutectic solidification of aluminum-silicon alloys, *Metallurgical and Materials Transactions A*, 35 (2004) 3038-3043.
- [7] H. Baker, H. Okamoto, Alloy phase diagrams, *ASM Handbook*, 3 (1992) 2.
- [8] M.M. Makhlof, H.V. Guthy, The aluminum–silicon eutectic reaction: mechanisms and crystallography, *Journal of Light Metals*, 1 (2001) 199-218.
- [9] J.L. Murray, A.J. McAlister, The Al-Si (aluminum-silicon) system, *Bulletin of Alloy Phase Diagrams*, 5 (1984) 74-84.
- [10] H. Ye, An overview of the development of Al-Si-alloy based material for engine applications, *Journal of Materials Engineering and Performance*, 12 (2003) 288-297.
- [11] M. Warmuzek, Aluminum-silicon casting alloys: an atlas of microfractographs, *ASM International*, 2004.
- [12] H. Torabian, J. Pathak, S. Tiwari, Wear characteristics of Al-Si alloys, *Wear*, 172 (1994) 49-58.
- [13] W. Hume-Rothery, G.V. Raynor, The structure of metals and alloys, *Institute of Metals*, 1988.
- [14] L.F. Mondolfo, Aluminum alloys: structure and properties, *Butterworths London*, 1976.
- [15] J.R. Davis, Properties and selection: nonferrous alloys and special-purpose materials, *ASM International*, 1990.
- [16] W.S. Miller, L. Zhuang, J. Bottema, A.J. Wittebrood, P. DeSmet, A. Haszler, A. Vieregge, Recent development in aluminium alloys for the automotive industry, *Materials Science and Engineering: A*, 280 (2000) 37-49.

- [17] M.E. Seniw, J.G. Conley, M.E. Fine, The effect of microscopic inclusion locations and silicon segregation on fatigue lifetimes of aluminum alloy A356 castings, *Materials Science and Engineering: A*, 285 (2000) 43-48.
- [18] M.D. Dighe, A.M. Gokhale, Relationship between microstructural extremum and fracture path in a cast Al-Si-Mg alloy, *Scripta Materialia*, 37 (1997) 1435-1440.
- [19] E. Hornbogen, The electron microscope investigation of precipitation in aluminium-copper solid solutions. III, *Aluminium*, 43 (1967) 163-166.
- [20] H. Okamoto, Desk handbook: phase diagrams for binary alloys, 2nd Edition, ASM International, 2010.
- [21] I. Polmear, Light alloys: from traditional alloys to nanocrystals, 4th Edition, Butterworth-Heinemann, 2005.
- [22] M.J. Starink, A.M. Zahra,  $\beta'$  and  $\beta$  precipitation in an Al-Mg alloy studied by DSC and TEM, *Acta Materialia*, 46 (1998) 3381-3397.
- [23] H. Okamoto, Al-Mg (aluminum-magnesium), *Journal of Phase Equilibria*, 19 (1998) 598-598.
- [24] J. Robinson, Serrated flow in aluminium base alloys, *International Materials Reviews*, 39 (1994) 217-227.
- [25] A.A. Nayeb-Hashemi, J.B. Clark, Phase diagrams of binary magnesium alloys, ASM International, 1988.
- [26] A. Rollett, F. Humphreys, G.S. Rohrer, M. Hatherly, Recrystallization and related annealing phenomena, 2nd Edition, Elsevier, 2004.
- [27] S. Shivkumar, C. Keller, D. Apelian, Aging behavior in cast Al-Si-Mg alloys, *AFS Trans*, 98 (1990) 905-911.
- [28] K. Kashyap, S. Murali, K. Raman, K. Murthy, Casting and heat treatment variables of Al-7Si-Mg alloy, *Materials Science and Technology*, 9 (1993) 189-204.
- [29] S. Murali, K. Raman, K. Murthy, Effect of magnesium, iron (impurity) and solidification rates on the fracture toughness of Al-7Si-0.3 Mg casting alloy, *Materials Science and Engineering: A*, 151 (1992) 1-10.
- [30] A. Joenoes, J. Gruzleski, Magnesium effects on the microstructure of unmodified and modified Al-Si alloys, *Cast Metals*, 4 (1991) 62-71.
- [31] L. B äckerud, G. Chai, J. Tamminen, Solidification characteristics of aluminium alloys: foundry alloys, AFS/Skanaluminium, 1990.
- [32] M.S. Salleh, M.Z. Omar, J. Syarif, M. Mohammed, An overview of semisolid processing of aluminium alloys, *International Scholarly Research Notices*, 2013 (2013).

- [33] Q. Zhu, S.P. Midson, C.W. Ming, H.V. Atkinson, Casting and heat treatment of turbocharger impellers thixocast from alloy 201, *Solid State Phenomena*, 192 (2013) 556-561.
- [34] Z. Li, A.M. Samuel, F.H. Samuel, C. Ravindran, S. Valtierra, Effect of alloying elements on the segregation and dissolution of  $\text{CuAl}_2$  phase in Al-Si-Cu 319 alloys, *Journal of Materials Science*, 38 (2003) 1203-1218.
- [35] F.H. Samuel, Incipient melting of  $\text{Al}_5\text{Mg}_8\text{Si}_6\text{Cu}_2$  and  $\text{Al}_2\text{Cu}$  intermetallics in unmodified and strontium-modified Al-Si-Cu-Mg (319) alloys during solution heat treatment, *Journal of Materials Science*, 33 (1998) 2283-2297.
- [36] G. Wang, X. Bian, W. Wang, J. Zhang, Influence of Cu and minor elements on solution treatment of Al-Si-Cu-Mg cast alloys, *Materials Letters*, 57 (2003) 4083-4087.
- [37] L. Lasa, J. Rodriguez-Ibabe, Characterization of the dissolution of the  $\text{Al}_2\text{Cu}$  phase in two Al-Si-Cu-Mg casting alloys using calorimetry, *Materials Characterization*, 48 (2002) 371-378.
- [38] S.G. Shabestari, M. Malekan, Assessment of the effect of grain refinement on the solidification characteristics of 319 aluminum alloy using thermal analysis, *Journal of Alloys and Compounds*, 492 (2010) 134-142.
- [39] E.J. Martínez D, M.A. Cisneros G, S. Valtierra, J. Lacaze, Effect of strontium and cooling rate upon eutectic temperatures of A319 aluminum alloy, *Scripta Materialia*, 52 (2005) 439-443.
- [40] Z. Li, A.M. Samuel, F.H. Samuel, C. Ravindran, H.W. Doty, S. Valtierra, Parameters controlling the performance of AA319-type alloys: part II. impact properties and fractography, *Materials Science and Engineering: A*, 367 (2004) 111-122.
- [41] D.B. Spencer, R. Mehrabian, M.C. Flemings, Rheological behavior of Sn-15 pct Pb in the crystallization range, *Metallurgical Transactions*, 3 (1972) 1925-1932.
- [42] Z. Fan, Semisolid metal processing, *International Materials Reviews*, 47 (2002) 49-85.
- [43] <http://aluminium.matter.org.uk/content/html/eng/default.asp?catid=&pageid=1>, 04/08/2013.
- [44] C.J. Quaak, L. Katgerman, W.H. Kool, in: Kirkwood D H, Kapranos P (Eds.) *Proc. 4th Int. Conf. Semi Solid Processing of Alloys and Composites*, Sheffield, UK, 1996, pp. 35-39.
- [45] European Patent 0745694A1, Method and apparatus of shaping semisolid metals, UBE Industries Ltd, 1996.
- [46] K. Hall, H. Kaufmann, A. Mundl, in: G.L. Chiarmetta, M. Rosso (Eds.) *Proc. 6th Int. Conf. Semi Solid Processing of Alloys and Composites*, Turin, Italy, September, 2000, pp. 23-28.

- [47] H.V. Atkinson, Modelling the semisolid processing of metallic alloys, *Progress in Materials Science*, 50 (2005) 341-412.
- [48] D.H. Kirkwood, M. Su éry, P. Kapranos, H.V. Atkinson, K.P. Young, Experimental determination of rheological behavior, *Semi-solid Processing of Alloys*, Springer Berlin Heidelberg, 2010, pp. 45-69.
- [49] D.H. Kirkwood, M. Suery, P. Kapranos, H.V. Atkinson, K.P. Young, Experimental determination of rheological behavior, *Semi-Solid Processing of Alloys*, 124 (2010) 45-69.
- [50] S. Chayong, H.V. Atkinson, P. Kapranos, Thixoforming 7075 aluminium alloys, *Materials Science and Engineering A-Structural Materials Properties Microstructure and Processing*, 390 (2005) 3-12.
- [51] H.V. Atkinson, P. Kapranos, D.H. Kirkwood, Alloy development for thixoforming, *Proceedings of the 6th International Conference "Semi-solid Processing of Alloys and Composites"*, Turin, 2000, pp. 445-446.
- [52] R. Kopp, D. Neudenberger, G. Winning, Different concepts of thixoforging and experiments for rheological data, *Journal of Materials Processing Technology*, 111 (2001) 48-52.
- [53] P. Kapranos, P.J. Ward, H.V. Atkinson, D.H. Kirkwood, Near net shaping by semi-solid metal processing, *Materials & Design*, 21 (2000) 387-394.
- [54] D.H. Kirkwood, Semisolid metal processing, *International Materials Reviews*, 39 (1994) 173-189.
- [55] M. Garat, S. Blais, C. Pluchon, W. Loue, Aluminium semi-solid processing: from the billet to the finished part, *Proc. 5th Int. Conf. on Semi-solid Processing of Alloys and Composites*, Colorado, USA, 1998, pp. 199-213.
- [56] D. Saha, D. Apelian, R. DasGupta, Semi solid processing of hypereutectic alloys, *Transactions of the American Foundry Society and the One Hundred Eighth Annual Metalcasting Congress*, 2004, pp. 325-337.
- [57] Y. Birol, Cooling slope casting and thixoforming of hypereutectic A390 alloy, *Journal of Materials Processing Technology*, 207 (2008) 200-203.
- [58] E. Tzimas, A. Zavaliangos, Materials selection for semisolid processing, *Materials and Manufacturing Processes*, 14 (1999) 217-230.
- [59] S. Nafisi, D. Emadi, R. Ghomashchi, Semi solid metal processing: the fraction solid dilemma, *Materials Science and Engineering: A*, 507 (2009) 87-92.
- [60] Y. Birol, Solid fraction analysis with DSC in semi-solid metal processing, *Journal of Alloys and Compounds*, 486 (2009) 173-177.
- [61] R.A. Swalin, *Thermodynamics of solids*, Wiley, 1972.

- [62] F.C. Andrews, Thermodynamics: principles and applications, Wiley-Interscience, 1971.
- [63] D. Elwell, A.J. Pointon, Classical thermodynamics, Penguin Harmondsworth, 1972.
- [64] C. Kittel, H. Kroemer, Thermal physics, Macmillan, 1980.
- [65] C.J. Adkins, Equilibrium thermodynamics, Cambridge University Press, 1983.
- [66] A. Cottrell, An introduction to metallurgy, Universities Press (India) Pvt. Limited, 1990.
- [67] P. Perrot, A to Z of thermodynamics, Oxford University Press, 1998.
- [68] D.R. Gaskell, Introduction to metallurgical thermodynamics, 5th Edition, Hemisphere Publishing Corporation New York, 2008.
- [69] D.M. Stefanescu, J.R. Davis, J. Destefani, Metals handbook, vol. 15-casting, ASM International, (1988) 937.
- [70] W. Kurz, H. Esaka, Solidification microstructures, Praktische Metallographie, 25 (1988) 207-213.
- [71] K. Fisher, W. Kurz, Fundamentals of solidification, Trans Tech Publications, (1986).
- [72] M.F. Ashby, D.R.H. Jones, Engineering materials 2: an introduction to microstructures and processing, 4th Edition, Butterworth-Heinemann, 2012.
- [73] A. Tomer, Structure of metals through optical microscopy, 1991.
- [74] J. Harris, Engineering metallurgy: part 1 applied physical metallurgy, International Materials Reviews, 39 (1994) 213-214.
- [75] M.C. Flemings, Solidification processing, Metallurgical Transactions, 5 (1974) 2121-2134.
- [76] I.M. Lifshitz, V.V. Slyozov, The kinetics of precipitation from supersaturated solid solutions, Journal of Physics and Chemistry of Solids, 19 (1961) 35-50.
- [77] C. Wagner, Theory of precipitate change by redissolution, Z. Elektrochem, 65 (1961) 581-591.
- [78] [http://www.npl.co.uk/upload/pdf/mtdata\\_calphad\\_paper.pdf](http://www.npl.co.uk/upload/pdf/mtdata_calphad_paper.pdf), 04/06/2013.
- [79] E. Scheil, Bemerkungen zur schichtkristallbildung, Zeitschrift für Metallkunde, 34 (1942) 70-72.
- [80] L. Kaufman, H. Bernstein, Computer calculation of phase diagrams with special reference to refractory metals, Academic Press New York, 1970.
- [81] S.W. Chen, C.C. Huang, Solidification curves of Al-Cu, Al-Mg and Al-Cu-Mg alloys, Acta Materialia, 44 (1996) 1955-1965.



- [82] A.A. Kazakov, Alloy compositions for semisolid forming, *Advanced Materials & Processes*, 157 (2000) 31-34.
- [83] Y.Q. Liu, Z. Fan, Magnesium alloy selection for semi-solid metal processing, *Proceeding of the 7th Int Conf Semi-solid Processing of Alloys and Composites*. Tsukuba, Japan: National Institute of Advanced Industrial Science and Technology, Japan Society for Technology of Plasticity, 2002, pp. 587-592.
- [84] Y.Q. Liu, Z. Fan, J. Patel, Thermodynamic approach to aluminium alloy design for semisolid metal processing, *Proceedings of the 7th S2P Advanced Semi-Solid Processing of Alloys and Composites*. Tsukuba, Japan: National Institute of Advanced Industrial Science and Technology, 2002, pp. 599-604.
- [85] A.M. Camacho, H. Atkinson, P. Kapranos, B. Argent, Thermodynamic predictions of wrought alloy compositions amenable to semi-solid processing, *Acta Materialia*, 51 (2003) 2319-2330.
- [86] E. Tzimas, A. Zavaliangos, Evaluation of volume fraction of solid in alloys formed by semisolid processing, *Journal of Materials Science*, 35 (2000) 5319-5330.
- [87] E. Tzimas, A. Zavaliangos, F. Froes, S. Ward-Close, P. McCormick, D. Eleizer, *Synthesis of lightweight metals III*, The Minerals, Metals and Materials Society, Warrendale, (1999) 195-203.
- [88] P.J. Uggowitzer, A. Wahlen, On the formation of eutectic phase in magnesium alloys during cooling from the semisolid state, *6th conference on semisolid processing of alloys and composites*, Turin, Italy, 2000, pp. 429-435.
- [89] F. Islam, M. Medraj, Thermodynamic modelling of the Mg-Al-Ca system, *Canadian Metallurgical Quarterly*, 44 (2005) 523-536.
- [90] J. Gröbner, D. Kevorkov, I. Chumak, R. Schmid-Fetzer, Experimental investigation and thermodynamic calculation of ternary Al-Ca-Mg phase equilibria, *Zeitschrift für Metallkunde*, 94 (2003) 976-982.
- [91] S. Liang, R. Chen, E. Han, Thermodynamic predictions of Mg – Al – Ca alloy compositions amenable to semi-solid forming, *International Journal of Materials Research*, 101 (2010) 256-264.
- [92] Q. Chen, B. Sundman, Computation of partial equilibrium solidification with complete interstitial and negligible substitutional solute back diffusion, *Materials Transactions*, 43 (2002) 551-559.
- [93] P.F. Shi, A. Engström, L. Höglund, Q. Chen, B. Sundman, J. Ågren, M. Hillert, Computational thermodynamics and kinetics in materials modelling and simulations, *Journal of Iron and Steel Research International*, 14 (2007) 210-215.
- [94] Q. Chen, A. Engström, L. Höglund, H. Strandlund, B. Sundman, Thermo-Calc program interface and their applications-direct insertion of thermodynamic and kinetic data into modelling of materials processing, structure and property, *Materials Science Forum*, Trans Tech Publ, 2005, pp. 3145-3148.

- [95] A.R. Ubbelohde, The molten state of matter: Melting and crystal structure, Wiley Chichester, 1978.
- [96] F.A. Lindemann, The calculation of molecular eigen-frequencies, 1984.
- [97] C. Kittel, P. McEuen, Introduction to solid state physics, 8th Edition, Wiley New York, 2004.
- [98] S.A. Cho, Role of lattice structure on the Lindemann fusion theory of metals, Journal of Physics F: Metal Physics, 12 (1982) 1069.
- [99] L.H. Cohen, W. Klement Jr, G.C. Kennedy, Melting of copper, silver, and gold at high pressures, Physical Review, 145 (1966) 519.
- [100] M. Born, Thermodynamics of crystals and melting, The Journal of Chemical Physics, 7 (1939) 591.
- [101] J.L. Tallon, W.H. Robinson, S.I. Smedley, A melting criterion based on the dilatation dependence of shear moduli, Nature, 266 (1977) 337-338.
- [102] J.L. Tallon, W.H. Robinson, A model-free elasticity theory of melting, Physics Letters A, 87 (1982) 365-368.
- [103] S. Yip, J. Li, M. Tang, J. Wang, Mechanistic aspects and atomic-level consequences of elastic instabilities in homogeneous crystals, Materials Science and Engineering: A, 317 (2001) 236-240.
- [104] J. Wang, J. Li, S. Yip, S. Phillpot, D. Wolf, Mechanical instabilities of homogeneous crystals, Physical Review B, 52 (1995) 12627.
- [105] J. Wang, J. Li, S. Yip, D. Wolf, S. Phillpot, Unifying two criteria of Born: Elastic instability and melting of homogeneous crystals, Physica A: Statistical Mechanics and its Applications, 240 (1997) 396-403.
- [106] Y.I. Frenkel, Introduction to the theory of metals, Metallurgizdat, (1972) 424.
- [107] H. Eyring, M.S. Jhon, Significant liquid structures, New York: Wiley, 1969.
- [108] J. Frenkel, Kinetic theory of liquids, Dover New York, 1959.
- [109] L.W. Wang, L. Zhang, K. Lu, Vacancy-decomposition-induced lattice instability and its correlation with the kinetic stability limit of crystals, Philosophical Magazine Letters, 85 (2005) 213-219.
- [110] K. Lu, Y. Li, Homogeneous nucleation catastrophe as a kinetic stability limit for superheated crystal, Physical Review Letters, 80 (1998) 4474.
- [111] J.E. Lennard-Jones, A.F. Devonshire, Critical and co-operative phenomena. III. a theory of melting and the structure of liquids, Proceedings of the Royal Society of London. Series A, Mathematical and Physical Sciences, 169 (1939) 317-338.

- [112] N.F. Mott, Imperfections in nearly perfect crystals, National Research Council Symposium, Wiley, 1952, pp. 173.
- [113] S. Mizushima, Dislocation model of liquid structure, Journal of the Physical Society of Japan, 15 (1960) 70-77.
- [114] A. Ookawa, A model theory of liquid, Journal of the Physical Society of Japan, 15 (1960) 2191-2197.
- [115] R. Cotterill, E. Jensen, W.D. Kristensen, A molecular dynamics study of the melting of a three-dimensional crystal, Physics Letters A, 44 (1973) 127-128.
- [116] R. Cotterill, J. Madsen, Crystal instability and melting, Nature, 299 (1982) 188.
- [117] J.W. Frenken, P.M. Marée, J.F. van der Veen, Observation of surface-initiated melting, Physical Review B, 34 (1986) 7506.
- [118] D.W. Oxtoby, New perspectives on freezing and melting, Nature, (1990) 725-730.
- [119] D. Tolla, D. Francesco, T. Erio, E. Furio, Interplay of melting, wetting, overheating and faceting on metal surfaces: theory and simulation, Conference Proceedings-Italian Physical Society, Editrice Compositori, 1996, pp. 345-400.
- [120] Q.S. Mei, K. Lu, Melting and superheating of crystalline solids: from bulk to nanocrystals, Progress in Materials Science, 52 (2007) 1175-1262.
- [121] W.I. Pumphrey, J.V. Lyons, The behaviour the crystal boundaries of aluminium at temperatures near the melting point, Aluminium Development Association, 1953.
- [122] A.M. Alsayed, M.F. Islam, J. Zhang, P.J. Collings, A.G. Yodh, Premelting at defects within bulk colloidal crystals, Science, 309 (2005) 1207-1210.
- [123] P.N. Pusey, Freezing and melting: Action at grain boundaries, Science, 309 (2005) 1198-1199.
- [124] K. Myhra, A phase field crystal study of freezing and melting, University of Oslo, 2011.
- [125] D. Webster, The effect of low melting point impurities on the properties of aluminum-lithium alloys, Metallurgical Transactions A, 18 (1987) 2181-2193.
- [126] [www.npl.co.uk/npl/cmmmt/mtdata](http://www.npl.co.uk/npl/cmmmt/mtdata), 08/10/2013.
- [127] A. Borgenstam, L. Höglund, J. Ågren, A. Engström, DICTRA, a tool for simulation of diffusional transformations in alloys, Journal of Phase Equilibria, 21 (2000) 269-280.
- [128] J.O. Andersson, T. Helander, L. Höglund, P. Shi, B. Sundman, Calphad-based ThermoCalc and DICTRA method, Calphad, 26 (2002) 273-312.
- [129] J. Ågren, Thermodynamics and diffusion coupling in alloys: application-driven science, Metallurgical and Materials Transactions A, 43 (2012) 3453-3461.

- [130] <http://www.crct.polymtl.ca/sgte/index.php?how=1&calphad=1>, 02/08/2013.
- [131] [http://www.thermocalc.com/res/Manuals/Thermo-Calc\\_UsersGuide.pdf](http://www.thermocalc.com/res/Manuals/Thermo-Calc_UsersGuide.pdf), 03/08/2013.
- [132] [http://www.thermocalc.com/res/Manuals/TC\\_databaseguide.pdf](http://www.thermocalc.com/res/Manuals/TC_databaseguide.pdf), 05/08/2013.
- [133] [http://www.thermocalc.com/res/pdfDICTRAflyers/DICTRA27\\_UsersGuide.pdf](http://www.thermocalc.com/res/pdfDICTRAflyers/DICTRA27_UsersGuide.pdf), 05/08/2013.
- [134] P.J. Spencer, A brief history of CALPHAD, *Calphad*, 32 (2008) 1-8.
- [135] <http://www.thermocalc.com/products-services/software/dictra/>, 20/01/2015.
- [136] M. Hillert, Phase equilibria, phase diagrams, and phase transformations: their thermodynamic basis, 2nd Edition, Cambridge University Press, 2007.
- [137] S. Crusius, G. Inden, U. Knoop, L. Höglund, J. Ågren, On the numerical treatment of moving boundary problems, *Zeitschrift für Metallkunde*, 83 (1992) 673-678.
- [138] A. Schneider, G. Inden, Computer simulation of diffusion controlled phase transformations, *Continuum Scale Simulation of Engineering Materials: Fundamentals-Microstructures-Process Applications*, (2004) 1-36.
- [139] M.I. Pope, M. Judd, *Differential thermal analysis: a guide to the technique and its applications*, Heyden, 1977.
- [140] R.C. Mackenzie, *Differential thermal analysis*, Academic Press, 1970.
- [141] S.W. Chen, C.C. Lin, C. Chen, Determination of the melting and solidification characteristics of solders using differential scanning calorimetry, *Metallurgical and Materials Transactions A*, 29 (1998) 1965-1972.
- [142] G. Hähne, W.F. Hemminger, H.J. Flammersheim, *Differential scanning calorimetry*, 2nd Edition, Springer, 2003.
- [143] D. Larouche, C. Laroche, M. Bouchard, Analysis of differential scanning calorimetric measurements performed on a binary aluminium alloy, *Acta Materialia*, 51 (2003) 2161-2170.
- [144] H.B. Dong, J.D. Hunt, A numerical model of a two-pan heat flux DSC, *Journal of Thermal Analysis and Calorimetry*, 64 (2001) 167-176.
- [145] H.B. Dong, J.D. Hunt, A numerical model for a heat flux DSC: determining heat transfer coefficients within a DSC, *Materials Science and Engineering: A*, 413 (2005) 470-473.
- [146] *Metals handbook*, vol. 15, ASM, Metals Park, OH, 1985, p.182
- [147] H.B. Dong, Development of a novel scanning calorimeter and its application in solidification study, 2000.

- [148] H.B. Dong, M.R.M. Shin, E.C. Kurum, H. Cama, J.D. Hunt, Determination of liquid fraction during solidification of aluminium alloys using a single-pan scanning calorimeter, *Fluid phase equilibria*, 212 (2003) 199-208.
- [149] H.B. Dong, M.R.M. Shin, E.C. Kurum, J.D. Hunt, H. Cama, A study of microsegregation in Al-Cu using a novel single-pan scanning calorimeter, *Metallurgical and Materials Transactions A*, 34 (2003) 441-447.
- [150] B.E. Warren, *X-ray diffraction*, Courier Dover Publications, 1969.
- [151] B.D. Cullity, *Elements of X-ray diffraction*, 3rd Edition, Addison-Wesley, 2001.
- [152] M. Ohring, *Engineering materials science*, Academic Press, 1995.
- [153] J. Williams, *Engineering tribology*, 3rd Edition, Cambridge University Press, 2005.
- [154] <http://www.thermocalc.com/products-services/databases/thermodynamic>, 09/06/2013.
- [155] G. Wallace, A.P. Jackson, S.P. Midson, Q. Zhu, High-quality aluminum turbocharger impellers produced by thixocasting, *Transactions of Nonferrous Metals Society of China*, 20 (2010) 1786-1791.
- [156] J.G. Kaufman, E.L. Rooy, *Aluminum alloy castings: properties, processes, and applications*, ASM International, 2004.
- [157] <http://www.thermocalc.com/products-services/databases/mobility>, 08/09/2013.
- [158] <http://www.webelements.com/>, 07/08/2013.
- [159] W.F. Gale, T.C. Totemeier, *Smithells metals reference book*, 8th Edition, Elsevier Science, 2003.
- [160] Y. Du, Y.A. Chang, B. Huang, W. Gong, Z. Jin, H. Xu, Z. Yuan, Y. Liu, Y. He, F.Y. Xie, Diffusion coefficients of some solutes in fcc and liquid Al: critical evaluation and correlation, *Materials Science and Engineering: A*, 363 (2003) 140-151.
- [161] H. Li, L. Salamanca-Riba, The concept of high angle wedge polishing and thickness monitoring in TEM sample preparation, *Ultramicroscopy*, 88 (2001) 171-178.
- [162] P.J. Heaney, E.P. Vicenzi, L.A. Giannuzzi, K.J. Livi, Focused ion beam milling: a method of site-specific sample extraction for microanalysis of Earth and planetary materials, *American Mineralogist*, 86 (2001) 1094-1099.
- [163] <http://www.bruker.com/products/x-ray-diffraction-and-elemental-analysis/x-ray-diffraction/xrd-software/overview/eva.html>, 05/09/2013.
- [164] <http://www.bruker.com/products/x-ray-diffraction-and-elemental-analysis/x-ray-diffraction/xrd-software/overview/topas.html>, 06/09/2013.

- [165] F. Czerwinski, A. Zielinska-Lipiec, P.J. Pinet, J. Overbeeke, Correlating the microstructure and tensile properties of a thixomolded AZ91D magnesium alloy, *Acta Materialia*, 49 (2001) 1225-1235.
- [166] A.K. Gupta, A.K. Jena, M.C. Chaturvedi, Insoluble phase in Al-1.52Cu-0.75Mg alloys containing silicon, *Materials Science and Technology*, 3 (1987) 1012-1018.
- [167] S. Shivkumar, S. Ricci, C. Keller, D. Apelian, Effect of solution treatment parameters on tensile properties of cast aluminum alloys, *Journal of Heat Treating*, 8 (1990) 63-70.
- [168] A. Samuel, J. Gauthier, F. Samuel, Microstructural aspects of the dissolution and melting of Al<sub>2</sub>Cu phase in Al-Si alloys during solution heat treatment, *Metallurgical and Materials Transactions A*, 27 (1996) 1785-1798.
- [169] D. Zhang, H.V. Atkinson, H.B. Dong, Q. Zhu, Comparison between prediction of liquid fraction versus temperature and experimental results from DSC and SPSC, *Solid State Phenomena*, 217-218 (2015) 442-449.
- [170] A.T. Dinsdale, SGTE data for pure elements, *Calphad*, 15 (1991) 317-425.
- [171] Thermocalc software AB, Stockholm Sweden, 2006.
- [172] J. Gröbner, H.L. Lukas, F. Aldinger, Thermodynamic calculation of the ternary system Al-Si-C, *Calphad*, 20 (1996) 247-254.
- [173] X.G. Lu, M. Selleby, B. Sundman, Assessments of molar volume and thermal expansion for selected bcc, fcc and hcp metallic elements, *Calphad*, 29 (2005) 68-89.
- [174] I. Ansara, A.T. Dinsdale, M.H. Rand, COST 507-final report: thermodynamic database for light metal Al-alloys, 1998.
- [175] N. Saunders, A review and thermodynamic assessment of the Al-Mg and Mg-Li Systems, *Calphad*, 14 (1990) 61-70.
- [176] H.A. Oonk, CALPHAD XXXIV 2005 conference summary, *Calphad*, 30 (2006) 97-130.
- [177] P. Gupta, What is process window?, *ACM SIGDA Newsletter*, 40 (2010) 1-1.
- [178] O. Lashkari, R. Ghomashchi, Deformation behavior of semi-solid A356 Al-Si alloy at low shear rates: effect of fraction solid, *Materials Science and Engineering: A*, 486 (2008) 333-340.
- [179] G.H. Rodway, J.D. Hunt, Thermoelectric investigation of solidification of lead I. pure lead, *Journal of crystal growth*, 112 (1991) 554-562.
- [180] G.H. Rodway, J.D. Hunt, Thermoelectric investigation of solidification of lead II. lead alloys, *Journal of crystal growth*, 112 (1991) 563-570.

## Appendices

### ***Appendix A: Code for DICTRA Solidification Simulation (Al-Si Alloy)***

```
go da
@@-----Select database thermodynamic databases
@@-----Define system
@@-----Reject previous phases and select phases for computation
sw
ttal7
def-sys Al Si
rej_ph * all
rest-ph liq fcc
get
@@----- Select mobility database
app mob2
def-sys al si
rej_ph * all
rest-ph liq fcc
get
@@----- Enter Dictra Monitor
go d-m
set_cond glob T 0
973.15-time*0.16667;
1800
y
673;
*
n
@@-----Enter grid
enter-region smalta
enter-grid
smalta
1e-4
double
60
1.11
0.9
@@-----Enter Active/Inactive phases
ent-ph act smalta matrix liq
ent-ph inact smalta yes fcc al 1e-5 closed
enter-phase inact smalta no diamond si 1e-5
@@-----Enter Compositions using .dat files
ent-comp smalta liq al w-p
si
read si_profiles.dat
@@-----set-time for simulation
```

```
s-s-tim 2000 yes 1,,,,,,,,,
s-s-c 0 1 2 yes,n,,,,,,,,
save al_si y
sim
@@-----Open post processor
post
set-title Al-Si
enter func fs=1-ivv(liquid);
s-d-a y ivv(liq)
s-d-a x t-c
set-axis-text y n Liquid_Fraction
s-p-c interf smalta lower
la_cu y
set-inter
pl
```



## ***Appendix B Code for DICTRA Solidification Simulation (Al-Cu Alloy)***

```
go da
@@-----Select database thermodynamic databases
@@-----Define system
@@-----Reject previous phases and select phases for computation
sw
ttal7
def-sys Al Cu
rej_ph * all
rest-ph liq fcc
get
@@-----Select mobility database
app mob2
def-sys al cu
rej_ph * all
rest-ph liq fcc
get
@@-----Enter Dictra Monitor
go d-m
set_cond glob T 0
973.15-time*0.16667;
1800
y
673;
*
n
@@-----Enter grid
enter-region smalta
enter-grid
smalta
1e-4
double
60
1.11
0.9
@@-----Enter Active/Inactive phases
ent-ph act smalta matrix liq
ent-ph inact smalta no fcc,,
@@-----Enter Compositions using .dat files
ent-comp smalta liq al w-p
cu
read cu_profiles.dat
@@-----set-time for simulation
s-s-tim 2000 yes 1,,,,,,,,,
s-s-c 0 1 2 yes,n,,,,,,,,
save al_si y
sim
```

```
@ @-----Open post processor
post
set-title Al-Cu
enter func fs=1-ivv(liquid);
s-d-a y ivv(liq)
s-d-a x t-c
set-axis-text y n Liquid_Fraction
s-p-c interf smalta lower
la_cu y
set-inter
pl
```

### ***Appendix C Code for DICTRA Solidification Simulation (Al-Mg Alloy)***

```
go da
@@-----Select database thermodynamic databases
@@-----Define system
@@-----Reject previous phases and select phases for computation
sw
ttal7
def-sys Al Mg
rej_ph * all
rest-ph liq fcc
get
@@-----Select mobility database
app mob2
def-sys al mg
rej_ph * all
rest-ph liq fcc
get
@@-----Enter Dictra Monitor
go d-m
set_cond glob T 0
973.15-time*0.16667;
1800
y
673;
*
n
@@-----Enter grid
enter-region smalta
enter-grid
smalta
1e-4
double
60
1.11
0.9
@@-----Enter Active/Inactive phases
ent-ph act smalta matrix liq
ent-ph inact smalta no fcc,,
@@-----Enter Compositions using .dat files
ent-comp smalta liq al w-p
mg
read mg_profiles.dat
@@-----set-time for simulation
s-s-tim 2000 yes 1,,,,,,,,,
s-s-c 0 1 2 yes,n,,,,,,,,
save al_si y
sim
```

```
@ @-----Open post processor
post
set-title Al-Mg
enter func fs=1-ivv(liquid);
s-d-a y ivv(liq)
s-d-a x t-c
set-axis-text y n Liquid_Fraction
s-p-c interf smalta lower
la_cu y
set-inter
pl
```

### ***Appendix D Code for DICTRA Heating Simulation (Al-5.08wt%Si Alloy)***

```
go da
@@-----SELECT THERMODYNAMIC DATABASE
sw
ttal7
@@-----DEFINE WHAT SYSTEM WE WANT TO WORK WITH
def-species al si
@@ EXCLUDE THE THERMODYNAMIC DATA FOR THE PHASES
rej ph /all
res ph fcc liq diamond
@@-----RETRIEVE DATA FROM DATABASE FILE
get
@@----- SWITCH TO MOBILITY DATABASE AND APPEND DATA
app
mob2
def-sys al si
rej ph /all
res ph fcc liq
get
@@ -----ENTER THE DICTRA MONITOR
go d-m
@@----- ENTER GLOBAL CONDITION T.
@@ -----LET US LOWER THE TEMPERATURE WITH A RATE OF 1 K/S
set_cond glob T 0
850.15+time*1;
*
n
@@----- ENTER A REGION CALLED smalta
enter-region smalta
@@----- ENTER A DOUBLE GEOMETRIC GRID INTO THE REGION.
enter-grid
smalta
1e-4
double
60
1.11
0.9
@@-----ENTER ACTIVE PHASES INTO REGION
enter-phase
act
smalta
matrix
fcc
@@----- ENTER INACTIVE PHASES INTO REGION
enter-phase
inact
smalta
```

```

yes
liq
al
1e-5
closed

enter-phase
inact
smalta
no
diamond
si
1e-5
@@----- ENTER START COMPOSITION
enter-composition
smalta
fcc
al
w-p
si lin 5.08 5.08
@@ SET THE SIMULATION TIME
set-simulation-time
300
@@----- CHECK INTERFACE POSSITION
s-s-c
yes
no
@@----- SAVE THE SETUP ON A NEW STORE FILE AND EXIT DICTRA
save 508si Y
set-inter
exit
@@-----Open post processor
post
set-title Al-5_08Si
enter func fs=1-ivv(liquid);
s-d-a y fs
s-d-a x t-c
set-axis-text y n Liquid_Fraction
s-p-c interf smalta lower
la_cu y
set-inter, pl

```

***Appendix E Code for DICTRA Re-heating Simulation (Al-5.08wt%Si Alloy)***

```
go da
@@----- SELECT THERMODYNAMIC DATABASE
sw
ttal7
@@ DEFINE WHAT SYSTEM WE WANT TO WORK WITH
def-species al si
@@ EXCLUDE THE THERMODYNAMIC DATA FOR THE PHASES
rej ph /all
res ph fcc liq diamond
@@ RETRIEVE DATA FROM DATABASE FILE
get
@@ SWITCH TO MOBILITY DATABASE AND APPEND DATA
app
mob2
def-sys al si
rej ph /all
res ph fcc liq
get
@@ ENTER THE DICTRA MONITOR
go d-m
@@ ENTER GLOBAL CONDITION T.
@@ LET US LOWER THE TEMPERATURE WITH A RATE OF 1 K/S
set_cond glob T 0
850.15+time*1;
*
n
@@ ENTER A REGION CALLED smalta
enter-region smalta
@@ ENTER A DOUBLE GEOMETRIC GRID INTO THE REGION.
enter-grid
smalta
1e-4
double
60
1.11
0.9
@@ ENTER ACTIVE PHASES INTO REGION
enter-phase
act
smalta
matrix
liq
@@ ENTER INACTIVE PHASES INTO REGION
enter-phase
```

```

inact
smalta
yes
fcc
al
1e-5
closed
enter-phase
inact
smalta
no
diamond
si
1e-5
@@ ENTER START COMPOSITION
enter-composition
smalta
liq
al
w-p
si lin 5.08 5.08
@@ SET THE SIMULATION TIME
set-simulation-time
300
@@ CHECK INTERFACE POSSITION
s-s-c
yes
no
@@ SAVE THE SETUP ON A NEW STORE FILE AND EXIT DICTRA
save 508si Y
set-inter
exit
@@-----Open post processor
post
set-title Al-5_08Si
enter func fs=1-ivv(liquid);
s-d-a y fs
s-d-a x t-c
set-axis-text y n Liquid_Fraction
s-p-c interf smalta lower
la_cu y
set-inter, pl

```